Low-Reynolds Number Direct Numerical Analysis of an Iced NLF-0414 Airfoil

François Lepage

Thesis submitted to the University of Ottawa
in partial fulfillment of the requirements for the degree of

Master of Applied Science
in Mechanical Engineering

Department of Mechanical Engineering
Faculty of Engineering
University of Ottawa

Abstract

A Direct Numerical Simulation of an iced Natural Laminar Flow NLF-0414 airfoil is carried out using a high-order spectral element method for low chord Reynolds numbers ($O(10^5)$). This study aims to advance the state-of-the-art for accurate computational modeling of transition, iced airfoil aerodynamics, and irregular surface spectral element method Direct Numerical Simulation. Ice accretion over an aircraft, ranging from light to severe, changes the aerodynamic profile of the airfoil and alters the overall performance. The literature presents simulations that have been carried out with a range of turbulence models which fail to accurately capture the complex physics of these flows. The iced profiles being studied, Run 606 and 622-2D, were obtained from a Technical Publication by NASA on iced airfoils including the NLF-0414, and were selected as they are relatively lightly iced profiles of the NLF-0414. The largest bottleneck with the current advancement in High Performance Computing is the computation time required for Direct Numerical Simulation. Results such as lift, drag, pressure, and skin friction coefficients, for a clean NLF-0414 and two lightly iced NLF-0414 airfoils at chord Reynolds numbers of $Re_c = 1\text{x}10^5$ and $Re_c = 2\text{x}10^5$ are visualized and discussed, showing the degradation of the natural laminar flow due to ice accretion. Turbulence statistics are calculated to study the effective contributions of turbulent fluctuations in the flow to further understand the flow physics near transition. The detailed study of these six cases has led us to 1) further understand the complexities of the transition process on iced airfoils, 2) observe and explain the sometimes unexpected changes in aerodynamic performance due to varying iced geometries, and 3) establish a methodology for spectral element method Direct Numerical Simulations.

Keywords : Direct Numerical Simulation, Spectral Element Method, High-Order Numerical Methods, Icing, Natural Laminar Flow, Transition to Turbulence

Acknowledgements

I would like to thank my Supervisor Dr. Catherine Mavriplis for guiding me through my masters studies and helping me thru the many hurdles that I faced with her abundant knowledge. I would also like to thank Dr. Gbemeho Agbaglah for helping me troubleshoot anything related to LINUX, my code, and Nek5000 [1].
This research was supported by the Natural Sciences and Engineering Research Council of Canada through Discovery Grant (RGPIN-2017-05320). This research was enabled in part by support provided by Compute Ontario [2] and Compute Canada [3]. I would like to thank Compute Canada for allocating Resources for Research Groups (RRG) (RRG-mavripli id-3435) and for technical support.

Contents

List of Figures

List of Tables

Nomenclatures

Upper-case Roman

C_d	drag coefficient
C_f	skin friction coefficient
C_l	lift coefficient
C_p	pressure coefficient
Re_c	chord Reynolds number

Lower-case Roman

c	chord
y^+	dimensionless wall distance

Lower-case Greek

μ dynamic viscosity

ρ density

Abbreviations

2D	two-dimensional
3D	three-dimensional
AMG	Algebraic Multigrid
AOA	Angle of Attack
APG	adverse pressure gradient
BDFk	k-step Backward-Difference
BL	Boundary Layer
CCW	Counter-Clockwise
CFD	Computational Fluid Dynamics
CFL	Courant Friedrichs Lewy
CW	Clockwise
DES	detached eddy simulation
DNS	Direct Numerical Simulation
EXTk	k-th order Extrapolation
FDM	Finite Difference Method
FEM	Finite Element Method
FENSAP	Finite Element Navier-Stokes Analysis Package
FVM	Finite Volume Method
HPC	high performance computing
LE	Leading Edge
LES	Large Eddy Simulation
N-S	Navier-Stokes
NASA	National Aeronautics and Space Administration
NLF	Natural Laminar Flow
PDE	Partial Differential Equations
RANS	Reynolds-Averaged Navier-Stokes
RRG	Resources for Research Groups
S-A	Spalart-Allmaras
SAS	scale adaptive simulation
SEM	Spectral Element Method
SM	Spectral Method
SRS	scale resolving simulation
SST	Shear Stress Turbulence
TE	Trailing Edge
TP	Technical Publication
URANS	unsteady Reynolds-Averaged Navier-Stokes

1 Introduction

1.1 Motivation

The inspiration behind this research stems from the growing drive from industry and academia to understand the flow physics for iced airfoils. With the current advancement in high performance computing (HPC) more robust Computational Fluid Dynamics (CFD) methods such as Direct Numerical Simulation (DNS) can be used to overcome the inability to accurately and reliably predict complex flow physics [4]. Furthermore, the availability of the open-source high order spectral element DNS code Nek5000 [1] allows for high precision simulation with a highly scalable structure for cost efficient higher Reynolds numbers simulations. Nek5000 has been used in many different fields, from nuclear engineering to biomedical device simulation, including a few calculations of flow over airfoils and wings, but has not been previously used on iced airfoils due to their irregular surface characteristics. Ideally the goal is to prove that the often said unforgiving spectral element DNS code is able to properly simulate the flow physics for uneven geometries while giving insight on the effects of ice accretion in low Reynolds number flights.

The roughness induced by ice accretion on airfoils is known to accelerate transition to turbulence via separation bubbles and turbulent reattachment. Transition prediction remains a challenge for computational aerodynamics. High precision DNS codes are necessary for such predictions as turbulence models in general do not model the process, with the exception of the Langtry-Menter 4-equation Transitional Shear Stress Turbulence (SST) Model [5] [6], which still needs to be validated with DNS and experimental transition studies.

A second motivation for this work is therefore to demonstrate the accurate and detailed analysis of transition using a high order DNS code. In so doing, we respond to NASA's CFD Vision 2030 goals [4]. In 2014, NASA's Vision 2030 report outlined the state-of-the-art in computational analysis in the aerosciences, explained the limitations at the time and set out recommendations for the next 16 years. While DNS was not considered achievable by 2030 in the report, lower-fidelity Large Eddy Simulation (LES) and other hybrid Reynolds-Averaged Navier-Stokes (RANS)/LES models are still considered to be in low technology readiness levels. Integrated separation and transition prediction capabilities are targeted in the report for significant development over the next decades. This study aims to advance the state-of-the-art for accurate computational modeling of transition and iced airfoil aerodynamics, as well as DNS.

1.2 Aircraft Flight Certification

Aircraft flight certification upholds very strict design and safety regulations that have changed substantially in recent years and are ever changing. Flight safety can be split into three factors [7] : human, environment, and machine. Most accidents come down to human error but are usually a combination of all three factors. Ice accretion (an environmental factor) is one major cause of accidents and has caused certification authorities to have stricter requirements concerning aircraft operations [8] [9] [10]. Ice accretion has also brought attention to surface roughness studies in aircraft flight.

Furthermore, there is a current push in aircraft design and testing to develop a "certification by analysis" process whereby a mathematical or numerical model, as a basis for computational simulation of a physical phenomena, is used in the certification process in place of experiments or flight tests. The push to use certification by analysis applies to various different areas (structural design, in-flight simulations, flight safety, engine design, extreme or abnormal operating conditions) with the goal of improving the efficiency and reducing the amount of physical testing required in the design and development process [11]. Having validated certification by analysis would be beneficial in physical testing conditions, such as icing prediction and analysis, where the conditions are practically impossible or too costly to reproduce. Ideally costly wind tunnel testing could be largely replaced with testing by computational analysis [12]. A CFD-based approach to largely replace wind tunnel testing would remove the need for scaling or similitude studies, eliminate any experimental inaccuracies associated with using tunnels, and improve the multidisciplinary collaboration between testing and design largely reducing costs and certification times [13]. For that to be possible, accurate computational modeling and prediction of iced airfoils will be necessary. This push for certification by analysis in aircraft design and testing falls inline with goals stated in NASA's CFD Vision 2030 Study [4].

1.3 Ice Accretion

Ice accretion over an aircraft, ranging from light to severe, changes the aerodynamic profile of the airfoil and has negative effects on the overall performance. The largest amount of ice buildup is found on the Leading Edge (LE) of the airfoil and comes in different types and shapes. The LE geometry of an airfoil is critical for determining aerodynamic characteristics such as lift, drag and stall angle. Ice accretion tends to increase drag, decrease lift and stall angle by changing the airfoil geometry. Many experiments have been performed in the past looking at different ice shapes and their effects on the aerodynamic performance. Experimental results are hard to obtain as icing conditions are difficult and costly to simulate in the laboratory on a large scale. Small scale experiments have to be performed on various different airfoils for various icing shapes and icing conditions. In most cases the experiments are limited to simpler airfoils such as the NACA-0012. NASA has produced a large database of experimental results. More specifically, they produced results for three modern airfoils [14]: a business jet airfoil profile, a commercial transport airfoil profile, and a general aviation airfoil profile. This work will be looking at the general aviation airfoil, the Natural Laminar Flow (NLF) NLF-0414.

1.3.1 Types of Accretion

Ice accretion is characterized by two different types of ice formation known as Rime ice and Clear (Glaze) ice. Rime ice is formed when supercooled droplets freeze on impact with the surface of the aircraft. Rime ice has an opaque milky white colour because it traps air within the ice [9] [15]. Rime ice usually occurs in colder temperatures with small sized droplets. Rime ice is less dense than its counterpart clear ice. Clear ice occurs in near freezing temperatures ($0°C$) with large droplets. The large droplets impact the surface of the aircraft but do not freeze immediately on contact. Instead they partially freeze and run-back along

the surface of the aircraft. This is in part caused by the latent heat released from the initial freezing and the kinetic energy at the LE of the airfoil. The ice is transparent and usually grows in irregular shapes sometimes consisting of one or two horns. There is also mixed ice which is a mix of both rime and glaze ice. All three types of ice can take various different shapes as shown in Figure 1.

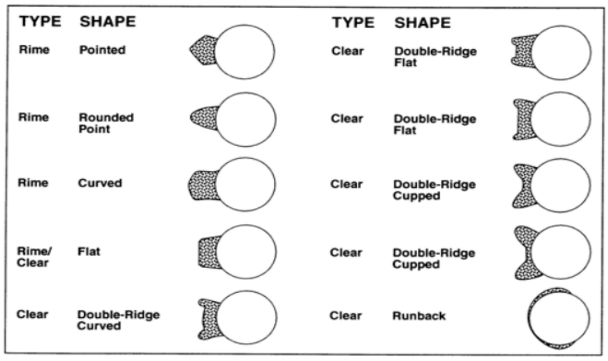

Figure 1: Ice Shapes and Types Observed on a Cylinder in the NASA Icing Wind Tunnel [16]

1.4 Natural Laminar Flow Airfoil

Natural Laminar Flow airfoils are designed to sustain laminar flow as long as possible at low to high Reynolds numbers. Sustaining laminar flow greatly reduces drag, resulting in better fuel efficiency. In most cases NLF airfoils are designed iteratively based on desired parameters such as pressure distribution or velocity distribution [17]. The NLF-0414 has a minimum lift coefficient (C_l) of 0.4 with a maximum thickness of 14% chord (c). The NLF-0414 airfoil design objectives were to achieve a 70% chord natural laminar flow on both surfaces at Re_c = 10x10^6 [18]. Another design objective was to achieve significantly lower profile drag coefficients (C_d) at cruise than existing NLF airfoils. To achieve these objectives designers used a thick LE for increased C_l, a thin Trailing Edge (TE) for a low drag C_l range, and a concave pressure recovery area to reduce turbulent separation problems during transition. The NACA 67-314 airfoil has similar flight conditions as the desired NLF-0414 conditions and is used to highlight design improvements through comparison. Figure 2 shows a comparison between the pressure distribution of the NLF-0414 and the NACA 67-314 airfoils in terms of pressure coefficient (C_p). A thicker leading edge and the desired concave pressure recovery area are illustrated in Figure 2.

Most applications of the NLF-0414 airfoil involve general aviation purposes, for which Re_c = 1x10^6 to 10x10^6, but it is also used in other fields such as a high lift low drag race car wing for which $Re_c < O(10^5)$ [19]. Our choice of the NLF airfoil allows us to concentrate on the impact of icing on transition: its changed location on the airfoil and pertinent quantities such as the pressure distribution shown in Figure 2 and the skin friction coefficient (C_f) as will be shown in Section 5.4.3.

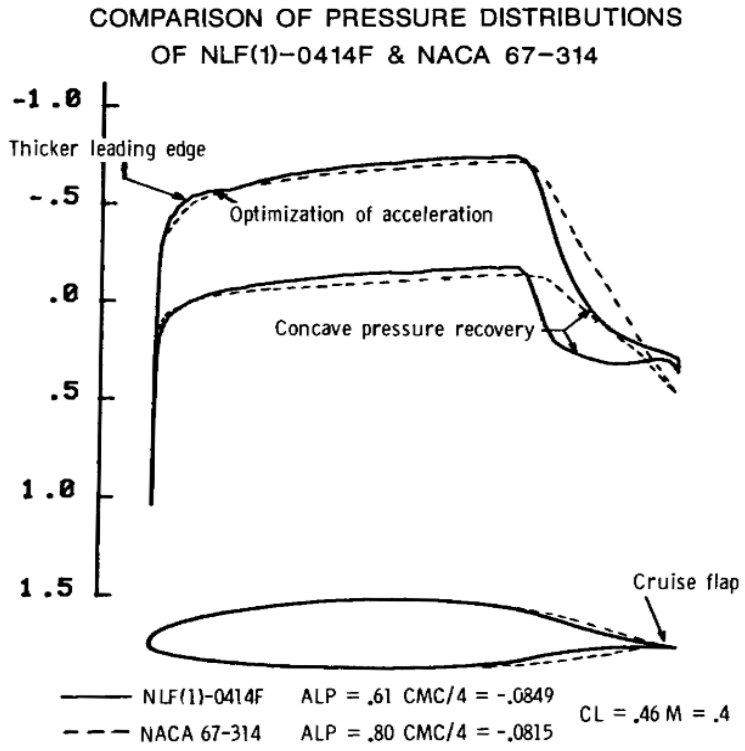

Figure 2: Comparison of Pressure Distributions for the NLF-0414F and the NACA 67-314 airfoils [18]

1.5 Thesis Outline

This research aims to analyze the low Reynolds number effects of ice accretion on an NLF-0414 airfoil by way of Direct Numerical Simulation (DNS) by using a high-order Spectral Element Method (SEM). This thesis is separated into chapters as described below.

Section 2 presents previous work related to the present study: simulations of iced airfoils, including the NLF-0414, using other methods than DNS, some DNS work (without icing) with and without SEM, and currently used ice accretion codes that have been developed. Section 2 also gives some theoretical background on the numerical methods used as well as an overview of the open-source code used. Section 3 covers the methodology used for the iced airfoil two-dimensional (2D) grid generation and the parameters used to set up the DNS 2D simulations. Section 4 covers the domain and grid resolution study. Results such as aerodynamic characteristics, velocity profiles, and turbulence statistics are discussed in Section 5. Lastly, a conclusion of the present work can be found in Section 6.

2 Literature and Background

2.1 Literature

2.1.1 Iced NLF-0414

Chung and Addy [20], of the NASA Glenn Research Center, looked at a numerical evaluation of icing effects on the Natural Laminar Flow airfoil NLF-0414. They compared experimental data from a 6 and 22.5 minute ice accretion run to computational data from the NASA WIND code. WIND is a finite volume Navier-Stokes (N-S) solver. The simulation was run in 2D. Simulations over a range of $Re_c = 3\text{x}10^6$ to $10\text{x}10^6$ were computed using turbulence models with the best results coming from the Spalart-Allmaras (S-A) and SST turbulence models. Lift characteristics show good agreement at the higher Reynolds number range and poorer agreement at the lower Reynolds number range. Lift coefficients show good agreement at lower Angle of Attack (AOA) but lose precision closer to stall. Pressure distribution is well captured for the 6 minute iced run but shows relatively poor agreement with the 22.5 minute iced run. In all cases the use of turbulence models shows relatively poor agreement with the experimental results.

Mirzaei et al. [21] analyzed the flow field characteristics around a large horned iced NLF-0414 in the chord Reynolds number of $Re_c = 0.5\text{x}10^6$ and $Re_c = 1.8\text{x}10^6$ at AOA of 0° to 6°. They discretized the incompressible N-S equations using a Finite Volume approach as well as using the $k - \epsilon$ turbulence model. The results are problematic near stall but show relatively good agreement with the experimental data. The numerical results show overshoot for both reattachment location and turbulence intensity when compared to the experimental results.

Ebrahimi et al. [22] investigated the effects that a large double horned ice geometry has on the aerodynamic performance of the NLF-0414. The ice profile, a 15 minute spray run, is pulled from the NASA Lewis Research Center database. Pressure distribution results were evaluated at AOA of -2° to 6° for a Reynolds number of $Re = 0.7\text{x}10^6$. They show that the iced shape negatively affects the aerodynamic characteristics due to the change in pressure distribution caused by the separation bubbles found on the top and bottom surfaces.

Broeren and Bragg [23] analyzed the effects of airfoil geometry on performance with simulated intercycle ice accretions. They analyzed the iced profiles, using wing-tunnel testing, of a NACA 23012, NACA 3415, and NLF-0414 at $Re = 1.8\text{x}10^6$. Results show a 13% and 27% reduction in C_l for the NACA 23012 and NLF-0414 respectively when comparing their clean C_l to the iced C_l. They point out that the ice has the effect of changing the pressure distribution on the suction side of the airfoil which reduces the amount of lift it can produce.

2.1.2 DNS

We could not find any DNS simulations of iced airfoils in the literature. There is a small number of DNS simulations of airfoils and wings in the literature. Among them, we cite Balakumar [24], who studied the DNS of flows over the NACA-0012 airfoil for a chord Reynolds number of $Re_c = 50\text{x}10^3$ and $Re_c = 1\text{x}10^6$ at an AOA of 5° and 15° respectively. He used a body-fitted O-type curvilinear grid system with a radius of 15 chords with 3001x501

points around the airfoil in 2D and 3001x501x201 points in three-dimensional (3D). He solved the 3D unsteady compressible N-S equations in conservation form using higher order compact schemes with domain decomposition. The results show the effects that the different terms in the turbulent kinetic-energy balance equations have on the flow. They especially look at the turbulence statistics around the separation bubble and how they change downstream.

Vinuesa et al. [25] studied the DNS of the flow around a wing section using high-order parallel spectral element methods. They simulated the flow over a NACA4412 profile for a chord Reynolds number of $Re_c = 400,000$ at an AOA of 5° using the high-order spectral element code Nek5000 [1], that we also use in this work. They used a C-mesh with a total domain length of 6.2c horizontally, 2c vertically, and 0.1c spanwise. They used an 11^{th} order polynomial in all directions resulting in 3.2x10^7 grid points for a grid of 1.85x10^6 elements. The simulations required 3 million CPU core hours per flow-over time on 16,384 cores on a CrayXC40. Turbulence statistics results show good agreement with other numerical experiments and papers studying turbulent boundary layer flows. They also show that their analysis of the effects of an adverse pressure gradient is consistent with previous analyses.

2.1.3 Computational Fluid Dynamics Ice Accretion Codes

In most cases ice accretion experiments can be expensive and dangerous to execute on a larger scale. For these reasons codes such as FENSAP-ICE and LEWICE have been created to study the ice accretion and to reduce costs. These codes are proven to be able to predict and reproduce experimental results with the use of CFD.

FENSAP-ICE by Habashi et al. : The FENSAP-ICE [26] [27] code uses a combination of four conjugated Partial Differential Equations (PDE) modules to predict ice accretion. The first module, the flow solver, solves the clean and degraded flows via the Finite Element Navier-Stokes Analysis Package (FENSAP). The FENSAP package can solve the viscous N-S equations using the S-A turbulence model. The second module is a droplet flow solver which uses the 3D Eulerian droplet impingement method module DROP3D. DROP3D computes the collection efficiency distribution. The third module is the 3D ice accretion shapes predictor module ICE3D that uses the shallow-water icing model. The last module is the conjugate heat transfer problem solver module CHT3D that calculates the heat flux in the metal skin. This code has been used to predict ice accretion on helicopter rotors [28] and rotorcraft engine air intakes [29] to show advancements in multiphase modeling.

LEWICE by NASA : The LEWICE [30] software, version 3.2, uses four main modules to 1) solve the clean and iced flow field, 2) calculate the particle (droplet) trajectory and impingement, 3) calculate the ice growth and thermodynamics, and 4) modify the geometry and mesh by adding the ice growth. The flow field is solved, in 1), on a time-stepping basis as the ice accretion increases in time. The flow can either be solved using a potential flow module or a more accurate and expensive N-S program named WIND [31]. WIND can solve the N-S equations using a delta form node-centered Finite-Volume approach. WIND uses turbulence modeling such as S-A and SST turbulence models. The LEWICE software then combines the results from the flow solver with the other three modules to predict the ice accretion and its aerodynamic characteristics. Most applications of the LEWICE code

analyze the different airfoils that pass through their Glenn Research Center Icing Research Tunnel [32].

These codes concentrate more on ice accretion and impingement predictions with less emphasis on the flow calculation for faster less expensive results at the cost of precision. In most cases the ice accretion predictions are in agreement with experimental results but the flow characteristics such as lift, drag, and stall point lack the precision that other methods like DNS can provide. The lack of precision comes from the flow modeling that fails to capture the small perturbations that arise from the small cracks and crevasses in the ice structure on the surface of the airfoil.

2.2 Numerical Methods

Numerical methods allow us to discretize partial differential equations to simulate fluids flows using computational power. Complex flows and geometries can lead to high computational costs. The equations are discretized in time and space to be more manageable computationally. Depending on the precision required, either DNS, LES, or RANS can be used to model the flow. Most aerodynamic calculations are done with inviscid (Euler) solvers or with N-S solvers coupled with turbulence models. However, the presence of ice severely affects the boundary layer and can cause separation and vortex shedding early along the chord, the details of which cannot be captured by a turbulence model, especially for a NLF airfoil which is designed for laminar flow over most of the chord. We therefore, choose to use DNS to resolve all the features of the flow. For the desired conditions, we choose to study the flow using the incompressible N-S equations.

2.2.1 Incompressible Navier-Stokes

The incompressible Navier-Stokes equations are defined as follows:

$$\nabla \cdot \mathbf{u} = 0, \tag{1}$$

Continuity

$$\rho\big(\frac{\partial \mathbf{u}}{\partial t} + \mathbf{u} \cdot \nabla \mathbf{u}\big) = -\nabla P + \mu\big(\nabla^2 \mathbf{u}\big) + \rho \mathbf{f} \tag{2}$$

Momentum

where ρ is density, $\mathbf{u}$ is the velocity vector(), P is pressure, μ is viscosity,and $\mathbf{f}$ is an external force or forcing function.

2.3 Direct Numerical Simulation

DNS is computationally expensive as it attempts to solve every feature of turbulent flow. Until now DNS has been disregarded for aerodynamic flows due to limited computational resources. With advancements in computing technology DNS is becoming more feasible. This work examines the low Reynolds number ($Re_c = O(10^5)$) aerodynamic performance of 2D iced NLF-0414 airfoils using DNS.

2.3.1 Turbulence Models

Turbulence modeling can be split into two different categories, LES and RANS. LES mainly uses filtered N-S equations for the large scale eddies and uses models to simulate the effects of the small scale eddies. LES is lighter computationally than DNS but is not as accurate. LES is more expensive than RANS but is more accurate. RANS uses mathematical models based on average values to model turbulent behavior. Models can range from one equation models such as the S-A model to two equations models such as the $k-\epsilon$ models, $k-\omega$ models, and SST models. Higher order and more complex models also exist. Within the two different categories there are hybrid methods such as the detached eddy simulation (DES) that uses modified RANS models combined with LES. DES uses RANS to solve near-wall regions and LES to solve the regions that are detached from the wall. An unsteady version of RANS known as unsteady Reynolds-Averaged Navier-Stokes (URANS) is a more complex more computationally-intensive version of RANS. Other combinations of hybrid methods such as scale resolving simulation (SRS) and scale adaptive simulation (SAS) exist and are well explained in work by John Hart [29]. Different models tend to be better in different circumstances based on how the models are developed. RANS is good for low accuracy low computational demand calculations but can miss some parts of the turbulent flow that would be caught with the more computational expensive LES and DNS. In order of complexity and cost these models are: RANS, URANS, hybrid methods (DES, SRS, SAS), LES, and DNS.

Laminar-to-turbulent transition has a large impact on aerodynamic performance, especially on C_f, and is known to be one of the most difficult parts to model properly using turbulent models. DNS is usually used to capture this laminar-to-turbulent transition because it is not case/Reynolds number specific and resolves all the relevant scales and perturbations that lead to transition [33]. LES, as the name implies, solves the large scale turbulence eddies which are a large part of turbulent flow but models the small scale eddies which are a large part of transition [34]. Since the small scale eddies are modeled in LES a lack of precision in transition location occurs which is a critical point of interest for aerodynamic drag. This lack of precision can be seen in work by Lozano-Durán [35] when comparing LES to DNS. RANS is usually avoided for laminar-to-turbulent prediction as it eliminates the effects of linear disturbance growth [34] which leads to missing the transition location completely. The Langtry-Menter 4-equation Transitional SST Model [5] [6] is one exception to using turbulence models in transition prediction as it has been shown to be compatible with modern CFD techniques but still needs to be validated with DNS and experimental studies for airfoil and wing geometries.

2.4 Discretization

The N-S equations can be solved using different methods such as the Finite Difference Method (FDM), Finite Volume Method (FVM), Finite Element Method (FEM), and high order Spectral Method (SM). Each method has its own advantages and disadvantages depending on the type of problem being studied and its desired level of accuracy.

2.4.1 Spectral Element Methods

In order to solve the N-S equations in detail, we need a powerful discretization method that will provide high accuracy at a reasonable computational cost. We choose the SEM as it is a high order version of FEM that combines the geometric flexibility of FEM with the high order accuracy of SM. The domain is split into a series of macro-elements, in which the solution is approximated using high-order polynomials [36]. SEM has been shown to have an exponential convergence with low dissipation and dispersion errors as the order increases. This method is good for high precision results of sensitive instabilities such as transition from laminar to turbulent flows. The high order precision captures minute disturbances that would be dissipated by other lower-order methods. The main disadvantage of SEM is that it has a higher computational expense than the other methods.

2.4.2 Spatial Discretization

The data is represented on sets of non-overlapping sub-domains, Ω^n, within the entire domain Ω_f.

$$\Omega_f = \bigcup_{n=1}^{N_f} \Omega^n. \tag{3}$$

Any given variable, $\phi(x)$, inside each element Ω^n is represented by

$$\phi(\mathbf{x})|_{\Omega^n} = \phi(x,y,z)|_{\Omega^n} = \sum_{k=0}^{N}\sum_{j=0}^{N}\sum_{i=0}^{N} \phi_{ijk}^n h_i(r) h_j(s) h_k(t), \tag{4}$$

where $h_i(r)$ are N^{th} order one-dimensional Lagrangian interpolant Legendre polynomials evaluated at Gauss Lobatto Legendre quadrature points, ϕ_{ijk}^n are the basis coefficients (the values of ϕ at the quadrature points), and $\mathbf{r} = (r,s,t)$ are the coordinates in the canonical reference element $\hat{\Omega} = [-1,1]^3$. For $\mathbf{x} = (x,y,z) \in \Omega^n$, an iso-parametric mapping is given by

$$\mathbf{x}|_{\Omega^n} = \sum_{k=0}^{N}\sum_{j=0}^{N}\sum_{i=0}^{N} \mathbf{x}_{ijk}^n h_i(r) h_j(s) h_k(t). \tag{5}$$

The pressure space can be discretized using the Lagrangian interpolants of order $N-2$ also known as $\mathbb{P}_N - \mathbb{P}_{N-2}$ staggering. This formulation is very useful to remove the occurrence of unwanted (spurious) pressure modes that can arise in the Navier-Stokes equations and the requirement of pressure boundary conditions [37].

2.4.3 Temporal Discretization

Nek5000 implements a semi-implicit time-stepping method. The non-linear terms are treated with an explicit k-th order Extrapolation (EXTk) scheme with $k \leq 3$. The viscous terms are treated implicitly using a k-step Backward-Difference (BDFk) scheme with $k \leq 3$ [38]. In this work, a second-order accurate BDF2/EXT2 time-stepping scheme was used [39].

A restriction can be imposed on the step size Δt on the explicit formulation of the convective terms to maintain global stability during time-marching. Stability is governed by the Courant Friedrichs Lewy (CFL) condition number, which can be written as

$$\Delta t < C \times min_{\Omega_f}\left(\frac{\Delta x}{|u|}, \frac{\Delta y}{|v|}, \frac{\Delta z}{|w|}\right), \tag{6}$$

where C represents the CFL number, min_{Ω_f} indicates minimum over the entire flow field, $\Delta x, \Delta y, \Delta z$ are the x, y, z distances between the collocation points, and u, v, w are the velocities in the x, y, z directions.

2.4.4 Time Splitting Scheme and General Solution Procedure

The semi-discrete formulation described in Karniadakis et al. [40] is briefly discussed in this section. Equation 2 is rewritten as follows:

$$\frac{\partial \mathbf{u}}{\partial t} = -\nabla P + \nu \mathbf{L}(\mathbf{u}) + \mathbf{N}(\mathbf{u}) + \mathbf{f} \qquad in\ \ \Omega, \tag{7}$$

where vectors are represented by bold letters, P is now P/ρ and ν is the kinematic viscosity. $\mathbf{L}$ and $\mathbf{N}$ represent the linear and non-linear operators, respectively, defined as

$$\mathbf{N}(\mathbf{u}) = -\mathbf{u} \cdot \nabla \mathbf{u}, \tag{8}$$

$$\mathbf{L}(\mathbf{u}) = \nabla^2 \mathbf{u}. \tag{9}$$

Further, Equation 7 can be split into three sub-steps using a k-th order scheme from the Adams-Bashforth family as follows:

$$\widehat{\mathbf{u}} = \sum_{j=1}^{k} a_j \mathbf{u}^{n+1-j} + \Delta t \left(\sum_{j=1}^{k} b_j \mathbf{N}(\mathbf{u}^{n+1-j}) + \mathbf{f}^{n+1} \right) \qquad in\ \ \Omega, \tag{10}$$

$$\widehat{\widehat{\mathbf{u}}} = \widehat{\mathbf{u}} - \Delta t\ \nabla P^{n+1} \qquad in\ \ \Omega, \tag{11}$$

$$\mathbf{u}^{n+1} = \widehat{\widehat{\mathbf{u}}} + \Delta t\ \nu\ \mathbf{L}(\mathbf{u}^{n+1}) \qquad in\ \ \Omega. \tag{12}$$

Here $\widehat{\mathbf{u}}$ and $\widehat{\widehat{\mathbf{u}}}$ are intermediate velocity fields; a_j and b_j refer to the k coefficients of the k-step backward differentiation formula (BDFk) and the k coefficients of the explicit extrapolation scheme of order k (EXTk), respectively. Finally, an elliptic equation (Poisson equation) for the pressure with Neumann boundary conditions can be written as follows:

$$\nabla^2 P^{n+1} = \frac{1}{\Delta t} \nabla \cdot \widehat{\mathbf{u}}. \tag{13}$$

The final velocity field $\mathbf{u}^{n+1}$ is obtained by solving the Helmholtz Equation 12 where velocity field $\widehat{\widehat{\mathbf{u}}}$ acts as a forcing term. All Poisson/Helmholtz equations (Equations 12 and 13) are then solved by the preconditioned Algebraic Multigrid (AMG) method explained in Section 2.5.1.

2.5 Nek5000

Nek5000 [1], developed by Argonne National Laboratory, is a high order CFD solver that uses SEM to solve the incompressible N-S equations. Nek5000 is a highly scalable code applicable to many fields such as fluid flow, thermal convection, combustion and magneto-hydrodynamics. Nek5000 supports structured grids with either quadrilateral or hexahedral elements in 2D and 3D respectively.

Nek5000 solves the incompressible Navier-Stokes equations (Equations 1 and 2) which can be written in non-dimensional form,

$$\frac{\partial \mathbf{u^*}}{\partial t^*} + \mathbf{u^*} \cdot \nabla \mathbf{u^*} = -\nabla P^* + \frac{1}{Re}\left(\nabla^2 \mathbf{u^*}\right) + \mathbf{f^*}, \tag{14}$$

where $\mathbf{u}^* = \frac{\mathbf{u}}{U_\infty}$, $t^* = \frac{tU_\infty}{c}$, $\mathbf{f}^* = \frac{\mathbf{f}c}{U_\infty^2}$, $P^* = \frac{P}{\rho U_\infty^2}$, and U_∞ is the freestream velocity.

The velocities are solved on a Gauss-Lobatto-Legendre mesh (including boundary points). Pressure is solved using a $\mathbb{P}_N - \mathbb{P}_{N-2}$ approach where the pressure is solved on a N - 2 (order) Gauss-Legendre mesh (without boundary points) [1] as shown in Figure 3 [39]. Pressure can be solved on a P_{N-2} approach as it is not required for the pressure to be continuous at the element boundaries [41].

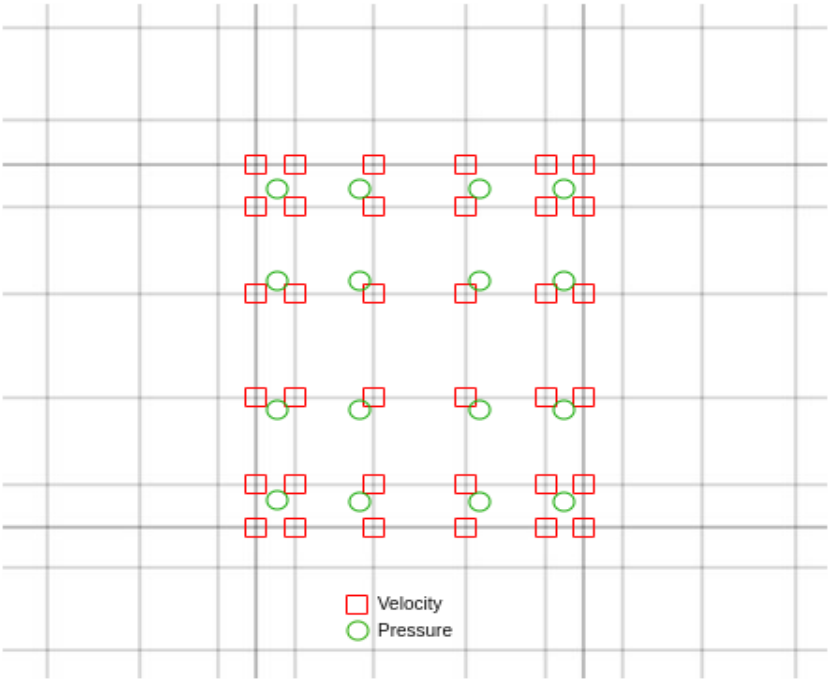

Figure 3: Spectral Element Collocation Point Grid of Order N = 5 for Velocity (Red Square) and Order N = 3 for Pressure (Green Circle)

2.5.1 Preconditioners

Nek5000 uses preconditioners to solve Poisson/Helmholtz equations such as the conjugate gradient method for meshes smaller than 300,000 elements and recommends the AMG method for larger meshes. In this work all meshes are preconditioned using the semg_AMG code which is an implementation of the AMG setup created by James Lottes [42]. For this work the Ruege-Stuben coarsening method is used with the "classical modified interpolation" interpolation method. A total of 30 levels is used for the AMG with a 0.5 smoother tolerance.

3 Methodology

The Methodology covers every step from the case selections and the meshing, to the setup parameters required to run the simulations of the clean and iced NLF-0414 airfoils using the open-source code Nek5000 [1]. Nek5000 is a DNS solver of the incompressible N-S equations using SEM. The size of the calculation using an SEM code such as Nek5000 is based on the number of spectral collocation points (# elements x (N+1) x (N+1) where N is the polynomial order) in 2D. Increasing to 3D increases the number of spectral collocation points by a factor of N+1. Due to computational limitation and the large increase in calculation time required for a 3D simulation only the 2D simulations were considered. The profiles being studied, the clean NLF-0414 and the iced Run 606 and 622-2D, were obtained from the NASA TP by Addy [14]. Runs 606 and 622-2D were selected for this first attempt of DNS analysis of iced airfoils, as they are relatively lightly iced profiles of the NLF-0414.

3.1 Case Selections

A total of six cases have been selected to study the effects of ice accretion on the flow field. The selected cases are given in Table 1 with respect to chord Reynolds number (Re_c) and AOA. Run 606 has a lightly iced profile as seen in Figure 4a. Run 622-2D has a sharper iced profile as well as a small horn on the topside of the LE as seen in Figure 4b. A clean non-iced NLF-0414 is used for comparison. The three different runs are simulated at Re_c of 1 x 10^5 and 2 x 10^5 and zero AOA.

Table 1: Selected Cases

Case	Run	Re_c	AOA
Case 1	Clean	1 x 10^5	0°
Case 2	Run 606	1 x 10^5	0°
Case 3	Run 622-2D	1 x 10^5	0°
Case 4	Clean	2 x 10^5	0°
Case 5	Run 606	2 x 10^5	0°
Case 6	Run 622-2D	2 x 10^5	0°

3.2 Geometry

The coordinates for the clean NLF-0414 are pulled from the NASA TP by Addy [14]. The coordinates for the iced Runs 606 and 622-2D are not provided in the technical publication but pictures of the iced profiles are available as shown in Figures 4a and 4b.

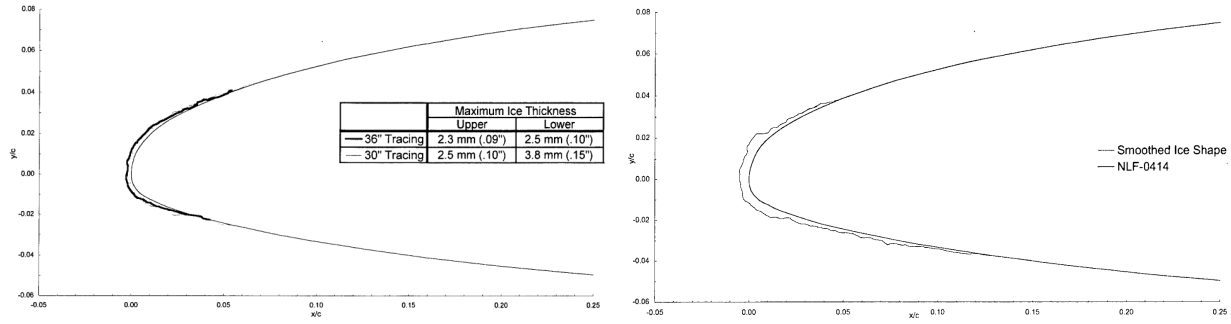

(a) Run 606 NLF-0414 Airfoil Profile

(b) Run 622-2D NLF-0414 Airfoil Profile

Figure 4: Iced NLF-0414 Profiles from the NASA TP [14]

3.3 Mapping

The iced profiles from Figures 4a and 4b are imported into the open-source program GIMP (GNU Image Manipulation Program) [43]. The profiles are mapped using the Layer/Path function and saved into a ***.svg file. The ***.svg file gives the (x,y) coordinates of the iced profiles in pixels. A code is then used to convert the coordinates from a pixel based coordinate system into a more convenient (x/c,y/c) coordinate system using the scales provided in Figures 4a and 4b. The resulting iced profiles (solid lines) from Runs 606 and 622-2D are traced over a clean NLF-0414 airfoil (dashed lines) in Figures 5a and 5b.

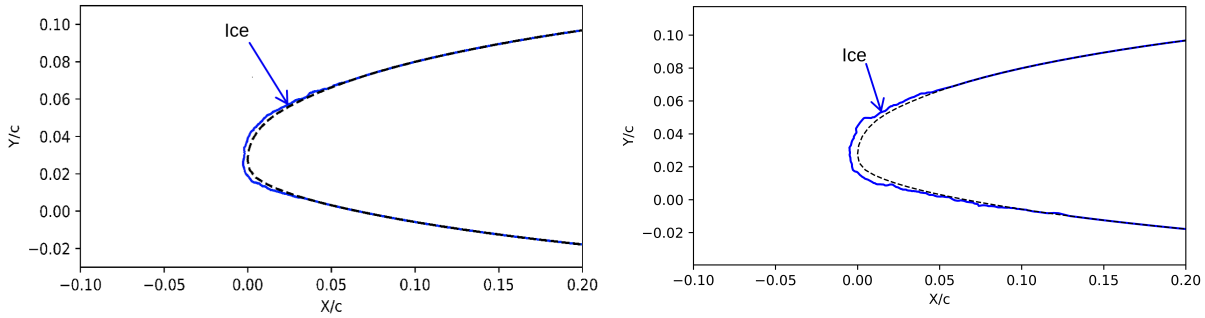

(a) Run 606

(b) Run 622-2D

Figure 5: Mapped Leading Edge Iced Profile Over a Clean NLF-0414 Airfoil

3.4 Computational Domain

The 2D domains were generated using the open-source software Gmsh [44]. A C-grid multi-block structure approach was used to define the computational domains for all six cases as shown in Figures 6, 7, and 8. The multi-block approach helps to create meshes that will properly solve for boundary layer effects [45] as well as reduce the overall number of elements while keeping a good precision. Each domain has an overall horizontal length of 6c, 2c upstream, 3c downstream, and 6c vertically which resembles the validated domain used in [25].

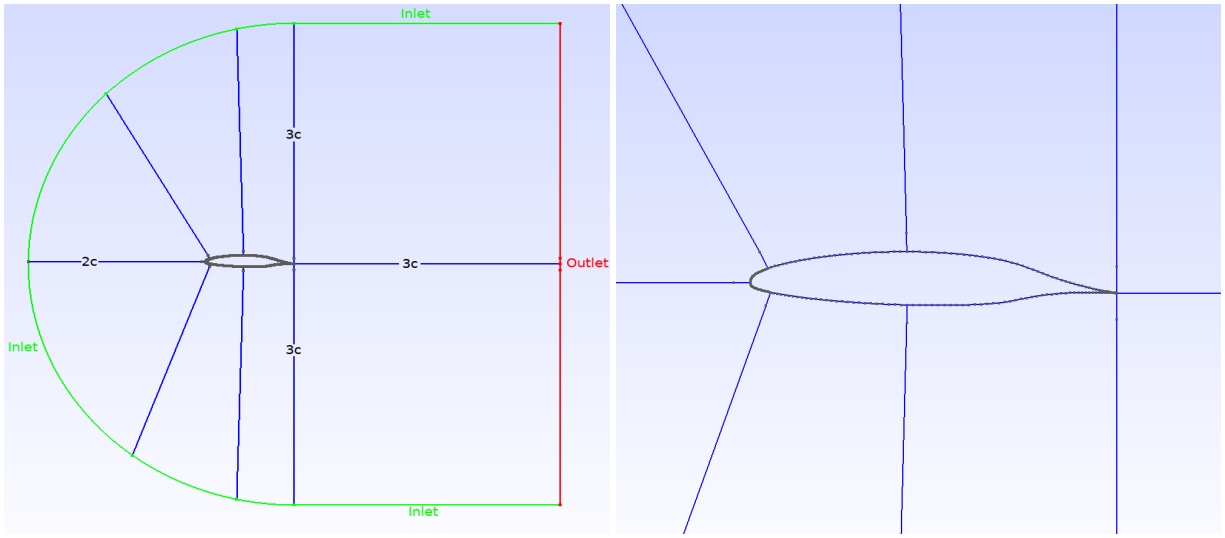

(a) Full Domain (b) Airfoil Close-up

Figure 6: Computational Domain with Boundary Conditions for the Clean NLF-0414 (c = chord length)

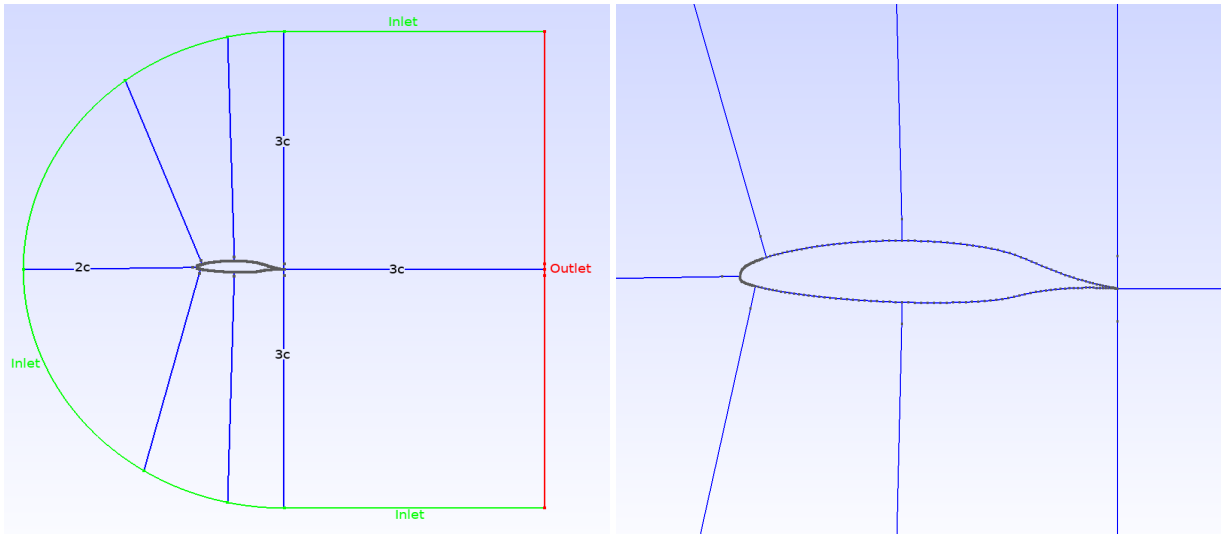

(a) Full Domain (b) Airfoil Close-up

Figure 7: Computational Domain with Boundary Conditions for Run 606 (c = chord length)

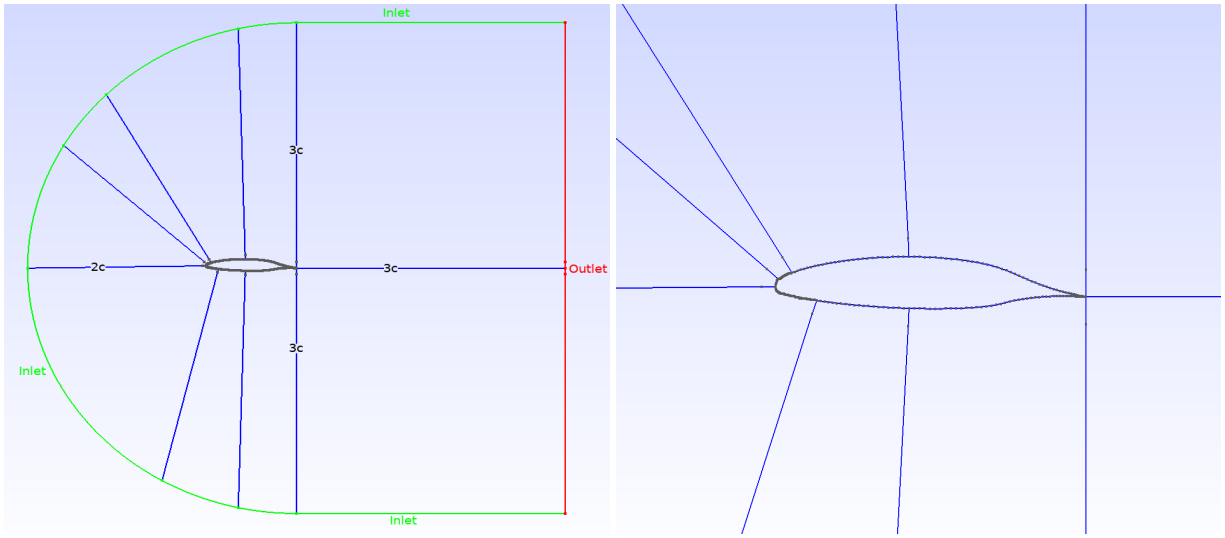

(a) Full Domain (b) Airfoil Close-up

Figure 8: Computational Domain with Boundary Conditions for Run 622-2D (c = chord length)

The clean NLF-0414 and Run 606 domains shown in Figures 6 and 7 are separated into 24 blocks. The 622-2D domain, shown in Figure 8, is separated into 26 blocks. The two extra blocks for Run 622-2D are placed at the LE near the small horn to help with a structured mesh generation.

3.5 Meshing

The meshes were generated using Gmsh [44] with the domains from Figures 6, 7, and 8. The element distributions for all six domains are shown in Figure 9 and the parameters are given in Table 2. As per Gmsh convention the values given in Table 2 give the number of points used to split a "line" into elements (# elements = # points - 1). Each gray point seen in Figure 9a and 9b represents the domain coordinates and the reference coordinates for the clean and iced NLF-0414. Each variable represents the number of elements found between each gray point in the domain and on the airfoil. The C variable represents the number of vertical elements used in the Boundary Layer (BL) region around the airfoil. Variables D, E, F, and G represent the number of elements used in the chordwise direction along the airfoil. The H variable represents the number of elements used in the LE region of the airfoil and is also the variable used in the extra block needed for Runs 622-2D. The values were determined iteratively and are explained in Section 4.3.

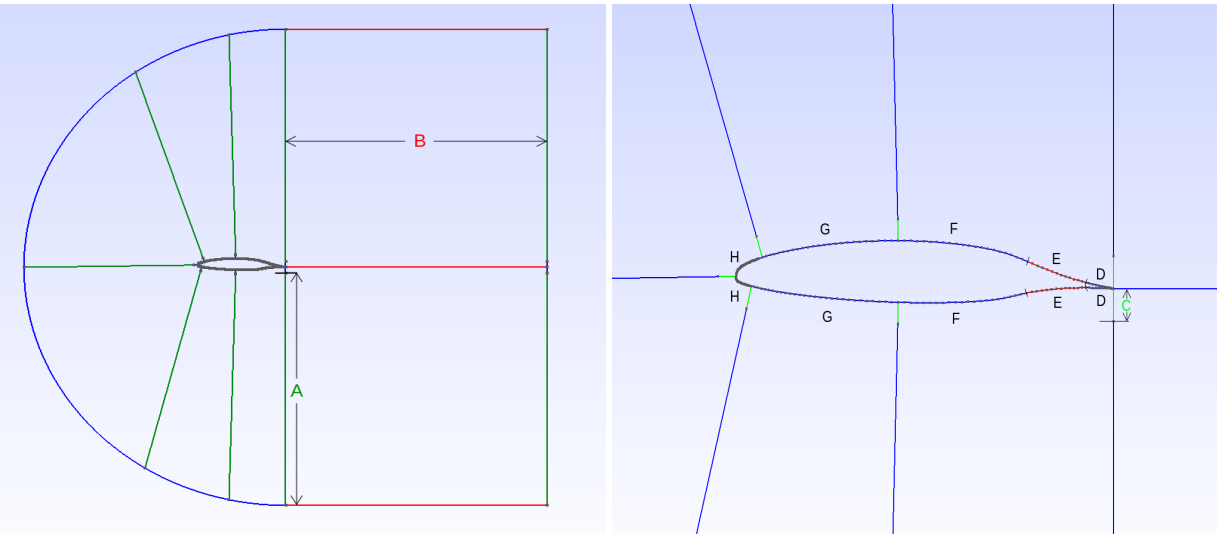

(a) Wake and Far Field Element Distribution (b) Element Distribution Around Airfoil

Figure 9: Element Distribution Across Domain (Letters A-H Represent Mesh Parameters Detailed in Table 2)

Table 2: Element Distribution Parameters (Letters A-H Represent Mesh Parameters Detailed in Figure 9)

Variable	Clean $Re_c = 1$ x 10^5	Iced $Re_c = 1$ x 10^5	Clean $Re_c = 2$ x 10^5	Iced $Re_c = 2$ x 10^5
A	50	50	50	50
B	550	550	650	650[a] and 620[b]
C	130	130	180	180
D	5	5	7	7
E[c]	10	10	14	14
F	5	5	7	7
G	2	2	4	4
H	3	2	5	2

[a] Run 606
[b] Run 622-2D
[c] Region of high perturbations

The meshes were formed with quadrilateral elements as Nek5000 supports that type of structured mesh. Figures 10, 11, 12, 13, 14, and 15 show the meshes for Cases 1 through 6 as defined in Table 1.

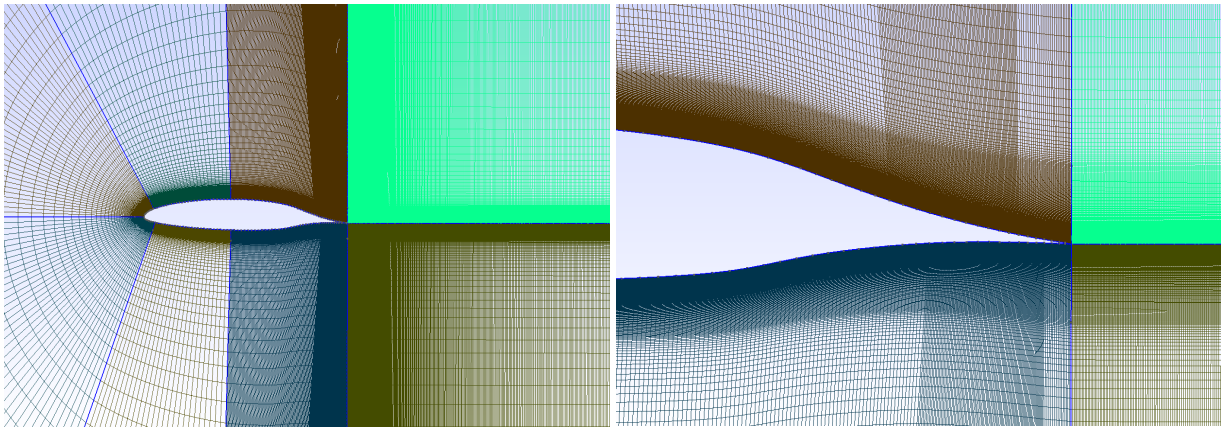

(a) Mesh Near Airfoil (b) Trailing Edge Mesh

Figure 10: Clean NLF-0414 Airfoil Mesh at $Re_c = 1$ x 10^5

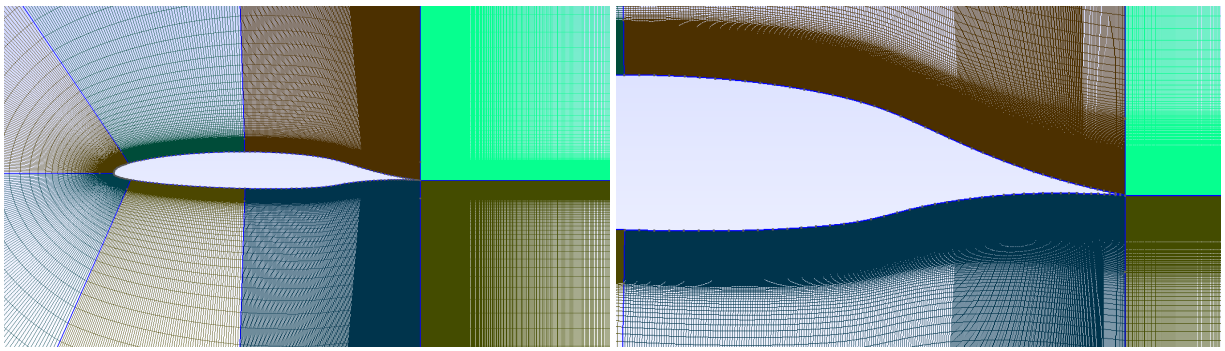

(a) Mesh Near Airfoil (b) Trailing Edge Mesh

Figure 11: Clean NLF-0414 Airfoil Mesh at $Re_c = 2$ x 10^5

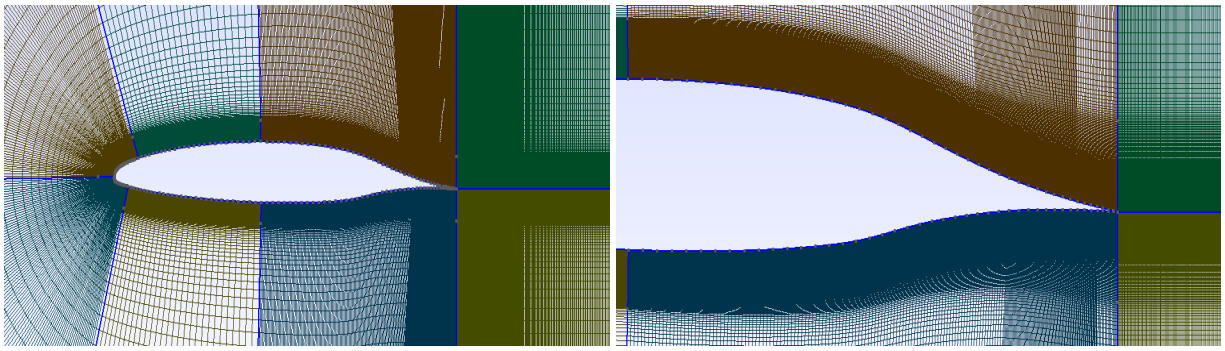

(a) Mesh Near Airfoil (b) Trailing Edge Mesh

Figure 12: Run 606 Mesh at $Re_c = 1$ x 10^5

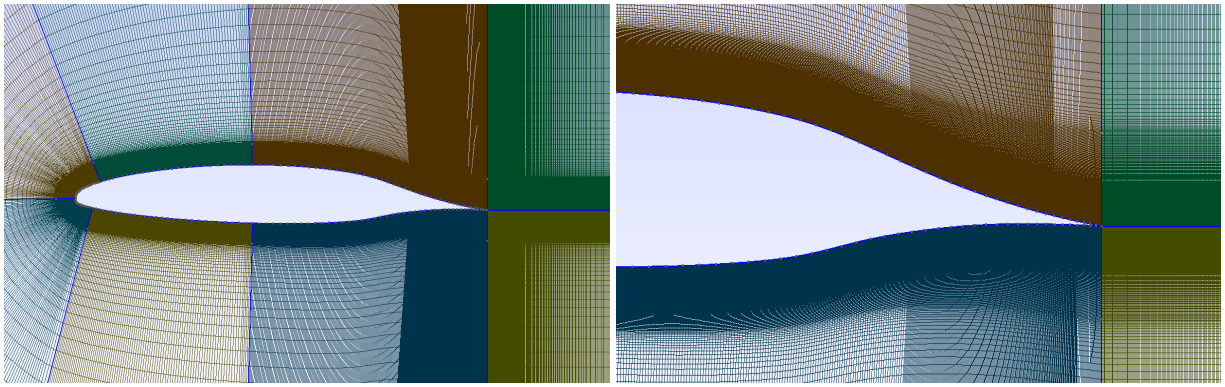

(a) Mesh Near Airfoil (b) Trailing Edge Mesh

Figure 13: Run 606 Mesh at $Re_c = 2$ x 10^5

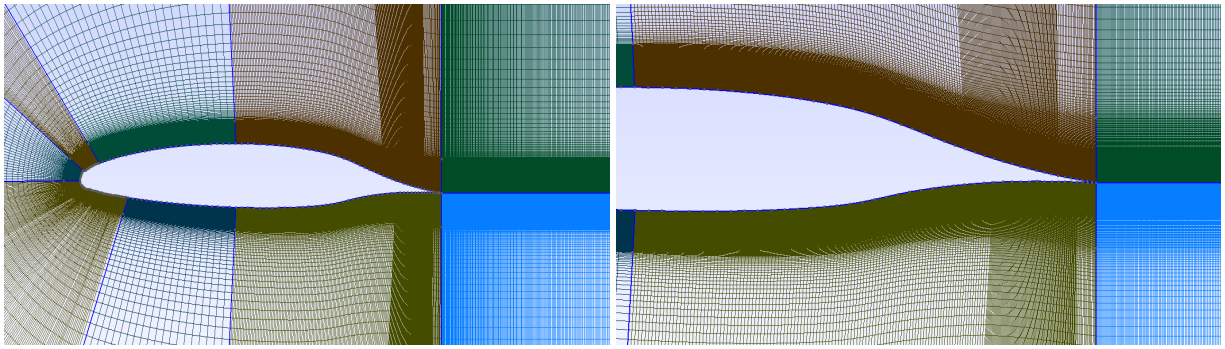

(a) Mesh Near Airfoil (b) Trailing Edge Mesh

Figure 14: Run 622-2D Mesh at $Re_c = 1$ x 10^5

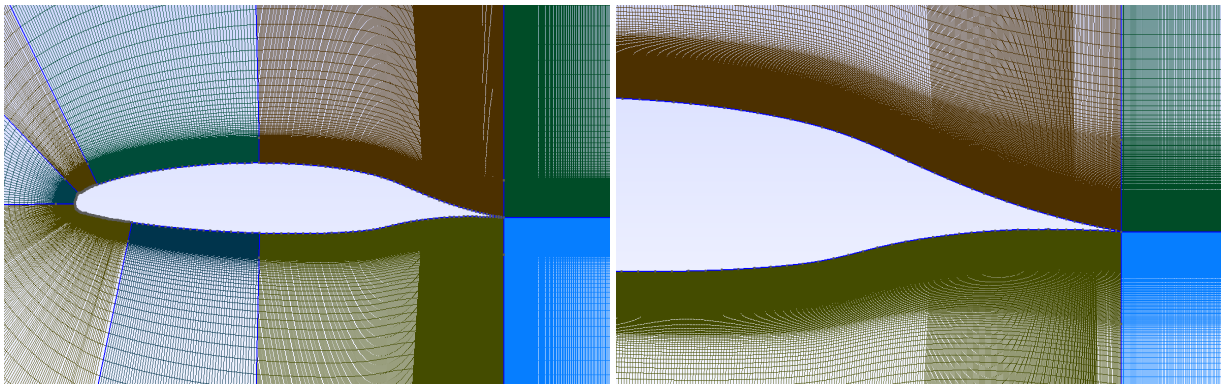

(a) Mesh Near Airfoil (b) Trailing Edge Mesh

Figure 15: Run 622-2D Mesh at $Re_c = 2$ x 10^5

In all six cases a higher concentration of elements is used around the airfoil to properly capture the BL effects. This high concentration is progressive in element size where the smallest elements are placed at the surface of the airfoil and grow larger as we progress outwards. A second concentration of elements can be observed at the TE of the airfoil. The smallest elements are placed at the trailing edge and grow in size downstream toward the outlet. A horizontal (chordwise) increased element density can also be seen near the end of the airfoil to help capture the shedding of the vortices. For the cases at Re_c = 1 x 10^5 the regions of increased element density for the top and bottom sides of the airfoil are from 0.8372c to 0.9528c and 0.8728c to 0.9760c respectively. For the cases at Re_c = 2 x 10^5 the regions of increased element density for the top and bottom sides of the airfoil are from 0.8118c to 0.9528c and 0.8099c to 0.9760c respectively. The location of this increase in elements is based on the design of the NLF-0414 (Section 1.4) as well as observations of the flow at the TE where an increase in element density will help properly capture the large amount of eddy shedding found in those locations (Section 4.3).

The multi-block approach helps generate a smoother mesh with fewer elements as it allows for increasing and decreasing the amount of elements per specific area. As an example, Figure 16 shows a close-up of the Run 622-2D mesh at the LE horn. Figure 16a shows the horn mesh without the extra block and Figure 16b shows the meshed horn peak as being the delimitation of two separate blocks. A separate block allows for an increase in elements for the sharp angle ice profile without having to increase the number of elements across the entire LE. This small increase in elements seen on the right side of Figure 16b helps with the convergence of the Nek5000 solver as it reduces skewness of the quadrilateral elements, as seen in Figure 16.

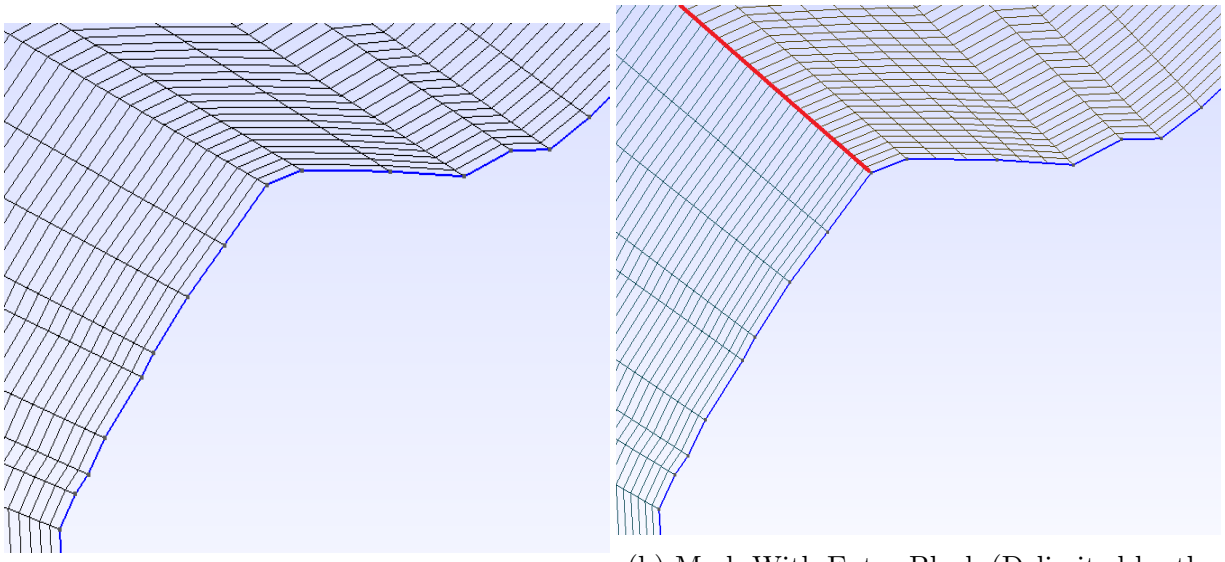

(a) Mesh Without Extra Block

(b) Mesh With Extra Block (Delimited by the Red Line)

Figure 16: Close-Up of Run 622-2D Mesh at the Leading Edge Horn

The gmsh2nek [46] converter was used to convert the mesh from the Gmsh ***.msh format

into a ***.re2 file that can be read by Nek5000. A run-time mesh smoother [47] specifically written for Nek5000 was used to smooth out the mesh. Table 3 gives the Re_c, the total number of elements, and polynomial order for each case.

Table 3: Mesh Parameters

Case	Run	Dimension	Re_c	# of Elements	Polynomial Order	Collocation Points
Case 1	Clean	2D	1 x 10^5	304,730	N = 5	7,618,250
Case 2	Run 606	2D	1 x 10^5	323,228	N = 5	8,080,700
Case 3	Run 622-2D	2D	1 x 10^5	325,574	N = 5	8,139,350
Case 4	Clean	2D	2 x 10^5	538,650	N = 5	13,466,250
Case 5	Run 606	2D	2 x 10^5	547,298	N = 5	13,682,450
Case 6	Run 622-2D	2D	2 x 10^5	531,694	N = 5	13,292,350

3.6 Flow Parameters

The incompressible N-S equation (Section 2.2.1) implementation in Nek5000 is used for the simulations. For this study the use of clean Re_c is used to define the flow parameters as follows,

$$Re_c = \frac{\rho U_\infty c}{\mu}, \tag{15}$$

where ρ is the unit density, U_∞ is the freestream velocity, c is the chord length, and μ is the dynamic viscosity. Table 4 gives the flow parameters used in Nek5000 where ρ, c, and μ are kept constant through all six cases and the U_∞ is changed between the two different Reynolds numbers.

Table 4: Flow Parameters

Variable	Value
ρ	1
U_∞	200[a] or 400[b]
c	1
μ	1/500

[a] Re_c = 1 x 10^5
[b] Re_c = 2 x 10^5

3.7 Initial and Boundary Conditions

The initial conditions were set to the free-stream velocity, given in Table 4, everywhere in the flow. Boundary conditions were set when creating the mesh with Gmsh. Figures 6,

7, and 8 show the locations of the inlets, outlets and airfoil surfaces. The inlet condition is set as a user defined constant velocity (v) [48] entering the domain and is defined as a Dirichlet boundary condition. The airfoil surface is set as a Wall (W) boundary condition and is defined as a no-slip Dirichlet boundary condition. The outlet is set as an Outflow (O), an open boundary condition with zero pressure, defined as a Neumann boundary condition. The outflow condition is a natural boundary condition from the variational formulation of the incompressible momentum equation. For these simulations, the no-stress formulation of the outflow is given as follows,

$$[-p\mathbf{I} + \mu(\nabla \mathbf{u})].\mathbf{n} = 0 \tag{16}$$

where $\mathbf{I}$ is the identity tensor, μ is dynamic viscosity, and $\mathbf{n}$ is the normal unit vector. The Neumann boundary condition is imposed on the top and bottom of the computation domain for all velocity components given by

$$\frac{\partial \mathbf{u}}{\partial y} = 0. \tag{17}$$

3.8 Sponge Forcing

A sponge forcing function is applied to the outflow condition due to the small domain relative to the Reynolds number. The sponge forcing function prevents any possibility of back-flow that could arise at the outflow boundary caused by the intensity of the vortices shedding off of the airfoil. The "Spongebox" code used was pulled from the Swedish KTH github by Peplinski et al. [49]. The sponge forcing function defined by Peplinski et al. [50] uses a volume forcing function to restrain the flow to a reference velocity. For the present cases, the sponge was applied to a small region at the end of the domain right before the outflow condition. The sponge forcing term can be defined as follows,

$$\mathbf{F}(x,t) = \lambda_f(x)[\mathbf{U}_f(x) - \mathbf{U}(x,t)], \tag{18}$$

where $\mathbf{U}_f$ indicates the forcing velocity (unit value in presented simulations) and $\mathbf{U}$ indicates the instantaneous velocity. The λ_f is a sponge function given by

$$\lambda_f(x) = \lambda_{max}\left[S\left(\frac{x_{min} + \Delta_{wl} - x}{\Delta_{dl}}\right) - S\left(\frac{x - x_{max} + \Delta_{wr}}{\Delta_{dr}}\right)\right], \tag{19}$$

where λ_{max} is the sponge strength, $S(x)$ a step function defined by Equation 20, Δ_{wl} and Δ_{wr} are the left and right sponge section width, and Δ_{dl} and Δ_{dr} are the left and right sponge section drop width.

$$S(x) = \begin{cases} 0 & x \leq x_{min} \\ 1/(1 + e^{((x-1)^{-1} + x^{-1})}) & x_{min} < x \leq x_{max} \\ 1 & x > x_{max} \end{cases} \tag{20}$$

with $x_{min} = 0.02$ and $x_{max} = 0.98$. The x_{min} and x_{max} are relative to 98% of the selected sponge zone. For the given cases above, as defined by the "Spongebox" code, the following

parameters, given in Table 5, were used to set up the sponge to force the desired reference velocity based on the desired Re_c.

Table 5: Sponge Forcing Parameters

Equation	Spongebox Variable	Value
λ_{max}	strength	100.0
Δ_{wl}	widthlx	0.2
Δ_{wr}	widthrx	0.2
Δ_{dl}	droplx	0.1
Δ_{dr}	droprx	0.1

3.9 Computation Time

The computations were carried out on the Compute Canada clusters (mostly Graham) [2] [3]. The Nek5000 spectral element solver is proven by N.Offermans et al. [51] to be highly scalable on Petascale systems. Table 6 gives the number of cores used, the average core time used per output dump (# cores x physical time) and the total core time needed for one flow-through (# cores x physical time x # dumps).

Table 6: Computation Time

Case	Run	Re_c	# Cores	Average Core Time/ Per Dump (hrs)	Core Time per Flow-Through
Case 1	Clean	1 x 10^5	256	46.22	610 days = 1.67 years
Case 2	Run 606	1 x 10^5	640	161.89	2113 days = 5.80 years
Case 3	Run 622-2D	1 x 10^5	320	113.88	1488 days = 4.09 years
Case 4	Clean	2 x 10^5	640	146.33	4047 days = 11.11 years
Case 5	Run 606	2 x 10^5	800	358.12	9520 days = 26.14 years
Case 6	Run 622-2D	2 x 10^5	640	240.80	6484 days = 17.80 years

4 Resolution Study

This section covers the mesh resolution study. This section looks at meshed domain size and selected polynomial order as well as the mesh refinement process used to select a proper mesh for the given cases. Section 5.4.4 also covers the dimensionless wall distance y^+ sometimes utilized in resolution studies to confirm the accuracy of turbulence calculations.

4.1 3 Chord Length vs 5 Chord Length Domains

Initially, the domain size was studied to be able to decrease computational expenses by reducing the overall computational domain. A 5 chord mesh of Run 622-2D was compared to a 3 chord mesh of Run 622-2D at $Re_c = 1\text{x}10^5$. When referring to the 5 chord mesh it is a C-grid mesh with a total horizontal length of 10 chords, 5 chords upstream and 5 chords downstream from the TE as seen in Figure 17a. When referring to the 3 chord mesh it is a C-grid mesh with a total horizontal length of 6 chords, 3 chords upstream and 3 chords downstream from the TE as seen in Figure 17b. The 3 chord mesh resembles the domain used by R.Vinuesa et al. [25]. The 5 chord mesh has a total of 376,000 elements and the 3 chord mesh has a total of 325,574 elements. Figure 17 shows a pressure field comparison between the 5 chord mesh and the 3 chord mesh solutions. The pressure fields show good agreement as well as having close maximum and minimum pressure. The maximum and minimum pressures for the 5 chord mesh are 2.018 x 10^4 and -3.010 x 10^4. The maximum and minimum pressures for the 3 chord mesh are 2.042 x 10^4 and -3.098 x 10^4.

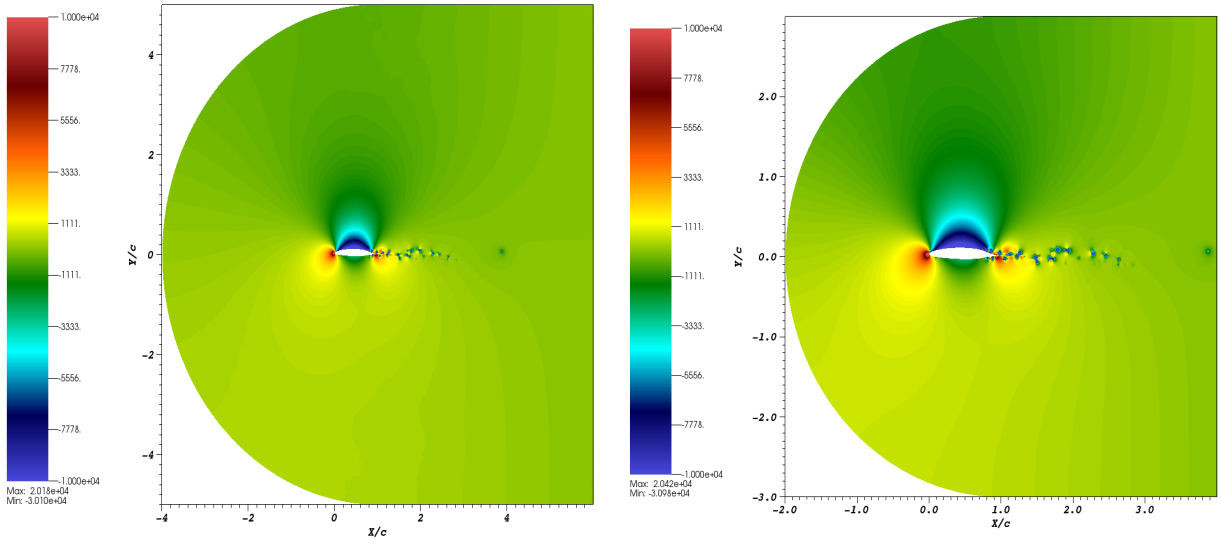

(a) Pressure Field of the 5 Chord Mesh

(b) Pressure Field of the 3 Chord Mesh

Figure 17: Pressure Field Comparison Between a 5 Chord and 3 Chord Mesh Solutions (Run 622-2D at $Re = 1\text{x}10^5$)

Figure 18 shows the C_p comparison between the 5 chord mesh and the 3 chord mesh solutions. Again, good agreement is confirmed between the 5 chord mesh C_p and the 3 chord mesh C_p.

The slight difference in C_p at the LE ($0 < x/c < 0.1$) can be explained by the further mesh refinement made on the 3 chord mesh shown in Section 4.3.

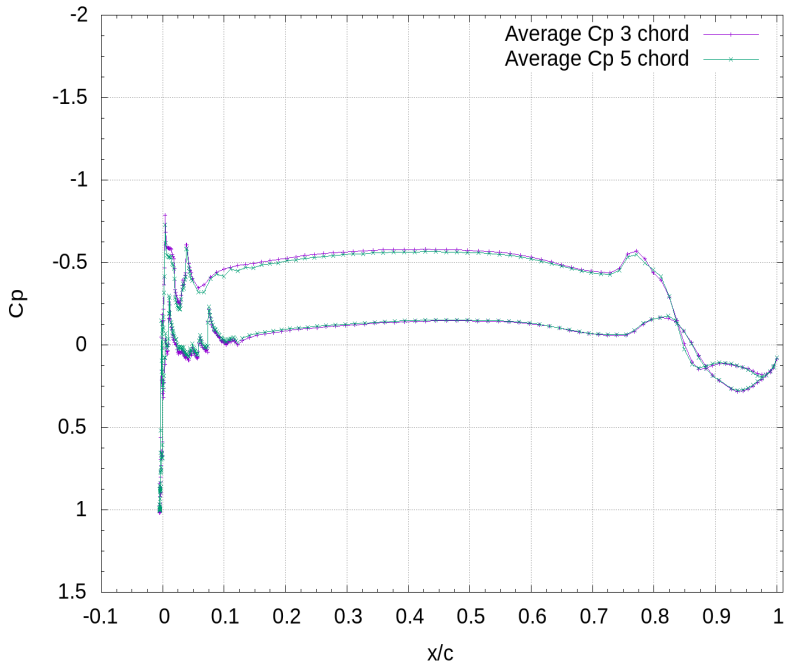

Figure 18: Pressure Coefficient Comparison Between the 5 Chord and 3 Chord Mesh (Run 622-2D at $Re_c = 1\text{x}10^5$)

4.2 Polynomial Order

In SEM increasing the order of the polynomial increases the precision of the solution but also increases the computational demand. Figure 19 gives a comparison between the time-varying drag coefficient (C_d) of a Clean NLF-0414 $Re_c = 1\text{x}10^5$ case with 5^{th} and 7^{th} order polynomials. Figure 19a shows that the 5^{th} and 7^{th} order runs are in good agreement. Figure 19b shows a close-up of a peak in time to show the small difference in C_d at a given peak. Table 7 gives the drag coefficients at the peak shown in Figure 19b as well as the average drag coefficients and the errors.

Table 7: Validation of Polynomial Order Choice via Comparison of Drag Coefficient (Clean NLF-0414 at $Re_c = 1\text{x}10^5$)

Order (N)	Variable	Location	Value	Deviation
N = 5	C_d	Peak	0.432782	-
N = 7	C_d	Peak	0.432318	0.107%
N = 5	C_d	Average	0.744509	-
N = 7	C_d	Average	0.742932	0.212%

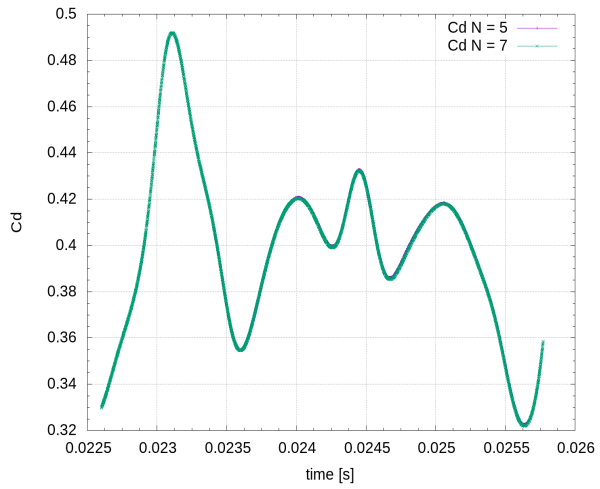

(a) Drag Coefficient : N = 5 vs N = 7

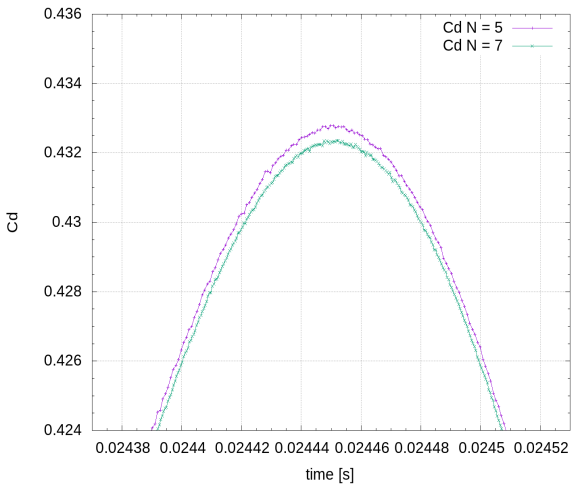

(b) Peak Close-Up of Drag Coefficient

Figure 19: Drag Coefficient Comparison Between 5^{th} and 7^{th} Order Polynomials (Clean NLF-0414 $Re_c = 1\text{x}10^5$ Run)

Figure 20 gives the comparison between the C_p of the 5^{th} and 7^{th} order runs. There is good agreement from the LE to 0.8c and thereafter a small difference exists. The average deviation in C_p from $0.0c < x/c < 0.8c$ is 0.59%. The overall average deviation in C_p from $0.0c < x/c < 1.0c$ is 2.60%. The largest deviations can be found in the steep slope from $0.8c < x/c < 0.9c$ on the upper surface with the largest deviation found at x/c = 0.85c. The steep slopes for both the top and bottom surfaces coincide with the region of vortex shedding. The steep slopes and highly unsteady vortex shedding region are the reasons the small difference in deviation exists for $0.8c < x/c < 1.0c$.

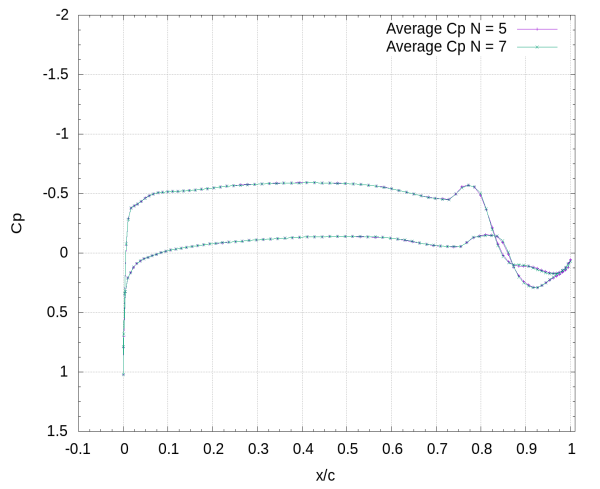

(a) Pressure Coefficient : N = 5 vs N = 7 (N = Polynomial Order)

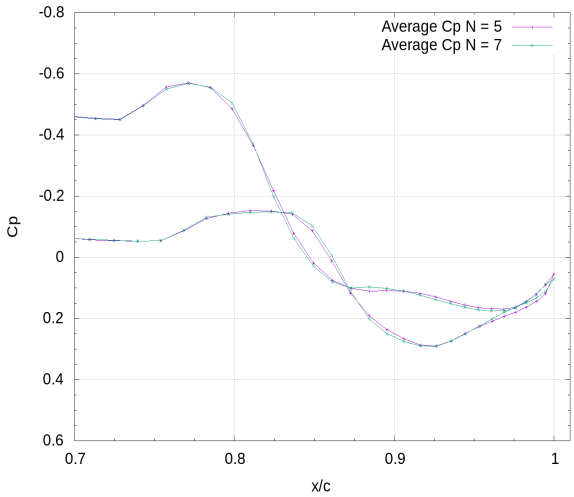

(b) Trailing Edge Close-Up of the Pressure Coefficient : N = 5 vs N = 7

Figure 20: Pressure Coefficient Comparison Between 5^{th} and 7^{th} Order Polynomials (Clean NLF-0414 $Re = 1\text{x}10^5$ Run)

4.3 Mesh Refinement

The mesh refinement process was based on the amount of noise found in the TE vorticity. Vorticity was chosen because a derivative variable is more sensitive to perturbations compared to a first order variable such as velocity and pressure. Some noise can be seen in front of the vortex at 90% X/c in Figure 21a on an initial test mesh with 220,000 elements. After a couple iterations of mesh adjustment, the current mesh for Run 606 at $Re_c = 1$ x 10^5 seen in Figure 21b exhibits no noise in front of the vortex at 90% X/c. The element distribution parameters in Table 2 from Section 3.5 were increased for regions of higher noise. A parameter of interest is variable E, where the location of its start and end (chordwise) as well as the number of elements used were tuned to properly capture the shedding of vortices. The same iterative mesh refinement process was used for the clean NLF-0414 and Run 622-2D at both desired chord Reynolds numbers with slight variations between the $Re_c = 1$ x 10^5 cases and $Re_c = 2$ x 10^5 cases parameters.

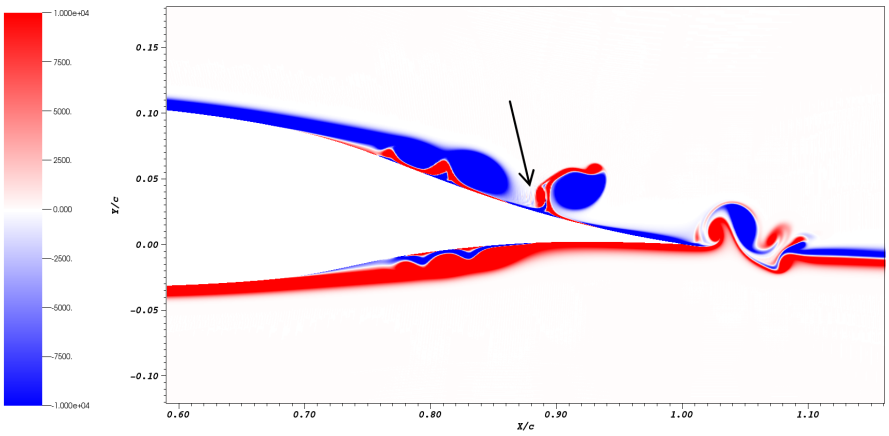

(a) Trailing Edge Vorticity of Run 606 Mesh with 220,000 Elements (A Region of Noise is Indicated by the Arrow)

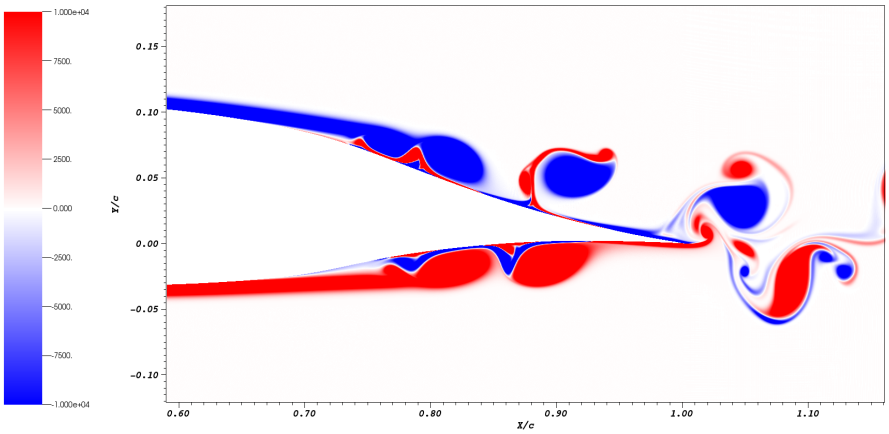

(b) Improved Trailing Edge Vorticity of Run 606 Mesh with 318,000 Elements

Figure 21: Mesh Refinement of Trailing Edge Vorticity for Run 606 at $Re_c = 1$ x 10^5

5 Results

Sections 5.1, 5.2, and 5.3 display the X- and Y- velocity fields, pressure fields, and vorticity fields for all six cases. Section 5.4 shows the aerodynamic characteristics for all six cases. Section 5.5 shows the velocity profiles for the LE and TE for all six cases. Section 5.6 shows the turbulent statistics that have been calculated for all six cases.

5.1 Clean NLF-0414: Cases 1 and 4

Case 1 consists of the results for the Clean NLF-0414 at Re_c = 1 x 10^5 and Case 4 consists of the results for the Clean NLF-0414 at Re_c = 2 x 10^5.

5.1.1 Velocity

Figures 22 and 23 give a comparison of the X- and Y- velocity fields between the Re_c = 1 x 10^5 clean NLF-0414 case and the Re_c = 2 x 10^5 clean NLF-0414 case. As stated in Section 3.6 the freestream velocity (X-velocity) is set to 200 and 400 for the Re_c = 1 x 10^5 cases and Re_c = 2 x 10^5 cases respectively. Figures 22a and 23a as well as Figures 22b and 23b are similar to each other with the exception of the scale.

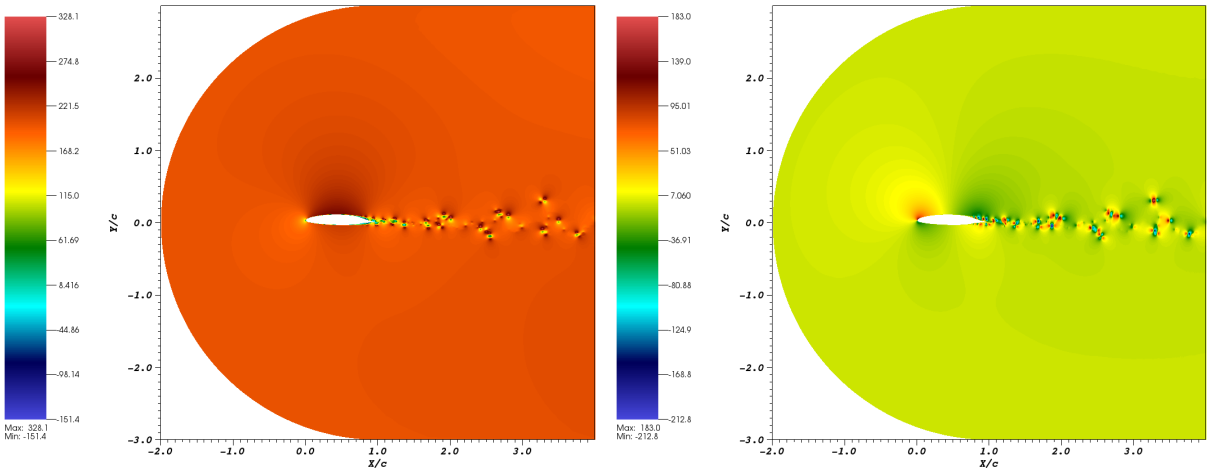

(a) X-Velocity Field for Case 1: Clean NLF-0414 at Re_c = 1 x 10^5

(b) Y-Velocity Field for Case 1: Clean NLF-0414 at Re_c = 1 x 10^5

Figure 22: X- and Y-Velocity Fields for Case 1: Clean NLF-0414 at Re_c = 1 x 10^5

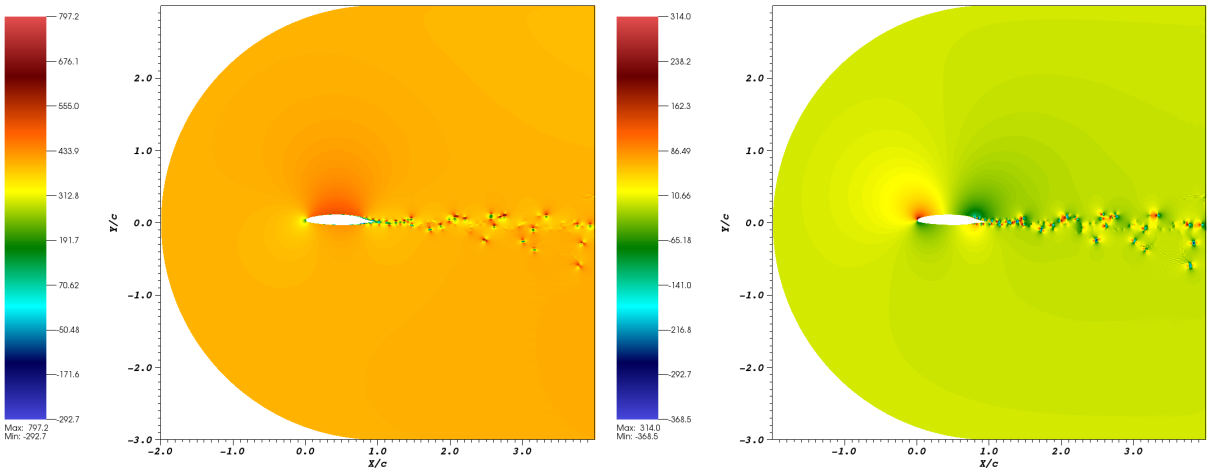

(a) X-Velocity Field for Case 4: Clean NLF-0414 at Re_c = 2 x 10^5

(b) Y-Velocity Field for Case 4: Clean NLF-0414 at Re_c = 2 x 10^5

Figure 23: X- and Y-Velocity Fields for Case 4: Clean NLF-0414 at Re_c = 2 x 10^5

5.1.2 Pressure

Figures 24 and 25 show the pressure fields for the clean NLF-0414 cases at Re_c = 1 x 10^5 and Re_c = 2 x 10^5. Both pressure fields are similar with different scaling. Both pressure fields properly show the stagnation point at the LE of the airfoil as well as the suction zone (negative pressure) on top of the airfoil.

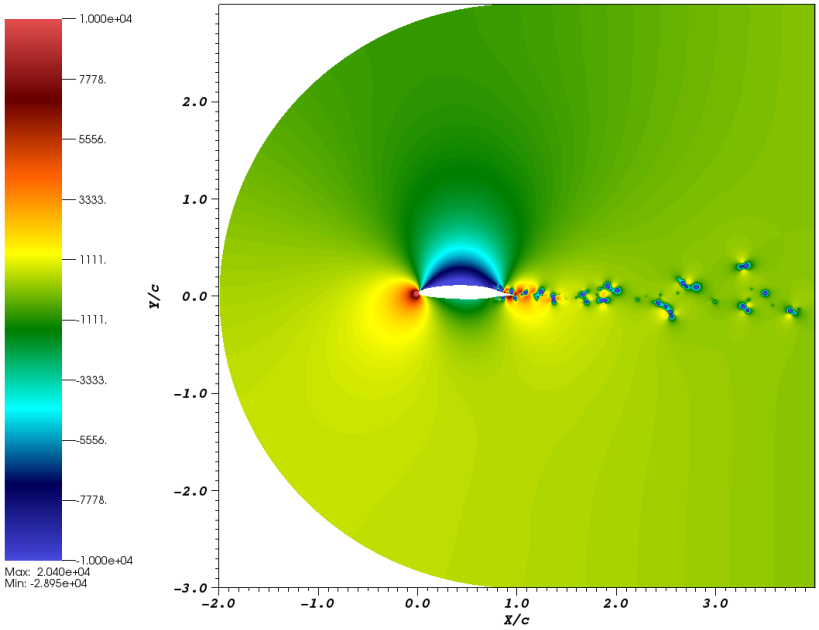

Figure 24: Pressure Field for Case 1: Clean NLF-0414 at Re_c = 1 x 10^5

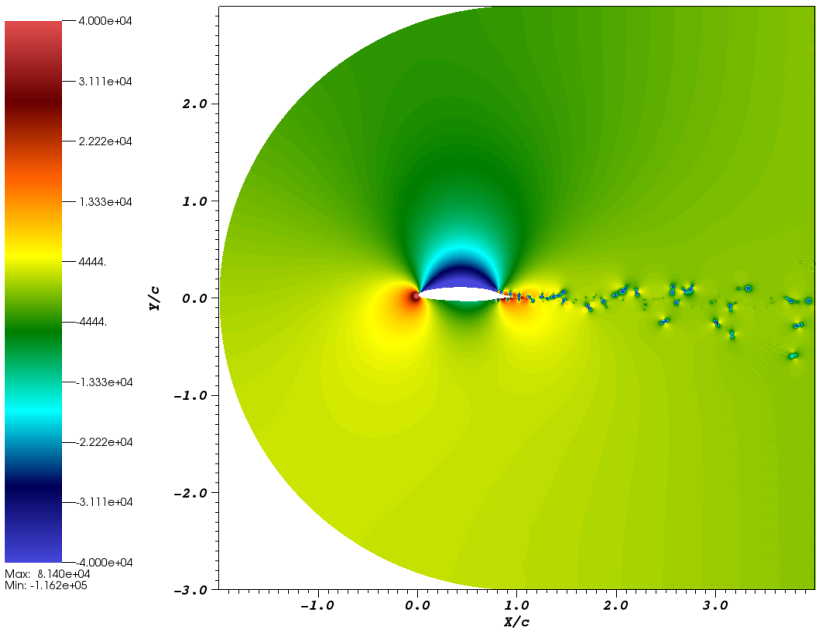

Figure 25: Pressure Field for Case 4: Clean NLF-0414 at Re_c = 2 x 10^5

5.1.3 Vorticity

Figures 26 and 27 show the vorticity comparison between Case 1 and Case 4, the clean NLF-0414 at Re_c = 1 x 10^5 and Re_c = 2 x 10^5. The blue indicates Clockwise (CW) circulation and the red indicates Counter-Clockwise (CCW) circulation. The shedding at the TE (Figures 26b and 26b) is well captured due to proper mesh refinement. Case 4 (Re_c = 2 x 10^5) has a higher shedding frequency with finer structures and smaller sized vortices than its counterpart Case 1 (Re_c = 1 x 10^5).

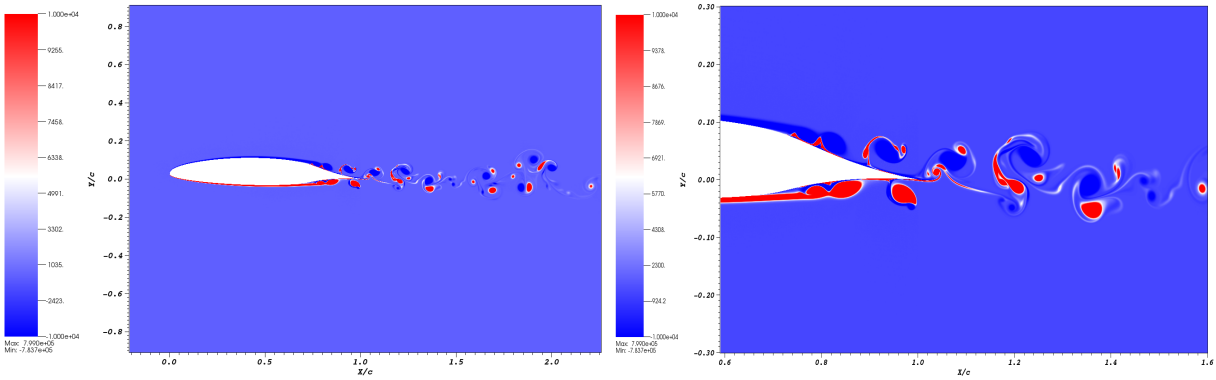

(a) Vorticity Field for Case 1: Clean NLF-0414 at Re_c = 1 x 10^5

(b) Trailing Edge Vorticity Field for Case 1: Clean NLF-0414 at Re_c = 1 x 10^5

Figure 26: Vorticity Field for Case 1: Clean NLF-0414 at Re_c = 1 x 10^5

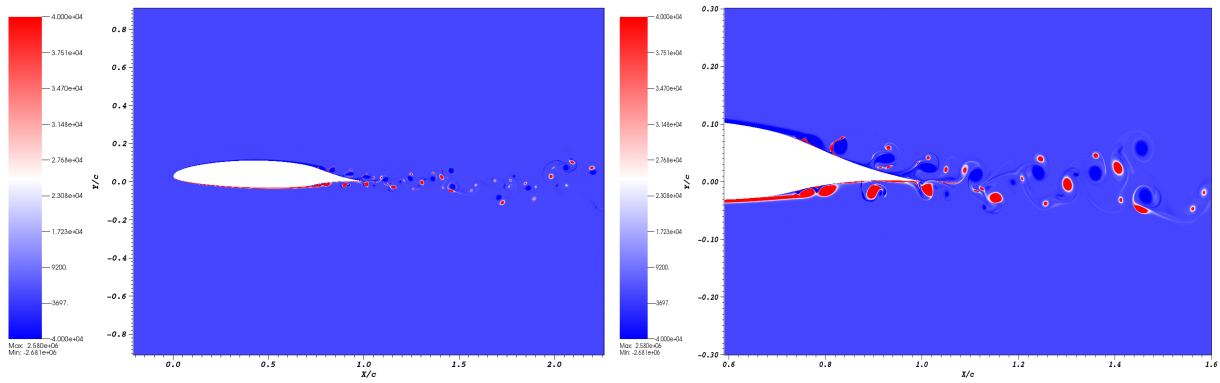

(a) Vorticity Field for Case 4: Clean NLF-0414 at $Re_c = 2$ x 10^5

(b) Trailing Edge Vorticity Field for Case 4: Clean NLF-0414 at $Re_c = 2$ x 10^5

Figure 27: Vorticity Field for Case 4: Clean NLF-0414 at $Re_c = 2$ x 10^5

Figure 28 shows the LE vorticity comparison for the clean NLF-0414 cases at $Re_c = 1$ x 10^5 and $Re_c = 2$ x 10^5. Figure 28b (clean NLF-0414 at $Re_c = 2$ x 10^5) has a thinner BL due to its higher Reynolds number compared to Figure 28a.

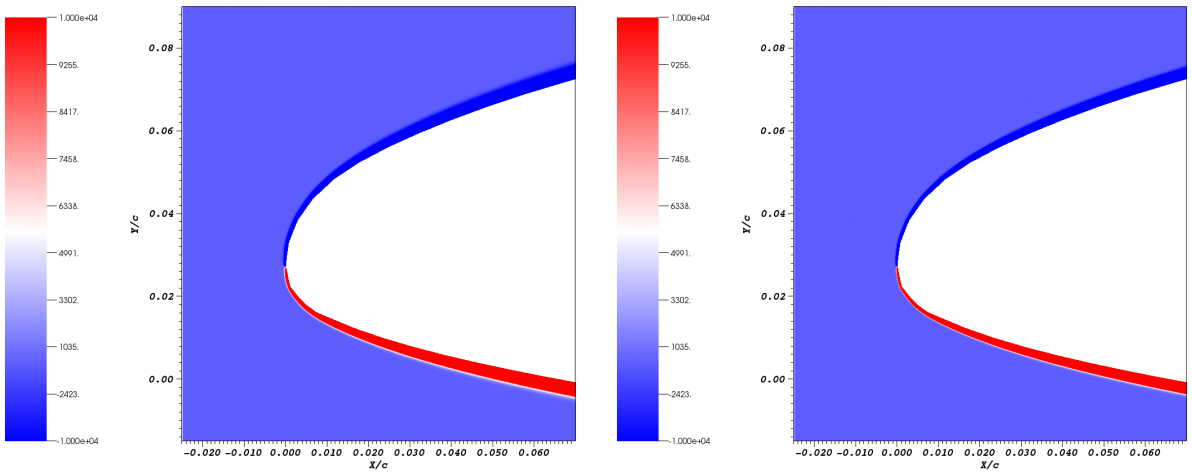

(a) Leading Edge Vorticity Field for Case 1: Clean NLF-0414 at $Re_c = 1$ x 10^5

(b) Leading Edge Vorticity Field for Case 4: Clean NLF-0414 at $Re_c = 2$ x 10^5

Figure 28: Leading Edge Vorticity Field Comparison Between the Clean NLF-0414 Cases at $Re_c = 1$ x 10^5 and $Re_c = 2$ x 10^5

5.2 Run 606: Cases 2 and 5

Case 2 consists of the results for the Run 606 at Re_c = 1 x 10^5 and Case 5 consists of the results for the Run 606 at Re_c = 2 x 10^5.

5.2.1 Velocity

Figures 29 and 30 give a comparison of the X- and Y- velocity fields between the Re_c = 1 x 10^5 Run 606 case and the Re_c = 2 x 10^5 Run 606 case. The maximum X- and Y- velocity values for Case 2 (Re_c = 1 x 10^5) are higher than the ones from Case 1 (Figure 22 (Re_c = 1 x 10^5)) and the minimum values are almost equal. The maximum and minimum X- and Y- velocity values for Case 5 (Re_c = 2 x 10^5) are all almost equal to the ones from Case 4 (Figure 23 (Re_c = 2 x 10^5)) with the exception of the maximum Y-velocity (Figure 30b) being higher that the clean Y-velocity at Re_c = 2 x 10^5 (Figure 23b). This would indicate that the lightly iced Run 606 upper surface velocity at Re_c = 1 x 10^5 is easier to accelerate compared to the Re_c = 2 x 10^5 Run 606 case upper surface velocity.

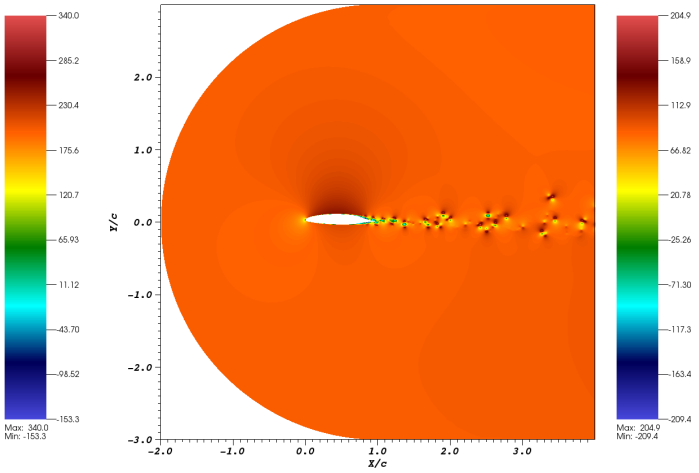

(a) X-Velocity Field for Case 2: Run 606 at Re_c = 1 x 10^5

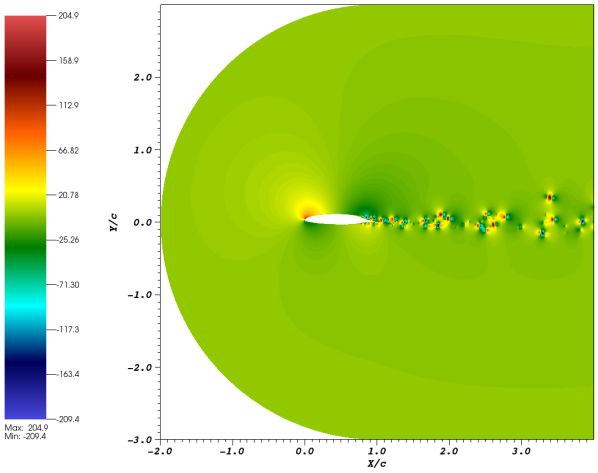

(b) Y-Velocity Field for Case 2: Run 606 at Re_c = 1 x 10^5

Figure 29: X- and Y-Velocity Fields for Case 2: Run 606 at Re_c = 1 x 10^5

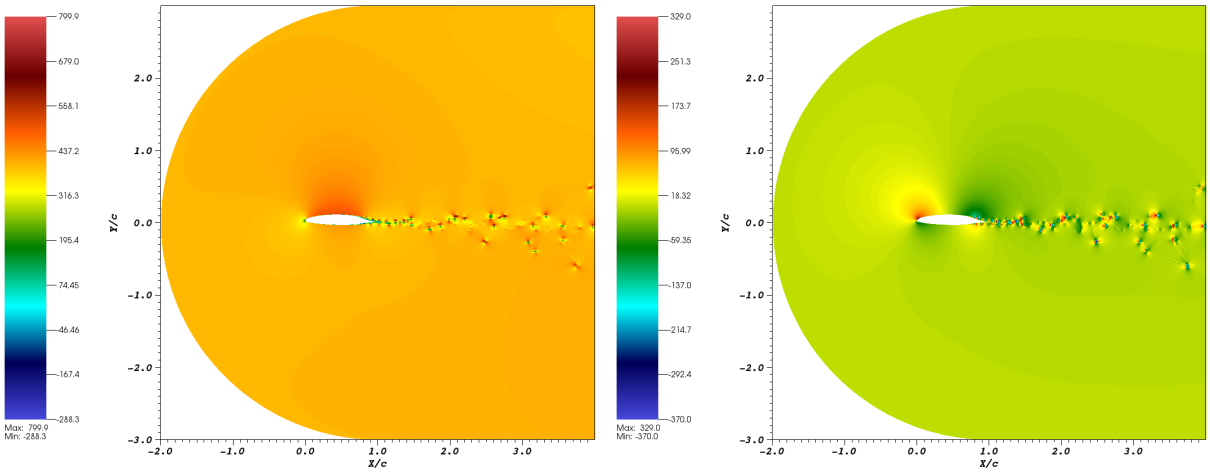

(a) X-Velocity Field for Case 5: Run 606 at Re_c = 2 x 10^5

(b) Y-Velocity Field for Case 5: Run 606 at Re_c = 2 x 10^5

Figure 30: X- and Y-Velocity Fields for Case 5: Run 606 at Re_c = 2 x 10^5

5.2.2 Pressure

Figures 31 and 32 show the pressure fields for the Run 606 cases at Re_c = 1 x 10^5 and Re_c = 2 x 10^5. Pressure field maximum pressure values are almost equal when comparing the Run 606 values to the Clean NLF-0414 values (Figures 24 and 25) but the minimum pressure value for Case 2 is smaller than Case 1 while Case 5 is larger than Case 2.

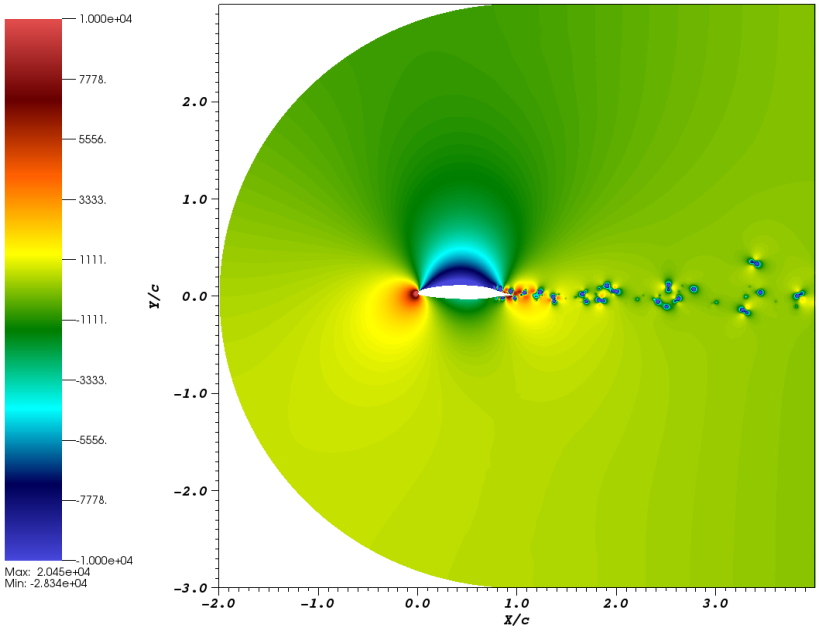

Figure 31: Pressure Field for Case 2: Run 606 at Re_c = 1 x 10^5

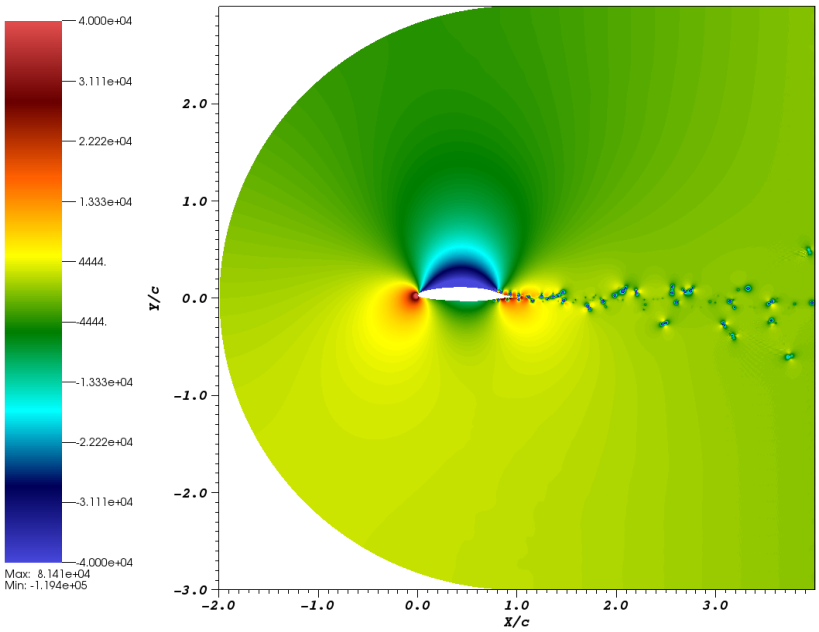

Figure 32: Pressure Field for Case 5: Run 606 at Re_c = 2 x 10^5

5.2.3 Vorticity

Figures 33 and 34 show the vorticity comparison between Case 2 and Case 5, Run 606 at Re_c = 1 x 10^5 and Re_c = 2 x 10^5. The higher Reynolds case has a finer structure and a higher shedding frequency.

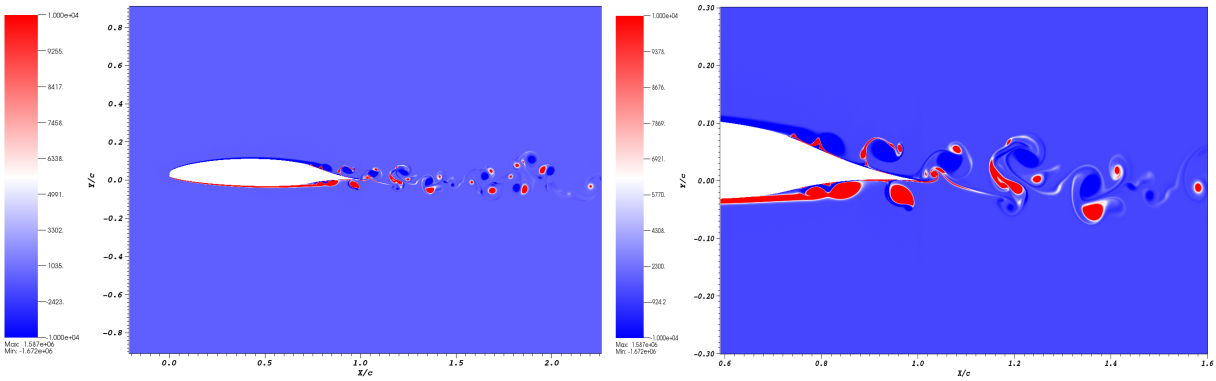

(a) Vorticity Field for Case 2: Run 606 at Re_c = 1 x 10^5

(b) Trailing Edge Vorticity Field for Case 2: Run 606 at Re_c = 1 x 10^5

Figure 33: Vorticity Field for Case 2: Run 606 at Re_c = 1 x 10^5

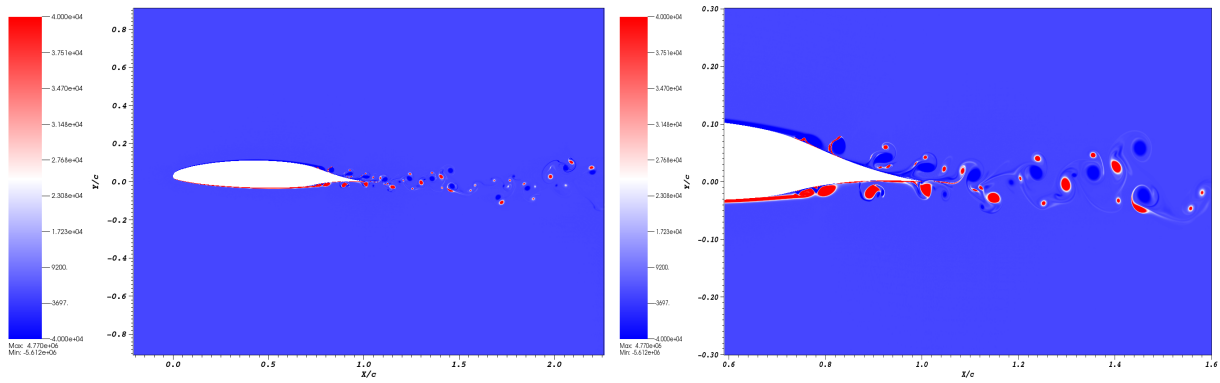

(a) Vorticity Field for Case 5: Run 606 at Re_c = 2 x 10^5

(b) Trailing Edge Vorticity Field for Case 5: Run 606 at Re_c = 2 x 10^5

Figure 34: Vorticity Field for Case 5: Run 606 at Re_c = 2 x 10^5

Figure 35 shows the LE vorticity comparison between Case 2 (Re_c = 1 x 10^5) and Case 5 (Re_c = 2 x 10^5). A thicker BL can be observed in Figure 35a (Re_c = 1 x 10^5). The small red zones in the upper surfaces crevasses are known as a recirculation zone. Recirculation zones usually introduce energy by pushing the boundary layer away from the surface of the airfoil that ultimately changes the aerodynamic profile. In some cases this could have a "tripping" effect and force faster transition into the turbulent regime. Recirculation zones can be observed in both Reynolds number cases on the upper and lower surfaces of the LE with the recirculation zones being slightly thicker in the Re_c = 2 x 10^5. The thicker recirculation zone in the Re_c = 2 x 10^5 case would indicate a more active sub-layer in the BL in the ice crevasses.

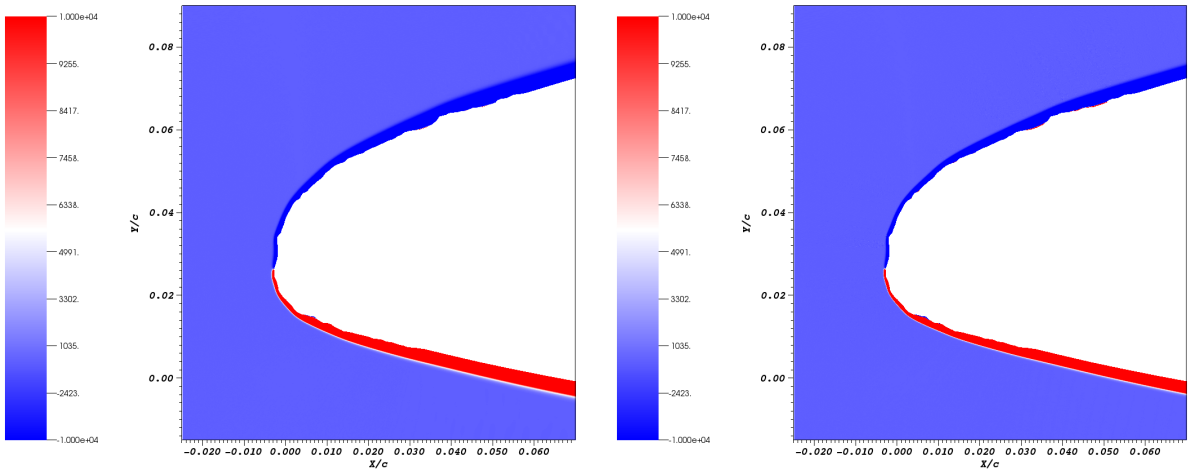

(a) Leading Edge Vorticity Field for Case 2: Run 606 at Re_c = 1 x 10^5

(b) Leading Edge Vorticity Field for Case 5: Run 606 at Re_c = 2 x 10^5

Figure 35: Leading Edge Vorticity Field Comparison Between the Run 606 Cases at Re_c = 1 x 10^5 and Re_c = 2 x 10^5

5.3 Run 622-2D: Cases 3 and 6

Case 3 consists of the results for the Run 622-2D at Re_c = 1 x 10^5 and Case 6 consists of the results for the Run 622-2D at Re_c = 2 x 10^5.

5.3.1 Velocity

Figures 36 and 37 give a comparison of the X- and Y- velocity fields between the Re_c = 1 x 10^5 Run 622-2D case and the Re_c = 2 x 10^5 Run 622-2D case. Case 3 (Re_c = 1 x 10^5) has the highest maximum X-velocity and lowest (absolute) minimum Y-velocity out of all three cases at Re_c = 1 x 10^5. The minimum X-velocities for all three cases are almost equal. The maximum Y-velocities for Case 3 (Run 622-2D) and Case 1 (clean NLF-0414) are equal and the maximum Y-velocity for Case 2 (Run 606) is the highest. The maximum and minimum values indicates that as the amount of ice increases so does the maximum X-velocity while the minimum Y-velocity decreases for the three cases at Re_c = 1 x 10^5.

Case 6 (Re_c = 2 x 10^5) has the lowest maximum X-velocity, the highest maximum Y-velocity, and the highest (absolute) minimum Y-velocity out of all three Re_c = 2 x 10^5 cases. The minimum X-velocity is almost equal for all three cases at Re_c = 2 x 10^5. The maximum and minimum values indicate that as the amount of ice increases so does the maximum and minimum (absolute) Y-velocity while the maximum X-velocity decreases for the three cases at Re_c = 2 x 10^5. The X- and Y- velocity fields act differently between the Re_c = 1 x 10^5 cases and the Re_c = 2 x 10^5 cases.

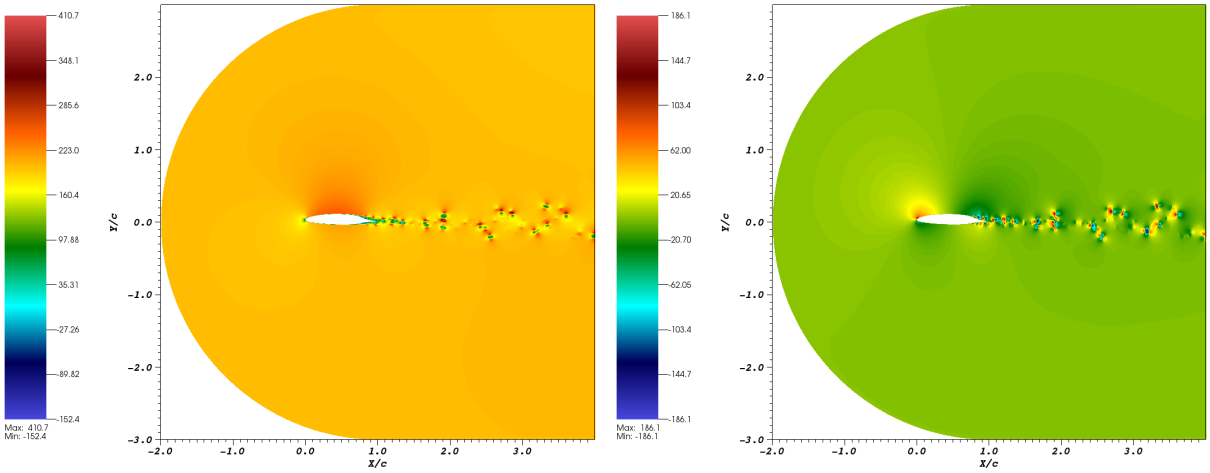

(a) X-Velocity Field for Case 3: Run 622-2D at Re_c = 1 x 10^5

(b) Y-Velocity Field for Case 3: Run 622-2D at Re_c = 1 x 10^5

Figure 36: X- and Y-Velocity Fields for Case 3: Run 622-2D at Re_c = 1 x 10^5

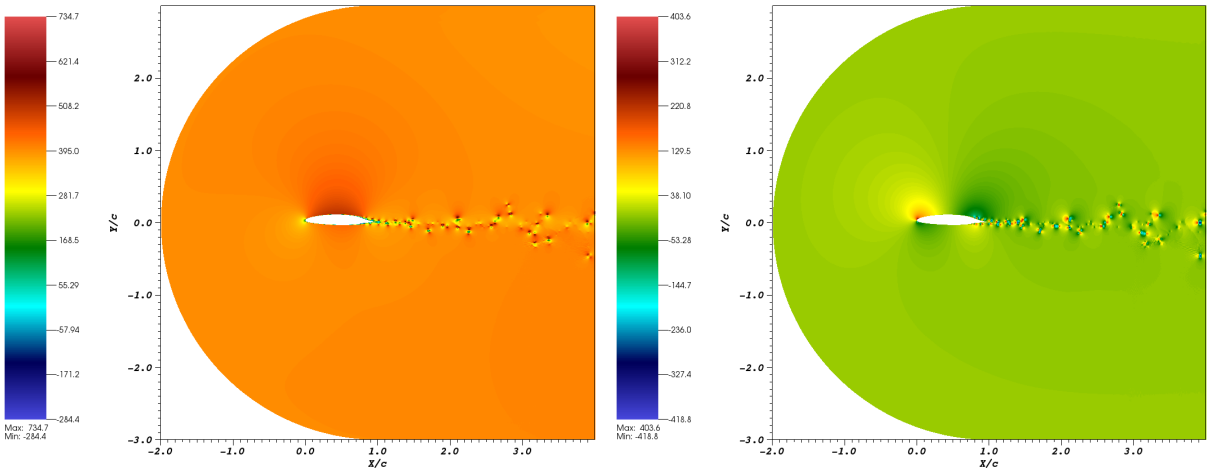

(a) X-Velocity Field for Case 6: Run 622-2D at Re_c = 2 x 10^5

(b) Y-Velocity Field for Case 6: Run 622-2D at Re_c = 2 x 10^5

Figure 37: X- and Y-Velocity Fields for Case 6: Run 622-2D at Re_c = 2 x 10^5

5.3.2 Pressure

Figures 38 and 39 show the pressure fields for the Run 622-2D cases at Re_c = 1 x 10^5 and Re_c = 2 x 10^5. Case 3 and Case 6 (Run 622-2D) have the highest maximum pressure. Case 1 (clean NLF-0414) has the highest (absolute) minimum pressure out of the Re_c = 1 x 10^5 cases and Case 5 (Run 606) has the highest (absolute) minimum pressure out of the Re_c = 2 x 10^5 cases. As the amount of ice increase so does the maximum pressure. The minimum pressure also increases with the presence of ice with the minimum pressure of Case 5 (Run 606) and Case 6 (Run 622-2D) being almost equal.

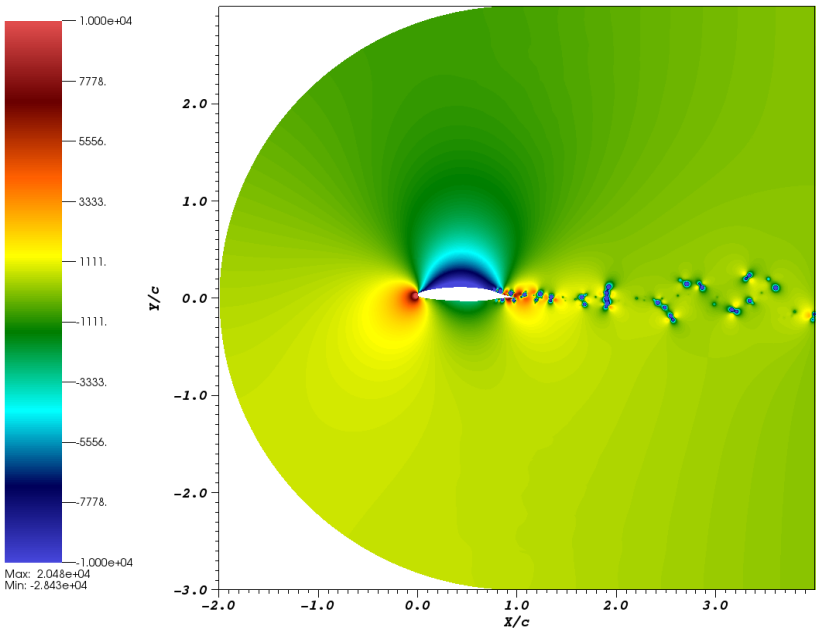

Figure 38: Pressure Field for Case 3: Run 622-2D at Re_c = 1 x 10^5

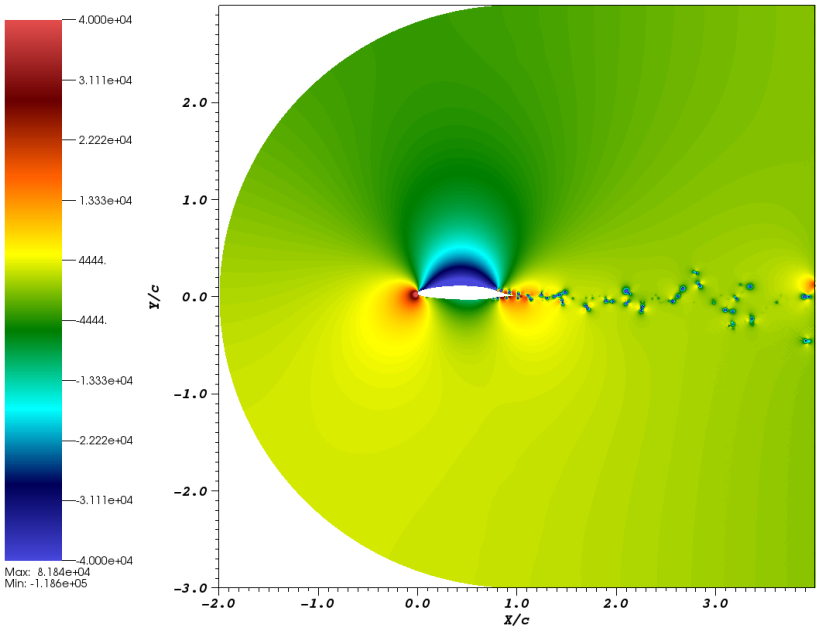

Figure 39: Pressure Field for Case 6: Run 622-2D at Re_c = 2 x 10^5

5.3.3 Vorticity

Figures 40 and 41 show the vorticity comparison between Case 3 and Case 6, Run 622-2D at $Re_c = 1$ x 10^5 and $Re_c = 2$ x 10^5. Case 1, Case 2, and Case 3 have similar structures and very similar shedding frequencies and the same can be said for the cases at $Re_c = 2$ x 10^5.

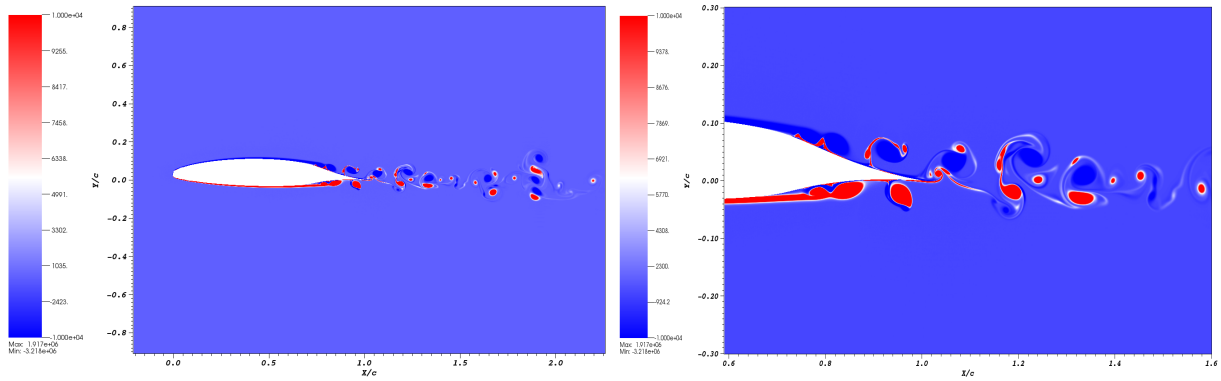

(a) Vorticity Field for Case 3: Run 622-2D at $Re_c = 1$ x 10^5

(b) Trailing Edge Vorticity Field for Case 3: Run 622-2D at $Re_c = 1$ x 10^5

Figure 40: Vorticity Field for Case 3: Run 622-2D at $Re_c = 1$ x 10^5

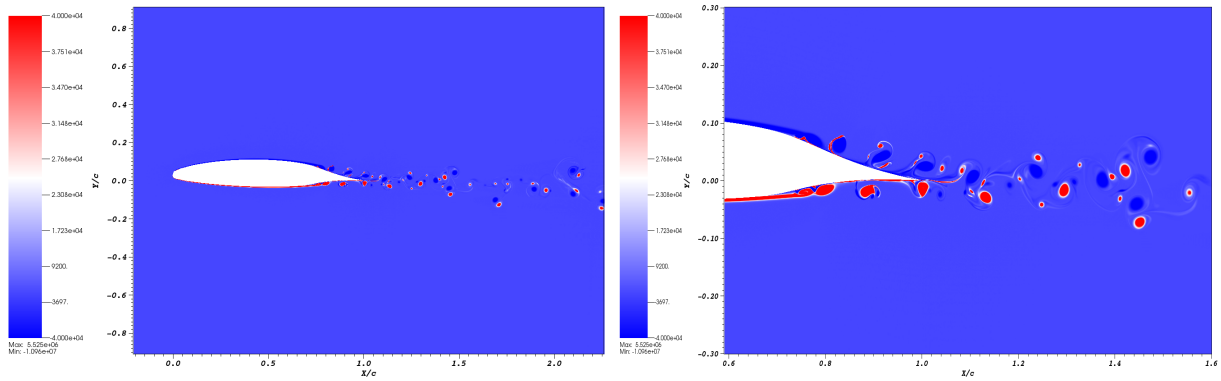

(a) Vorticity Field for Case 6: Run 622-2D at $Re_c = 2$ x 10^5

(b) Trailing Edge Vorticity Field for Case 6: Run 622-2D at $Re_c = 2$ x 10^5

Figure 41: Vorticity Field for Case 6: Run 622-2D at $Re_c = 2$ x 10^5

Figure 42 shows the LE vorticity comparison between Cases 3 and 6, Run 622-2D at $Re_c = 1$ x 10^5 and $Re_c = 2$ x 10^5. The size of the boundary layer in the $Re_c = 1$ x 10^5 case is thicker compared to that of the $Re_c = 2$ x 10^5 case which is tighter to the surface of the airfoil. The faster the velocity the harder it is for the recirculation zone to change the aerodynamic profile of the flow. The Run 622-2D recirculation zones are the biggest and most intense and would change the aerodynamics profile the most.

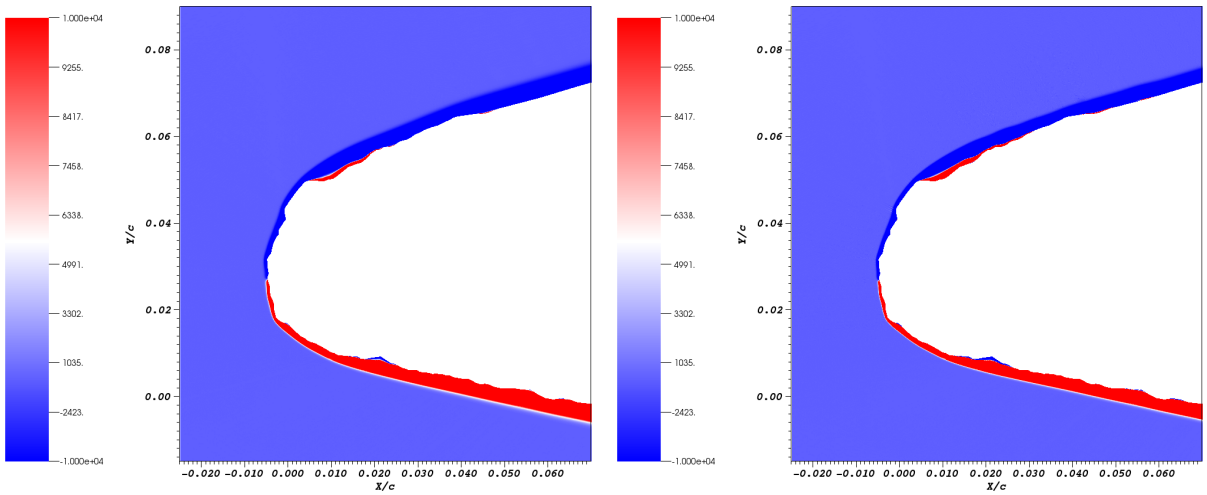

(a) Leading Edge Vorticity Field for Case 3: Run 622-2D Re_c = 1 x 10^5

(b) Leading Edge Vorticity Field for Case 6: Run 622-2D Re_c = 2 x 10^5

Figure 42: Leading Edge Vorticity Field Comparison Between the Run 622-2D Cases at Re_c = 1 x 10^5 and Re_c = 2 x 10^5

5.4 Aerodynamics Characteristics

This section will look at the aerodynamic characteristics such as C_l, C_d, C_p, and C_f (i.e. lift, drag, pressure, and skin friction coefficients, respectively). Individual results for C_l, C_d, C_p, and C_f can be found in Appendix B. The aerodynamic characteristics are defined as follows:

$$C_l = \frac{L}{\frac{1}{2}\rho {U_\infty}^2 A_x} \tag{21}$$

$$C_d = \frac{D}{\frac{1}{2}\rho {U_\infty}^2 A_y} \tag{22}$$

$$C_p = \frac{P - P_\infty}{\frac{1}{2}\rho {U_\infty}^2} \tag{23}$$

$$C_f = \frac{\tau_w}{\frac{1}{2}\rho {U_\infty}^2} \tag{24}$$

where L and D are the lift and drag force, ρ is the density, U_∞ is the freestream velocity, A_x is the relevant surface area for lift (chord x 1 (unit width)), A_y is the relevant surface area for drag (maximum thickness x 1), P is the pressure, and τ_w is the local wall shear stress.

5.4.1 Lift and Drag Coefficient

Figures 43a and 43b show a comparison of the lift and drag coefficients for the Re_c = 1 x 10^5 Cases 1, 2, and 3. The C_l and C_d for the clean (green) and Run 606 (blue) overlap each other and the Run 622-2D (orange) shows a slight shift. The discrepancy for the Run 622-2D (orange) can be attributed to the earlier start of shedding that is one cycle earlier compared to the two other runs. When comparing the Run 622-2D (orange) first peak-to-peak for both C_l and C_d to the Clean (green) and Run 606 (blue) second peak-to-peak they show good agreement and overlap as seen in Figures 45 and 46. This early shedding for Run 622-2D is most likely caused by the small recirculation zones found at the LE explained in Section 5.3.3.

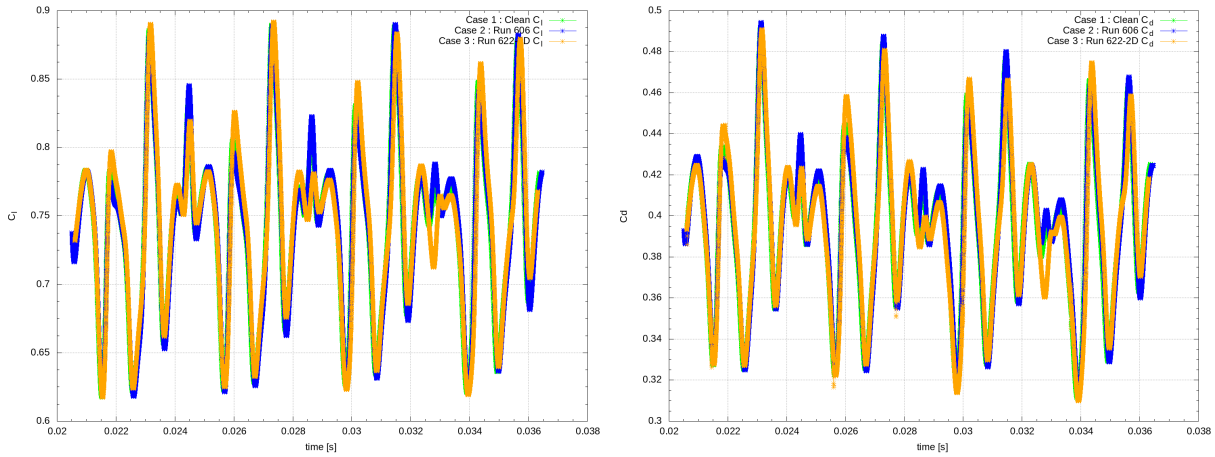

(a) Lift Coefficients for Cases 1, 2, and 3

(b) Drag Coefficients for Cases 1, 2, and 3

Figure 43: Lift and Drag Coefficients for Cases 1, 2, and 3: Clean, Run 606, and Run 622-2D all at Re_c = 1 x 10^5

Figures 44a and 44b show a comparison of the lift and drag coefficients for the Re_c = 2 x 10^5 Cases 4, 5, and 6. The same observations can be made as for the lower Reynolds number cases but at a higher shedding frequency.

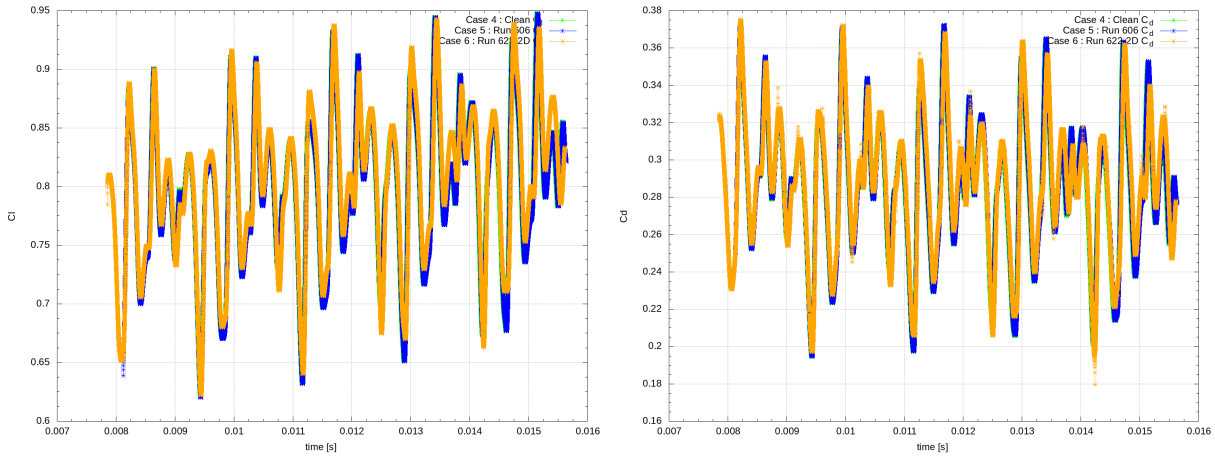

(a) Lift Coefficients for Cases 4, 5, and 6

(b) Drag Coefficients for Cases 4, 5, and 6

Figure 44: Lift and Drag Coefficients for Cases 4, 5, and 6: Clean, Run 606, and Run 622-2D all at Re_c = 2 x 10^5

Figures 45 and 46 show the lift and drag coefficients for Cases 1 through 6 with the Run 622-2D (orange) C_l and C_d shifted over (in time) by one cycle showing proper overlap.

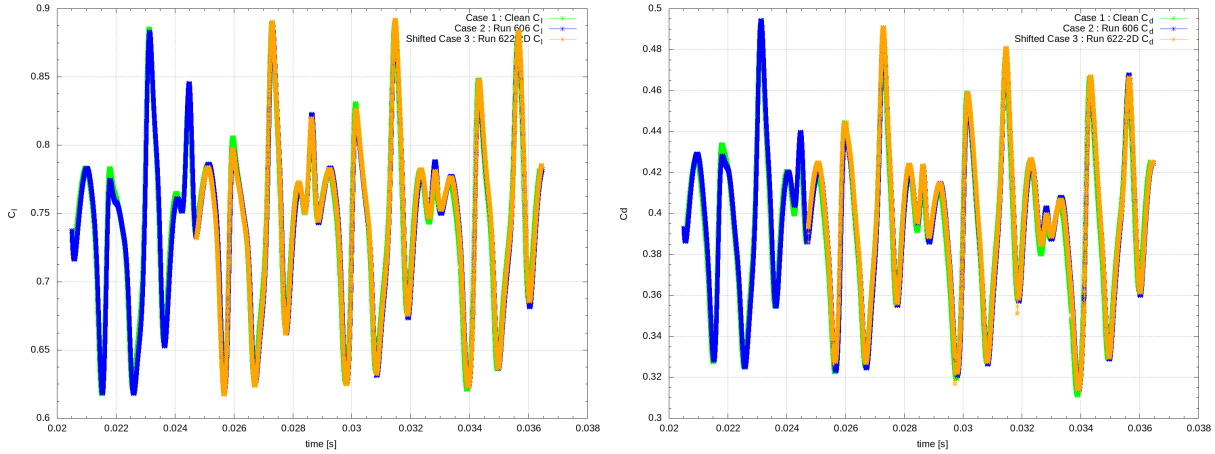

(a) Shifted Lift Coefficients for Cases 1, 2, and 3

(b) Shifted Drag Coefficients for Cases 1, 2, and 3

Figure 45: Shifted Lift and Drag Coefficients for Cases 1, 2, and 3: Clean, Run 606, and Run 622-2D all at Re_c = 1 x 10^5

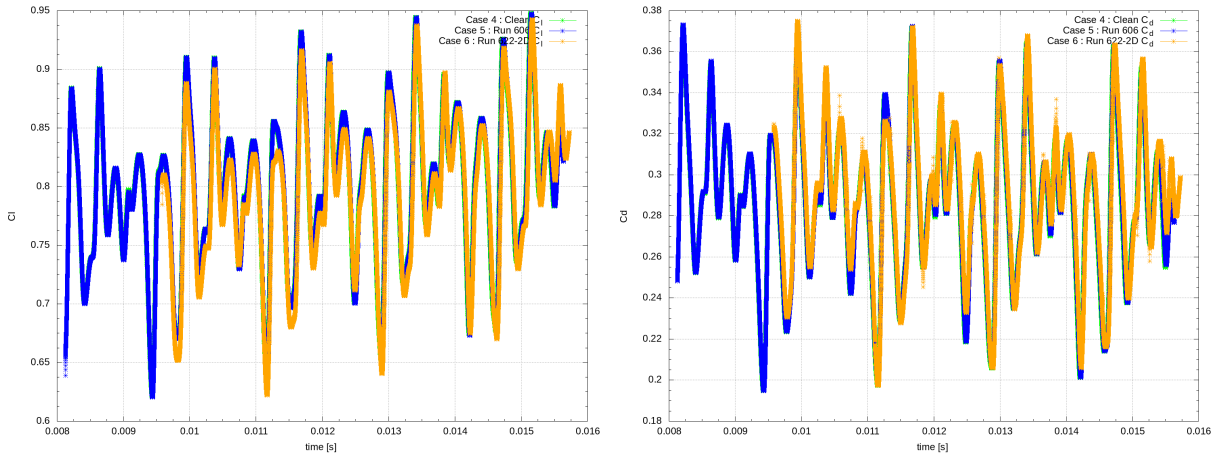

(a) Shifted Lift Coefficients for Cases 4, 5, and 6

(b) Shifted Drag Coefficients for Cases 4, 5, and 6

Figure 46: Shifted Lift and Drag Coefficients for Cases 4, 5, and 6: Clean, Run 606, and Run 622-2D all at $Re_c = 2$ x 10^5

Table 8 gives the values for C_l and C_d for all six cases. In both Reynolds number ranges an increase in C_l and C_d can be observed with larger C_l and C_d values when comparing the clean run to the iced runs. The only deviation from this is the C_d for Case 3; it has a higher C_d than Case 1 but a lower C_d than Case 2. This is most likely caused by the recirculation zones that change the aerodynamic profile in a positive way for the specific $Re_c = 1$ x 10^5.

Table 8: Lift and Drag Coefficients

Case	Name	C_l	C_l Deviation	C_d	C_d Deviation
Case 1	Clean $Re_c = 1$ x 10^5	0.740256	-	0.391802	-
Case 2	Run 606 $Re_c = 1$ x 10^5	0.742455	0.30%	0.395245	0.88%
Case 3	Run 622-2D $Re_c = 1$ x 10^5	0.743855	0.49%	0.394152	0.60%
Case 4	Clean $Re_c = 2$ x 10^5	0.797236	-	0.282420	-
Case 5	Run 606 $Re_c = 2$ x 10^5	0.797915	0.09%	0.285292	1.02%
Case 6	Run 622-2D $Re_c = 2$ x 10^5	0.801560	0.54%	0.286903	1.59%

5.4.2 Pressure Coefficient

The pressure coefficient C_p is used to determine the locations of low and high pressure around the airfoil. Figures 47 and 48 show the C_p comparison for both the $Re_c = 1$ x 10^5 and $Re_c = 2$ x 10^5 cases where the Clean NLF-0414, Run 606 and Run 622-2D are represented by green, blue, and orange respectively. The pressure spikes seen in Figures 47b and 48b are caused by the ice on the LE of Run 606 and Run 622-2D. Due to Run 622-2D (orange) having a larger ice structure than Run 606 it has more spikes and larger spikes. The large spike (orange) on the upper surface of the LE corresponds with the small horn in Run 622-2D. Each valley, on both the upper and lower surfaces, corresponds to a recirculation zone.

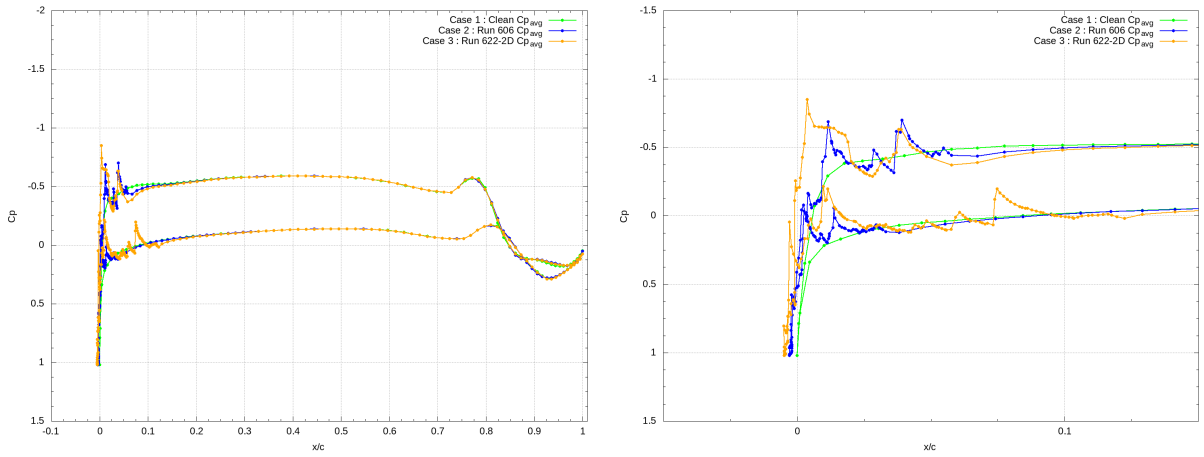

(a) Pressure Coefficients for Cases 1, 2, and 3

(b) Leading Edge Close-up of Pressure Coefficients for Cases 1, 2, and 3

Figure 47: Pressure Coefficients for Cases 1, 2, and 3: Clean, Run 606, and Run 622-2D all at $Re_c = 1$ x 10^5

The large Run 622-2D (orange) peaks on the upper surface in Figures 47b and 48b have an initial spike, a plateau followed by a valley and another spike. The last spikes on the upper surface for both Reynolds number are similar in height and size. The Run 622-2D (orange) $Re_c = 1$ x 10^5 case has a small plateau with a rounded valley. The Run 622-2D (orange) $Re_c = 2$ x 10^5 has a larger flat plateau and its valley is less rounded, smaller and found further down the upper surface. This would indicate that the $Re_c = 1$ x 10^5 Run 622-2D is affected more by the recirculation zone which in turn affects other values such as C_l and C_d. This could explain the lower C_d of Run 622-2D at $Re_c = 1$ x 10^5 compared to the less iced Run 606 at the same Reynolds number. Run 606 cases at $Re_c = 1$ x 10^5 and $Re_c = 2$ x 10^5 have a very similar C_p profile but the $Re_c = 2$ x 10^5 case has slightly higher peaks. This would explain the consistency in C_l and C_d values for Run 606 at both Reynolds numbers.

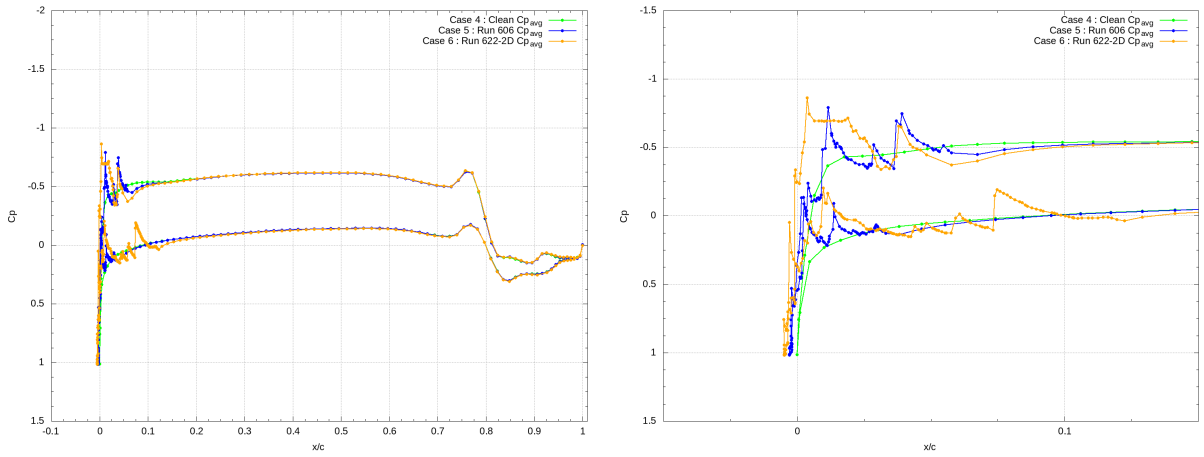

(a) Pressure Coefficients for Cases 4, 5, and 6

(b) Leading Edge Close-up of Pressure Coefficients for Cases 4, 5, and 6

Figure 48: Pressure Coefficients for Cases 4, 5, and 6: Clean, Run 606, and Run 622-2D all at $Re_c = 2$ x 10^5

The TE pressure coefficient distribution at $Re_c = 1$ x 10^5 has a different shape compared to the $Re_c = 2$ x 10^5 one as well as other higher Reynolds number TE profiles like the design C_p graph in Figure 2. The difference is that the TE lower surface pressure recovery peak for the $Re_c = 1$ x 10^5 case is found further down the surface making it overlap with the TE upper surface. A concave pressure recovery area, also known as an adverse pressure gradient (APG) [52], is when the C_p distribution, goes from its minimum (negative C_p) to a positive C_p and is associated with boundary layer transition when the APG is too severe. The TE lower surface pressure recovery peak moves upstream as the Reynolds number increases in the $Re_c = 2$ x 10^5 case. The shifted pressure recovery area ($Re_c = 1$ x 10^5) has a negative effect on the C_d values for the $Re_c = 1$ x 10^5 cases as it decreases the area in the C_p graph thus increasing TE pressure drag. An appropriately used pressure recovery area would explain the large decrease in C_d when comparing the $Re_c = 1$ x 10^5 cases to the $Re_c = 2$ x 10^5.

Other differences when comparing the low Reynolds numbers cases to the design C_p distribution (Figure 2) include a small valley before the pressure recovery area (X/c ≈ 0.7) on both the upper and lower surfaces whereas the design C_p distribution does not have these valleys. Theses valleys disappear with an increase in Reynolds number as the pressure recovery area moves upstream to the design location of X/c = 0.7. In the design C_p distribution the lower surface peak of the pressure recovery area is found slightly before the upper surface peak whereas in all six cases the lower surface peaks are found after. This shift upstream also increases the area between the upper and lower surfaces in the TE C_p distribution which contributes to increased lift. In both Reynolds number cases the end of the C_p distribution curls upward toward zero whereas the design C_p distribution points downward (positive C_p). The TE pressure determines the severity of the APG which is associated with transition and separation.

While the concave pressure recovery area that was designed into the NLF-0414 to reduce tur-

bulent separation problems during transition (Section 1.4) is still present, the lower Reynolds numbers clearly alter the location of the concave pressure recovery areas and the final TE pressure substantially, causing a drop in lift locally (i.e. a smaller area between the top and bottom surface pressure coefficient curves). However, the overall lift is increased due to the peaks and plateaus at the LE near the ice accretion.

5.4.3 Skin Friction Coefficient

The skin friction coefficient (C_f) is calculated to numerically pinpoint the transition from laminar to turbulent flow. Figures 49 and 50 show the skin friction coefficient comparison for Re_c = 1 x 10^5 and Re_c = 2 x 10^5 respectively. Transition is indicated when C_f converges to a zero value and spikes up afterward as seen in the close-up Figures 49b and 50b. There are two lows, defined by initial low and second low, before it spikes up to the peak. Table 9 gives the X/c location of the lows and the peaks for both the upper and lower surfaces. In all six cases the upper surface has the highest peak while the lower surface has a lower double peak.

In the Re_c = 1 x 10^5 cases (Fig. 49) the upper surface starts transitioning (sudden rise to sudden rise) earlier on the airfoil at X/c = 0.66605 than the lower surface at X/c = 0.67849. The distance between the initial low and the second low is shorter for the lower surface than the upper surface. The second low upper surface locations (X/c = 0.72845) are all the same for the three Re_c = 1 x 10^5 cases. The second low lower surface locations (X/c = 0.73948) are also all the same for all three Re_c = 1 x 10^5 cases. Both iced runs (Run 606 and Run 622-2D) at Re_c = 1 x 10^5 have their upper surface peaks further down the surface at X/c = 0.81175 than the clean case at X/c = 0.79856. The Clean NLF-0414 and Run 622-2D at Re_c = 1 x 10^5 have their lower surface peaks at X/c = 0.86096 while Run 606 has it at X/c = 0.84872. The upper surface peak maximum C_f values for the clean NLF-0414, Run 606, and Run 622-2D at Re_c = 1 x 10^5 are 0.018215, 0.017735, and 0.017741 respectively. The lower surface peak maximum C_f values for the clean NLF-0414, Run 606, and Run 622-2D at Re_c = 1 x 10^5 are 0.012321, 0.012737, and 0.012593 respectively. The maximum C_f for the upper surface is lower than the clean NLF-0414 case in both iced cases but is higher than the clean NLF-0414 for the lower surface.

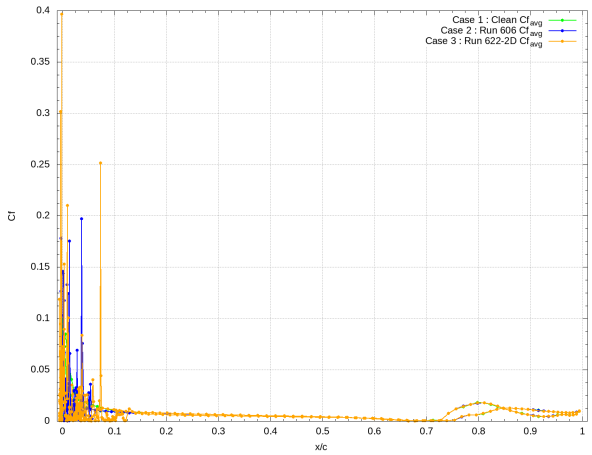

(a) Skin Friction Coefficients for Cases 1, 2, and 3: Re_c = 1 x 10^5

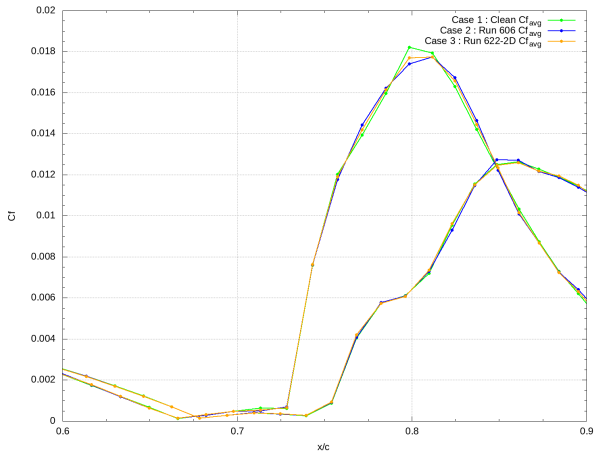

(b) Skin Friction Coefficients Close-up for Cases 1, 2, and 3: Re_c = 1 x 10^5

Figure 49: Skin Friction Coefficient for Cases 1, 2, and 3: Clean, Run 606, and Run 622-2D all at Re_c = 1 x 10^5

For the Re_c = 2 x 10^5 cases (Fig. 50b) the peaks are more compact in X (faster transition) and the lower surface transitions slightly before the top surface. The initial low (lowest C_f) location of the upper surface (X/c = 0.68211) is higher up the airfoil (X/c) than the lower surface (X/c = 0.69418) while the upper surface second low (X/c = 0.72845) is past the lower surface second low (X/c = 0.72468). The second low lower surface location is moving upstream the same way the pressure recovery area does in Section 5.4.2. The upper surface peak maximum values for the clean NLF-0414, Run 606, and Run 622-2D at Re_c = 2 x 10^5 are 0.015969, 0.016018, and 0.015880 respectively. The lower surface peak maximum C_f values for the clean NLF-0414, Run 606, and Run 622-2D at Re_c = 1 x 10^5 are 0.011464, 0.011456, and 0.011395 respectively.

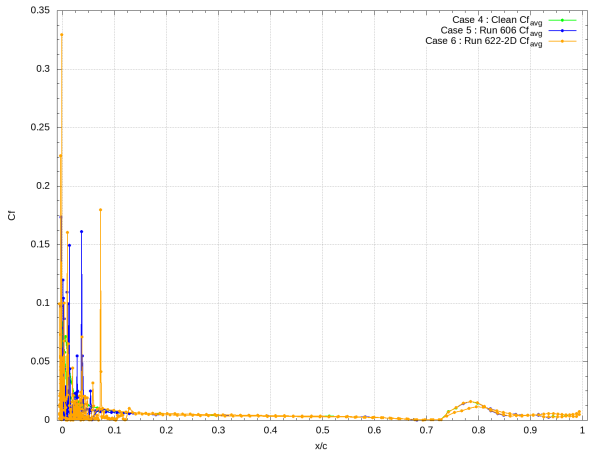

(a) Skin Friction Coefficients for Cases 4, 5, and 6: Re_c = 2 x 10^5

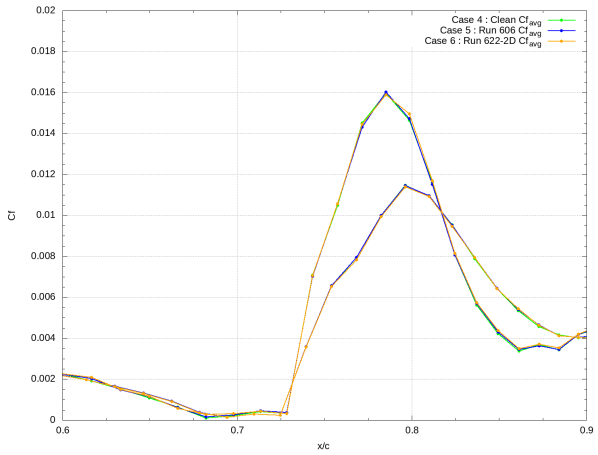

(b) Skin Friction Coefficients Close-up for Cases 4, 5, and 6: Re_c = 2 x 10^5

Figure 50: Skin Friction Coefficient for Cases 4, 5, and 6: Clean, Run 606, and Run 622-2D all at Re_c = 2 x 10^5

The ice from Run 606 and Run 622-2D has no effect on the initial and second lows as their locations are the same as the clean NLF-0414 for the same Reynolds numbers. The Re_c = 1 x 10^5 cases upper and lower surfaces have their initial lows higher up the airfoil (X/c) than the Re_c = 2 x 10^5 cases' indicating earlier transition in the Re_c = 1 x 10^5 cases. The second low for the lower surface Re_c = 2 x 10^5 cases is higher up the airfoil (X/c) than for the Re_c = 1 x 10^5 cases. The second low for the upper surface is at the same location for both Reynolds numbers. The Re_c = 2 x 10^5 cases have more energy indicated by the smaller distance between the initial low and second low than the Re_c = 1 x 10^5 cases. Both the upper and lower surface peak locations are higher up the airfoil (X/c) and closer together in the Re_c = 2 x 10^5 cases than in the Re_c = 1 x 10^5 cases.

Table 9: Location (X/c) of C_f Peaks and Lows

Case	Name	Initial Low		Second Low		Peak	
		Upper Surface	Lower Surface	Upper Surface	Lower Surface	Upper Surface	Lower Surface
Case 1	Clean[a]	0.66605	0.67849	0.72845	0.73948	0.79856	0.86096
Case 2	Run 606[a]	0.66605	0.67849	0.72845	0.73948	0.81175	0.84872
Case 3	Run 622-2D[a]	0.66605	0.67849	0.72845	0.73948	0.81175	0.86096
Case 4	Clean[b]	0.68211	0.69418	0.72845	0.72468	0.78519	0.79635
Case 5	Run 606[b]	0.68211	0.69418	0.72845	0.72468	0.78519	0.79635
Case 6	Run 622-2D[b]	0.68211	0.69418	0.72845	0.72468	0.78519	0.79635

[a] Re_c = 1 x 10^5
[b] Re_c = 2 x 10^5

The only inconsistent value is the Run 606 at Re_c = 1 x 10^5 with its lower surface peak being upstream of the clean NLF-0414 and Run 622-2D cases but Run 606 C_f values at X/c = 0.84872 and X/c = 0.86096 are almost equal as shown by the plateau in Figure 49b. The ice accretion from Run 606 and Run 622-2D causes a thicker BL on the top surface that changes the aerodynamic profile which could move the upper surface peaks further down the airfoil. This shows that the ice has some effect on the Re_c = 1 x 10^5 cases by slightly moving the locations of the upper and lower surface peaks but past a Re_c = 1 x 10^5 the freestream velocity has more of an impact on the lows and peaks locations.

5.4.4 Dimensionless Wall Distance y^+

The dimensionless wall distance (y^+) is often used to characterize proper meshing in turbulent regions. In most DNS studies meshes resolving up to a $y^+ \approx 1.0$ are desired to properly capture the flow characteristics. The viscous sublayer (dominated by viscous effects) is defined by $y^+ < 5$, the logarithmic layer (dominated by turbulence stresses) is defined by $y^+ > 30$, and the buffer layer (mixed viscous-turbulence stress region) is defined by $5 < y^+ < 30$ [53]. The dimensionless wall distance y^+ is defined as:

$$y^+ = \frac{Y\, u_\tau}{\nu} \tag{25}$$

where u_τ is the friction velocity at the nearest wall, and ν is the kinematic viscosity. The friction velocity u_τ is defined as:

$$u_\tau = \sqrt{\frac{\tau_w}{\rho}} \tag{26}$$

where τ_w is the wall shear stress and ρ is the fluid density. Taking the Y coordinate of the first node point in the mesh (in the direction normal to the surface area) leads us to estimate the y^+ that is resolved. Figure 51 gives the y^+ with respect to the first normal Gmsh node around the surface of the airfoil for all six cases. With the exception of the iced cases with high values of y^+ in the LE ice, the maximum y^+ is on the $O(1)$. Values of y^+ between $X/c = 0.1$ and $X/c = 0.7$ are below 1.5 and the maximum value is achieved at $X/c \approx 0.80$ for $Re_c = 1$ x 10^5 cases and at $X/c \approx 0.79$ for $Re_c = 2$ x 10^5 cases with a $y^+ < 2$. Since we use high order methods, a larger y^+ than in low order methods is permissible. The actual y^+ is lower depending on the high order method used (i.e. for 5^{th} order the first collocation point is at $1/6^2$ of the element height (the Y used in the y^+ value above): y^+ resolved $\sim O(1)/36 \sim O(10^{-2})$). We thus confirm that we have resolved the turbulent boundary layer sufficiently, recalling that $y^+ < 5$ represents the viscous sublayer and $y^+ > 30$ represents the log region. With 5^{th} order polynomials, these y^+ values (at the LE and beyond the transition point) are well within the range of accuracy desired.

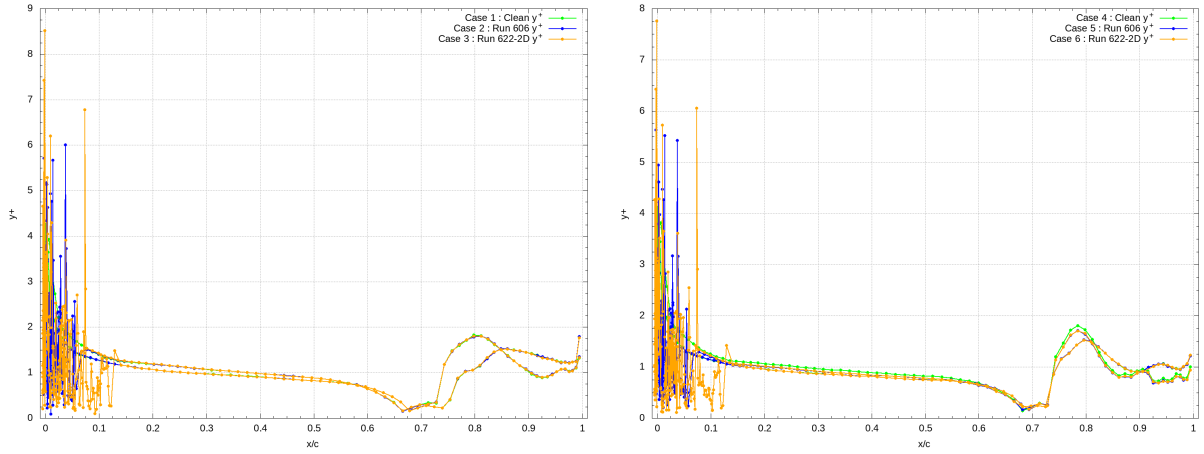

(a) Dimensionless Wall Distance y^+ for Cases 1, 2, and 3: $Re_c = 1$ x 10^5

(b) Dimensionless Wall Distance y^+ for Cases 4, 5, and 6: $Re_c = 2$ x 10^5

Figure 51: Dimensionless Wall Distance y^+ of First Normal Gmsh Node for All Six Cases: Clean, Run 606, and Run 622-2D at $Re_c = 1$ x 10^5 and $Re_c = 2$ x 10^5

5.5 Velocity Profiles

This section covers the LE and TE X-velocity profiles as a function of height (Y) for all six cases. Figures 52 and 53 show the location of the LE and TE probe lines, on an X-velocity field background, used for the velocity profiles. Figure 53 shows the vorticity, taken at the same time, with the same probe line for better understanding of the flow. The probe line colours in Figures 52 and 53 match the colours used for the velocity profiles. In Figures 52a, 52b, and 52c the yellow probe lines on the lower surface of the LE are all located at the same X/c for comparison. Figures of LE velocity profiles (Section 5.5.1) are split into two: (a) Airfoil Leading Edge, (b) Airfoil Leading Edge Close-Up of the surface near the airfoil. The LE velocity profiles are defined by a letter label and corresponding colour seen in Figure 52. The letter labels for the clean NLF-0414 LE Figure 52a are A (dark green) and B (yellow). The letter labels for the Run 606 (Figure 52b) and Run 622-2D (Figure 52c) LE are A (purple), B (dark green), C (red), D (neon green), and E (yellow). Figures of TE velocity profiles (Section 5.5.2) are split into four: (a) Airfoil Trailing Edge Upper Surface, (b) Airfoil Trailing Edge Upper Surface Close-Up, (c) Airfoil Trailing Edge Lower Surface, and (d) Airfoil Trailing Edge Lower Surface Close-Up. Each TE velocity profile is defined by a location (X/c) and corresponding colour seen in Figure 53. The locations are 65% X/c (purple), 70% X/c (dark green), 74% X/c (red), 77% X/c (orange), 80% X/c (neon green), and 90% X/c (blue). The 65% X/c (purple) location is taken ahead of any separation/transition point (see Section 5.4.3) for comparison. When the velocity profiles have a negative value of u/U_∞ it indicates a change in direction of the u velocity. A negative u/U_∞ also indicates the start of the BL separation from the surface of the airfoil. When the velocity profile transitions from a horizontal slope to a vertical slope the velocity profile exits the BL.

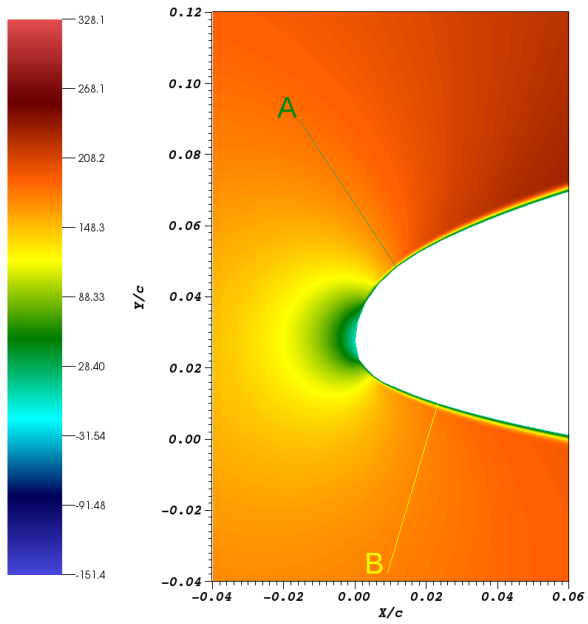

(a) Clean Leading Edge X-Velocity Field with Probe Lines

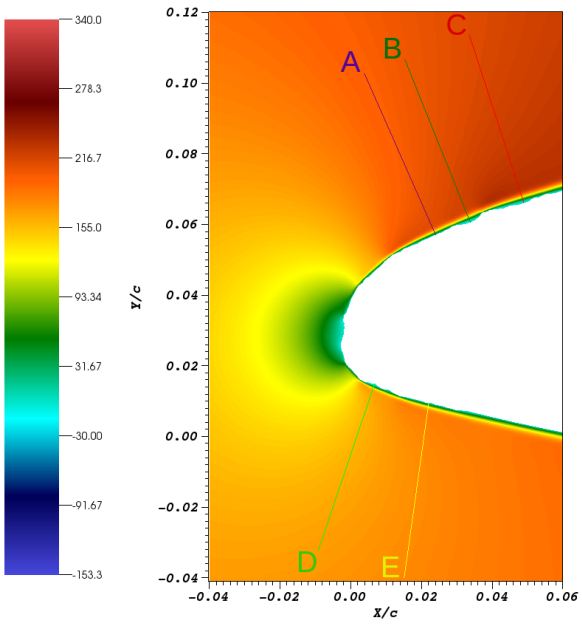

(b) Run 606 Leading Edge X-Velocity Field with Probe Lines

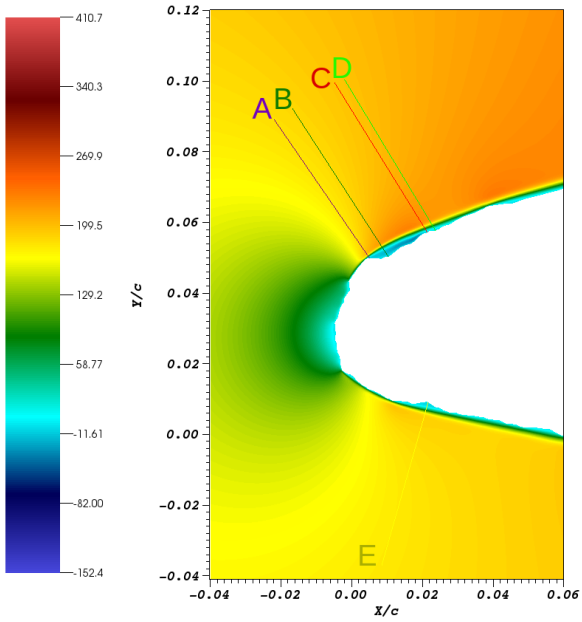

(c) Run 622-2D Leading Edge X-Velocity Field with Probe Lines

Figure 52: Leading Edge X-Velocity Probe Line Locations

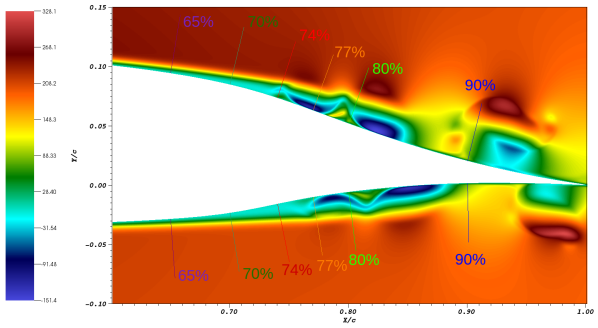

(a) Case 1: Trailing Edge X-Velocity Field with Probe Lines

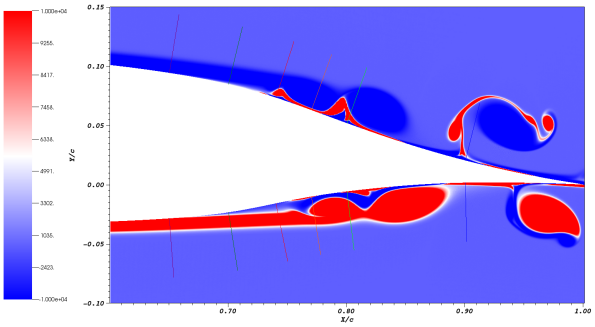

(b) Case 1: Trailing Edge Vorticity Field with Probe Lines

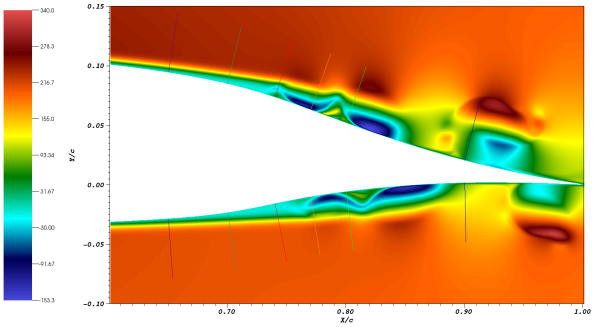

(c) Case 2: Trailing Edge X-Velocity Field with Probe Lines

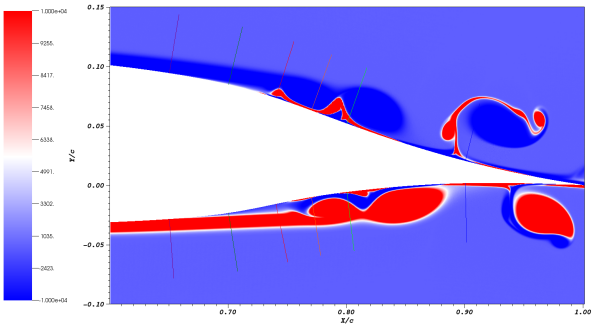

(d) Case 2: Trailing Edge Vorticity Field with Probe Lines

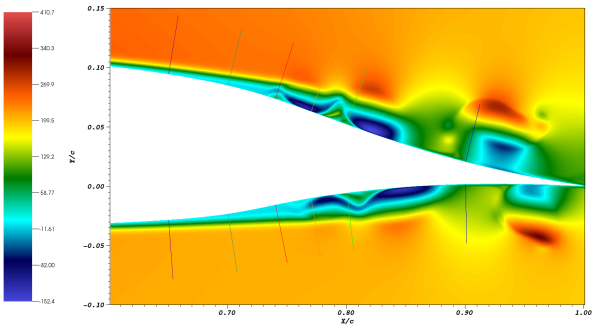

(e) Case 3: Trailing Edge X-Velocity Field with Probe Lines

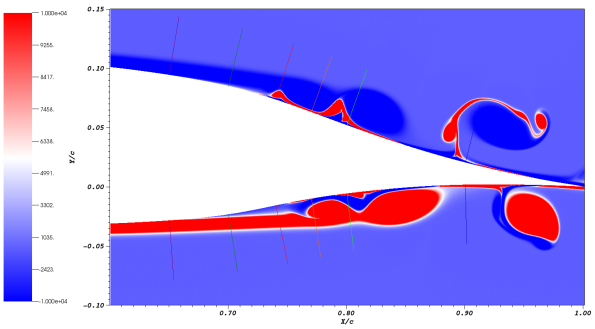

(f) Case 3: Trailing Edge Vorticity Field with Probe Lines

Figure 53: Trailing Edge X-Velocity and Vorticity Fields with Probe Lines [see (a) for example: 65% (purple), 70% (dark green), 74% (red), 77% (orange), 80% (neon green), 90% (blue)]

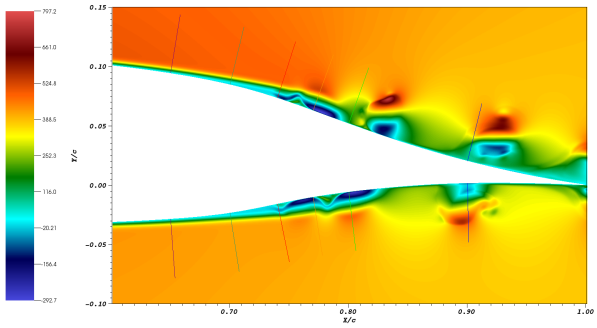

(g) Case 4: Trailing Edge X-Velocity Field with Probe Lines

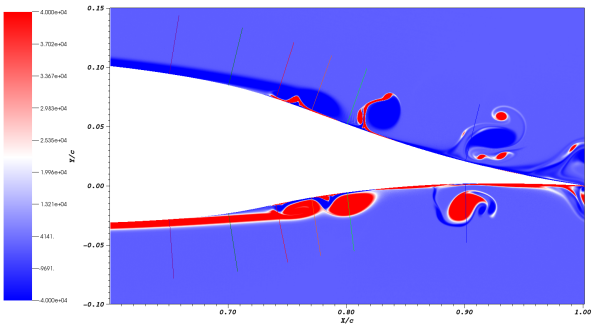

(h) Case 4: Trailing Edge Vorticity Field with Probe Lines

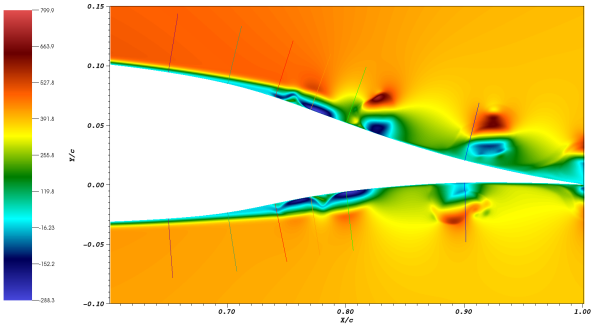

(i) Case 5: Trailing Edge X-Velocity Field with Probe Lines

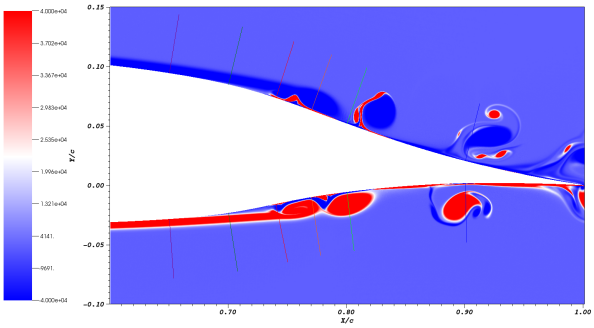

(j) Case 5: Trailing Edge Vorticity Field with Probe Lines

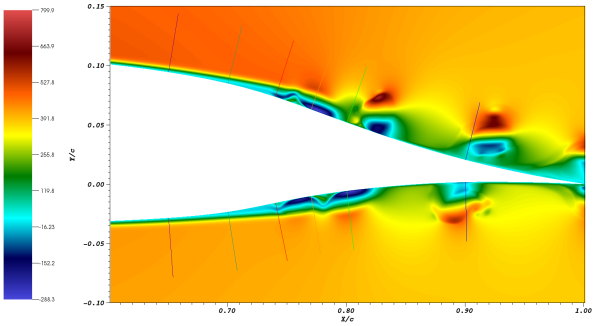

(k) Case 6: Trailing Edge X-Velocity Field with Probe Lines

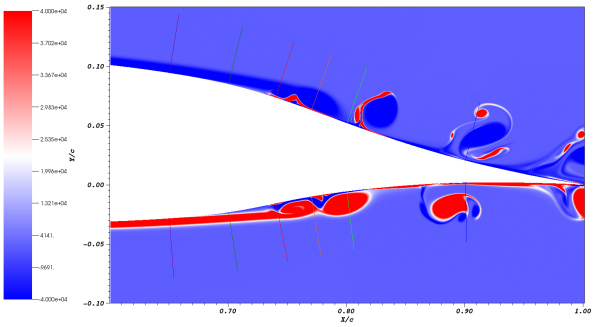

(l) Case 6: Trailing Edge Vorticity Field with Probe Lines

Figure 53: Trailing Edge X-Velocity and Vorticity Fields with Probe Lines [see (a) for example: 65% (purple), 70% (dark green), 74% (red), 77% (orange), 80% (neon green), 90% (blue)]

The velocity and vorticity fields above are taken at the same time but due to the ice changing the velocity near the airfoil some of the cases are slightly more advanced than the others. For the Re_c = 1 x 10^5 upper surface, in order from most advanced to slowest, are clean NLF-0414 (Case 1), Run 622-2D (Case 3), and Run 606 (Case 2) but for the lower surface are Clean NLF-0414 (Case 1), Run 606 (Case 2), and Run 622-2D (Case 3). For the Re_c = 2 x 10^5 upper and lower surfaces: Clean NLF-0414 (Case 4), Run 606 (Case 5), and Run 622-2D (Case 6). The faster velocity on the upper surface of the Re_c = 1 x 10^5 Run 622-2D (Case 3) compared to the Run 606 (Case 2) could explain the variation in C_d seen in Table 8 from Section 5.4.1.

5.5.1 Leading Edge Velocity Profiles

Figures 54 and 55 show the LE velocity profiles for the clean NLF-0414 cases at Re_c = 1 x 10^5 and Re_c = 2 x 10^5. The velocity profiles A (green)(upper surface) and B (yellow)(lower surface) for both Reynolds number cases have the same shape. In Figure 55b the upper surface flow (green) is more accelerated and the lower surface flow (yellow) is less accelerated in comparison to its Re_c = 1 x 10^5 counterparts. This observation correlates with the C_f lows shifting upstream. The reduced height (Y) of the velocity profiles in Figure 55b indicates a thinner BL at the LE. In both Reynolds number cases the maximum values for u/u_∞ are below 1 which indicates the flow has not accelerated back to freestream value on both the upper and lower surfaces of this curved leading edge (as expected).

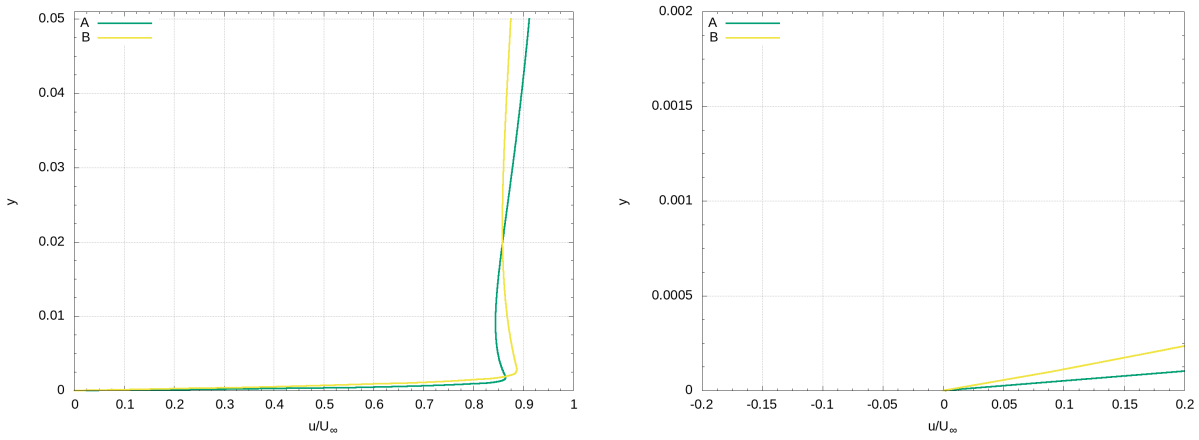

(a) Airfoil Leading Edge (b) Airfoil Leading Edge Close-Up

Figure 54: Nondimensional Velocity Profile – Case 1: Clean NLF-0414 Leading Edge at Re_c = 1 x 10^5

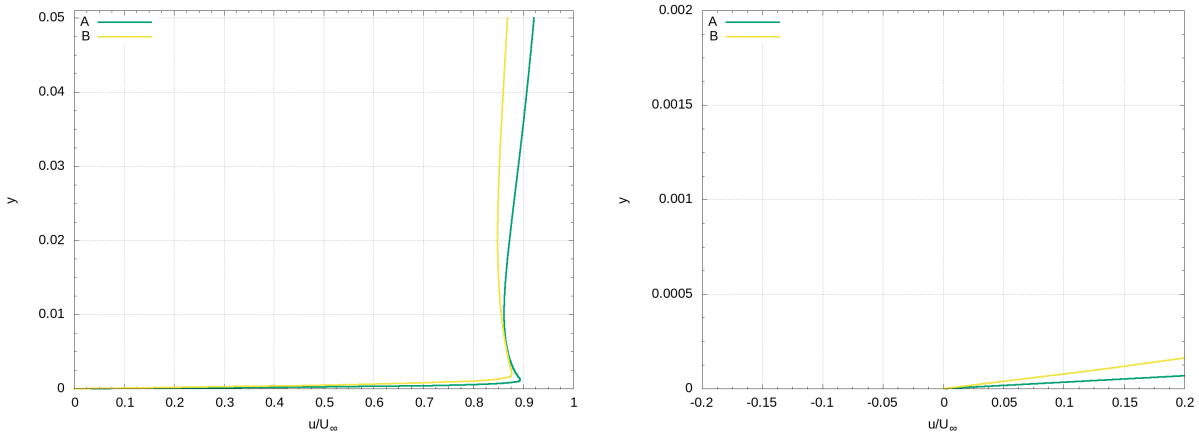

(a) Airfoil Leading Edge (b) Airfoil Leading Edge Close-Up

Figure 55: Nondimensional Velocity Profile – Case 4: Clean NLF-0414 Leading Edge at Re_c = 2 x 10^5

Figures 56 and 57 show the LE velocity profiles for the Run 606 cases at Re_c = 1 x 10^5 and Re_c = 2 x 10^5. Velocity profiles A (purple), B (dark green), and C (red) are on the LE upper surface while D (neon green) and E (yellow) are on the LE lower surface of the airfoil. Velocity profiles B (dark green), C (red), and D (neon green) are located in ice crevasses as seen in Figure 53c. In both Reynolds number cases the upper surface velocity is accelerated as indicated by u/U_∞ values higher than 1 while the lower surface velocity remains under 1. A negative u/U_∞ indicates a recirculation zone as the velocity changes direction. The A (purple) and E (yellow) velocity profiles are sharply sloped in the positive direction while the other three are rounded and go upwards. In Figure 56b the C (red) velocity profile goes vertical but stays positive while B (dark green) and D (neon green) have a slight curve in the negative direction. This indicates that a very small amount of recirculation can be found in those locations. C (red) has a curved profile because it is located in a crevasse downstream from B (dark green) where the BL is pushed up by the ice. In Figure 57b the B (dark green), C (red), and D (neon green) velocity profiles show a more important recirculation than the Re_c = 1 x 10^5 case but all three profiles have similar values.

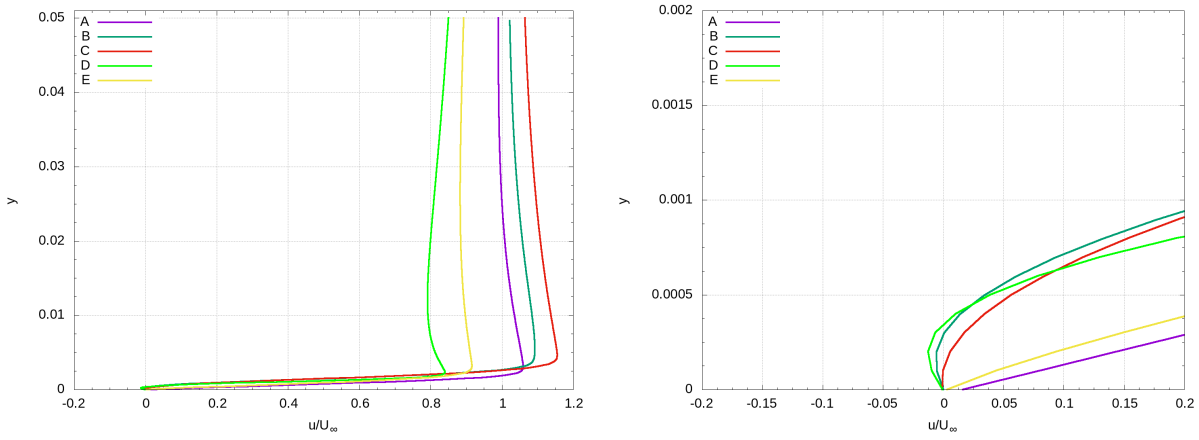

(a) Airfoil Leading Edge

(b) Airfoil Leading Edge Close-Up

Figure 56: Nondimensional Velocity Profile – Case 2: Run 606 Leading Edge at Re_c = 1 x 10^5

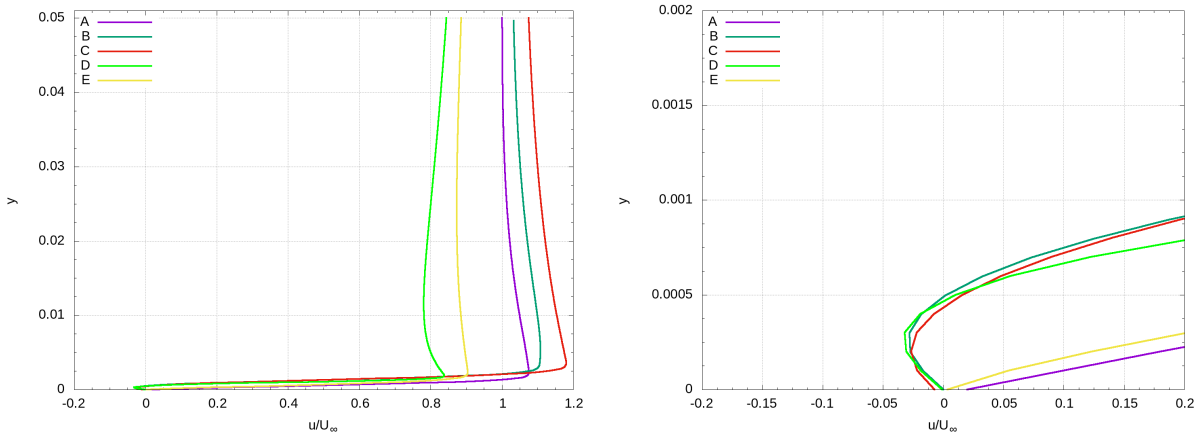

(a) Airfoil Leading Edge

(b) Airfoil Leading Edge Close-Up

Figure 57: Nondimensional Velocity Profile – Case 5: Run 606 Leading Edge at Re_c = 2 x 10^5

Figures 58 and 59 show the LE velocity profiles for the Run 622-2D cases at Re_c = 1 x 10^5 and Re_c = 2 x 10^5. Velocity profiles A (purple), B (dark green), C (red), and D (neon green) are on the LE upper surface while E (yellow) is on the LE lower surface of the airfoil. Velocity profile A (purple) is located right after the small horn and C (red) is located right at the peak of a crevasse downstream of A (purple). Velocity profiles B (dark green), D (neon green), and E (yellow) are located in crevasses as seen in Figure 53e. Every velocity profile close-up for both Reynolds numbers starts with a negative u/U_∞. In Figure 58b a large recirculation can be observed for B (dark green) while a small amount of recirculation can be observed for the other four velocity profiles. In Figure 59b the B (dark green) velocity value is slightly smaller than for the Re_c = 1 x 10^5 case but has a larger area of effect (Y). The recirculation zone on the upper surface of the Re_c = 2 x 10^5 case increases in size and intensity based on the large value increase for both C (red) and D (neon green). The recirculation zone for both Reynolds numbers can also been observed in Figure 42 by looking at the vorticity field. The increase in recirculation observed for the lower surface velocity profile E (yellow) is much less than at other locations when increasing from Re_c = 1 x 10^5 to Re_c = 2 x 10^5.

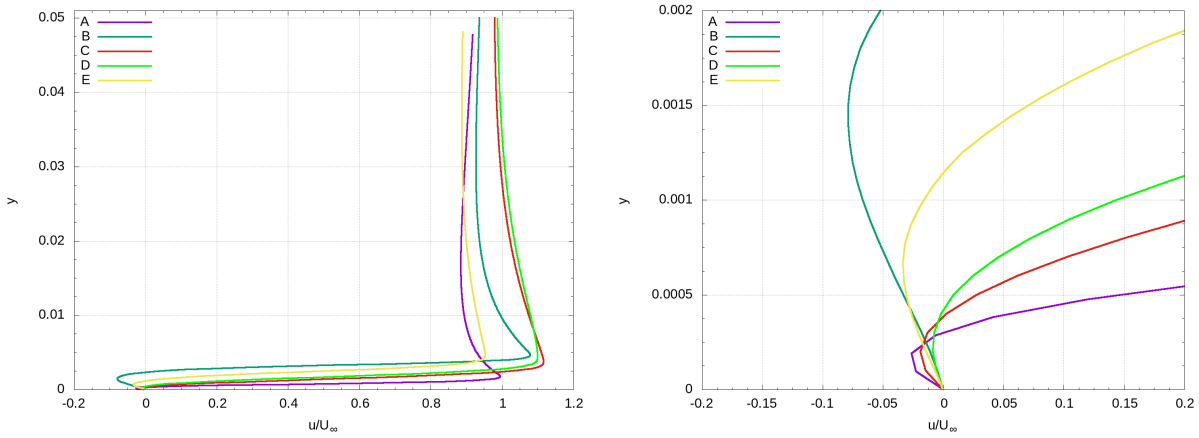

(a) Airfoil Leading Edge (b) Airfoil Leading Edge Close-Up

Figure 58: Nondimensional Velocity Profile – Case 3: Run 622-2D Leading Edge at Re_c = 1 x 10^5

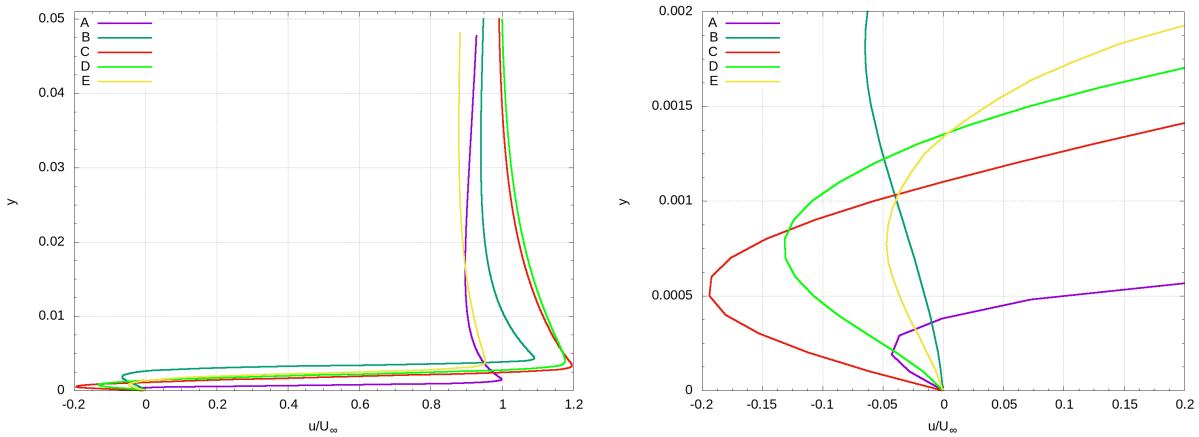

(a) Airfoil Leading Edge (b) Airfoil Leading Edge Close-Up

Figure 59: Nondimensional Velocity Profile – Case 6: Run 622-2D Leading Edge at Re_c = 2 x 10^5

The u/U_∞ maximum values for the yellow velocity profiles in Figures 54 and 55 (Clean NLF-0414 at Re_c = 1 x 10^5 and Re_c = 2 x 10^5) are 0.8872 and 0.8770, while the maximum u/U_∞ values for Figures 56, 57 (Run 606 NLF-0414 at Re_c = 1 x 10^5 and Re_c = 2 x 10^5), 58,and 59 (Run 622-2D NLF-0414 at Re_c = 1 x 10^5 and Re_c = 2 x 10^5) are 0.9162, 0.9046, 0.9537, and 0.9540 respectively. The u/U_∞ maximum values show that as the amount of ice increases so does the u velocity at the outer edge of the BL. The clean cases show only positive values of u/U_∞, the Run 606 cases show positive and near zero negatives values and the Run 622-2D cases show near zero and negatives values.

5.5.2 Trailing Edge Velocity Profiles

Figure 60 shows the upper and lower TE velocity profiles for the clean NLF-0414 case at Re_c = 1 x 10^5. Both the upper and lower surfaces 65% X/c (purple) velocity profiles show no separation while the upper and lower surfaces 70% X/c (dark green) velocity profiles show the start of the BL separation. In Figure 60b, the 70% X/c (dark green) velocity profile has a slightly larger separation than the one in Figure 60d indicating that the BL separation starts earlier on the upper surface than the lower surface.

The upper surface 74% (red) probe line goes through the tail end of the first visible vortex in the BL. This first vortex has a smaller square shape with the tail end sucking up the surface fluid. The upper 74% (red) velocity profile has an S-curve indicating two changes in velocity direction: from a positive to a negative and back to a positive. The upper 77% (orange) probe line goes through the middle of the smaller initial vortex. The upper 77% (orange) velocity profile has C-curve in the negative u/U_∞, a small inflection near the middle of the profile and a small overshoot near the end of the profile. The C-curve shows that the flow goes toward the front of the airfoil (negative direction) due to the initial vortex swirling. A C-curve also indicates CCW vorticity (positive-red) while an inverse C-curve indicates CW vorticity (negative-blue). The S-curve is a combination of an inverse C-curve and a C-curve. The inflection of the slope shows the inner structure of a vortex. The overshoot is an acceleration of the flow before exiting the BL caused by the swirl of a vortex sucking the flow forwards around the vortex. This acceleration is located between the middle and the tail end of the vortex right above the outer surface of the BL. The upper 80% (neon green) probe line goes through the tail of the leading vortex. The leading vortex is the last vortex still connected to the BL. The upper 80% (neon green) velocity profile has a larger S-curve as well as an overshoot near the end of the profile. Both the S-curve and the overshoot are larger than the other velocity profiles as the BL is thicker and the velocity is accelerated over the leading vortex. The upper 90% (blue) probe line goes through a separated vortex tail. The upper 90% (blue) velocity profile has an early inverse C-curve followed by a vertical slope then goes back to a horizontal slope when it reaches the separated vortex (Figure 53b). The inverse C-curve is accelerated by the small part of the vortex tail that is still attached to the surface of the airfoil.

The lower surface 74% (red) probe line goes through the laminar section of the separated BL and is located before any vortices. The lower 74% (red) velocity profile has a near zero separation for a larger Y than the 70% (dark green). The lower 77% (orange) probe line goes through the tail of the smaller initial vortex. The lower 77% (orange) velocity profile in Figure 60c has a small S-curve, a larger slope inflection, and a small overshoot when compared to the upper 77% (orange) velocity profile in Figure 60a. The swirl structure is more defined in the lower 77% (orange) velocity profile. The lower 80% (neon green) probe line goes through the front of the smaller initial vortex. The lower 80% (neon green) velocity profile has a large S-curve. The lower 90% (blue) probe line is located between the leading vortex and the recently shed vortex. The lower 90% (blue) velocity profile has an early change from a horizontal slope to a vertical slope at a low u/U_∞ and low Y as it goes through the smaller attached secondary BL on the lower surface of the airfoil.

The upper 80% (neon green), upper 90% (blue), lower 77% (orange), and lower 90% (blue) velocity profiles have their change in slope at $u/U_\infty \approx 0.42$, $u/U_\infty \approx 0.43$, $u/U_\infty \approx 0.42$, and $u/U_\infty \approx 0.42$ respectively. The upper 74% (red) and lower 80% (neon green) velocity profiles both have their change in slope at the same value of $u/U_\infty \approx 0.24$.

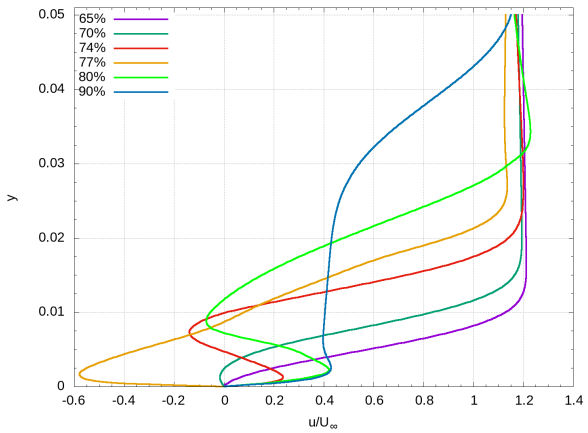

(a) Case 1: Airfoil Trailing Edge Upper Surface

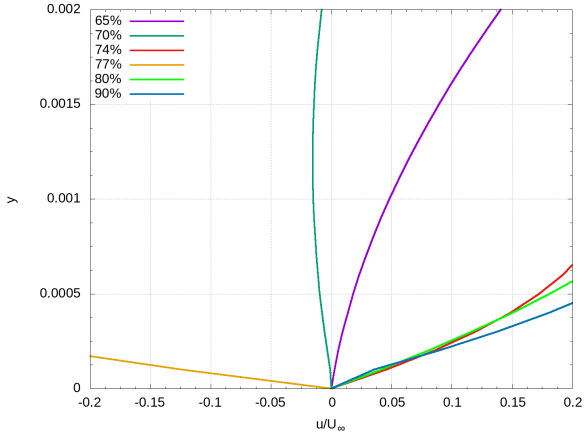

(b) Case 1: Airfoil Trailing Edge Upper Surface Close-Up

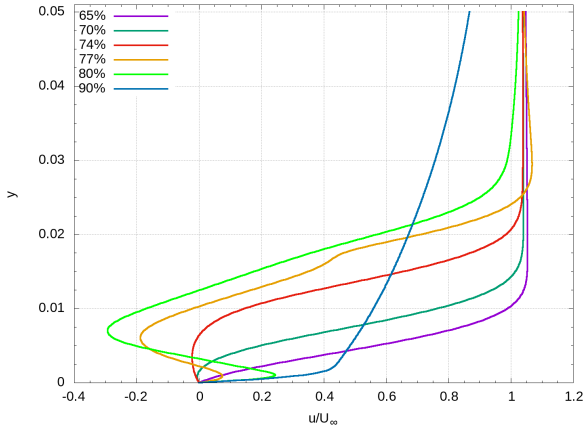

(c) Case 1: Airfoil Trailing Edge Lower Surface

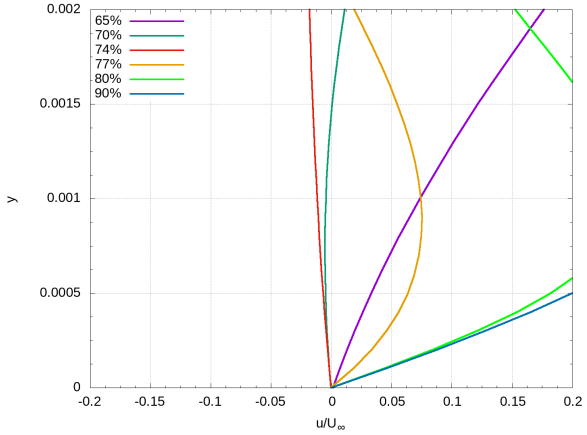

(d) Case 1: Airfoil Trailing Edge Lower Surface Close-Up

Figure 60: Nondimensional Velocity Profile – Case 1: Clean NLF-0414 Trailing Edge at Re_c = 1 x 10^5

Figure 61 shows the upper and lower TE velocity profiles for the clean NLF-0414 case at Re_c = 2 x 10^5. The 65% (purple) u/U_∞ is positive for both Reynolds numbers while the 70% (dark green) u/U_∞ is near zero but mostly positive. The 70% (dark green) u/U_∞ shows a BL separation start with a larger separation on the lower surface in Figure 61d suggesting that the lower surface starts its transition slightly earlier.

The upper surface 74% (red) probe line goes through the middle of the initial smaller vortex tail and its velocity profile has a small C-curve with an slope inflection in the middle of

the profile. The C-curve indicates an initial negative velocity while the inflection shows the vortex swirl structure. The upper 77% (orange) probe line goes through the leading vortex tail with an overshoot (accelerated by curl) in the velocity profile. The upper 80% (neon green) probe line is located right after the complete separation of the large BL. The upper 90% (blue) probe line goes through a separated vortex tail making its velocity profile change from a sharp horizontal slope (in the BL fluid) to a vertical slope (in the freestream fluid) twice.

The lower surface 74% (red) probe line goes through the smaller initial vortex tail and has an S-curve (tail pulling up) in its velocity profile. The lower 77% (orange) probe line goes through the front of the initial lower surface vortex. The lower 80% (neon green) probe line goes through the leading vortex and has an overshoot in its velocity profile caused by the BL curling inwards. The lower 90% (blue) velocity profile has a very large overshoot as well as a small S-curve near the surface of the airfoil caused by the separated vortex.

The upper surface 74% (red) and upper surface 80% (neon green) velocity profiles slope changes arise at a value of $u/U_\infty \approx 0.38$ and $u/U_\infty \approx 0.39$ respectively. The upper surface 90% (blue) and lower surface 74% (red) velocity profiles both have their change in slope at the same value of $u/U_\infty \approx 0.19$.

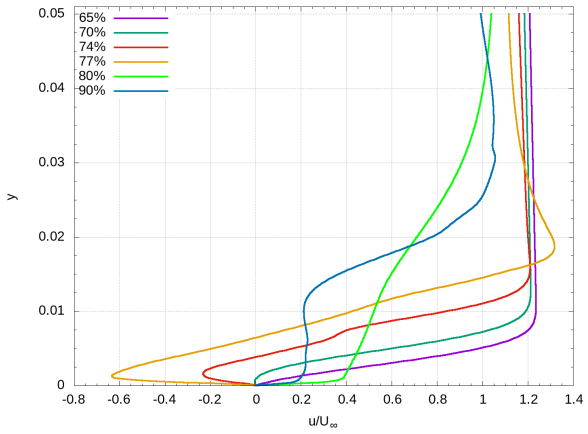

(a) Case 4: Airfoil Trailing Edge Upper Surface

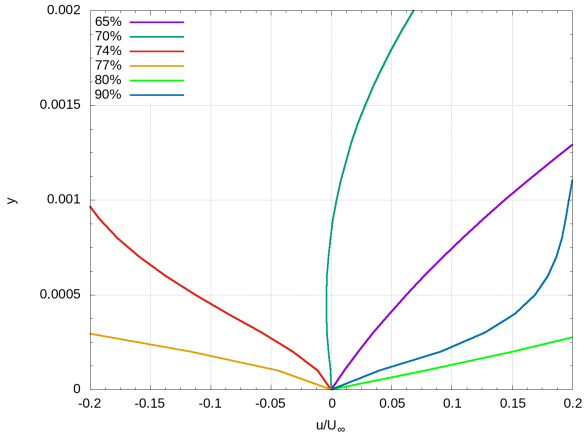

(b) Case 4: Airfoil Trailing Edge Upper Surface Close-Up

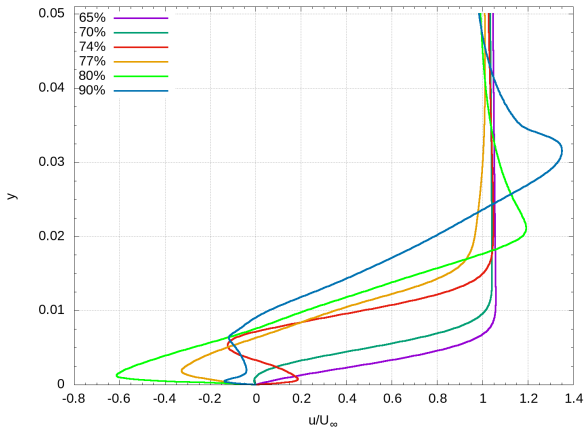

(c) Case 4: Airfoil Trailing Edge Lower Surface

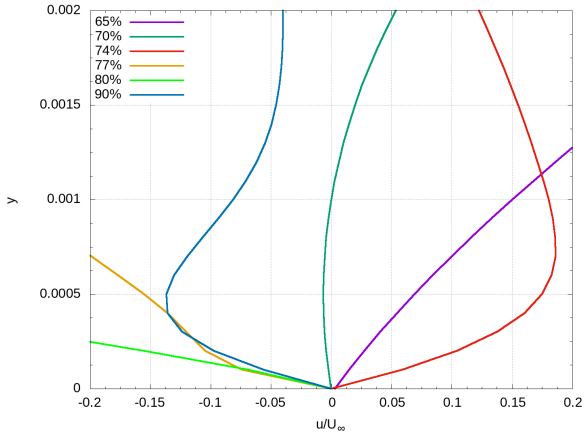

(d) Case 4: Airfoil Trailing Edge Lower Surface Close-Up

Figure 61: Nondimensional Velocity Profile – Case 4: Clean NLF-0414 Trailing Edge at Re_c = 2 x 10^5

The clean NLF-0414 Re_c = 1 x 10^5 case (Figure 60) and the clean NLF-0414 Re_c = 2 x 10^5 case (Figure 61) have similar 65% (purple) and 70% (dark green) velocity profiles with the Re_c = 2 x 10^5 case having a thinner BL (Y). The upper surfaces maximum u/U_∞ averages slightly under 1.2 while the lower surfaces maximum u/U_∞ averages slightly above 1.0 in both Reynolds number cases. In the Re_c = 1 x 10^5 case the upper surface starts its transition before the lower surface but in the Re_c = 2 x 10^5 case the lower surface starts its transition first. In both clean NLF-0414 cases the start of transition to turbulence matches the C_f results from Section 5.4.3. The Re_c = 2 x 10^5 velocity profiles have larger overshoots for both the upper and lower surfaces compared to the Re_c = 1 x 10^5 case. Both of the 90% (blue) probe lines are outside of the BL in the Re_c = 1 x 10^5 case while both the 90% (blue) and the upper 80% (neon green) probe lines are outside of the BL in the Re_c = 2 x 10^5 case. The lower surface 80% (neon green) probe line at Re_c = 1 x 10^5 and the lower surface 77%

(orange) probe line at $Re_c = 2$ x 10^5 are both located through the lower initial vortex but the 77% (orange)($Re_c = 2$ x 10^5) velocity profile shows a thinner BL with a C-curve while the 80% (neon green) has a thicker (Y) S-curve. The change from an S-curve to a C-curve would indicate that the $Re_c = 1$ x 10^5 case BL sub-layer on the surface of the airfoil is easier to suck up than the $Re_c = 2$ x 10^5 case. The lower surface 90% (blue) velocity profile from Figure 60c ($Re_c = 1$ x 10^5) and the upper surface 80% (neon green) velocity profile from Figure 61a ($Re_c = 2$ x 10^5) have the same profile with the lower 90% (blue)($Re_c = 1$ x 10^5) changing from a horizontal slope to a vertical one at $u/U_\infty \approx 0.42$ and the upper surface 80% (neon green)($Re_c = 2$ x 10^5) changing at at $u/U_\infty \approx 0.39$. The upper surface 80% (neon green)($Re_c = 2$ x 10^5) has a slight second inflection in its slope due to its proximity to the first shed vortex. This shows that the upper and lower surface have a velocity threshold before exiting the BL near $u/U_\infty \approx 0.4$. A secondary threshold can also be observed within the BL at a value of $u/U_\infty \approx 0.2$.

Figure 62 shows the upper and lower TE velocity profiles for the Run 606 case at $Re_c = 1$ x 10^5. The 65% (purple) and 70% (dark green) (upper and lower) velocity profiles both have positive or near positive u/U_∞ with the 70% (dark green) upper surface separating earlier in Figure 62b than in Figure 62d.

The upper 74% (red) probe line goes through the tail end of a smaller initial vortex indicated by the S-curve in the velocity profile. The upper 77% (orange) probe line goes through the middle of the smaller initial vortex, sucking the flow upwards, indicated by the C-curve in the velocity profile. The swirl structure can be seen in the upper 77% (orange) velocity profile indicated by the small slope inflection. The upper 80% (neon green) probe line goes through the tail of the leading vortex indicated by the S-curve and the overshoot in the velocity profile. The upper 90% (blue) probe line goes through a separated vortex tail indicated by the velocity profile going from a sharp horizontal slope to a vertical slope at a low u/U_∞ followed by a change back to a horizontal slope (in and out of the BL fluid).

The lower surface 74% (red) velocity profile is located before the initial lower surface vortex and shows a large BL separation indicated by a large area (Y) C-curve. The lower 77% (orange) probe line goes through the end of the smaller initial vortex indicated by the small S-curve in the velocity profile. The swirl structure (slope inflection) can be seen in the lower 77% (orange) velocity profile in Figure 62c. The lower 80% (neon green) probe line goes through the front of the smaller vortex indicated by the S-curve in the velocity profile. The lower 90% (blue) velocity profile is located between two different vortices indicated by the early change from the horizontal slope (secondary BL fluid) to a vertical slope (freestream fluid) at a low u/U_∞ and low y.

The upper 80% (neon green), upper 90% (blue), lower 77% (orange), and lower 90% (blue) velocity profiles have their change in slope at $u/U_\infty \approx 0.34$, $u/U_\infty \approx 0.26$, $u/U_\infty \approx 0.43$, and $u/U_\infty \approx 0.44$ respectively. The upper 74% (red) and lower 80% (neon green) velocity profiles have their change in slope at a value of $u/U_\infty \approx 0.23$ and $u/U_\infty \approx 0.30$.

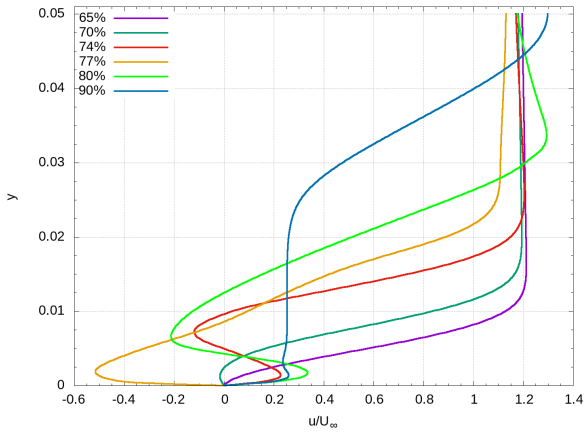

(a) Case 2: Airfoil Trailing Edge Upper Surface

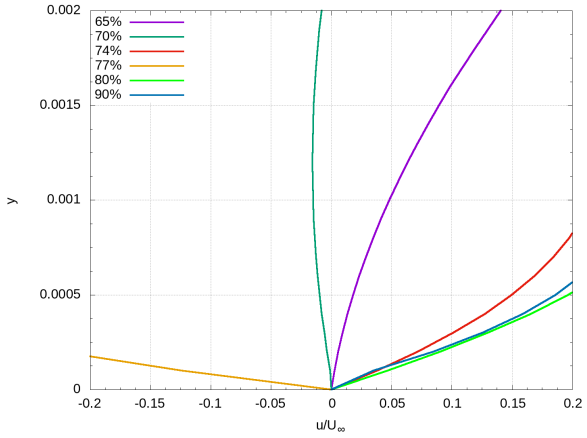

(b) Case 2: Airfoil Trailing Edge Upper Surface Close-Up

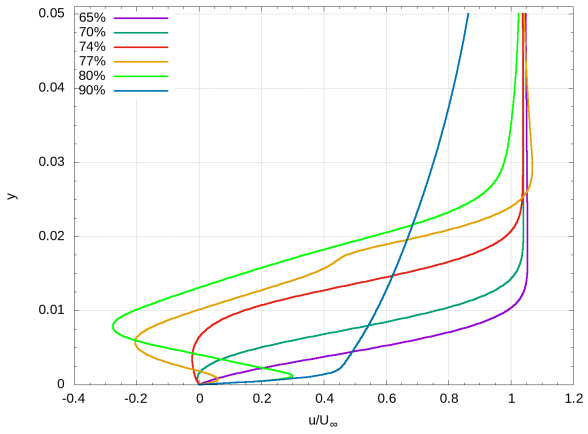

(c) Case 2: Airfoil Trailing Edge Lower Surface

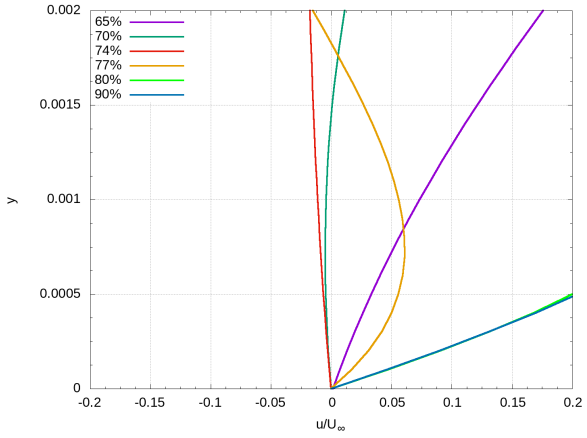

(d) Case 2: Airfoil Trailing Edge Lower Surface Close-Up

Figure 62: Nondimensional Velocity Profile – Case 2: Run 606 Trailing Edge at Re_c = 1 x 10^5

Figure 64 shows the upper and lower TE velocity profiles for the Run 606 case at Re_c = 2 x 10^5. The 65% (purple) and 70% (dark green) velocity profiles both have positive or near positive u/U_∞ with the lower surface 70% (dark green) separating earlier in Figure 64d than in Figure 64b.

The upper surface 74% (red) probe line goes through the middle of the initial vortex indicated by the C-curve and the slope inflection (swirl structure). The upper 77% (orange) probe line goes through the middle of the leading vortex indicated by a large C-curve and overshoot in the velocity profile. The upper 80% (neon green) probe line is located at the end of the large BL after complete separation and goes through the secondary BL on the surface of the airfoil indicated by the change in slope at a low height (Y). The upper 90% (blue) probe line goes through a separated elongated vortex indicated by the changes in slope direction (in and out of BL fluid). The upper 90% (blue) velocity profile changes often because of the

fine elongated vortex structure it goes through.

The lower surface 74% probe line goes through the tail of the initial vortex indicated by the S-curve in the velocity profile. The lower 77% (orange) probe line goes through the front tip of the initial vortex indicated by a very top heavy S-curve seen in Figure 64d. The small positive inverse C-curve in the lower 77% (orange) velocity profile shows the leading vortex tail starting to suck up the BL fluid from the surface of the airfoil. The lower 80% (neon green) probe line goes through the leading vortex indicated by a large C-curve and overshoot in its velocity profile. The lower 90% (blue) probe line goes through a separated rounded vortex indicated by the multiple changes in slope (in and out of BL fluid). The lower 90% (blue) velocity profile (Figure 64d) has an initial C-curve connected to an S-curve as it shows the secondary BL fluid, at the X/c = 0.9 line in Figure 63, separation/change in direction (blue vorticity) caused by the end of the vortex tail still being attached to the surface of the airfoil. The BL is thinner due to the vortex swirl pushing the secondary BL upstream seen at the X/c = 0.9 in Figure 63.

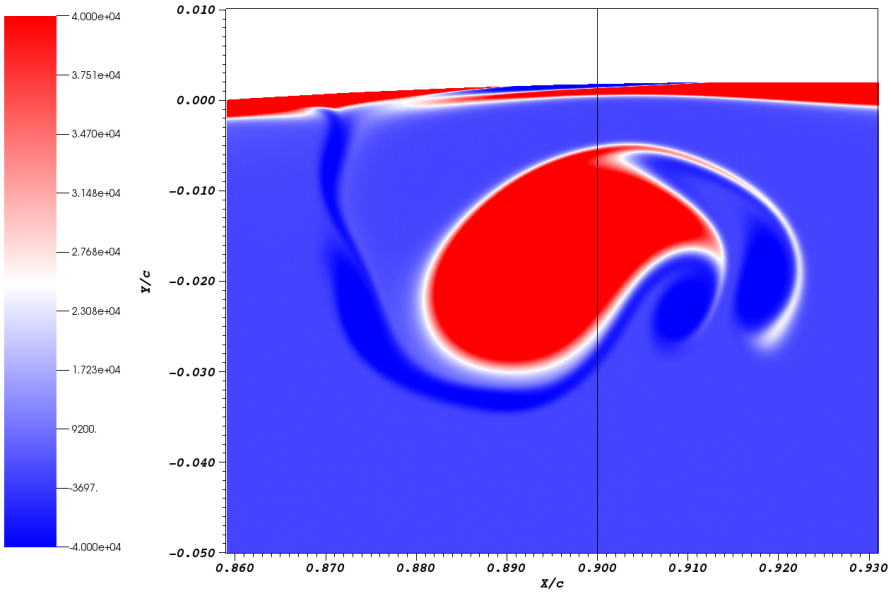

Figure 63: Case 5: Run 606 at Re_c = 2 x 10^5 Lower Surface Close-up of Separated Vortex at X/c = 90% From Figure 53j

The upper 74% (red) and upper 80% (neon green) velocity profiles' changes in slope arise at a value of $u/U_\infty \approx 0.34$ and $u/U_\infty \approx 0.47$. The upper 90% (blue) and lower 74% (red) velocity profiles both have their change in slope at a value of $u/U_\infty \approx 0.14$ and $u/U_\infty \approx 0.19$.

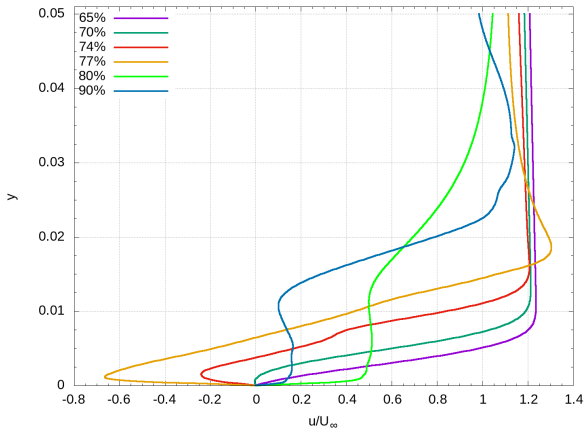

(a) Case 5: Airfoil Trailing Edge Upper Surface

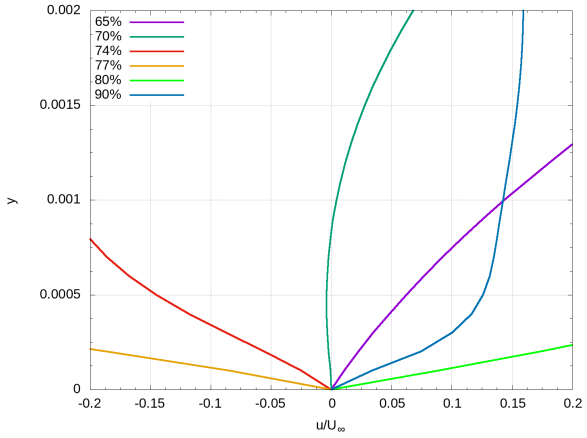

(b) Case 5: Airfoil Trailing Edge Upper Surface Close-Up

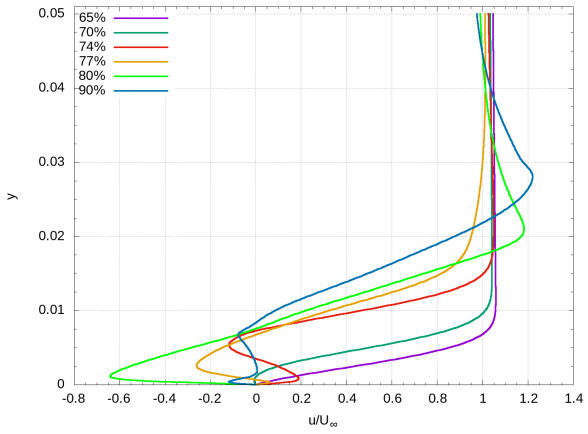

(c) Case 5: Airfoil Trailing Edge Lower Surface

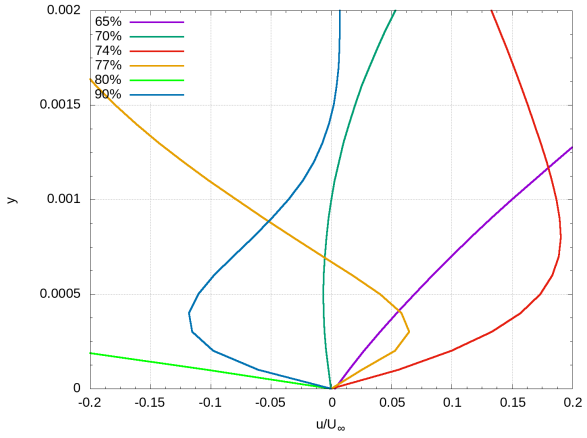

(d) Case 5: Airfoil Trailing Edge Lower Surface Close-Up

Figure 64: Nondimensional Velocity Profile – Case 5: Run 606 Trailing Edge at Re_c = 2 x 10^5

The Run 606 at Re_c = 1 x 10^5 case has a thicker BL (larger Y) than the Run 606 at Re_c = 2 x 10^5 when comparing the 65% (purple) and 70% (dark green) velocity profiles for both the upper and lower surfaces. The upper surface maximum u/U_∞ averages slightly under 1.2 while the lower surface maximum u/U_∞ averages slightly above 1.0 for both Reynolds number cases. The vortex structure of the Re_c = 2 x 10^5 vortices at the 90% marks are finer and more elongated making the velocity profile more chaotic due to the fast changes in velocity and the rotating nature of the vortices. The velocity profiles correlate with the C_p values and show that the transition to turbulence of the upper surface occurs before the lower surface in the Re_c = 1 x 10^5 case and that the lower surface transitions first in the Re_c = 2 x 10^5 case. The lower surface 80% (neon green)(Re_c = 1 x 10^5) and the lower 77% (orange)(Re_c = 2 x 10^5) are located at the front of the initial vortex and they both have an S-curve velocity profile but the lower 77% (orange)(Re_c = 2 x 10^5) has a top heavy S-curve

profile with a smaller BL. The lower surface 90% (blue) (Re_c = 1 x 10^5) velocity profile from Figure 62c and the upper surface 80% (neon green) (Re_c = 2 x 10^5) velocity profile from Figure 64a are located outside of the BL and have similar profiles with the lower 90% (blue)(Re_c = 1 x 10^5) changing from a horizontal slope to a vertical one at $u/U_\infty \approx 0.44$ while the upper surface 80% (neon green)(Re_c = 2 x 10^5) changes at $u/U_\infty \approx 0.47$. The upper surface 80% (neon green)(Re_c = 2 x 10^5) has a second inflection in its slope due to its proximity to the first separated vortex. The lightly iced Run 606 has the u/U_∞ threshold pushed up higher compared to the clean cases with the highest found in the Re_c = 2 x 10^5 case. The Run 606 Re_c = 1 x 10^5 case secondary threshold is higher with values of $u/U_\infty \approx 0.23$ and $u/U_\infty \approx 0.30$ compared to the Re_c = 2 x 10^5 case with $u/U_\infty \approx 0.14$ and $u/U_\infty \approx 0.19$.

Figure 65 shows the upper and lower TE velocity profiles for the Run 622-2D case at Re_c = 1 x 10^5. The 65% (purple) and 70% (dark green) velocity profiles both have positive or near positive u/U_∞ with the upper surface 70% (dark green) separating earlier in Figure 65b than in Figure 65d.

The upper surface 74% (red) probe line goes through the tail end of the initial vortex indicated by an S-curve in the velocity profiles. The 77% (orange) probe line goes through the front of the initial vortex and its velocity profiles has a C-curve and a small slope inflection. The upper 80% (neon green) probe line goes through the tail end of the leading vortex indicated by a large area (Y) S-curve and a overshoot in the velocity profiles. The upper 90% (blue) probe line goes through a separated vortex tail indicated by the two changes in slope direction (in and out of BL fluid).

The lower surface 74% (red) probe line goes through the laminar BL before any vortices indicated by the large area (Y) near-zero C-curve in the velocity profile. The lower 77% (orange) probe line goes through the tail end of a vortex indicated by an S-curve, an inflection (swirl structure), and a small overshoot in the velocity profiles. The lower 80% (neon green) probe line goes through the front of the initial vortex indicated by a large S-curve in its velocity profile. the lower 90% (blue) probe line goes through the secondary BL fluid and is located between the leading vortex and a separated vortex indicated by the slope change from a horizontal slope to a vertical slope at a low Y (exiting the secondary BL).

The upper 80% (neon green), upper 90% (blue), lower 77% (orange), and lower 90% (blue) velocity profiles have their change in slope at $u/U_\infty \approx 0.35$, $u/U_\infty \approx 0.29$, $u/U_\infty \approx 0.44$, and $u/U_\infty \approx 0.44$ respectively. The upper 74% (red) and lower 80% (neon green) velocity profiles have their change in slope at a value of $u/U_\infty \approx 0.24$ and $u/U_\infty \approx 0.38$.

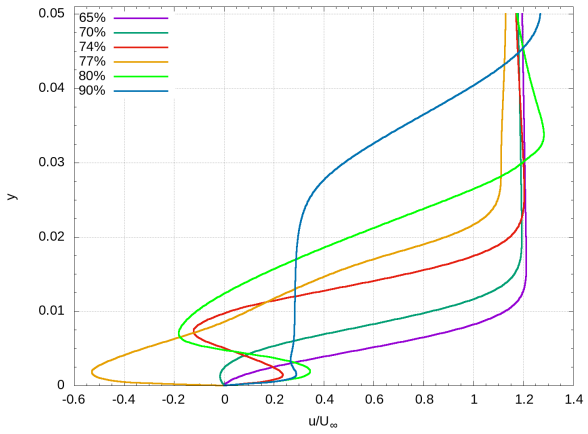

(a) Case 3: Airfoil Trailing Edge Upper Surface

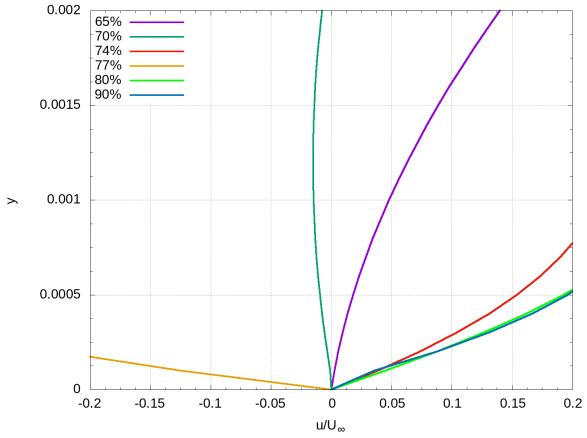

(b) Case 3: Airfoil Trailing Edge Upper Surface Close-Up

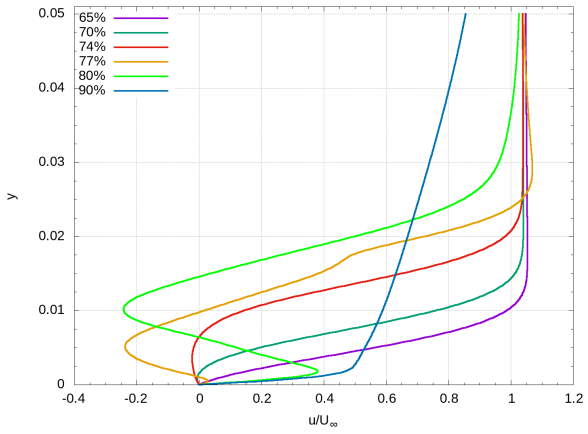

(c) Case 3: Airfoil Trailing Edge Lower Surface

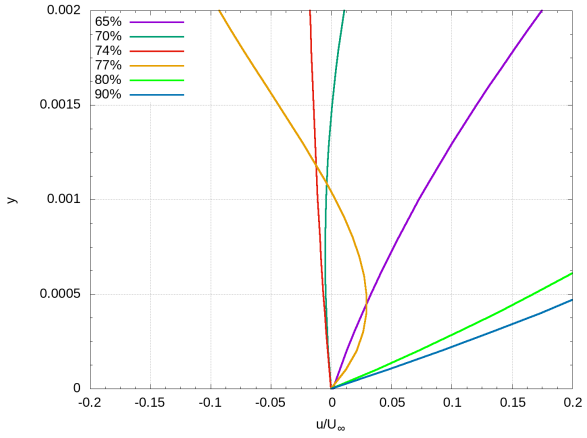

(d) Case 3: Airfoil Trailing Edge Lower Surface Close-Up

Figure 65: Nondimensional Velocity Profile – Case 3: Run 622-2D Trailing Edge at Re_c = 1 x 10^5

Figure 66 shows the upper and lower TE velocity profiles for the Run 622-2D case at Re_c = 2 x 10^5. The 65% (purple) and 70% (dark green) velocity profiles have positive or near positive u/U_∞ with the lower surface 70% (dark green) separating earlier in Figure 66d than in Figure 66b.

The upper 74% (red) and upper 77% (orange) probe lines go through the middle of the initial vortex and leading vortex respectively indicated by the C-curve and the inflection (swirl structure). The upper 74% (red) velocity profile has a larger slope inflection than the upper 77% (orange). The upper 77% (orange) velocity profile has an overshoot due to the leading vortex swirl it goes through. The upper 80% (neon green) probe line goes through the secondary BL fluid right after complete separation of the large BL indicated by the change in slope at a low height (Y). The upper 90% (blue) probe line goes through a separated elongated vortex indicated by the change in slope direction (in and out of BL

fluid). The upper 90% (blue) velocity profile changes direction often as the probe line goes through an elongate separated vortex with very fine structures.

The lower 74% (red) and lower 77% (orange) probe lines go through the tail and front tip of the initial vortex, respectively, in locations where the secondary BL is being sucked up indicated by an S-curve in the velocity profiles. The lower 80% (neon green) probe line goes through the middle of the leading vortex indicated by a large C-curve and overshoot in its velocity profile. The lower 90% (blue) probe line initially goes through two secondary BL, the vortex tail (blue CW) and the secondary BL (red CCW), and then the rounded separated vortex tail indicated by the initial negative u/U_∞ (Figure 66d) and the multiple change in slopes direction.

The upper 74% (red) and upper 80% (neon green) velocity profiles' changes in slope arise at a value of $u/U_\infty \approx 0.33$ and $u/U_\infty \approx 0.46$. The upper 90% (blue) and lower 74% (red) velocity profiles both have their change in slope at a value of $u/U_\infty \approx 0.05$ and $u/U_\infty \approx 0.18$.

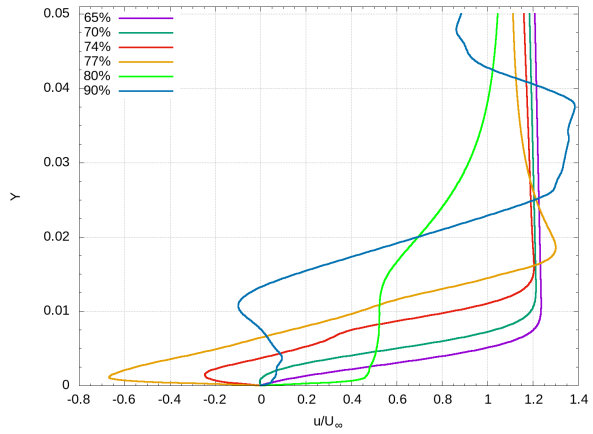

(a) Case 6: Airfoil Trailing Edge Upper Surface

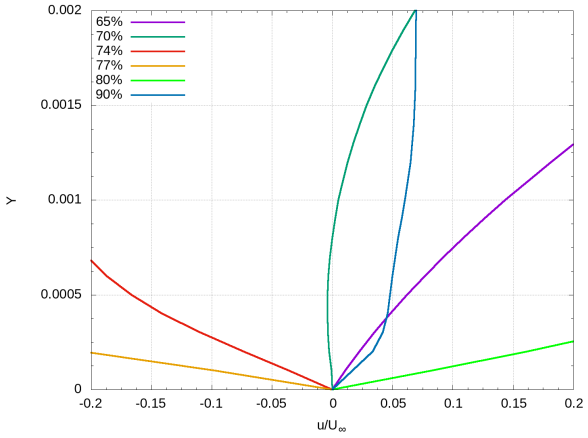

(b) Case 6: Airfoil Trailing Edge Upper Surface Close-Up

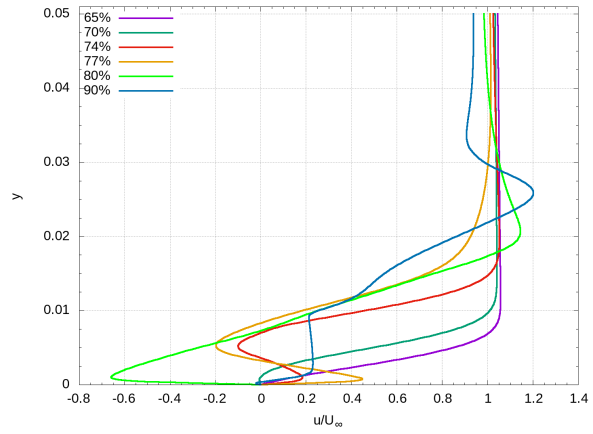

(c) Case 6: Airfoil Trailing Edge Lower Surface

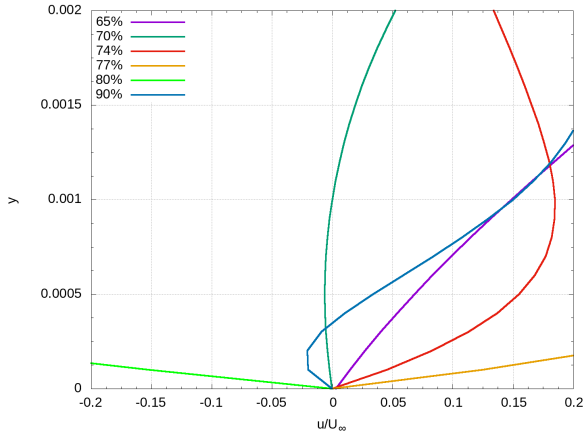

(d) Case 6: Airfoil Trailing Edge Lower Surface Close-Up

Figure 66: Nondimensional Velocity Profile – Case 6: Run 622-2D Trailing Edge at Re_c = 2 x 10^5

A thicker BL can be observed in the Run 622-2D case at Re_c = 1 x 10^5 than the Run 622-2D case at Re_c = 2 x 10^5 when comparing the 65% (purple) and 70% (dark green) velocity profiles for both the upper and lower surfaces. The upper surface maximum u/U_∞ averages slightly under 1.2 while the lower surface maximum u/U_∞ averages slightly above 1.0 for both Reynolds number cases. The vortex structures for the Re_c = 1 x 10^5 case at the 90% line are smoother and less chaotic than the vortex structures in the Re_c = 2 x 10^5 case due to the vortices having rounded profiles. The Re_c = 2 x 10^5 lower surface transitions before the upper surface as indicated by its velocity profile from Figure 66 as well as C_p results from Table 9. The Re_c = 1 x 10^5 case has its upper surface transition before the lower surface. The lower surface 80% (neon green)(Re_c = 1 x 10^5) and the lower 77% (orange)(Re_c = 2 x 10^5) velocity profiles, both located at the front of the initial vortex, have the same S-curve with the lower 80% (neon green)(Re_c = 1 x 10^5) S-curve having a larger BL (Y) and being

slightly shifted to the left. The lower 90% (blue)(Re_c = 1 x 10^5) and the upper 80% (neon green)(Re_c = 2 x 10^5) change from a horizontal slope to a vertical one at $u/U_\infty \approx 0.44$ and $u/U_\infty \approx 0.46$ respectively. The upper surface 80% (neon green)(Re_c = 2 x 10^5) has a large second inflection in its slope due to the proximity to the first separated vortex. The secondary thresholds for the Re_c = 1 x 10^5 case are of $u/U_\infty \approx 0.24$ and $u/U_\infty \approx 0.38$ for the upper 74% (red) and lower 80% (neon green) compared to the Re_c = 2 x 10^5 case upper 90% (blue) and lower 74% (red) with $u/U_\infty \approx 0.05$ and $u/U_\infty \approx 0.18$ respectively. The upper threshold is slightly higher in the Re_c = 2 x 10^5 case and the secondary threshold is lower for the Re_c = 2 x 10^5 case.

Tables 10 and 11 give the velocity profiles threshold u/U_∞ values at Re_c = 1 x 10^5 and Re_c = 2 x 10^5. Both tables show that the u/U_∞ values are mostly constant in the clean NLF-0414 cases for every location indicated but change when the ice is introduced. In Table 10 the upper surface 80% (neon green) and upper surface 90% (blue) show decreased values of u/U_∞ (inflection point) in the iced cases with the lowest values found in the Run 606 case at Re_c = 1 x 10^5. Inflection values for the lower surface 77% (orange) and lower surface 90% (blue) are slightly higher for the iced cases than for the clean NLF-0414 case. The upper surface 74% (red) inflection values stay constant at $u/U_\infty \approx 0.24$ while the lower surface 80% (neon green) values increase in the iced cases with the Run 622-2D case having the highest value. In Table 11 a slight decrease in inflection values can be seen for the upper 74% (red) in the iced cases with Run 622-2D (Re_c = 2 x 10^5) having the smallest inflection value of $u/U_\infty \approx 0.33$. An increase in inflection value can be seen in the iced cases upper surface 80% (neon green) with Run 606 having the highest inflection value. The clean upper surface 90% (blue) inflection value is the highest at $u/U_\infty \approx 0.19$ with the Run 622-2D being the lowest at $u/U_\infty \approx 0.05$. Inflection values for the lower surface 74% (red) stay constant between all three cases at Re_c = 2 x 10^5. While the data is taken at the same physical time, the flow fields advance at slightly different speeds, due to the airfoil geometries (clean and iced), causing the vortices to be in slightly different locations. This slight difference in location could explain the small variation (0.01) in inflection values between the iced cases in both Reynolds numbers cases. This slight difference in location would have more of an effect on the velocity profiles that go through vortices, such as the upper surface 90% (blue), as they are fast moving. As mentioned above, the upper surface velocity at Re_c = 1 x 10^5 is fastest in the Clean NLF-0414 case and slowest in the Run 606 case while the lower surface velocity at Re_c = 1 x 10^5 and the upper and lower surface velocities at Re_c = 2 x 10^5 are fastest in the Clean NLF-0414 case and slowest in the Run 622-2D case. When comparing the upper surfaces 90% (blue) inflection values at both Reynolds numbers the lowest inflection value in the upper surfaces 90% (blue) at Re_c = 1 x 10^5 is found in the Run 606 case and the lowest inflection in the upper surfaces 90% (blue) at Re_c = 2 x 10^5 can be found in the Run 622-2D case. The correlation between the inflection values and the flow field location is true for each value in Tables 10 and 11.

Table 10: Velocity Profiles Threshold Values (u/U_∞) at Re_c = 1 x 10^5

Re_c = 1 x 10^5	Clean NLF-0414	Run 606	Run 622-2D
Upper surface 80% (neon green)	0.42	0.34	0.35
Upper surface 90% (blue)	0.43	0.26	0.29
Lower surface 77% (orange)	0.42	0.43	0.44
Lower surface 90% (blue)	0.42	0.44	0.44
Upper surface 74% (red)	0.24	0.23	0.24
Lower surface 80% (neon green)	0.24	0.30	0.38

Table 11: Velocity Profiles Threshold Values (u/U_∞) at Re_c = 2 x 10^5

Re_c = 2 x 10^5	Clean NLF-0414	Run 606	Run 622-2D
Upper surface 74% (red)	0.38	0.34	0.33
Upper surface 80% (neon green)	0.39	0.47	0.46
Upper surface 90% (blue)	0.19	0.14	0.05
Lower surface 74% (red)	0.19	0.19	0.18

Figure 67 shows the upper surface comparisons between all six cases. The upper surface velocity profiles at Re_c = 1 x 10^5 (Figures 67a, 67c, and 67e) have similar profiles with the two iced cases being almost identical. The upper surface 90% (blue) velocity profiles inflection point for both iced cases are closer to zero compared to the clean NLF-0414 case. The Run 606 case is closest to zero with its inflection at $u/U_\infty \approx 0.26$, then the Run 622-2D inflection at $u/U_\infty \approx 0.29$ followed by the clean NLF-0414 at $u/U_\infty \approx 0.43$. The iced cases both have their upper surface 90% (blue) velocity profiles overshoot past $u/U_\infty = 1.2$ but the clean NLF-0414 case does not. The slight difference in flow field velocity, as mentioned above, most likely causes the two iced cases upper surface 90% (blue) velocity profiles to have similar inflection values and causes the overshoot (going through separated vortex, see Figure 53) but would not explain the difference between the clean and iced cases. The iced cases upper surface 80% (neon green) velocity profile S-curves have a smaller BL (smaller Y), are shifted to the left, and have a larger overshoot when compared to the clean case. The large overshoot indicates that the outer surface of the BL is faster in the iced cases than in the clean NLF-0414 case.

The upper surface velocity profiles at Re_c = 2 x 10^5 (Figures 67b, 67d, and 67f) have similar profiles with most of the differences found in the upper surface 80% (neon green) and upper surface 90% (blue) velocity profiles. The clean NLF-0414 and Run 606 upper surface 90% (blue) velocity profiles are similar and the Run 622-2D is largely different but this is caused by the slight difference in the velocity fields. One thing to point out is how much the secondary BL is being pushed upstream, seen in the upper surface 90% (blue) velocity profile, without any change in flow direction (changing to a negative u/U_∞). The large change from a vertical slope to a horizontal slope in the iced cases upper surface 80% (neon green) velocity profiles is due to the proximity of their probe lines to the recently separated vortex. The inflection points for the upper surface 80% (neon green) velocity profiles move to the right as the amount of ice increases.

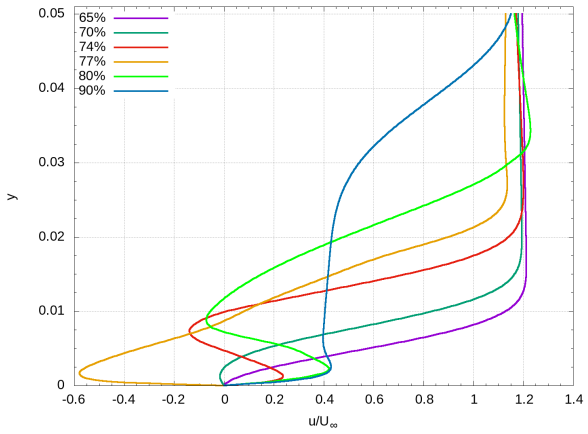

(a) Case 1: Clean NLF-0414 Airfoil Trailing Edge Upper Surface at $Re_c = 1$ x 10^5

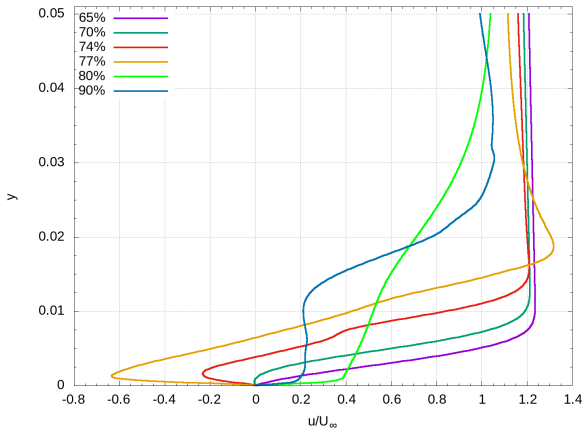

(b) Case 4: Clean NLF-0414 Airfoil Trailing Edge Upper Surface at $Re_c = 2$ x 10^5

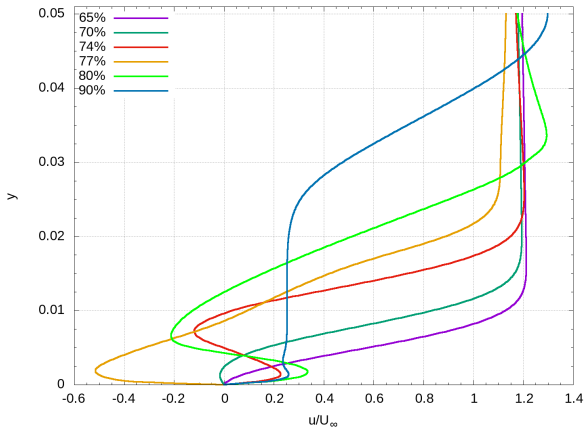

(c) Case 2: Run 606 Airfoil Trailing Edge Upper Surface at $Re_c = 1$ x 10^5

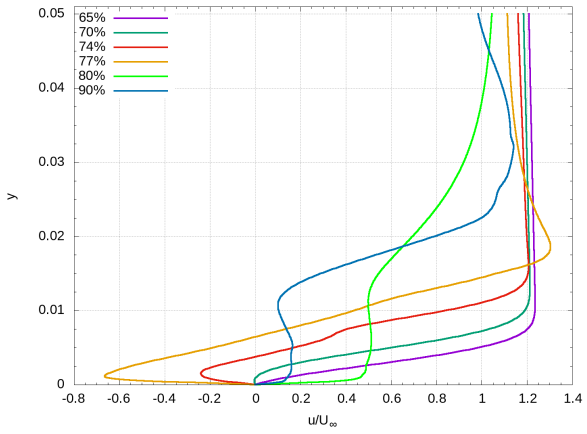

(d) Case 5: Run 606 Airfoil Trailing Edge Upper Surface at $Re_c = 2$ x 10^5

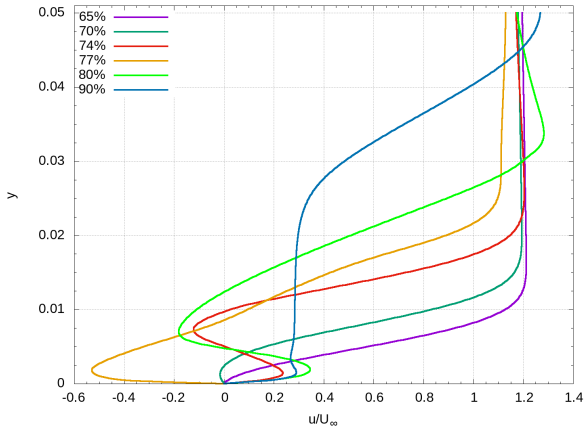

(e) Case 3: Run 622-2D Airfoil Trailing Edge Upper Surface at $Re_c = 1$ x 10^5

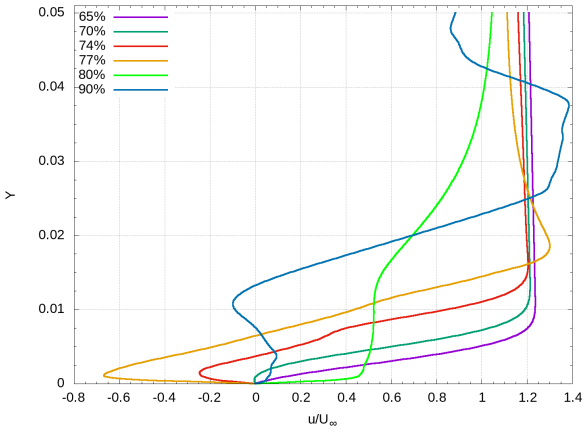

(f) Case 6: Run 622-2D Airfoil Trailing Edge Upper Surface at $Re_c = 2$ x 10^5

Figure 67: Nondimensional Velocity Profile – Airfoil Trailing Edge Upper Surfaces for Cases 1 Through 6

Figure 68 shows the lower surface comparisons between all six cases. The lower surface velocity profiles cases at Re_c = 1 x 10^5 (Figures 68a, 68c, and 68e) are almost identical with slight differences between the clean NLF-0414 and the iced cases. The iced cases lower surface 90% (blue) inflection points are further right compared to the clean NLF-0414. The lower surface 80% (neon green) S-curves move to the right as the amount of ice increase while the lower surface 77% (orange) S-curves move to the left. Even if the lower surface 77% (orange) S-curves move to the left their inflection points move to the right with the increase in ice. It is interesting to point out that even if the Run 622-2D has the slowest lower surface velocity field the lower surface 80% (orange) inflection point increases (moves right).

The lower surface velocity profiles cases at Re_c = 2 x 10^5 (Figures 68b, 68d, and 68f) have a few slight differences. The lower surface 90% velocity profiles are all different due to the slight difference in the velocity field where the clean NLF-0414 is the fastest and the Run 622-2D the slowest. Moving from the Run 622-2D to the clean NLF-0414 a clear change in direction (positive to negative u/U_∞) can be observed indicating a separation in the secondary BL due to the end of the vortex tail still being attached to the surface of the airfoil. This observation was not seen on the upper surface velocity profiles but can be observed in Figure 53. The entire lower surface 80% (neon green) velocity profiles move to the left with increased iced while the lower surface 77% (orange) moves right as well as changes from a C-curve (clean NLF-0414) to an S-curve (iced cases).

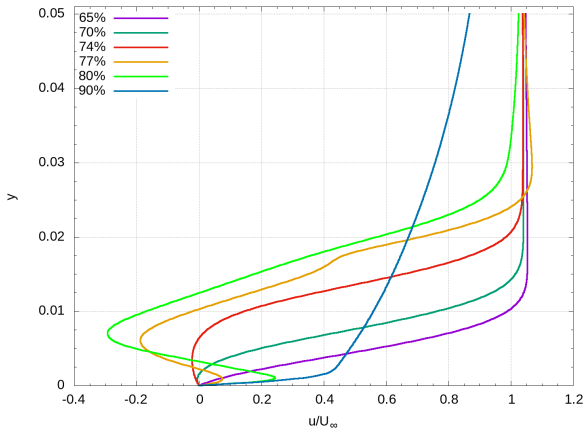

(a) Case 1: Clean NLF-0414 Airfoil Trailing Edge Lower Surface at $Re_c = 1$ x 10^5

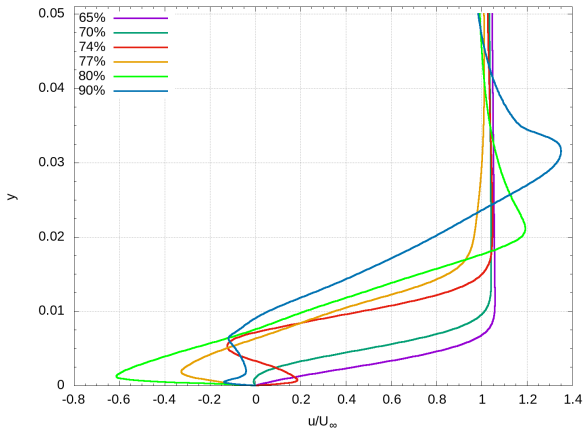

(b) Case 4: Clean NLF-0414 Airfoil Trailing Edge Lower Surface at $Re_c = 2$ x 10^5

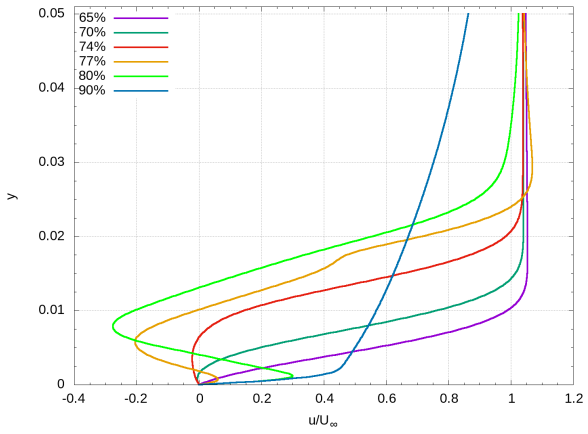

(c) Case 2: Run 606 Airfoil Trailing Edge Lower Surface at $Re_c = 1$ x 10^5

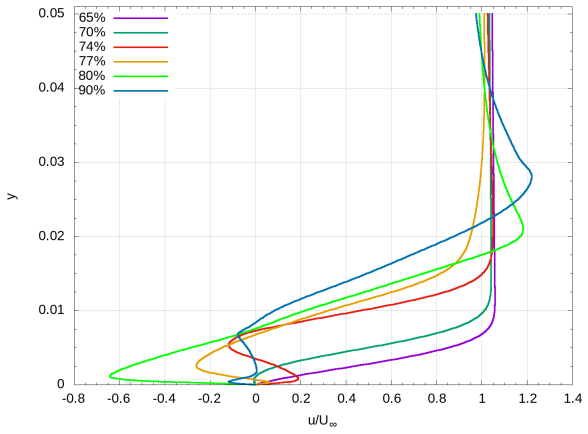

(d) Case 5: Run 606 Airfoil Trailing Edge Lower Surface at $Re_c = 2$ x 10^5

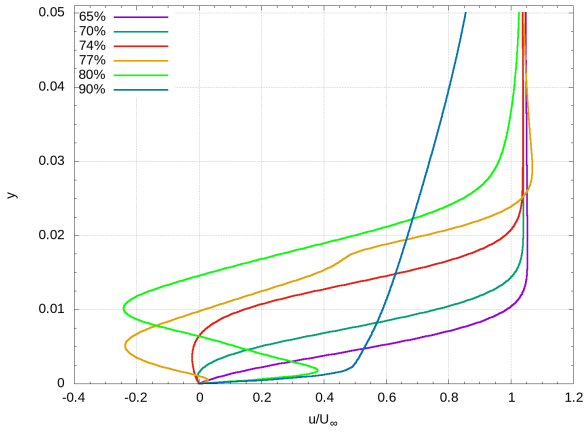

(e) Case 3: Run 622-2D Airfoil Trailing Edge Lower Surface at $Re_c = 1$ x 10^5

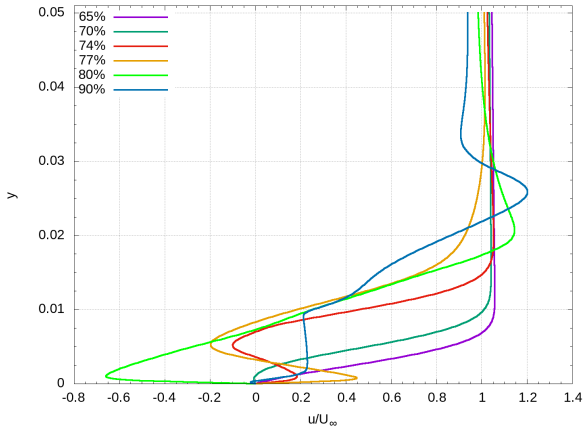

(f) Case 6: Run 622-2D Airfoil Trailing Edge Lower Surface at $Re_c = 2$ x 10^5

Figure 68: Nondimensional Velocity Profile – Airfoil Trailing Edge Lower Surfaces for Cases 1 Through 6

5.6 Turbulence Statistics

A Nek5000 calculation toolbox [54] combined with the turbulence statistics code [55], both from the Swedish KTH mechanics group [56], was used for the turbulence statistics outputs. Only a few components of the turbulence statistics code have been calculated and these are described below. The Reynolds-stress Tensor components are defined in 2D as follows:

$$\overline{u_i u_j} = \begin{pmatrix} \overline{u^2} & \overline{uv} \\ \overline{uv} & \overline{v^2} \end{pmatrix}, \tag{27}$$

and $\overline{u^2}$ is defined as:

$$\overline{u^2} = \overline{\tilde{u}^2} - U^2, \tag{28}$$

where $(\bar{\cdot})$ indicates time-averaged, $(\tilde{\cdot})$ indicates instantaneous velocity, and a capital letter indicates mean velocity. The Skewness Tensor components are defined in 2D as follows:

$$S_{i,j,1} = \begin{pmatrix} \overline{u^3} & \overline{u^2 v} \\ \overline{u^2 v} & \overline{u v^2} \end{pmatrix}, \quad S_{i,j,2} = \begin{pmatrix} \overline{u^2 v} & \overline{u v^2} \\ \overline{u v^2} & \overline{v^3} \end{pmatrix}. \tag{29}$$

The Production Tensor components are defined as follows:

$$P_{ij} = -\overline{u_i u_k}\frac{\partial U_j}{\partial x_k} - \overline{u_j u_k}\frac{\partial U_i}{\partial x_k}. \tag{30}$$

The Production Tensor components in 2D are decomposed as follows:

$$P_{xx} = -2\left(\overline{u^2}\frac{\partial U}{\partial x} + \overline{uv}\frac{\partial U}{\partial y}\right), \tag{31}$$

$$P_{xy} = -\left(\overline{u^2}\frac{\partial V}{\partial x} + \overline{uv}\frac{\partial U}{\partial x} + \overline{uv}\frac{\partial V}{\partial y} + \overline{v^2}\frac{\partial U}{\partial y}\right), \tag{32}$$

$$P_{yy} = -2\left(\overline{uv}\frac{\partial V}{\partial x} + \overline{v^2}\frac{\partial V}{\partial y}\right). \tag{33}$$

The equations are based off the work on the turbulent statistics code and toolbox [55] but a more in depth explanation of the turbulence quantities used can be found in work by Pitsch [57]. The turbulence statistic results in Sections 5.6.1, 5.6.2, and 5.6.3 are obtained after collecting statistics for a little over three flow-overs which is one flow-over less than was used in turbulent statistical results of Vinuesa et al. [25] using the same code at a higher Reynolds number ($4\text{x}10^5$). Three flow-overs would not be considered sufficient for obtaining fully converged turbulent statistics but the results below show convergence and are in line with theory. About four flow-overs were run before collecting results and were deemed sufficient to allow the flow around the airfoil (LE to TE) to fully develop. The goal of this work was not to obtain fully converged turbulent statistics, due in part to the time limitations (Section 3.9), but to give a good understanding of the flow physics near transition. The plots below have vertical grid lines at 70%, 74%, 77%, 80%, and 90% to match the TE velocity profiles outputs from Section 5.5.

5.6.1 Reynolds-stress Tensor Components

The Reynolds-stress Tensor components, as defined above, account for the turbulent fluctuation in the fluid momentum. The diagonal components $\overline{u^2}$ and $\overline{v^2}$ are normal stresses while the off-diagonal component $\overline{uv}$ is a shear stress [58]. Shear stresses have more of a dominant role in mean momentum transfer while the normal stresses have little to do with the transport of mean momentum. Figure 69 shows an overlay of vorticity over the Reynolds-stress Tensor Component $\overline{u^2}$ from Figure 70 giving a better understanding, physically, to $\overline{u^2}$. Figure 69 shows that the outer blocks, furthest away from the airfoil, match the extremities of the vortices. The red zones in the outer blocks show the location at which the vortices are most elongated in the X-direction and the lighter region between the red zones shows where the vortices are most elongated in the Y-direction as seen at the X/c = 0.90 line in Figure 69b (upper vortex (X-direction), lower vortex (Y-direction)). The start and end of the inner blocks red zones attached to the surfaces of the airfoil indicate the start and separation of the vortices in the BL. The Reynolds-stress Tensor Component $\overline{u^2}$ properly shows the horizontal (X-direction) fluctuation in fluid momentum by comparing it to vorticity.

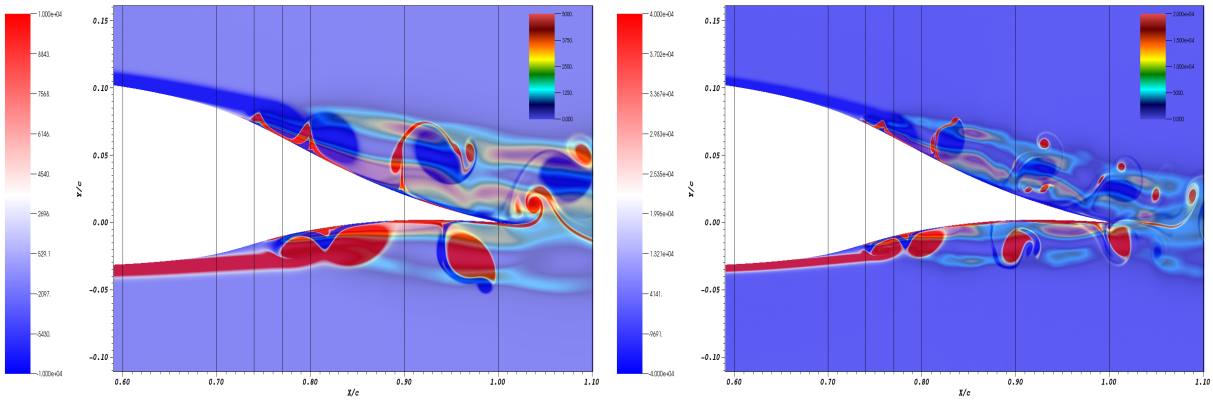

(a) Vorticity Over Reynolds-stress Tensor Component $\overline{u^2}$ for Case 1: Clean NLF-0414 at Re_c = 1 x 10^5

(b) Vorticity Over Reynolds-stress Tensor Component $\overline{u^2}$ for Case 4: Clean NLF-0414 at Re_c = 2 x 10^5

Figure 69: Vorticity Over Reynolds-stress Tensor Component $\overline{u^2}$ Comparison Between the Clean NLF-0414 Cases at Re_c = 1 x 10^5 and Re_c = 2 x 10^5

Figures 70, 71, and 72 show the Reynolds-stress Tensor component $\overline{u^2}$ comparison for all six cases. The Reynolds-stress Tensor component $\overline{u^2}$ results for the Re_c = 2 x 10^5 cases (Figures 70b, 71b, and 72b) show smaller and more defined structures (as expected) as the Reynolds number goes up. With the increase to Re_c = 2 x 10^5 the start of the lower surface $\overline{u^2}$, $\overline{uv}$, and $\overline{v^2}$ (non-zero values) moves upstream from X/c $\approx$ 0.77 to X/c $\approx$ 0.74 aligning themselves with the upper surface in all cases. All six cases can be split into an inner and outer block as defined in Figure 70a. The upper surface outer blocks have larger concentrations of velocity (red zones) than the lower surface outer blocks. For both Reynolds numbers the upper surface inner blocks form a tail separating from the surface of the airfoil while the lower surface inner blocks mostly stay attached to the surface.

When comparing Figures 70a, 71a, and 72a (Re_c = 1 x 10^5 cases) some slight differences can be observed in the intensity of the outer blocks between the clean NLF-0414 and the iced cases Run 606 and Run 622-2D. The inner blocks of the Re_c = 1 x 10^5 cases also have slight differences in intensity especially in the upper and lower tails in between X/c = 0.90 and X/c = 1.00 when comparing the clean NLF-0414 and Run 622-2D to the Run 606. Run 606 at Re_c = 1 x 10^5 lower surface tail at X/c = 1.00 is the largest out of all three cases. When comparing Figures 70b, 71b, and 72b (Re_c = 2 x 10^5 cases) the differences in intensity between the cases blocks are more apparent but the overall block structures are similar between all three cases at Re_c = 2 x 10^5. The Run 622-2D at Re_c = 2 x 10^5 has less red zones than the clean NLF-0414 and Run 606 as they are larger and attached to each other. The higher Reynolds number has a finer vortex structure that would cause the fluctuation in fluid momentum to change more in the Re_c = 2 x 10^5 cases.

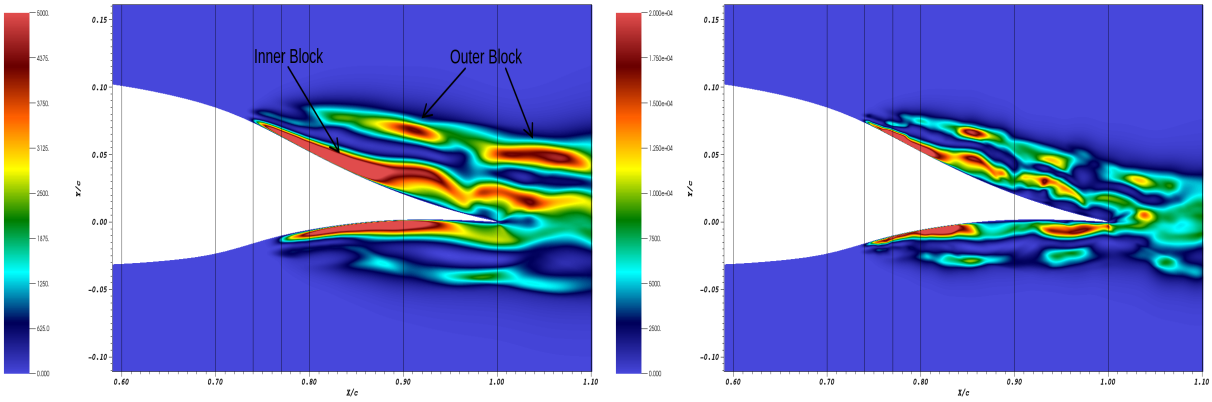

(a) Reynolds-stress Tensor Component $\overline{u^2}$ for Case 1: Clean NLF-0414 at Re_c = 1 x 10^5

(b) Reynolds-stress Tensor Component $\overline{u^2}$ for Case 4: Clean NLF-0414 at Re_c = 2 x 10^5

Figure 70: Reynolds-stress Tensor Component $\overline{u^2}$ Comparison Between the Clean NLF-0414 Cases at Re_c = 1 x 10^5 and Re_c = 2 x 10^5

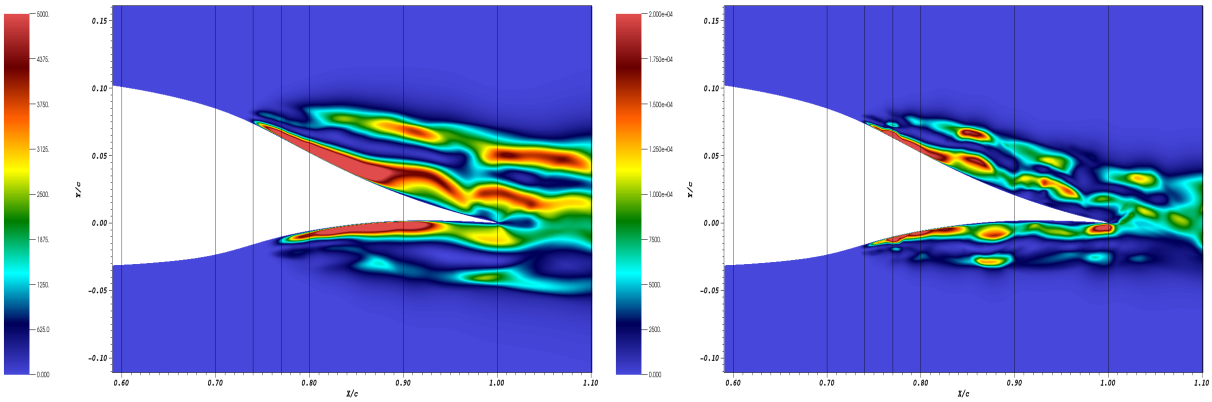

(a) Reynolds-stress Tensor Component $\overline{u^2}$ for Case 2: Run 606 at Re_c = 1 x 10^5

(b) Reynolds-stress Tensor Component $\overline{u^2}$ for Case 5: Run 606 at Re_c = 2 x 10^5

Figure 71: Reynolds-stress Tensor Component $\overline{u^2}$ Comparison Between the Run 606 Cases at Re_c = 1 x 10^5 and Re_c = 2 x 10^5

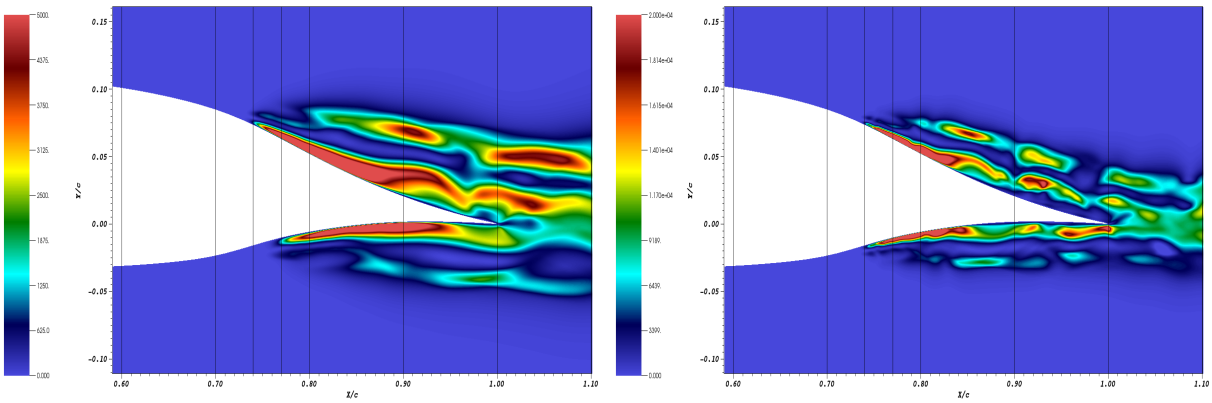

(a) Reynolds-stress Tensor Component $\overline{u^2}$ for Case 3: Run 622-2D at Re_c = 1 x 10^5

(b) Reynolds-stress Tensor Component $\overline{u^2}$ for Case 6: Run 622-2D at Re_c = 2 x 10^5

Figure 72: Reynolds-stress Tensor Component $\overline{u^2}$ Comparison Between the Run 622-2D Cases at Re_c = 1 x 10^5 and Re_c = 2 x 10^5

Figures 73 and 74 show the upper and lower non-dimensionalized velocity profiles for $\overline{u^2}$ probed on the same lines as in Section 5.5; the probe lines are also shown in Figure 118 in Appendix E. Appendix E also has the velocity profiles split into clean NLF-0414 at Re_c = 1 x 10^5 vs clean NLF-0414 at Re_c = 2 x 10^5 (Figure 119), Run 606 at Re_c = 1 x 10^5 vs Run 606 at Re_c = 2 x 10^5 (Figure 120), and Run 622-2D at Re_c = 1 x 10^5 vs Run 622-2D at Re_c = 2 x 10^5 (Figure 121). The velocity profiles show a better understanding of the red zones in the inner and outer blocks that are hidden by the scaling used in Figures 70, 71, and 72. Both the upper and lower surfaces have no fluctuation for the 65% (purple) and 70% (dark green) profiles at both Reynolds numbers. Due to the change in transition point on the lower surface between the Re_c = 1 x 10^5 cases and the Re_c = 2 x 10^5 cases the lower

surface Re_c = 2 x 10^5 profiles have a small fluctuation in the 74% (red) while the Re_c = 1 x 10^5 cases do not.

When comparing the Re_c = 1 x 10^5 cases upper surface velocity profiles (Figures 73a, 73c, and 73e) very few differences can be observed other than little fluctuations, due to the ice, arise near the upper surface of the airfoil at Re_c = 1 x 10^5. The upper 77% (orange) velocity profile peaks are almost equal for the clean NLF-0414 and Run 622-2D but are lower in the Run 622-2D case while the upper 80% (neon green) peak is highest in the Run 606 case and lower in the two other cases. The upper 90% (blue) profile shows the separation from the surface and the $\overline{u^2}$ tail structure as well as the inner and outer blocks profile. Both the inner and outer block peaks, in the upper 90% profile, are highest in the Run 622-2D case followed by the clean NLF-0414 case and the Run 606 case has the lowest peaks indicating that the ice has some effect on the fluctuation in fluid momentum.

When comparing the Re_c = 2 x 10^5 cases upper surface velocity profiles (Figures 73b, 73d, and 73f) a large difference in fluctuation peaks arises, due to the ice, in the Re_c = 2 x 10^5 cases compared to the Re_c = 1 x 10^5 cases. The velocity profiles structures are very similar with the exception of the iced cases being amplified compared to the clean NLF-0414 case. Both the clean NLF-0414 and the Run 606 have their 80% (neon green) peaks below their 77% (orange) peaks while the Run 622-2D has its 80% (neon green) peak over its 77% (orange) peak. Both the clean NLF-0414 and Run 606 90% (blue) profiles have the outer block peaks lower than the inner block peaks while Run 622-2D has the outer block peak higher than the inner block peaks as well as having the highest peaks out of the three cases.

When comparing the Re_c = 1 x 10^5 cases lower surface velocity profiles (Figures 74a, 74c, and 74e) a slight difference, larger than the upper surface one, can be observed between the velocity profiles. The velocity profiles peaks are highest in the Run 622-2D case, followed closely by the clean NLF-0414 case, and the Run 606 has the lowest peaks out of the three. The lower surface 90% (blue) profile peaks are similar in height to the upper surface 77% (orange) (Figures 73a, 73c, and 73e) profile but are thicker (in Y). The peaks on the lower surface are lower than the peaks on the upper surface due to the velocity on the lower surface being slower than the one on the upper surface.

When comparing the Re_c = 2 x 10^5 cases lower surface velocity profiles (Figures 74b, 74d, and 74f) the iced cases have higher peaks than the clean NLF-0414 case. The clean NLF-0414 and Run 622-2D 80% (neon green) profile peaks are higher than the 77% (orange) peaks while the Run 606 77% (orange) peak is higher than the 80% (neon green) peak. Only the clean NLF-0414 acts differently when comparing the upper (Figure 73a) and lower (Figure 74a) surfaces (at Re_c = 2 x 10^5) with its lower surface 80% (neon green) peak being higher than the lower 77% (orange) peak whereas the upper surface 80% (neon green) peak is below the upper 77% (orange) peak. The highest peaks in the lower 90% (blue) profiles are in the Run 622-2D case, then in Run 606 and lastly in the clean NLF-0414. The reason why lower surface 80% (neon green) peaks are over the 77% (orange) is that the Run 606 lower surface inner blocks is further up the airfoil while the clean NLF-0414 and Run 622-2D inner blocks are further down the airfoil.

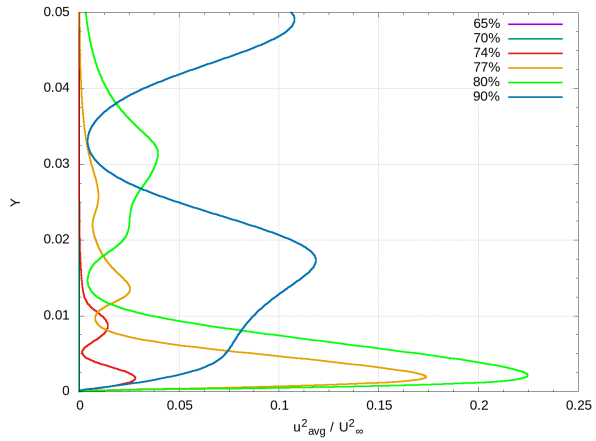

(a) Case 1: Airfoil Trailing Edge Upper Surface at $Re_c = 1$ x 10^5

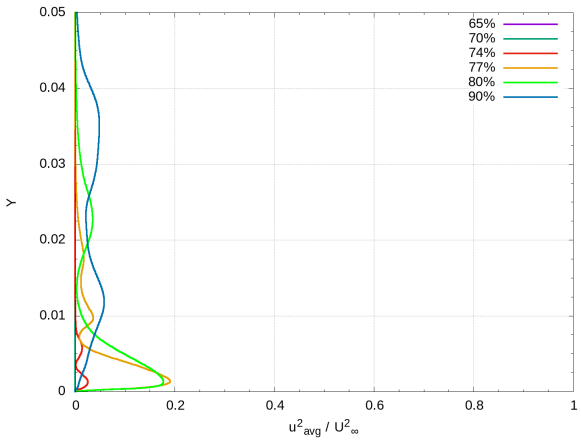

(b) Case 4: Airfoil Trailing Edge Upper Surface at $Re_c = 2$ x 10^5

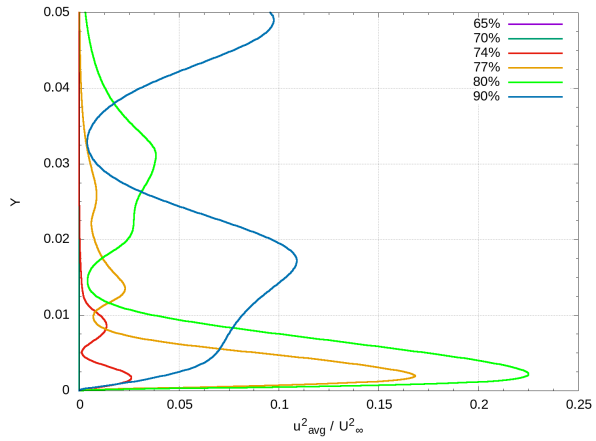

(c) Case 2: Airfoil Trailing Edge Upper Surface at $Re_c = 1$ x 10^5

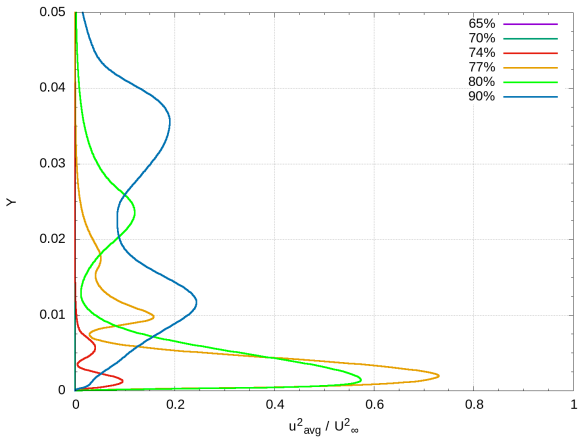

(d) Case 5 Airfoil Trailing Edge Upper Surface at $Re_c = 2$ x 10^5

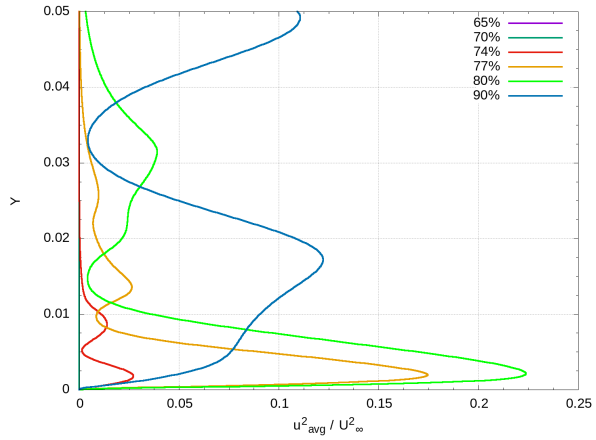

(e) Case 3: Airfoil Trailing Edge Upper Surface at $Re_c = 1$ x 10^5

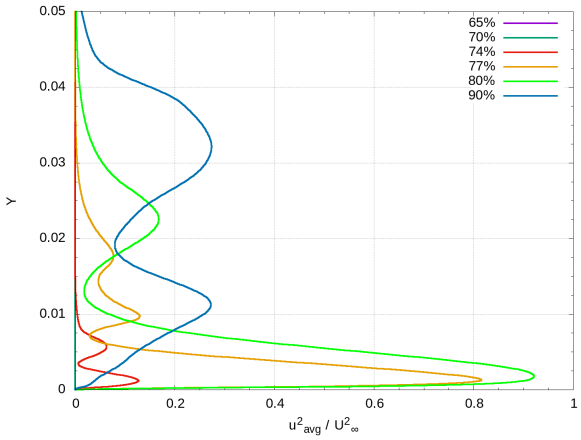

(f) Case 6 Airfoil Trailing Edge Upper Surface at $Re_c = 2$ x 10^5

Figure 73: Nondimensional Velocity Profile for Reynolds-stress Tensor Component $\overline{u^2}$ – Airfoil Trailing Edge Upper Surfaces for Cases 1 Through 6

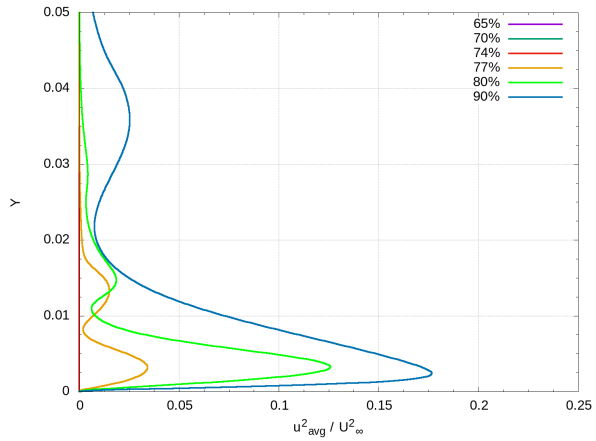

(a) Case 1: Airfoil Trailing Edge Lower Surface at $Re_c = 1$ x 10^5

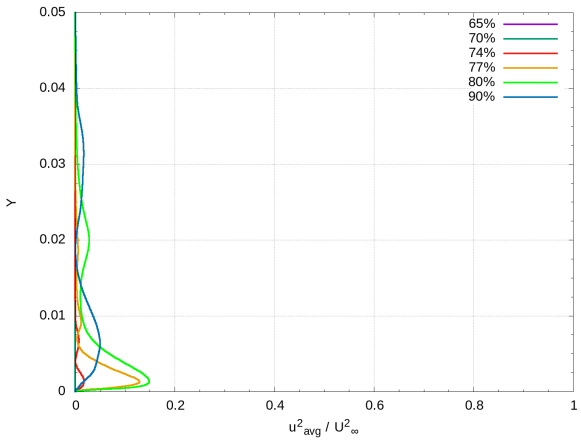

(b) Case 4: Airfoil Trailing Edge Lower Surface at $Re_c = 2$ x 10^5

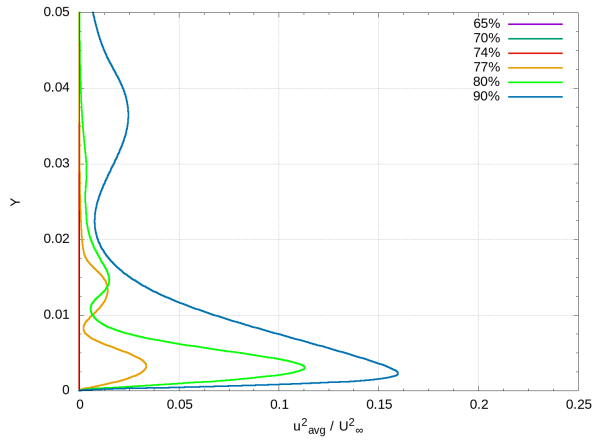

(c) Case 2: Airfoil Trailing Edge Lower Surface at $Re_c = 1$ x 10^5

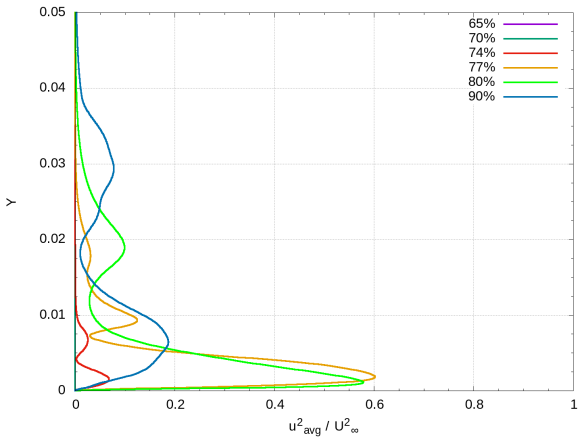

(d) Case 5: Airfoil Trailing Edge Lower Surface at $Re_c = 2$ x 10^5

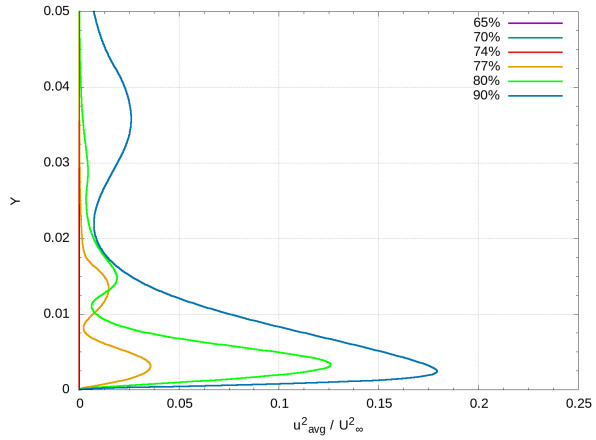

(e) Case 3: Airfoil Trailing Edge Lower Surface at $Re_c = 1$ x 10^5

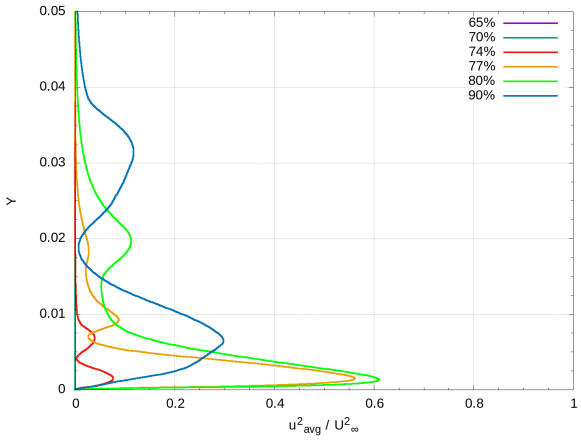

(f) Case 6: Airfoil Trailing Edge Lower Surface at $Re_c = 2$ x 10^5

Figure 74: Nondimensional Velocity Profile for Reynolds-stress Tensor Component $\overline{u^2}$ – Airfoil Trailing Edge Lower Surfaces for Cases 1 Through 6

Figure 75 shows an overlay of vorticity over the Reynolds-stress Tensor Component $\overline{uv}$ from Figure 76 at $Re_c = 1$ x 10^5 and $Re_c = 2$ x 10^5. Figures 76, 77, and 78 show the Reynolds-stress Tensor component $\overline{uv}$ comparison for all six cases. The Reynolds-stress Tensor component $\overline{uv}$ is a shear stress, rotating force, that gives the correlation between $\overline{u^2}$ and $\overline{v^2}$. The shear stress shows the energy transfer (correlation) between the normal stresses resulting in a rotating flow (vorticity field in Figure 75). The blue (upper surface) and red (lower surface) zones attached to the surface of the airfoil shows the flow interaction keeping the BL attached to the surface and its start and finish moves upstream with the increase in Reynolds number the same way C_p and C_f does. The change from red zones to blue zones shows the change in flow direction forcing the vortices to rotate. In both Reynolds cases the lower surface has an "upward draft" (large red zone) flow pushing the lower vortices into the upper surface flow at the TE tip. This is most likely caused by the lower surface flow being less develop, due to the airfoil geometry, and having more rotational energy at the TE tip.

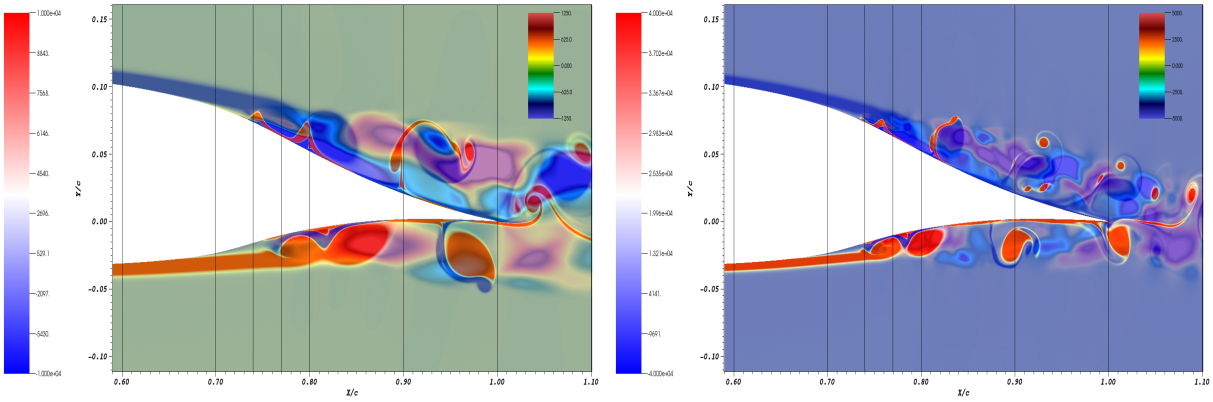

(a) Vorticity Over Reynolds-stress Tensor Component $\overline{uv}$ for Case 1: Clean NLF-0414 at $Re_c = 1$ x 10^5

(b) Vorticity Over Reynolds-stress Tensor Component $\overline{uv}$ for Case 4: Clean NLF-0414 at $Re_c = 2$ x 10^5

Figure 75: Vorticity Over Reynolds-stress Tensor Component $\overline{uv}$ Comparison Between the Clean NLF-0414 Cases at $Re_c = 1$ x 10^5 and $Re_c = 2$ x 10^5

When comparing the $Re_c = 1$ x 10^5 to the $Re_c = 2$ x 10^5 cases for Figures 76, 77, and 78 the $Re_c = 2$ x 10^5 cases have more red and blue zones with smaller, more intense structures. When comparing the clean NLF-0414, Run 606, and Run 622-2D the location and structures of the red and blue zones are slightly different but the overall flow structures are the same. The only deviation from this is the Run 606 at $Re_c = 2$ x 10^5 (Figure 77b) has a blue zone at X/c = 1.20 normal to the TE tip that is not seen in the two other cases at the same Reynolds number. This would show a more even mixing of Run 606 upper and lower surface flows compared to the clean NLF-0414 and Run 622-2D.

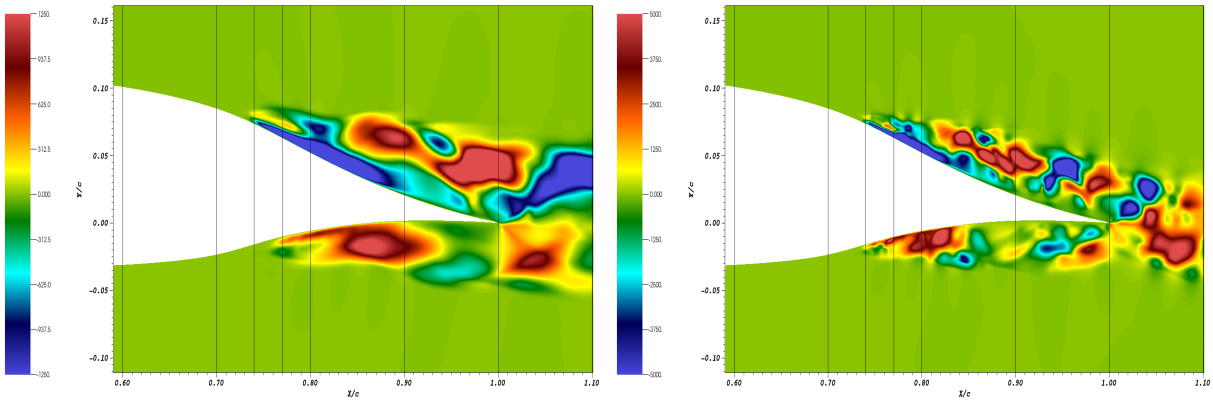

(a) Reynolds-stress Tensor Component $\overline{uv}$ for Case 1: Clean at Re_c = 1 x 10^5

(b) Reynolds-stress Tensor Component $\overline{uv}$ for Case 4: Clean at Re_c = 2 x 10^5

Figure 76: Reynolds-stress Tensor Component $\overline{uv}$ Comparison Between the Clean NLF-0414 Cases at Re_c = 1 x 10^5 and Re_c = 2 x 10^5

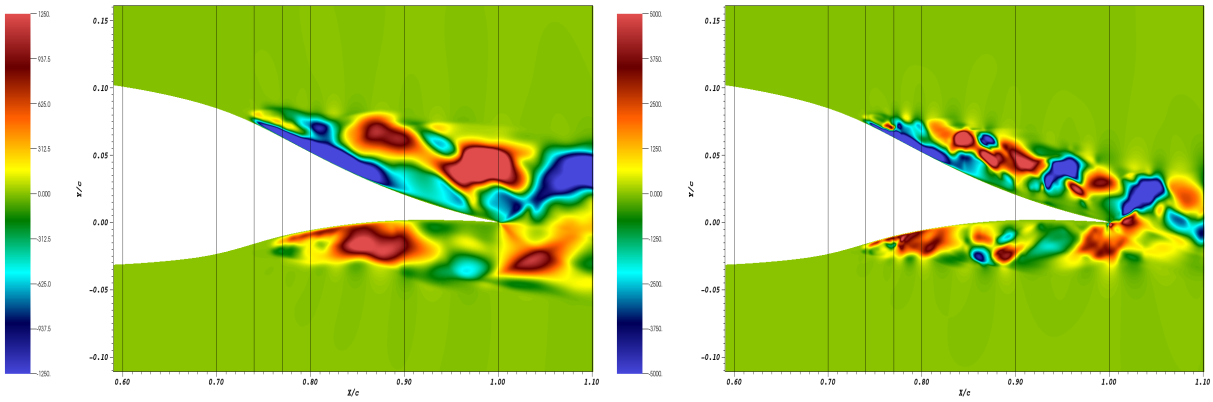

(a) Reynolds-stress Tensor Component $\overline{uv}$ for Case 2: Run 606 at Re_c = 1 x 10^5

(b) Reynolds-stress Tensor Component $\overline{uv}$ for Case 5: Run 606 at Re_c = 2 x 10^5

Figure 77: Reynolds-stress Tensor Component $\overline{uv}$ Comparison Between the Run 606 Cases at Re_c = 1 x 10^5 and Re_c = 2 x 10^5

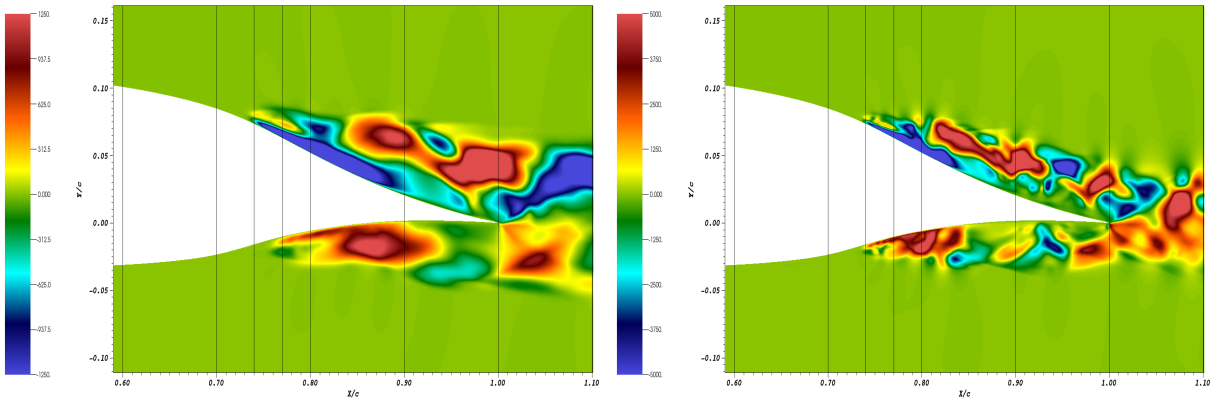

(a) Reynolds-stress Tensor Component $\overline{uv}$ for Case 3: Run 622-2D at Re_c = 1 x 10^5

(b) Reynolds-stress Tensor Component $\overline{uv}$ for Case 6: Run 622-2D at Re_c = 2 x 10^5

Figure 78: Reynolds-stress Tensor Component $\overline{uv}$ Comparison Between the Run 622-2D Cases at Re_c = 1 x 10^5 and Re_c = 2 x 10^5

Figure 79 shows an overlay of vorticity over the Reynolds-stress Tensor Component $\overline{v^2}$ from Figure 80. Figures 80, 81, and 82 show the Reynolds-stress Tensor component $\overline{v^2}$ comparison for all six cases. The Reynolds-stress Tensor Component $\overline{v^2}$ shows the vertical turbulent momentum fluctuations. The upper surfaces have more intense red zones compared to the lower surfaces suggesting a more developed flow on the upper surface. The lighter zones, between the red zones, mostly seen in the Re_c = 2 x 10^5 cases, show the locations where the vortices are most elongated in the X-direction.

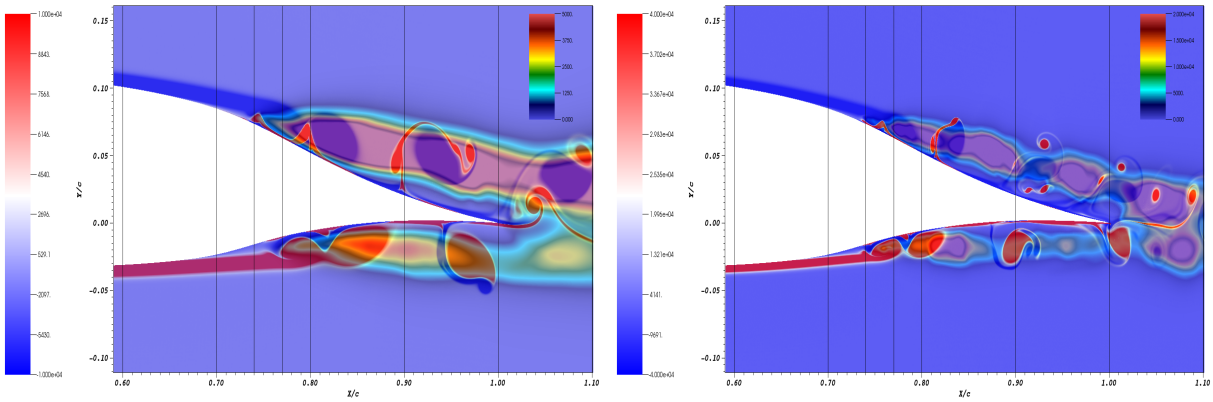

(a) Vorticity Over Reynolds-stress Tensor Component $\overline{v^2}$ for Case 1: Clean NLF-0414 at Re_c = 1 x 10^5

(b) Vorticity Over Reynolds-stress Tensor Component $\overline{v^2}$ for Case 4: Clean NLF-0414 at Re_c = 2 x 10^5

Figure 79: Vorticity Over Reynolds-stress Tensor Component $\overline{v^2}$ Comparison Between the Clean NLF-0414 Cases at Re_c = 1 x 10^5 and Re_c = 2 x 10^5

The overall flow structure stays the same when comparing the clean NLF-0414, Run 606, and Run 622-2D at the same Reynolds number. Some differences in intensity (red zones)

locations, especially in the $Re_c = 2$ x 10^5 cases, are seen on the lower surfaces. The location of the first lower surface red zone ($Re_c = 2$ x 10^5) is near the X/c = 0.80 mark for the clean NLF-0414 and Run 622-2D while in the Run 606 case it is closer to the X/c = 0.90 mark. The Run 606 second lower surface red zone (at X/c $\approx$ 1.00 in Figure 81b) would explain the vortices being pushed into the upper surface flow seen in the vorticity fields as explained in the $\overline{uv}$ section above. The clean NLF-0414 at $Re_c = 2$ x 10^5 (Figure 80b) has its lower surface second red zone at X/c $\approx$ 1.08 indicating flow mixing further away from the tip of the airfoil compared to the Run 606 case.

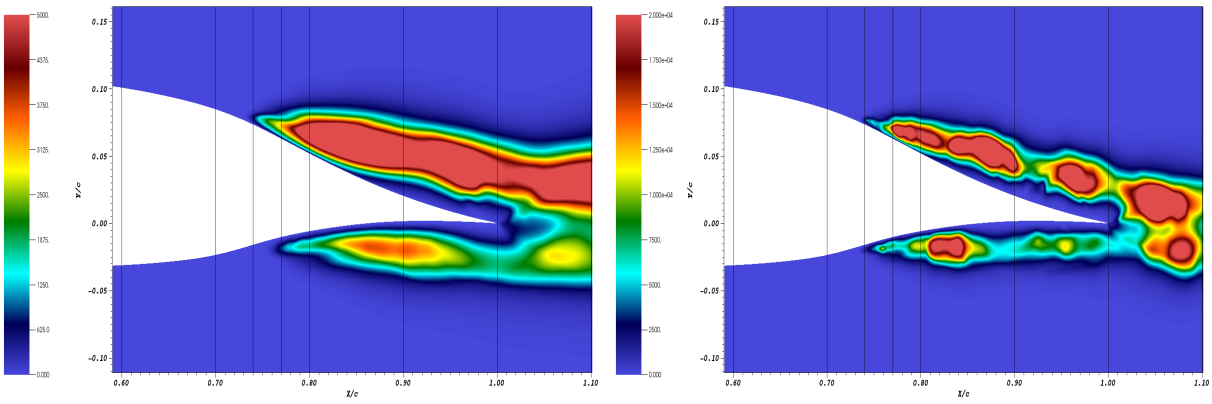

(a) Reynolds-stress Tensor Component $\overline{v^2}$ for Case 1: Clean at $Re_c = 1$ x 10^5

(b) Reynolds-stress Tensor Component $\overline{v^2}$ for Case 4: Clean at $Re_c = 2$ x 10^5

Figure 80: Reynolds-stress Tensor Component $\overline{v^2}$ Comparison Between the Clean NLF-0414 Cases at $Re_c = 1$ x 10^5 and $Re_c = 2$ x 10^5

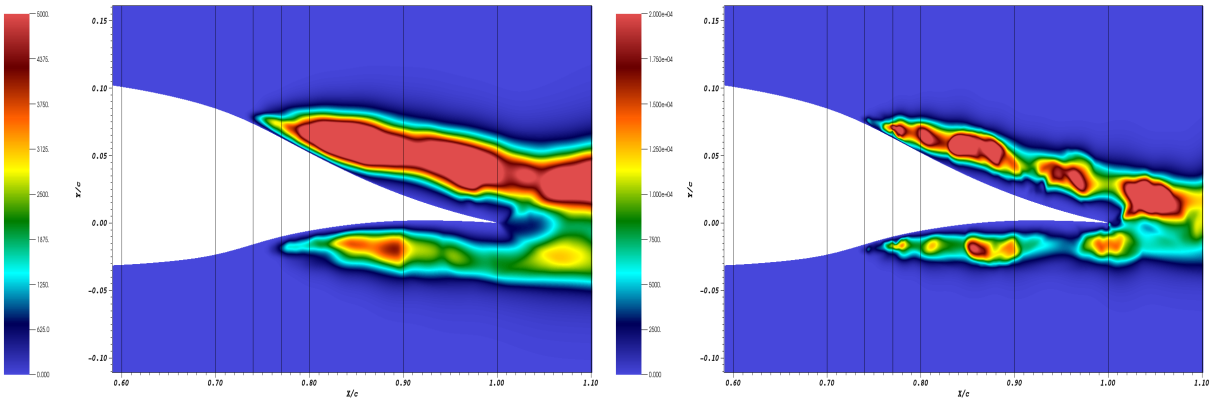

(a) Reynolds-stress Tensor Component $\overline{v^2}$ for Case 2: Run 606 at $Re_c = 1$ x 10^5

(b) Reynolds-stress Tensor Component $\overline{v^2}$ for Case 5: Run 606 at $Re_c = 2$ x 10^5

Figure 81: Reynolds-stress Tensor Component $\overline{v^2}$ Comparison Between the Run 606 Cases at $Re_c = 1$ x 10^5 and $Re_c = 2$ x 10^5

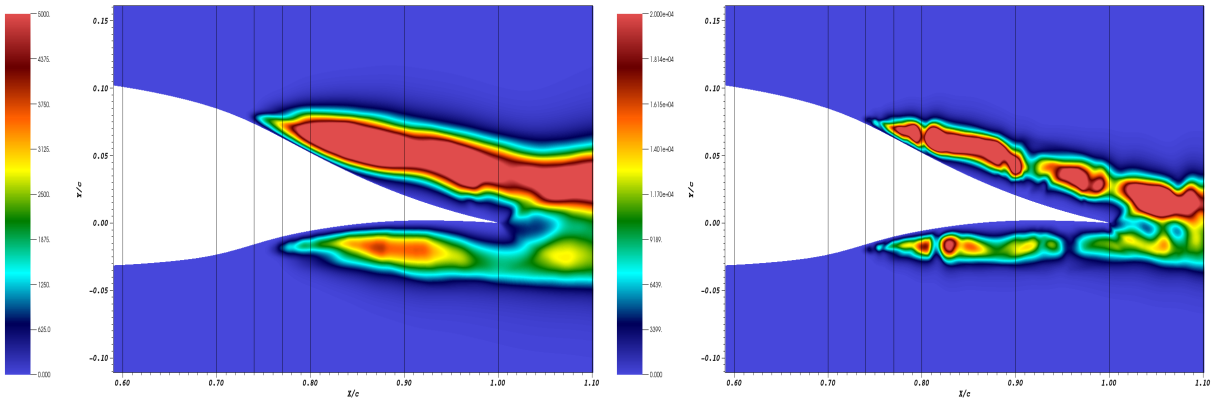

(a) Reynolds-stress Tensor Component $\overline{v^2}$ for Case 3: Run 622-2D at Re_c = 1 x 10^5

(b) Reynolds-stress Tensor Component $\overline{v^2}$ for Case 6: Run 622-2D at Re_c = 2 x 10^5

Figure 82: Reynolds-stress Tensor Component $\overline{v^2}$ Comparison Between the Run 622-2D Cases at Re_c = 1 x 10^5 and Re_c = 2 x 10^5

5.6.2 Skewness Tensor Components

The skewness is defined as the measurement of asymmetry in the probability distribution of a signal [59]. The Skewness Tensor components, as defined above, represent the measurement of asymmetry of the turbulent fluctuation in the fluid momentum. The $\overline{u^2v}$ Skewness Tensor component plots can be found in Appendix E. Figure 83 shows an overlay of vorticity over the Skewness Tensor Component $\overline{u^3}$ from Figure 84. The bump in $\overline{u^3}$ at X/c $\approx$ 0.95 on the TE upper surface, in the Re_c = 2 x 10^5 case (Figure 83b), corresponds to the location at which the vortices completely separate from the secondary BL by sucking the secondary BL away from the surface of the airfoil. The secondary BL in the Re_c = 1 x 10^5 case is also sucked up but with the lower velocity the secondary BL does not separate. This phenomenon is not seen on any of the lower surfaces due to the airfoil geometry. The start of the positive valued $\overline{u^3}$ blocks on both the upper and lower surfaces, for both Reynolds numbers, show the profile of the BL separating from the surface of the airfoil. The ends of the positive valued $\overline{u^3}$ blocks show the location of shedding.

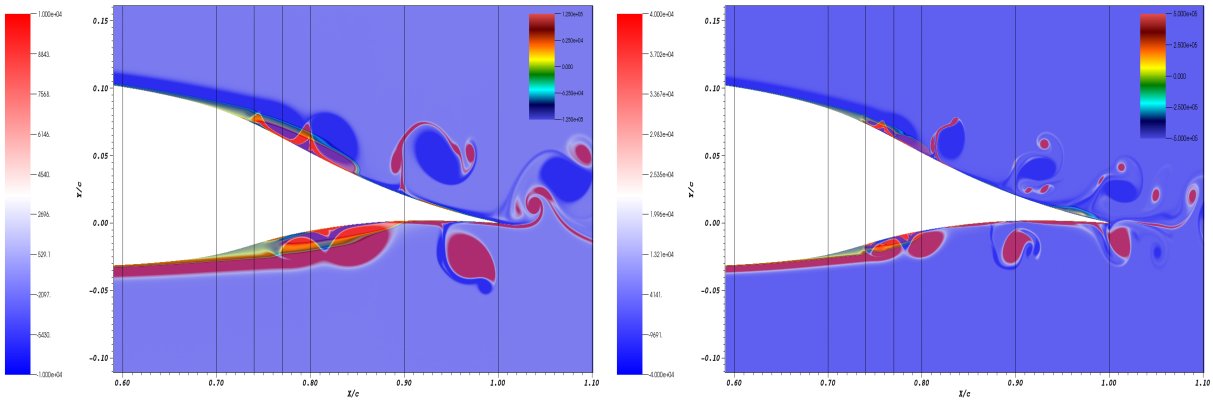

(a) Vorticity over Skewness Tensor Component $\overline{u^3}$ for Case 1: Clean NLF-0414 at Re_c = 1 x 10^5

(b) Vorticity Over Skewness Tensor Component $\overline{u^3}$ for Case 4: Clean NLF-0414 at Re_c = 2 x 10^5

Figure 83: Vorticity Over Skewness Tensor Component $\overline{u^3}$ Comparison Between the Clean NLF-0414 Cases at Re_c = 1 x 10^5 and Re_c = 2 x 10^5

Figures 84, 85, and 86 show the Skewness Tensor component $\overline{u^3}$ comparison for all six cases. As expected the Skewness Tensor component results for the Re_c = 2 x 10^5 cases (Figures (b)) show smaller and more defined structures. With the increase to Re_c = 2 x 10^5 the lower surface $\overline{u^3}$ and $\overline{v^3}$ regions move upstream from X/c $\approx$ 0.77 to X/c $\approx$ 0.74 aligning themselves with the upper surface in all cases.

Figures 84, 85, and 86 have very similar structures due to the fundamental definition of skewness. The Re_c = 1 x 10^5 cases' structures seem identical due to the scaling used but a more in-depth look into the velocities shows higher values in the iced cases as shown above in the velocity profile Figures 73 and 74. The Re_c = 2 x 10^5 cases' structures have different sized red zones in between X/c = 0.74 and X/c = 0.80. Both the clean NLF-0414 and Run 606 cases at Re_c = 2 x 10^5 have blue zones in between two red zones while Run 622-2D does not. The lack of blue zones would suggest higher asymmetry in the flow due to the ice in Run 622-2D. The clean NLF-0414 upper surface blue zone (in between the red zones) is at X/c $\approx$ 0.77 and its lower surface blue zone is at X/c $\approx$ 0.76. The Run 606 upper and lower surface blue zones (in between the red zones) align at X/c $\approx$ 0.77, as for the clean upper surface, suggesting a possible synchronisation of the upper and lower surfaces in the Run 606 case. The Re_c = 1 x 10^5 cases have a small $\overline{u^3}$ line bump (green = near zero) that can be observed on the TE upper surface near X/c = 0.95. The Re_c = 2 x 10^5 cases have a small $\overline{u^3}$ bubble near (orange-red = largely positive) that can be observed on the TE upper surface near X/c = 0.95 but starts at X/c $\approx$ 0.93. This spike in $\overline{u^3}$ at X/c $\approx$ 0.93 matches the bump in the Re_c = 2 x 10^5 C_p distributions at the same X/c in Section 5.4.2.

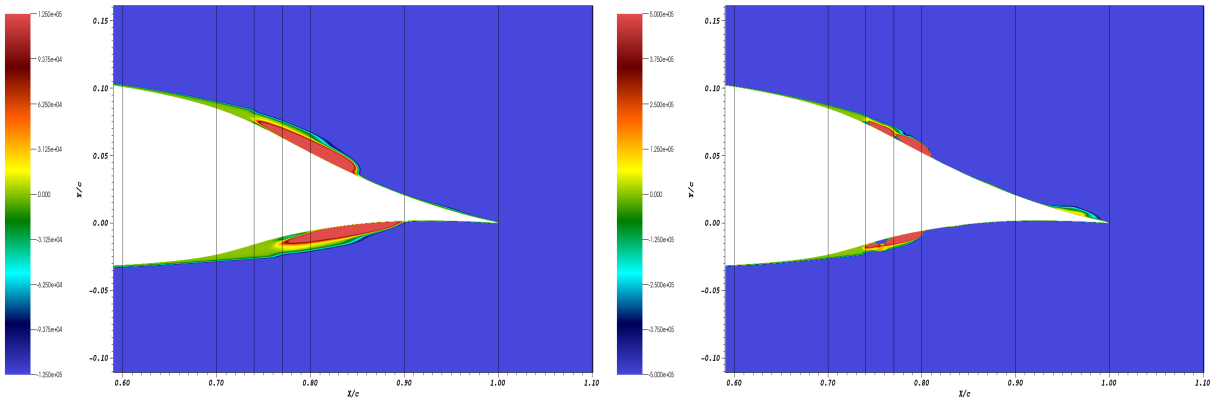

(a) Skewness Tensor Component $\overline{u^3}$ for Case 1: Clean at Re_c = 1 x 10^5

(b) Skewness Tensor Component $\overline{u^3}$ for Case 4: Clean at Re_c = 2 x 10^5

Figure 84: Skewness Tensor Component $\overline{u^3}$ Comparison Between the Clean NLF-0414 Cases at Re_c = 1 x 10^5 and Re_c = 2 x 10^5

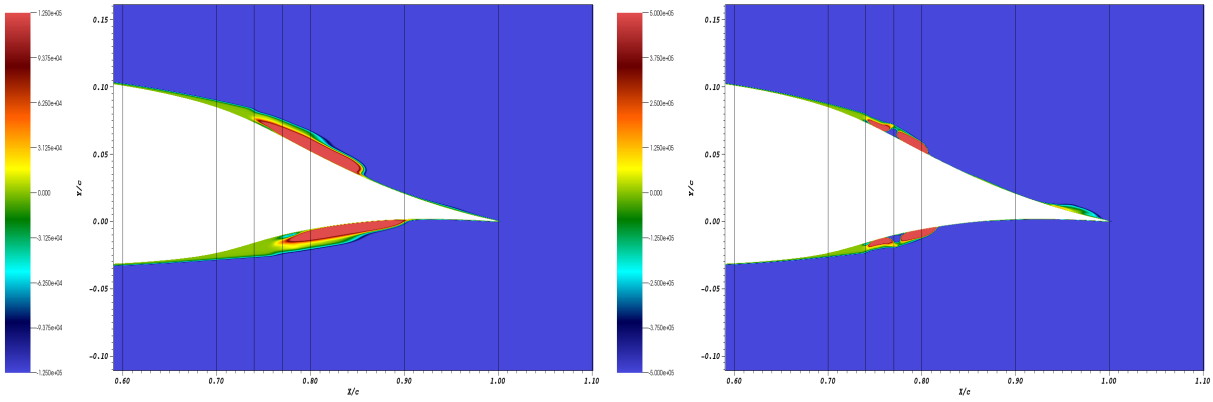

(a) Skewness Tensor Component $\overline{u^3}$ for Case 2: Run 606 at Re_c = 1 x 10^5

(b) Skewness Tensor Component $\overline{u^3}$ for Case 5: Run 606 at Re_c = 2 x 10^5

Figure 85: Skewness Tensor Component $\overline{u^3}$ Comparison Between the Run 606 Cases at Re_c = 1 x 10^5 and Re_c = 2 x 10^5

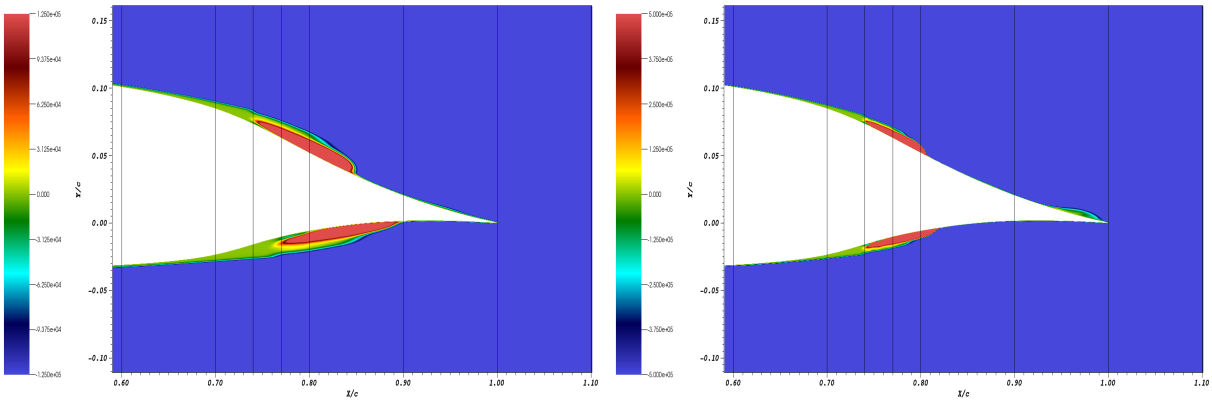

(a) Skewness Tensor Component $\overline{u^3}$ for Case 3: Run 622-2D at Re_c = 1 x 10^5

(b) Skewness Tensor Component $\overline{u^3}$ for Case 6: Run 622-2D at Re_c = 2 x 10^5

Figure 86: Skewness Tensor Component $\overline{u^3}$ Comparison Between the Run 622-2D Cases at Re_c = 1 x 10^5 and Re_c = 2 x 10^5

Figures 87, 88, and 89 show the Skewness Tensor component $\overline{v^3}$ comparison for all six cases. Figure 125, in Appendix E, shows an overlay of vorticity over the Skewness Tensor Component $\overline{v^3}$ from Figure 87. The Skewness Tensor component $\overline{v^3}$ shows the asymmetry in the Reynolds-stress Tensor $\overline{v^2}$ from Figures 80, 81, and 82. The structures for the Re_c = 1 x 10^5 cases are exactly the same with some slight intensity differences. The Re_c = 2 x 10^5 cases have the same overall structure but the clean NLF-0414 and Run 622-2D have the same amount of red and blue zones with a slight difference in location while the Run 606 red and blues zones are completely different. The only difference between the clean NLF-0414 and Run 622-2D is past the TE tip where the Run 622-2D red and blue zones are not as smooth and blocked as the clean NLF-0414 red and blue zones. The Run 606 has a large elongated red zone on the lower surface TE, in between X/c = 0.90 and X/c = 1.00, that is not seen in the other two cases. This elongated red zones have the effect of synchronising the upper and lower turbulent fluctuation asymmetry in fluid momentum that is not seen in the other cases. This phenomena could not be observed while looking at the Reynolds-stress Tensor $\overline{v^2}$ and could explain some of the inconsistencies observed for the Run 606 case above.

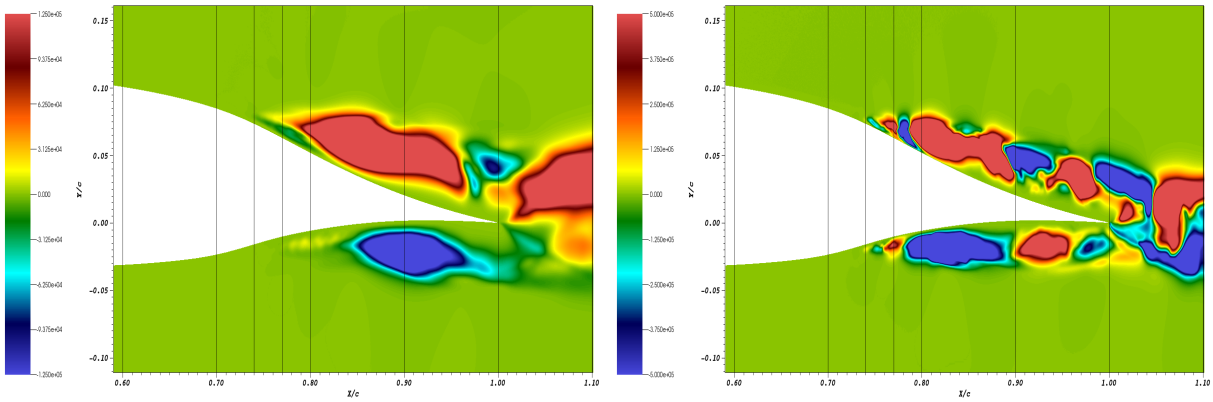

(a) Skewness Tensor Component $\overline{v^3}$ for Case 1: Clean at Re_c = 1 x 10^5

(b) Skewness Tensor Component $\overline{v^3}$ for Case 4: Clean at Re_c = 2 x 10^5

Figure 87: Skewness Tensor Component $\overline{v^3}$ Comparison Between the Clean NLF-0414 Cases at Re_c = 1 x 10^5 and Re_c = 2 x 10^5

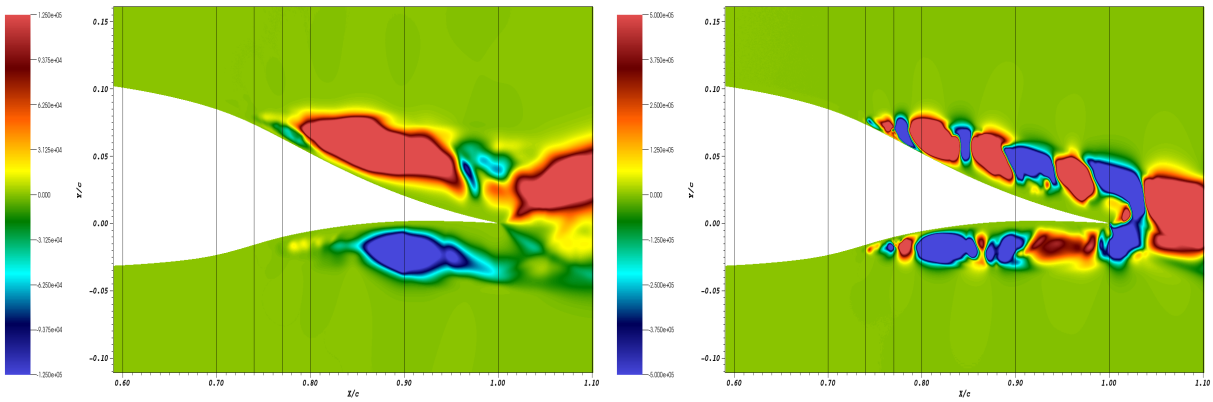

(a) Skewness Tensor Component $\overline{v^3}$ for Case 2: Run 606 at Re_c = 1 x 10^5

(b) Skewness Tensor Component $\overline{v^3}$ for Case 5: Run 606 at Re_c = 2 x 10^5

Figure 88: Skewness Tensor Component $\overline{v^3}$ Comparison Between the Run 606 Cases at Re_c = 1 x 10^5 and Re_c = 2 x 10^5

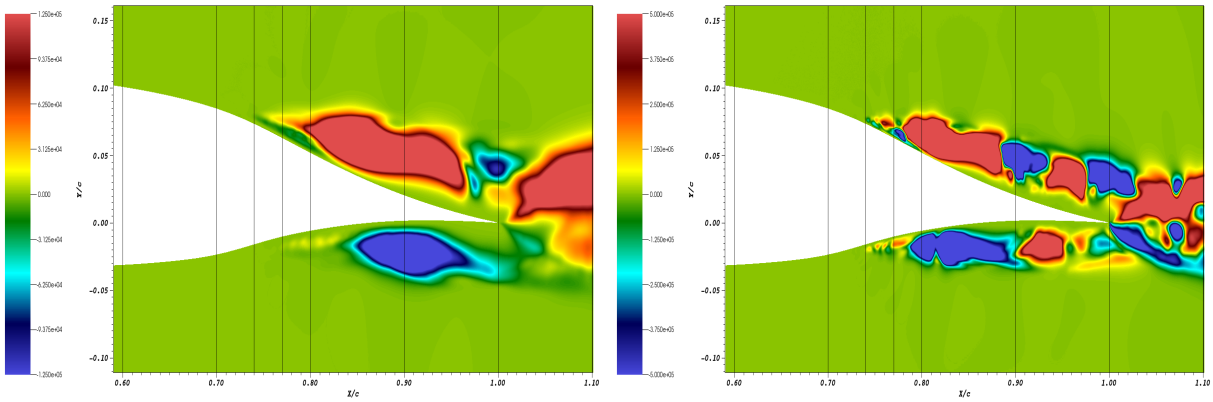

(a) Skewness Tensor Component $\overline{v^3}$ for Case 3: Run 622-2D at Re_c = 1 x 10^5

(b) Skewness Tensor Component $\overline{v^3}$ for Case 6: Run 622-2D at Re_c = 2 x 10^5

Figure 89: Skewness Tensor Component $\overline{v^3}$ Comparison Between the Run 622-2D Cases at Re_c = 1 x 10^5 and Re_c = 2 x 10^5

5.6.3 Production Tensor Components

The Production Tensor components involve the (negative) product of Reynolds-stress Tensor and the gradient of time-averaged velocity [57]. A more physical understanding would be the mean velocity gradients working against the Reynolds-stresses or the transfer of kinetic energy from the mean flow into the fluctuating velocity field [60]. The P_{xy} Production Tensor component plots (Figure 126), also known as the shear stress production plots, can be found in Appendix E. The same observation can be made for the Production Tensor components as for the other components above whereas the increase to Re_c = 2 x 10^5 shifts the lower surface upstream from X/c $\approx$ 0.77 to X/c $\approx$ 0.74 aligning themselves with the upper surface in all cases.

Figure 90 shows an overlay of vorticity over the Production Tensor Component $\overline{P_{xx}}$ from Figure 91. The start of the leftmost blue zones (upper and lower surfaces) in the $\overline{P_{xx}}$ component indicates the start of the initial vortex tails pulling the secondary sub-layer (blue vorticity on the surface of the airfoil) from the surface of the airfoil. The large blue zones indicate the separated vortices that are still attached to the secondary BL. The red zones attached to the surface of the airfoil indicate the separation between the vortices attached to the secondary BL and correspond with the separation/change in direction caused by the end of the vortex tail as explained in Section 5.5 above Figure 63.

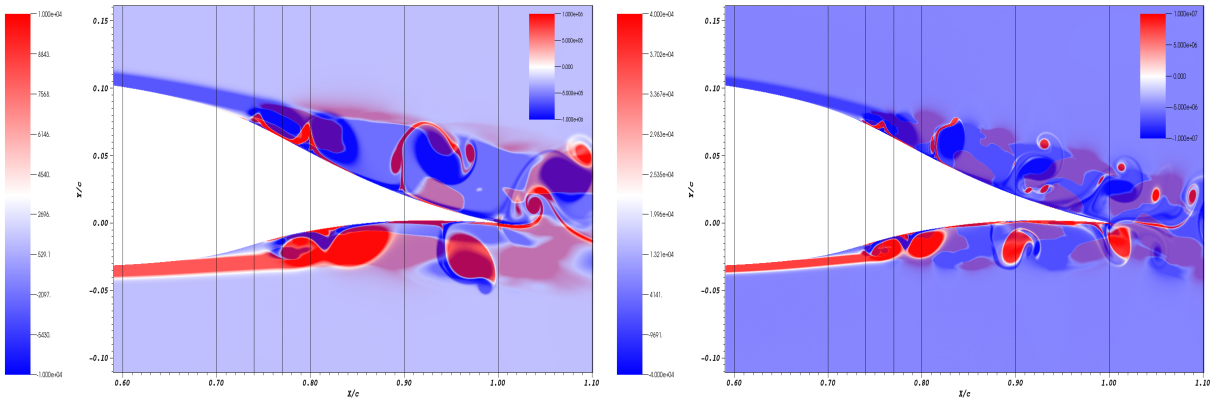

(a) Vorticity over Production Tensor Component P_{xx} for Case 1: Clean NLF-0414 at Re_c = 1 x 10^5

(b) Vorticity Over Production Tensor Component P_{xx} for Case 4: Clean NLF-0414 at Re_c = 2 x 10^5

Figure 90: Vorticity Over Production Tensor Component P_{xx} Comparison Between the Clean NLF-0414 Cases at Re_c = 1 x 10^5 and Re_c = 2 x 10^5

Figures 91, 92, and 93 show the Production Tensor component P_{xx} comparison for all six cases. Figures 91c and 91d give the Reynolds-stress Tensor Component $\overline{uv}$ for comparison with the Production Tensor component P_{xx} (Figures 91a and 91b). As with the other term in turbulent statistics few differences can be observed when comparing the Re_c = 1 x 10^5 cases P_{xx} Production Tensor component while the Re_c = 2 x 10^5 cases show more differences. The Production Tensor component P_{xx} resembles the $\overline{uv}$ component with a very large amplification (see Figure 91): referring to Equation 31, we see the variation in mean velocity in the second term is larger than the variation in mean velocity in the first term. Looking at the P_{xy} Equation 32 with the same understanding the Production Tensor component P_{xy} (Figures 126a and 126b) resembles the Reynolds-stress Tensor $\overline{u^2}$ (Figures 126c and 126d).

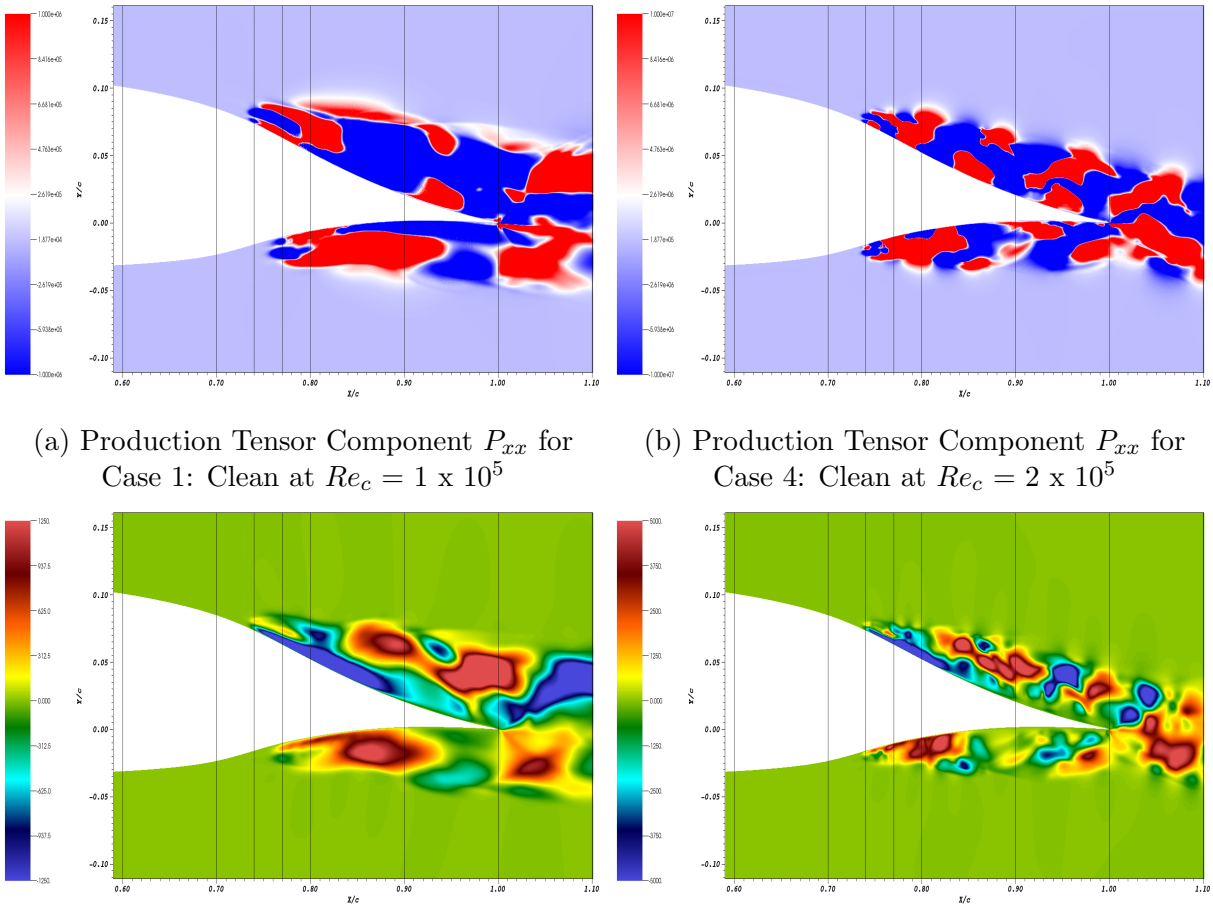

(a) Production Tensor Component P_{xx} for Case 1: Clean at Re_c = 1 x 10^5

(b) Production Tensor Component P_{xx} for Case 4: Clean at Re_c = 2 x 10^5

(c) Reynolds-stress Tensor Component $\overline{uv}$ for Case 1: Clean at Re_c = 1 x 10^5

(d) Reynolds-stress Tensor Component $\overline{uv}$ for Case 4: Clean at Re_c = 2 x 10^5

Figure 91: Production Tensor Component P_{xx} and Reynolds-stress Tensor Component $\overline{uv}$ Comparison Between the Clean NLF-0414 Cases at Re_c = 1 x 10^5 and Re_c = 2 x 10^5

When comparing Figures 91a, 91b, 92, and 93 at Re_c = 1 x 10^5 Run 606 is slightly different from the two other cases. Run 606 at Re_c = 1 x 10^5 has an extra red zone, on the lower surface, at X/c $\approx$ 0.97. This red zone is a good example of the combination of the production terms as this red zone does not arise completely from the Reynolds shear stresses (Figure 77a) but also from the Reynolds normal stresses (Figure 71a) at the same location (lower surface at X/c $\approx$ 0.97). When comparing the Re_c = 2 x 10^5 cases the Run 606 case also shows some synchronisation past the TE tip where the lower and upper surface red zones are combined, which is not seen in the two other cases.

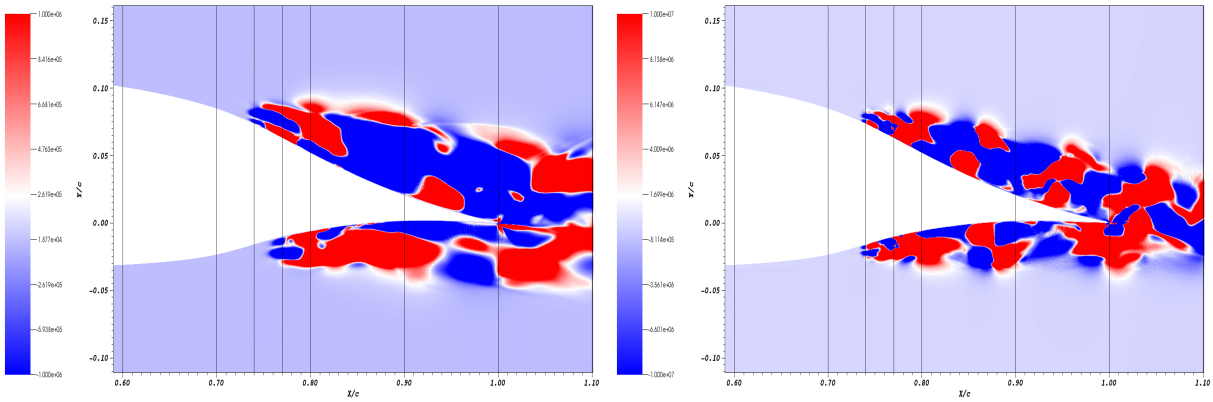

(a) Production Tensor Component P_{xx} for Case 2: Run 606 at $Re_c = 1$ x 10^5

(b) Production Tensor Component P_{xx} for Case 5: Run 606 at $Re_c = 2$ x 10^5

Figure 92: Production Tensor Component P_{xx} Comparison Between the Run 606 Cases at $Re_c = 1$ x 10^5 and $Re_c = 2$ x 10^5

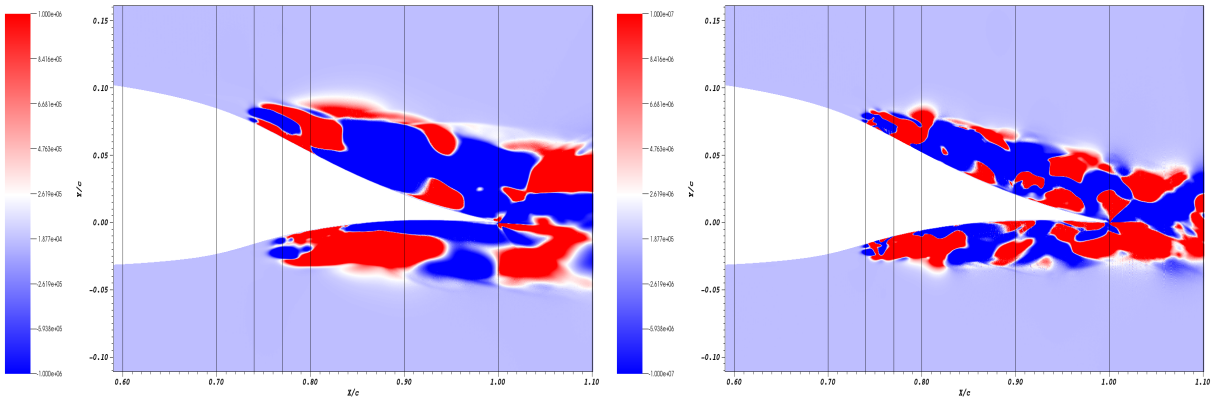

(a) Production Tensor Component P_{xx} for Case 3: Run 622-2D at $Re_c = 1$ x 10^5

(b) Production Tensor Component P_{xx} for Case 6: Run 622-2D at $Re_c = 2$ x 10^5

Figure 93: Production Tensor Component P_{xx} Comparison Between the Run 622-2D Cases at $Re_c = 1$ x 10^5 and $Re_c = 2$ x 10^5

Figures 94, 95, and 96 show the Production Tensor component P_{yy} comparison for all six cases. Figure 129, in Appendix E, shows an overlay of vorticity over the Production Tensor Component $\overline{P_{yy}}$ from Figure 94. Figures 94c and 94d show the Reynolds-stress Tensor Component $\overline{v^2}$ for comparison with the Production Tensor component P_{yy}. The overall structures between the $\overline{v^2}$ component and the P_{yy} component are similar in size but P_{yy} has a different internal structure due to the combination of normal stresses ($\overline{v^2}$) and the shear stresses ($\overline{uv}$). When looking at the lower surface of P_{yy} at $Re_c = 2$ x 10^5, no indication of the first red zones from either $\overline{v^2}$ (Figure 94d) or $\overline{uv}$ (Figure 76b) can be observed clearly indicating that no one term in P_{yy} is completely dominant.

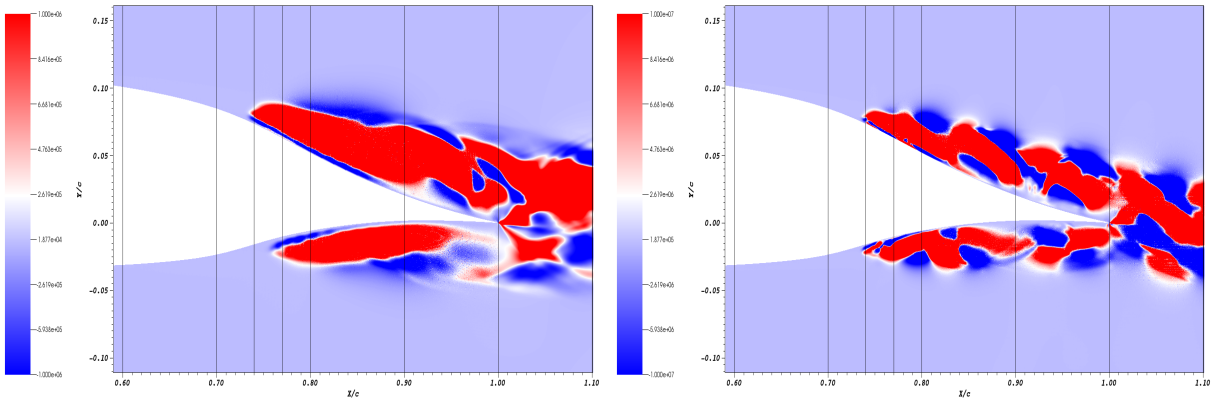

(a) Production Tensor Component P_{yy} for Case 1: Clean at Re_c = 1 x 10^5

(b) Production Tensor Component P_{yy} for Case 4: Clean at Re_c = 2 x 10^5

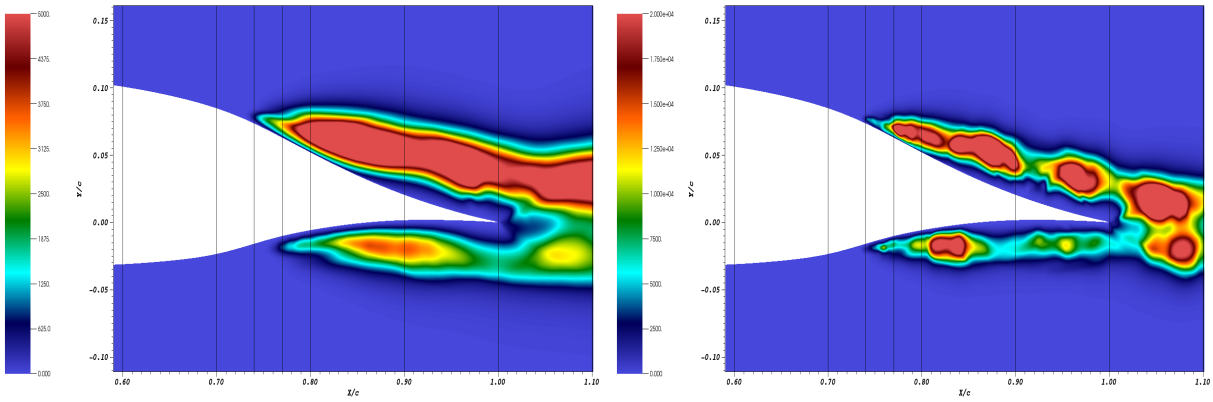

(c) Reynolds-stress Tensor Component $\overline{v^2}$ for Case 1: Clean NLF-0414 at Re_c = 1 x 10^5

(d) Reynolds-stress Tensor Component $\overline{v^2}$ for Case 4: Clean NLF-0414 at Re_c = 2 x 10^5

Figure 94: Production Tensor Component P_{yy} Comparison Between the Clean NLF-0414 Cases at Re_c = 1 x 10^5 and Re_c = 2 x 10^5

When comparing Figures 94a, 94b, 95, and 96 at Re_c = 1 x 10^5 each case has the same "X" red zone on the lower surface at X/c $\approx$ 1.10 that comes from the $\overline{uv}$ shear stresses (Figures 76, 77, and 78). When looking at the Re_c = 2 x 10^5 cases they all have different internal structures due to the fast changing nature of the Y-derivative in a X dominated flow ($U >> V$).

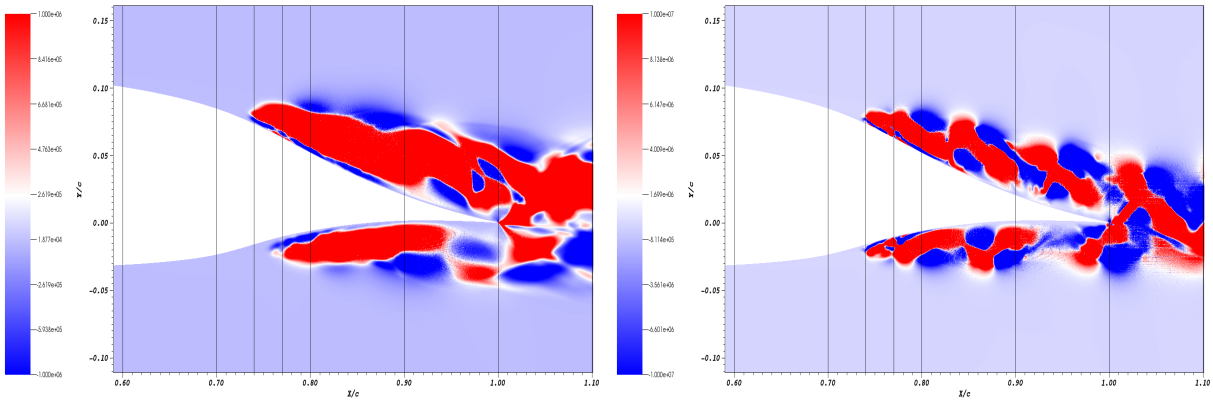

(a) Production Tensor Component P_{yy} for Case 2: Run 606 at $Re_c = 1$ x 10^5

(b) Production Tensor Component P_{yy} for Case 5: Run 606 at $Re_c = 2$ x 10^5

Figure 95: Production Tensor Component P_{yy} Comparison Between the Run 606 Cases at $Re_c = 1$ x 10^5 and $Re_c = 2$ x 10^5

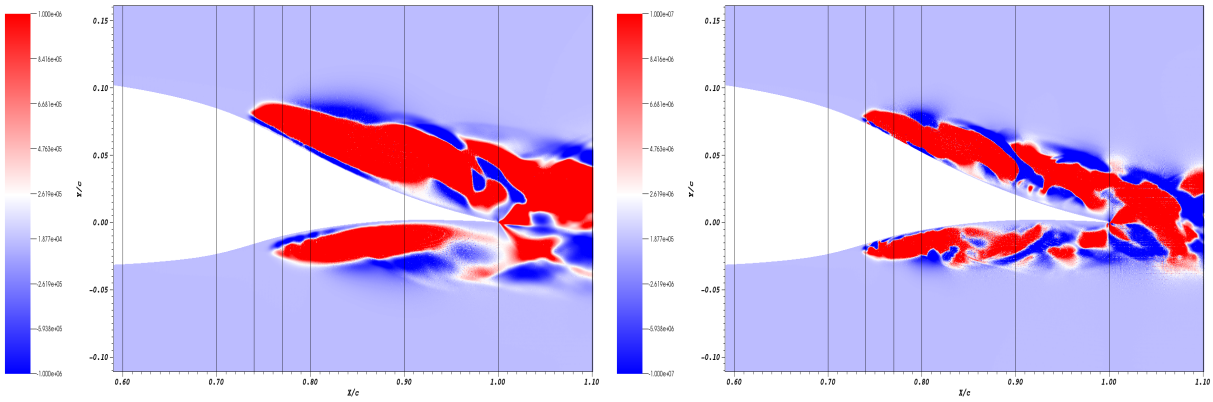

(a) Production Tensor Component P_{yy} for Case 3: Run 622-2D at $Re_c = 1$ x 10^5

(b) Production Tensor Component P_{yy} for Case 6: Run 622-2D at $Re_c = 2$ x 10^5

Figure 96: Production Tensor Component P_{yy} Comparison Between the Run 622-2D Cases at $Re_c = 1$ x 10^5 and $Re_c = 2$ x 10^5

6 Conclusions

To obtain the high accuracy results necessary for transition prediction, a numerical investigation using SEM to perform a DNS of the effects of ice on the flow about an NLF airfoil at low Reynolds numbers was performed. To the best of the author's knowledge, this is the first analysis of the effects of ice on an airfoil's aerodynamic performance using the open source DNS code Nek5000 [1]. One of the major reasons this works was not previously attempted was due to the large computational time and very large datasets required as well as the difficulty of meshing irregular iced geometries. One of the main goals of this thesis was to prove that Nek5000, which uses structured grids, could model irregular surfaces such as iced airfoils. The second goal of this work was to give a good understanding of the physics of the flow past iced airfoils, especially in the prediction of transition. The high-order high-accuracy results obtained could be used as a good dataset for comparison with other numerical methods such as RANS, LES, and other hybrid methods.

The flow past a clean NLF-0414 and two iced cases (Run 606 and Run 622-2D) from the NASA TP [14] was analyzed at $Re_c = 1$ x 10^5 and $Re_c = 2$ x 10^5. Run 606, a very lightly iced airfoil, and Run 622-2D, an iced airfoil with a slight horn and asymmetric accretion, were selected due to their particular geometries. An integral part of this work was to reduce the computational time by using proper mapping and meshing of the six cases. The mesh, without the use of spectral collocation points, was proven to be adequate by the dimensionless grid wall distance y^+ values being below $y^+ < 2$ at their highest. The actual y^+ values with the use of the collocations points are well within the desired $y^+ \approx 1$. A good dataset was output for the six cases to give a good understanding of the flow physics over the iced airfoils. Results from the iced cases, as expected, altered the aerodynamic performance of the NLF-0414.

Initially the velocity fields, pressure fields, and vorticity fields were studied and compared to visually understand the iced cases' impact on the flow when compared to the clean NLF-0414. X- and Y- velocities are clearly altered by the ice by either increasing or decreasing the velocities on the upper and lower surfaces. In the $Re_c = 1$ x 10^5 cases the Run 622-2D (most iced) has the highest X-velocity while Run 606 has the highest Y-velocity. In the $Re_c = 2$ x 10^5 cases the Run 622-2D has the highest Y-velocity while the clean NLF-0414 and Run 606 has the highest Y-velocities. The pressure fields show the intensity of the stagnation points and the low pressure on the suction side. In the $Re_c = 1$ x 10^5 cases Run 622-2D has the highest stagnation pressure and the clean NLF-0414 has the lowest suction zone pressure. In the $Re_c = 2$ x 10^5 cases Run 622-2D has the highest stagnation point and the lowest stagnation zone pressure. Run 606 and Run 622-2D have recirculation zones on the LE of the airfoil in the ice crevasse that cause changes in the BL behaviour down the surface. The size of the recirculation zones increase with the increase of Reynolds number.

Secondly, the aerodynamic characteristics were studied to quantify performance degradation. The lift (C_l), drag (C_d), pressure (C_p), and skin friction (C_f) coefficients were calculated to study the aerodynamic performance. Run 622-2D cases at both Reynolds numbers have a shifted C_l and C_d profile (Figures 45 and 46) indicating later laminar-to-turbulent transition (by one cycle) compared to the clean NLF-0414 and Run 606 cases. This shift is caused

by the change in velocity over the upper and lower surfaces as well as by the recirculation zones changing the inner structure of the BL. The C_l and C_d values increase with ice which is not as expected for C_l values but is for C_d values. Only the Run 622-2D at Re_c = 1 x 10^5 deviates from this and has a lower C_d than Run 606. The increase in lift with increased ice is explained by the LE spikes in the C_p distributions. Most of the spikes are found on the upper surface of the airfoil, changing the suction side pressure and thereby increasing the total lift. The size of the plateau and valleys of Run 622-2D at Re_c = 1 x 10^5 (Figure 47) compared to Run 622-2D at Re_c = 2 x 10^5 (Figure 48) shows how much the flow is changed by the recirculation zones. That combined with the asymmetric ice shape could alter the aerodynamic profile in a positive way at the specific Re_c = 1 x 10^5 decreasing the overall drag.

Skin friction coefficient (C_f) is an integral part of studying laminar-to-turbulent transition and results are slightly different from the design values. Transition to turbulence occurs earlier in the Re_c = 2 x 10^5 than in the Re_c = 1 x 10^5 which is expected as the Reynolds number increases and approaches the design Reynolds number. All six cases have their transition to turbulence past the 70% chord mark with the lower surface transition occurring downstream of the upper surface transition. In the Re_c = 1 x 10^5 cases the clean NLF-0414 upper surface transitions before the iced cases at X/c = 0.799 while the iced cases are closer to X/c = 0.812. The clean NLF-0414 and Run 622-2D (Re_c = 1 x 10^5) lower surface transitions at X/c = 0.861 while the Run 606 transitions earlier at X/c = 0.849. Laminar-to-turbulent transition is a very precise science and slight variations in transition location indicate subtle flow changes. The iced upper surfaces transition downstream of the clean NLF-0414 one due to the increase in energy from the recirculation zones. The increase in energy could also explain the earlier transition in the lower surface Run 606. The early transition on the lower surface of Run 606 could also explain the higher C_d for Run 606 than for Run 622 at Re_c = 1 x 10^5. In the Re_c = 2 x 10^5 cases the transition, for both the upper and lower surfaces, occurs upstream of the Re_c = 1 x 10^5 cases. The upper and lower surfaces at Re_c = 2 x 10^5 all transition near X/c = 0.785 and X/c = 0.796 respectively.

The velocity profiles are a very good tool for comparisons and studying the internal structure of the BL. The LE velocity profiles show the magnitude and size differences of Run 606 and Run 622-2D recirculation zones. The Run 622-2D (Re_c = 1 x 10^5) C (red) and D (neon green) velocity profiles (Figure 58b) show a very small recirculation zone while the velocity profiles at the same probe lines for Run 622-2D at Re_c = 2 x 10^5 (Figure 59b) show a larger and thicker recirculation zone even if the BL is thinner at the higher Reynolds number. A larger and faster recirculation zone will change the aerodynamics characteristics. This increase in recirculation does not occur on the lower surface velocity profile E (yellow) and there is no large increase between the Run 606 cases at Re_c = 1 x 10^5 and Re_c = 2 x 10^5. The TE velocity profiles help understand the velocity structure within the separated BL. The major difference between the Re_c = 1 x 10^5 cases and the Re_c = 2 x 10^5 cases is the thickness of the BL as well as the location of vortex shedding. The velocity profiles also show the different sub-layers within the BL.

A C-curve connected to an S-curve in the velocity profiles, only seen past the point of vortex separation, indicates a separation in the secondary BL between the vortices caused by the

vortices tail still being attached to the surface of the airfoil. Velocity threshold values in the BL, for the Run 622-2D case at Re_c = 1 x 10^5 (Table 10), are higher than the Run 606 ones but are lower than the Run 606 ones in the Re_c = 2 x 10^5 (Table 11) case. The velocity thresholds correlate with the inconsistent C_d value for the Run 622-2D at Re_c = 1 x 10^5. The iced cases have similar threshold values and are completely different from the clean cases which indicates that the ice alters the BL and slightly moves the shedding locations.

The turbulent statistics are used to look at higher order terms, past the point of transition, that cause or explain the changes in flow that cannot be seen from looking at the velocity and vorticity fields. The Reynolds-stress Tensors show the fluctuation in fluid momentum, giving an understanding of the forces that lead the flow to rotate. The normal stresses ($\overline{u^2}$ and $\overline{v^2}$) show the flow direction the vortices take while the shear stress ($\overline{uv}$) show the forces inducing rotation of the vortices. Nondimensional velocity profiles (Figures 73 and 74) of $\overline{u^2}$ show a more quantitative description of the Reynolds-stress Tensor Component $\overline{u^2}$ fields (Figures 70, 71, and 72). The nondimensional velocity profiles point out the differences in velocities between the iced cases and the clean NLF-0414 cases. Values for the Re_c = 2 x 10^5 cases drastically increase in the iced cases with the highest values observed in the Run 622-2D case. The quantitative and qualitative results are consistent with each other. The Skewness Tensor shows the asymmetry of the turbulent fluctuation in the fluid momentum. The Skewness Tensor component $\overline{u^3}$ at Re_c = 2 x 10^5 shows the location of separation of both the BL and secondary BL. The location of the secondary BL separation at the TE was only detected by studying the Skewness Tensor component $\overline{u^3}$. The Production Tensor shows the transfer of kinetic energy from the mean velocity into the fluctuating velocity field. The Production Tensor components show the importance of Reynolds shear stress in an X dominated flow ($U >> V$). The other components properly capture the start and separation of the BL but the Production Tensor components, especially P_{xx} (Figures 91a, 91b, 92, and 93), detects the small fluctuation within the BL to further understand the small fluctuations that start the formation of the vortices and induces transition.

In summary, we can conclude that the increase in Reynolds number has more of an effect on the lower surface than the upper surface, due to the NLF-0414 geometry, by moving the lower surface transition location upstream while barely moving the upper surface transition location. This can be observed in the C_p distributions, C_f distributions, y^+ distributions, velocity profiles, and turbulent statistics. The change of the transition locations combined with the Run 606 ice shape at Re_c = 2 x 10^5 caused the upper and lower surface shedding to synchronise. This synchronisation can be seen with the 80% (neon green) velocity profiles (Figures 73d and 74d) having the same profile with very similar peaks. The synchronisation can also be seen in the Skewness Tensor component $\overline{v^3}$ (Figure 88b). The changes in the transition location (Table 9) and subsequent turbulent structures due to the ice were relatively small in this study of lightly iced airfoils, however the velocity profiles revealed some differences in the boundary layer separation. Further studies with more severely iced geometries will no doubt present more significant changes.

Overall, the detailed study of these six cases has led us to 1) further understand the complexities of the transition process on iced airfoils, 2) observe and explain the sometimes unexpected changes in aerodynamic performance due to varying iced geometries, and 3)

establish a methodology for DNS studies of iced airfoils that can be expanded in the future.

6.1 Future Work

With this work showing that Nek5000 is a valid tool for iced airfoils a great amount of analysis could be added. To start off an in-depth study of the turbulent statistics could be accomplished with greater computational resources. Different iced shapes with more pronounced structures such as large or double horned iced geometries could be studied to push the Nek5000 code and analyze more dramatic changes in the transition location and the turbulent statistics. Other work should include increasing the Reynolds number, in 2D, into a range where experimental data is available to compare with our results. Ideally the goal would be to do the above mentioned simulations in 3D to study any other effects that could be overseen in 2D simulations. This work could also apply to the study of surface roughness (irregular surface) on airfoils used in aircraft and turbines [61]. Lastly, this new DNS capability could be used to validate and fine-tune the Langtry-Menter 4-equation Transitional SST [5] [6] turbulence model for airfoils, both clean and iced. This thesis is just working the surface of a very complex field that is evergoing and is crippled by current physical and theoretical hurdles [4].

References

[1] P. Fischer, A. Obabko, S. Kerkemeier, M. Min, J. Lottes, K. Heisey, S. Aithal, and Y. Peet, "Nek5000," 2021. [Online]. Available: https://nek5000.mcs.anl.gov/.

[2] Compute Ontario, "Compute Ontario," 2021. [Online]. Available: https://www.computeontario.ca/ (visited on 06/30/2021).

[3] Compute Canada, "Compute Canada," 2021. [Online]. Available: https://www.computecanada.ca/ (visited on 06/30/2021).

[4] J. Slotnick, A. Khodadoust, J. Alonso, W. Gropp, and D. Mavriplis, "CFD Vision 2030 Study: A Path to Revolutionary Computational Aerosciences," NASA, Tech. Rep. NASA/CR–2014-218178, 2014, p. 58. [Online]. Available: https://ntrs.nasa.gov/api/citations/20140003093/downloads/20140003093.pdf.

[5] R. B. Langtry and F. R. Menter, "Correlation-based transition modeling for unstructured parallelized computational fluid dynamics codes," *AIAA Journal*, vol. 47, no. 12, pp. 2894–2906, Dec. 2009, ISSN: 00011452. DOI: 10.2514/1.42362. [Online]. Available: https://arc.aiaa.org/doi/abs/10.2514/1.42362.

[6] J. Coder and C. Grabe, "Langtry-Menter 4-equation Transitional SST Model," 2021. [Online]. Available: https://turbmodels.larc.nasa.gov/langtrymenter_4eqn.html (visited on 06/28/2021).

[7] F. De Florio, *Airworthiness: An Introduction to Aircraft Certification and Operations*, 3rd editio. Elsevier, 2016, p. 528, ISBN: 978-0-08-100888-1. [Online]. Available: https://books.google.ca/books?hl=en&lr=&id=cXmLCwAAQBAJ&oi=fnd&pg=PP1&dq=aircraft+certification&ots=MnSjkfCe0c&sig=YeDJGlLY0JqoCMnwb0kGRA3hoZI#v=onepage&q=aircraft%20certification&f=false.

[8] T. Cebeci and F. Kafyeke, "Aircraft icing," *Annual Review of Fluid Mechanics*, vol. 35, pp. 11–21, Nov. 2003, ISSN: 00664189. DOI: 10.1146/annurev.fluid.35.101101.161217. [Online]. Available: https://www.annualreviews.org/doi/abs/10.1146/annurev.fluid.35.101101.161217.

[9] N. Czernkovich, "Understanding In-Flight Icing," 2004. [Online]. Available: http://www.aerosafety.ca/sources/aicraft_icing_paper.pdf.

[10] Y. Cao, W. Tan, and Z. Wu, "Aircraft icing: An ongoing threat to aviation safety," *Aerospace Science and Technology*, vol. 75, pp. 353–385, Apr. 2018, ISSN: 12709638. DOI: 10.1016/j.ast.2017.12.028. [Online]. Available: https://www.researchgate.net/publication/322849261_Aircraft_icing_An_ongoing_threat_to_aviation_safety.

[11] European Union Aviation Safety Agency, "Modelling Simulation – CS-25 Structural Certification Specifications," European Union Aviation Safety Agency, Tech. Rep. CM-S-014 Issue 01, 2020, p. 55. [Online]. Available: https://www.easa.europa.eu/sites/default/files/dfu/proposed_cm-s-014_modelling_simulation_-_for_consultation.pdf.

[12] American Institute of Aeronautics and Astronautics, *Recommended Practice: When Flight Modelling Is Used to Reduce Flight Testing Supporting Aircraft Certification (AIAA R-154-2021)*. American Institute of Aeronautics and Astronautics, Inc., Jan.

2021. DOI: 10.2514/4.106231. [Online]. Available: https://arc.aiaa.org/doi/abs/10.2514/4.106231.

[13] W. G. Habashi and J. P. S. Dow, "Icing Certification: Time to Consider 3D CFD," *International Civil Aviation Organization*, no. 1, pp. 38–40, 2017. [Online]. Available: http://digilib.mercubuana.ac.id/manager/t!@file_artikel_abstrak/Isi_Artikel_610195258764.pdf.

[14] H. E. Addy, "Ice Accretions and Icing Effects for Modern Airfoils," NASA, Tech. Rep. NASA TP-2000-210031 – DOT/ FAA/ AR-99/ 89, 2000, p. 292. [Online]. Available: https://ntrs.nasa.gov/search?q=nasa%20tp%202000-210031&search-type=ntrs.

[15] G. Mingione and M. Barocco, "Flight in Icing Conditions Summary." [Online]. Available: https://www.ecologie.gouv.fr/sites/default/files/Icing_flight_manual.pdf.

[16] P. J. Perkins and W. J. Rieke, *In-Flight Icing*, 2nd edition. Sporty's Pilot Shop, 2001, p. 42. [Online]. Available: https://www.amazon.com/Flight-Icing-Porter-J-Perkins/dp/B07GPPLLF4.

[17] J. Li, Z. Gao, J. Huang, and K. Zhao, "Robust design of NLF airfoils," *Chinese Journal of Aeronautics*, vol. 26, no. 2, pp. 309–318, Apr. 2013, ISSN: 10009361. DOI: 10.1016/j.cja.2013.02.007.

[18] H. L. Morgan and R. L. Campbell, "Design of the low-speed NLF(1)-0414F and the high-speed HSNLF(1)-0213 airfoils with high-lift systems," Tech. Rep. 19900003224, Dec. 1987. [Online]. Available: https://ntrs.nasa.gov/search.jsp?R=19900003224.

[19] P. Marques and P. N. Grimshaw, "Formula 1 aerodynamics: Versatility of the NLF(1)-0414F airfoil at low Reynolds numbers," in *14th Australian International Aerospace Congress, AIAC 2011*, 2011, pp. 1–10. [Online]. Available: https://hekyll.services.adelaide.edu.au/dspace/handle/2440/71999.

[20] J. J. Chung and H. E. Addy, "AIAA-2000-0096 A Numerical Evaluation of Icing Effects on a Natural Laminar Flow Airfoil," Institue for Computational Mechanics in Propulsion, Cleveland, Ohio, Tech. Rep. NASA/TM-2000-209775, 2000, p. 20. [Online]. Available: https://ntrs.nasa.gov/search.jsp?R=20000032523.

[21] M. Mirzaei, M. A. Ardekani, and M. Doosttalab, "Numerical and experimental study of flow field characteristics of an iced airfoil," *Aerospace Science and Technology*, vol. 13, no. 6, pp. 267–276, Jul. 2009. [Online]. Available: https://www.sciencedirect.com/science/article/abs/pii/S1270963809000200.

[22] A. Ebrahimi, M. Hajipour, and H. Hasheminasab, "Experimental investigation on the aerodynamic performance of NLF-0414 iced-airfoil," *Journal of Applied Fluid Mechanics*, vol. 9, no. 2, pp. 587–592, 2016. [Online]. Available: https://www.researchgate.net/publication/314241474_Experimental_Investigation_on_the_Aerodynamic_Performance_of_NLF-0414_Iced-Airfoil.

[23] A. P. Broeren and M. B. Bragg, "Effect of Airfoil Geometry on Performance with Simulated Intercycle Ice Accretions," Tech. Rep. AIAA-2003-0728, 2005. [Online]. Available: http://icing.ae.illinois.edu/papers/03/AIAA-2003-0728.pdf.

[24] P. Balakumar, "Direct numerical simulation of flows over an NACA-0012 airfoil at low and moderate reynolds numbers," in *47th AIAA Fluid Dynamics Conference, 2017*, American Institute of Aeronautics and Astronautics Inc, AIAA, 2017, ISBN:

9781624105005. DOI: 10.2514/6.2017-3978. [Online]. Available: https://arc.aiaa.org/doi/abs/10.2514/6.2017-3978.

[25] R. Vinuesa, L. Linn, S. M. Hosseini, A. Hanifi, D. S. Henningson, and P. Schlatter, "Direct Numerical Simulation of the Flow Around a Wing Section Using High-Order Parallel Spectral Methods," *International Symposium On Turbulence and Shear Flow Phenomena*, p. 6, 2015. [Online]. Available: http://www.tsfp-conference.org/proceedings/2015/v1/2B-3.pdf.

[26] W. Habashi, F. Morency, and H. Beaugendre, *FENSAP-ICE: a Comprehensive 3D Simulation Tool for In-flight Icing*, 2001. [Online]. Available: http://www.ase.uc.edu/~icfm7/ICFM7/33.pdf.

[27] H. Beaugendre, F. Morency, and W. G. Habashi, "Development of a second generation in-flight icing simulation code," *Journal of Fluids Engineering, Transactions of the ASME*, vol. 128, no. 2, pp. 378–387, Mar. 2006, ISSN: 00982202. DOI: 10.1115/1.2169807. [Online]. Available: https://hal.inria.fr/inria-00337571/document.

[28] D. Kelly, W. G. Habashi, G. Quaranta, P. Masarati, and M. Fossati, "Ice accretion effects on helicopter rotor performance, via multibody and CFD approaches," *Journal of Aircraft*, vol. 55, no. 3, pp. 1165–1176, 2018. DOI: 10.2514/1.C033962.

[29] G. B. Ahn, K. Y. Jung, R. S. Myong, H. B. Shin, and W. G. Habashi, "Numerical and experimental investigation of ice accretion on rotorcraft engine air intake," *Journal of Aircraft*, vol. 52, no. 3, pp. 903–909, Feb. 2015, ISSN: 15333868. DOI: 10.2514/1.C032839. [Online]. Available: https://arc.aiaa.org/doi/abs/10.2514/1.C032839.

[30] W. B. Wright, "User's Manual for LEWICE Version 3.2," NASA, Tech. Rep. NASA/CR—2008-214255, 2008, p. 454. [Online]. Available: https://ntrs.nasa.gov/citations/20080048307.

[31] R. H. Bush, A. Air, C. E. Towne, and G. D. Power, "WIND: The Production Flow Solver of the NPARC Alliance WIND: The Production Flow Solver of the NPARC Alliance," The Boeing Company, Tech. Rep. AIAA 98-0935, 1998, p. 15. [Online]. Available: https://arc.aiaa.org/doi/10.2514/6.1998-935.

[32] W. B. Wright, "Validation Results for LEWICE 3.0," NASA Center for Aerospace Information, Hanover, MD, Tech. Rep. NASA CR—2005-213561, AIAA–2005–1243, 2005. [Online]. Available: https://ntrs.nasa.gov/api/citations/20050160961/downloads/20050160961.pdf.

[33] M. Kim, J. Lim, S. Kim, S. Jee, J. Park, and D. Park, "Turbulent Transition Prediction Using Large-Eddy Simulation with the Stability Theory," Tech. Rep. ICCFD10-2018-0175, 2018. [Online]. Available: https://www.iccfd.org/iccfd10/papers/ICCFD10-175-Paper.pdf.

[34] H. S. Aly, K. M. Saqr, Y. A. Eldrainy, and M. N. Jaafar, "Can large eddy simulation (LES) predict laminar to turbulent flow transition?" *International Journal of Mechanical and Materials Engineering*, vol. 4, no. 1, pp. 42–48, 2009. [Online]. Available: https://www.researchgate.net/publication/252066992_Can_large_eddy_simulation_LES_predict_laminar_to_turbulent_flow_transition.

[35] A. Lozano-Durán, M. J. P. Hack, G. I. Park, and D. P. Moin, "Modeling boundary-layer transition in DNS and LES using parabolized stability equations," 2016. [Online]. Available: https://torroja.dmt.upm.es/media/adrian/publications/Lozano_brief_2016b.pdf.

[36] A. T. Patera, "A spectral element method for fluid dynamics: Laminar flow in a channel expansion," *Journal of Computational Physics*, vol. 54, no. 3, pp. 468–488, Jun. 1984, ISSN: 10902716. DOI: 10.1016/0021-9991(84)90128-1.

[37] E. M. Rønquist, "Optimal spectral element methods for the unsteady three-dimensional incompressible Navier-Stokes equations," PhD thesis, Massachusetts institute of Technology, 1988, p. 176. [Online]. Available: https://dspace.mit.edu/handle/1721.1/14365.

[38] P. Fischer, A. Obabko, S. Kerkemeier, M. Min, J. Lottes, K. Heisey, S. Aithal, and Y. Peet, "NEK5000 User's manual," Tech. Rep., 2015, p. 67. [Online]. Available: https://nek5000.github.io/NekDoc/.

[39] ——, "Nek5000 Tutorial," 2010. [Online]. Available: https://www.mcs.anl.gov/~fischer/nek5000/fischer_nek5000_dec2010.pdf (visited on 03/03/2021).

[40] G. E. Karniadakis, M. Israeli, and S. A. Orszag, "High-Order Splitting Methods for the Incompressible Navier-Stokes Equations," *Journal of Computational Physics*, vol. 97, p. 414 443, 1991. [Online]. Available: https://www.sciencedirect.com/science/article/pii/0021999191900078.

[41] A. Fournier, H.-P. Bunge, R. Hollerbach, and J.-P. Vilotte, "Application of the spectral-element method to the axisymmetric Navier-Stokes equations," *Geophys. J. Int*, vol. 156, pp. 682–700, 2004. DOI: 10.1111/j.1365-246X.2004.02149.x.

[42] J. Lottes, *Towards Robust Algebraic Multigrid Methods for Nonsymmetric Problems*. Springer International Publishing, 2017, ISBN: 978-3-319-56305-3. [Online]. Available: https://books.google.ca/books?hl=en&lr=&id=6PB5DgAAQBAJ&oi=fnd&pg=PR5&dq=Towards+Robust+Algebraic+Multigrid+Methods+for+Nonsymmetric+Problems+pdf&ots=6IHGtWwEQU&sig=DJMLkyqz_6v1JyuuY9wSxNQNesc#v=onepage&q&f=false.

[43] The GIMP Team, "GIMP - GNU Image Manipulation Program." [Online]. Available: https://www.gimp.org/ (visited on 01/14/2021).

[44] C. Geuzaine and J. Remacle, "Gmsh: a three-dimensional finite element mesh generator with built-in pre- and post-processing facilities," *International Journal for Numerical Methods in Engineering*, vol. 79, no. 11, pp. 1309–1331, 2009. [Online]. Available: https://onlinelibrary.wiley.com/doi/abs/10.1002/nme.2579.

[45] X. Chi, B. Zhu, T. I-P Shih, J. Slater, H. Addy, and Y. Choo, "Computing Aerodynamic Performance of a 2D Iced Airfoil: Blocking Topology and Grid Generation," Tech. Rep. 20030007845. [Online]. Available: https://ntrs.nasa.gov/search.jsp?R=20030007845.

[46] Yuan H., "Gmsh2nek," 2020. [Online]. Available: https://github.com/yhaomin2007/Nek5000/tree/master/tools/gmsh2nek.

[47] K. Mittal and P. Fischer, "Mesh Smoothing for the Spectral Element Method," *Journal of Scientific Computing*, vol. 78, no. 2, pp. 1152–1173, Feb. 2019, ISSN: 08857474. DOI: 10.1007/s10915-018-0812-9. [Online]. Available: https://link.springer.com/article/10.1007/s10915-018-0812-9.

[48] P. Fischer, "Boundary Conditions — Nek5000 17.0 documentation." [Online]. Available: https://nek5000.github.io/NekDoc/problem_setup/boundary_conditions.html (visited on 02/05/2021).

[49] A. Peplinski, "Sponge box Forcing," 2021. [Online]. Available: https://github.com/KTH-Nek5000/KTH_Toolbox/tree/master/utility/forcing/sponge_box (visited on 01/28/2021).

[50] A. Peplinski, P. Schlatter, P. F. Fischer, and D. S. Henningson, "Stability tools for the spectral-element code Nek5000: Application to Jet-in-Crossflow," *Lecture Notes in Computational Science and Engineering*, vol. 95, pp. 349–359, 2014, ISSN: 14397358. DOI: 10.1007/978-3-319-01601-6_28.

[51] N. Offermans, O. Marin, M. Schanen, J. Gong, P. Fischer, and P. Schlatter, "On the strong scaling of the spectral element solver Nek5000 on petascale systems," in *ACM International Conference Proceeding Series*, Association for Computing Machinery, Apr. 2016, ISBN: 9781450341226. DOI: 10.1145/2938615.2938617. arXiv: 1706.02970.

[52] N/A, "Airfoil Design," Los Angeles, 2021. [Online]. Available: https://mail.tku.edu.tw/095980/airfoil%20design.pdf.

[53] Jousefm, "What is y+ (yplus)? - Using SimScale / Fluid Flow / CFD - SimScale CAE Forum," 2020. [Online]. Available: https://www.simscale.com/forum/t/what-is-y-yplus/82394 (visited on 06/22/2021).

[54] SimEx, "KTH Mechanics · GitHub," 2021. [Online]. Available: https://github.com/KTH-Nek5000 (visited on 05/11/2021).

[55] R. Vinuesa, A. Peplinski, and M. Atzori, "Turbulence statistics in a spectral-element code : a toolbox for high-fidelity simulations," 2017. [Online]. Available: http://kth.diva-portal.org/smash/record.jsf?pid=diva2%3A1271879&dswid=4754.

[56] SimEx, "SimEx Group— KTH," 2021. [Online]. Available: https://www.kth.se/social/group/simex/ (visited on 05/13/2021).

[57] D. Pitsch, "Turbulence," Intitute for Combustion Technology, RWTH Aachen University, Germany, Tech. Rep., 2014, p. 77. [Online]. Available: https://cefrc.princeton.edu/sites/cefrc/files/Files/2014%20Lecture%20Notes/Pitsch/Lecture7_Turbulence_2014.pdf.

[58] H. Tennekes and J. Lumley, "A First Course In Turbulence," MIT Press, Cambridge, Massachusetts, 1972. [Online]. Available: https://www.academia.edu/34705775/A_FIRST_COURSE_IN_TURBULENCE.

[59] P. Schlatter and R. Örlü, "Quantifying the interaction between large and small scales in wall-bounded turbulent flows: A note of caution," *Physics of Fluids*, vol. 22, no. 5, pp. 1–4, May 2010, ISSN: 10706631. DOI: 10.1063/1.3432488. [Online]. Available: https://doi.org/10.1063/1.3432488.

[60] D. Lengani, D. Simoni, M. Ubaldi, P. Zunino, and F. Bertini, "Analysis of the Reynolds stress component production in a laminar separation bubble," *International Journal of Heat and Fluid Flow*, vol. 64, pp. 112–119, Apr. 2017, ISSN: 0142727X. DOI: 10.1016/j.ijheatfluidflow.2017.03.001.

[61] E. Ferrer and X. Munduate, "CFD predictions of transition and distributed roughness over a wind turbine airfoil," Tech. Rep. NASA/CR—2018-219771, 2018, p. 176. [Online]. Available: https://arc.aiaa.org/doi/abs/10.2514/6.2009-269.

Appendices

Appendix A Meshes

łabelSec:Appendix A

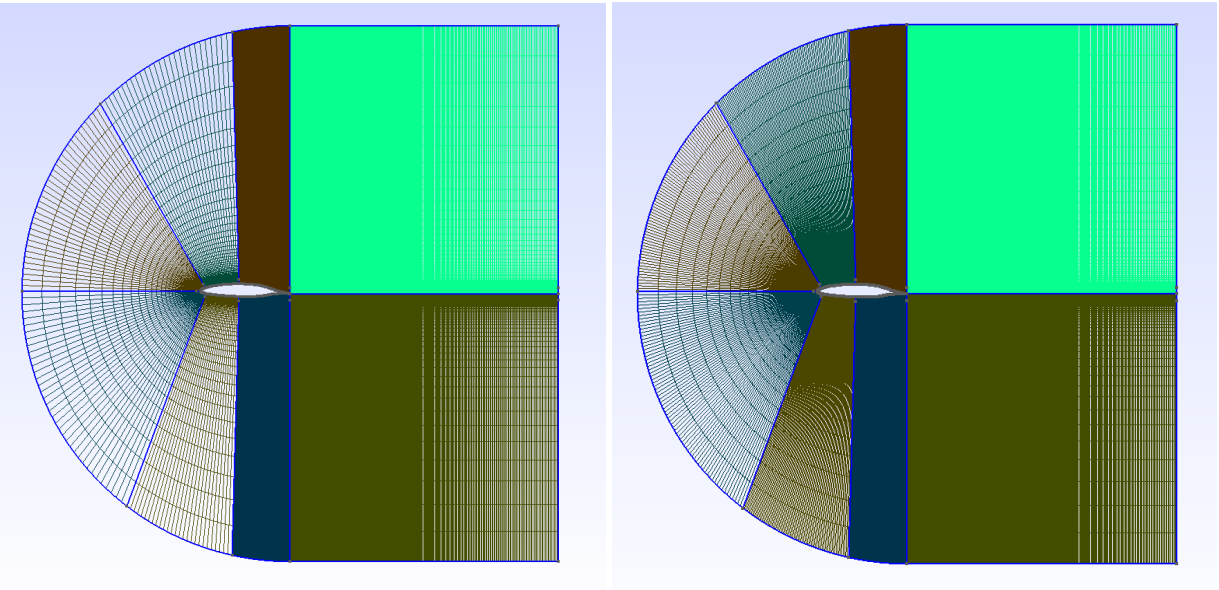

(a) Full Domain Mesh for Case 1: Clean NLF-0414 at Re_c = 1 x 10^5

(b) Full Domain Mesh for Case 4: Clean NLF-0414 at Re_c = 2 x 10^5

Figure 97: Full Domain Mesh for the Clean NLF-0414 Cases at Re_c = 1 x 10^5 and Re_c = 2 x 10^5

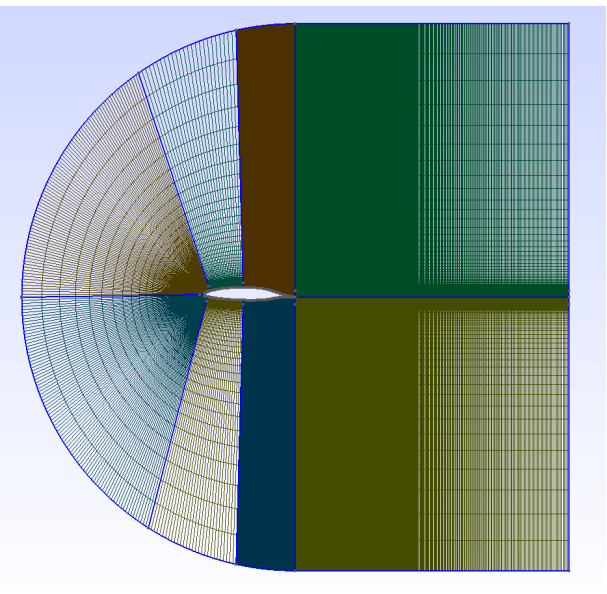

(a) Full Domain Mesh for Case 2: Run 606 at $Re_c = 1$ x 10^5

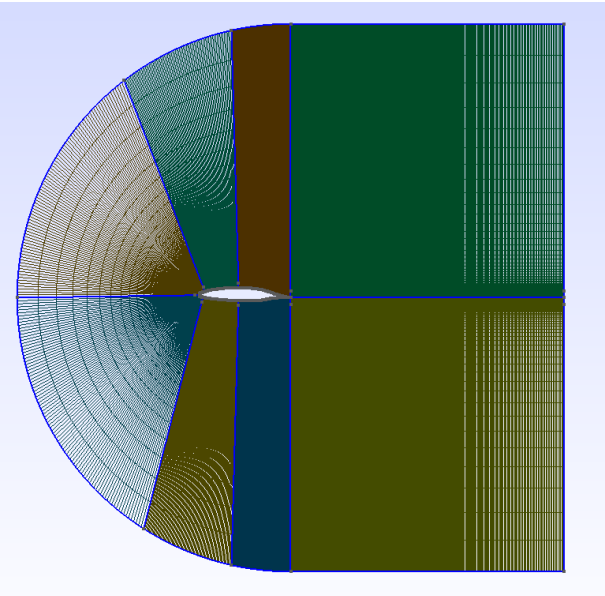

(b) Full Domain Mesh for Case 5: Run 606 at $Re_c = 2$ x 10^5

Figure 98: Full Domain Mesh for Run 606 Cases at $Re_c = 1$ x 10^5 and $Re_c = 2$ x 10^5

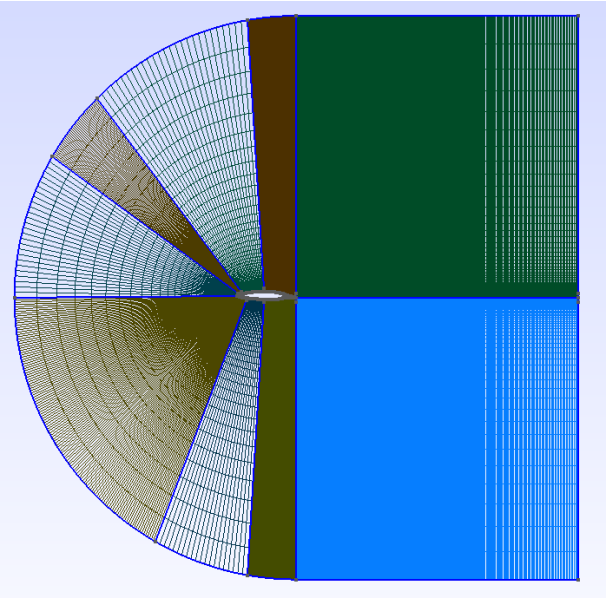

(a) Full Domain Mesh for Case 3: Run 622-2D at $Re_c = 1$ x 10^5

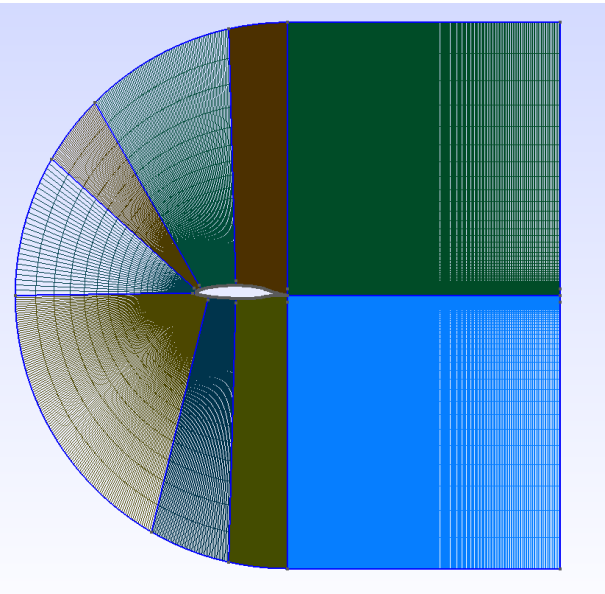

(b) Full Domain Mesh for Case 6: Run 622-2D at $Re_c = 2$ x 10^5

Figure 99: Full Domain Mesh for Run 622-2D Cases at $Re_c = 1$ x 10^5 and $Re_c = 2$ x 10^5

Appendix B Lift and Drag Coefficients

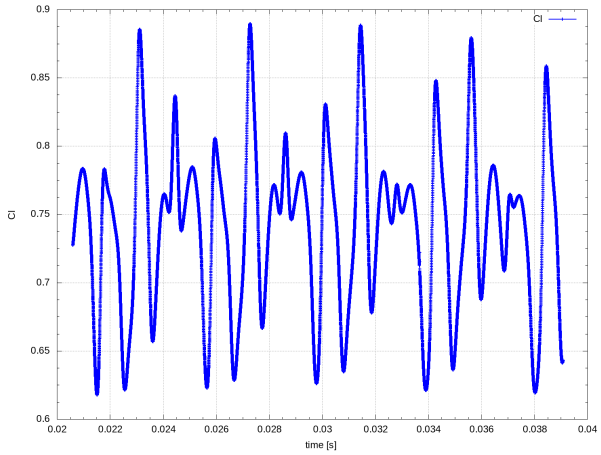

(a) Lift Coefficient for Case 1: Clean NLF-0414 at $Re_c = 1$ x 10^5

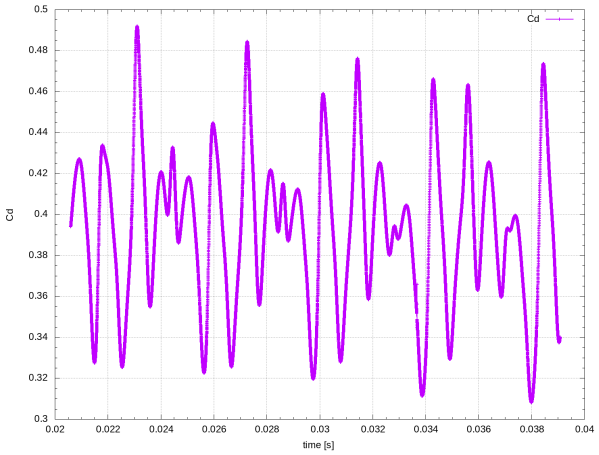

(b) Drag Coefficient for Case 1: Clean NLF-0414 at $Re_c = 1$ x 10^5

Figure 100: Lift and Drag Coefficient for Case 1: Clean NLF-0414 at $Re_c = 1$ x 10^5

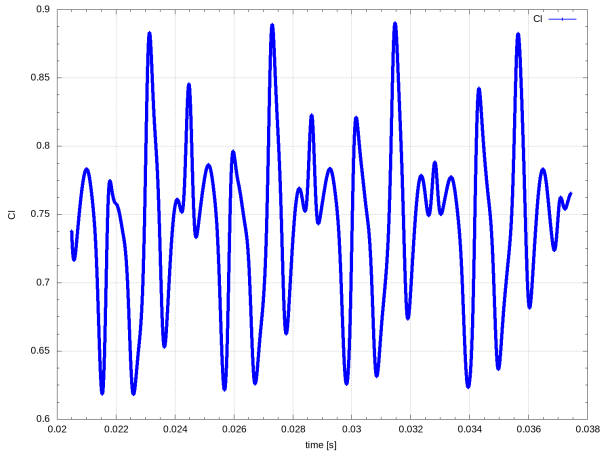

(a) Lift Coefficient for Case 2: Run 606 at $Re_c = 1$ x 10^5

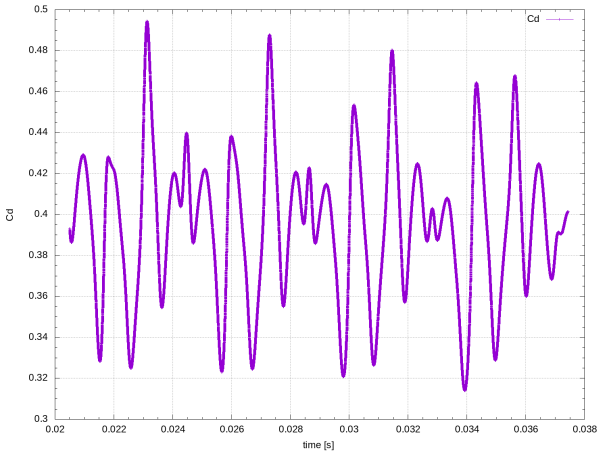

(b) Drag Coefficient for Case 2: Run 606 at $Re_c = 1$ x 10^5

Figure 101: Lift and Drag Coefficient for Case 2: Run 606 at $Re_c = 1$ x 10^5

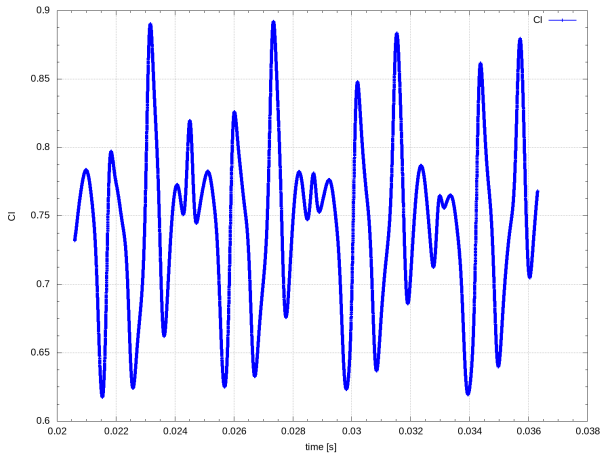

(a) Lift Coefficient for Case 3: Run 622-2D at $Re_c = 1$ x 10^5

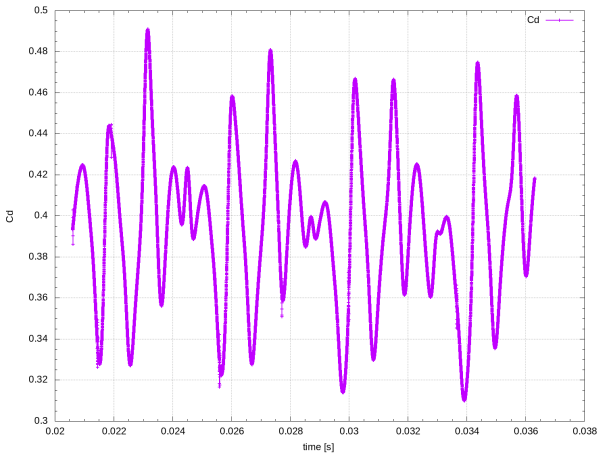

(b) Drag Coefficient for Case 3: Run 622-2D at $Re_c = 1$ x 10^5

Figure 102: Lift and Drag Coefficient for Case 3: Run 622-2D at $Re_c = 1$ x 10^5

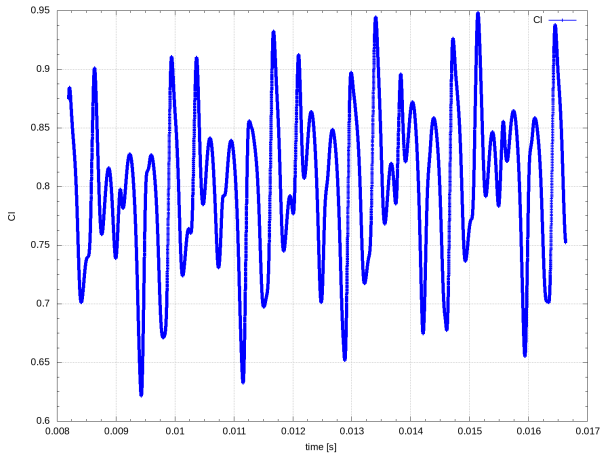

(a) Lift Coefficient for Case 4: Clean NLF-0414 at $Re_c = 2$ x 10^5

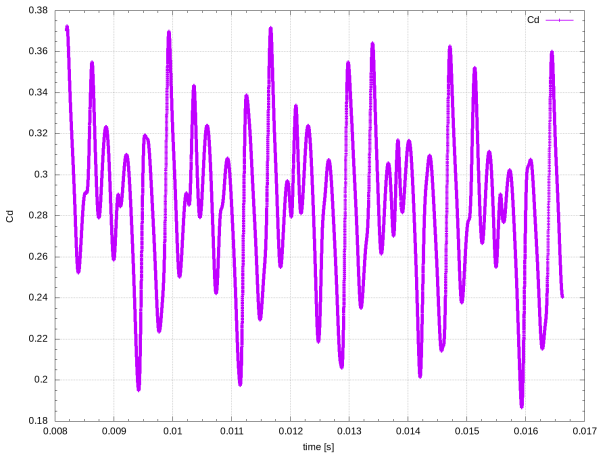

(b) Drag Coefficient for Case 4: Clean NLF-0414 at $Re_c = 2$ x 10^5

Figure 103: Lift and Drag Coefficient for Case 4: Clean NLF-0414 at $Re_c = 2$ x 10^5

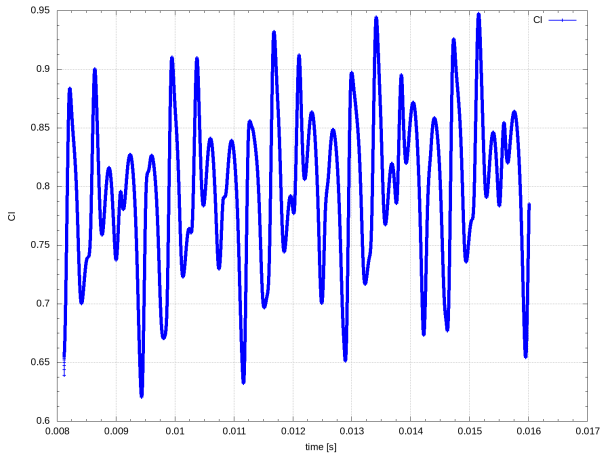

(a) Lift Coefficient for Case 5: Run 606 at $Re_c = 2$ x 10^5

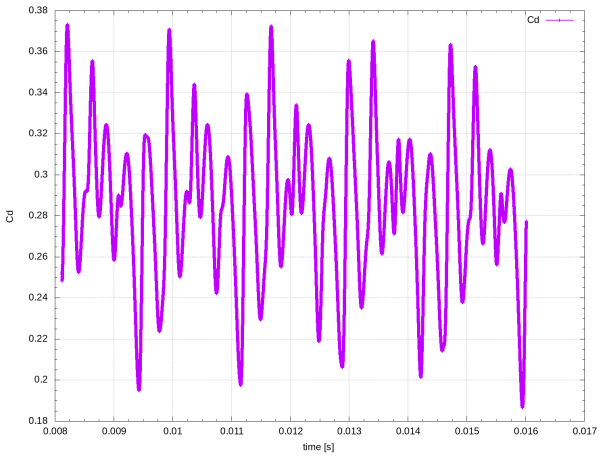

(b) Drag Coefficient for Case 5: Run 606 at $Re_c = 2$ x 10^5

Figure 104: Lift and Drag Coefficient for Case 5: Run 606 at $Re_c = 2$ x 10^5

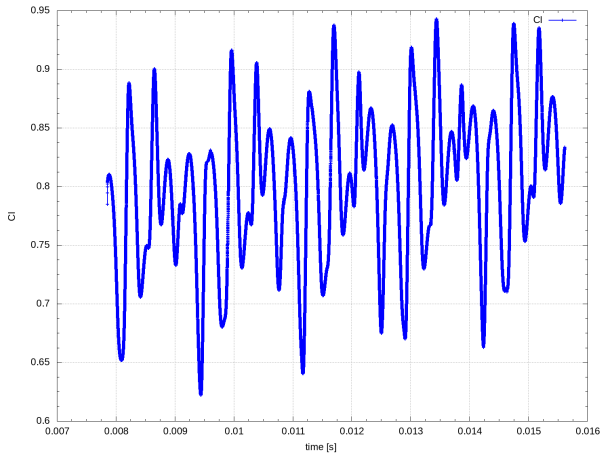

(a) Lift Coefficient for Case 6: Run 622-2D at $Re_c = 2$ x 10^5

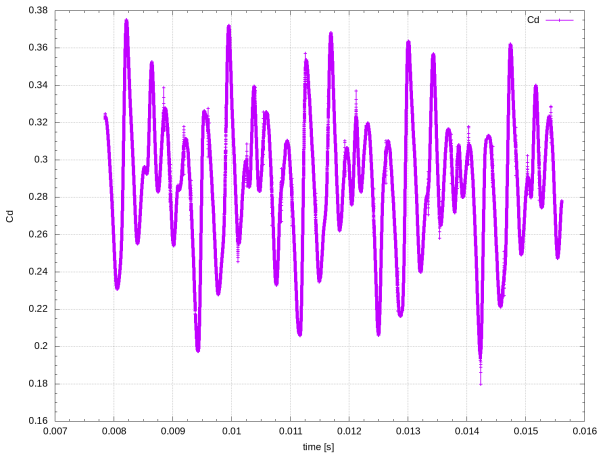

(b) Drag Coefficient for Case 6: Run 622-2D at $Re_c = 2$ x 10^5

Figure 105: Lift and Drag Coefficient for Case 6: Run 622-2D at $Re_c = 2$ x 10^5

Appendix C Pressure Coefficient

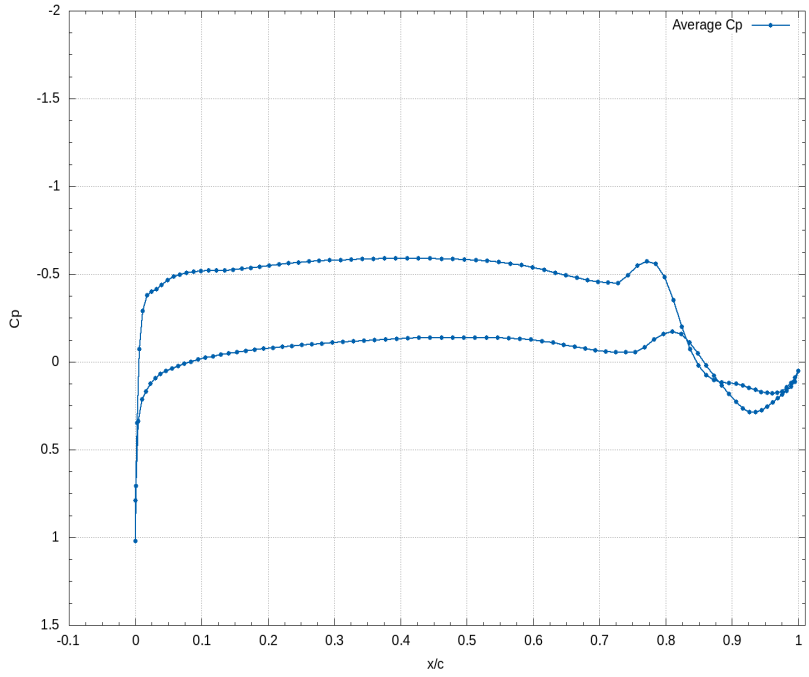

Figure 106: Pressure Coefficient for Case 1: Clean NLF-0414 at $Re_c = 1$ x 10^5

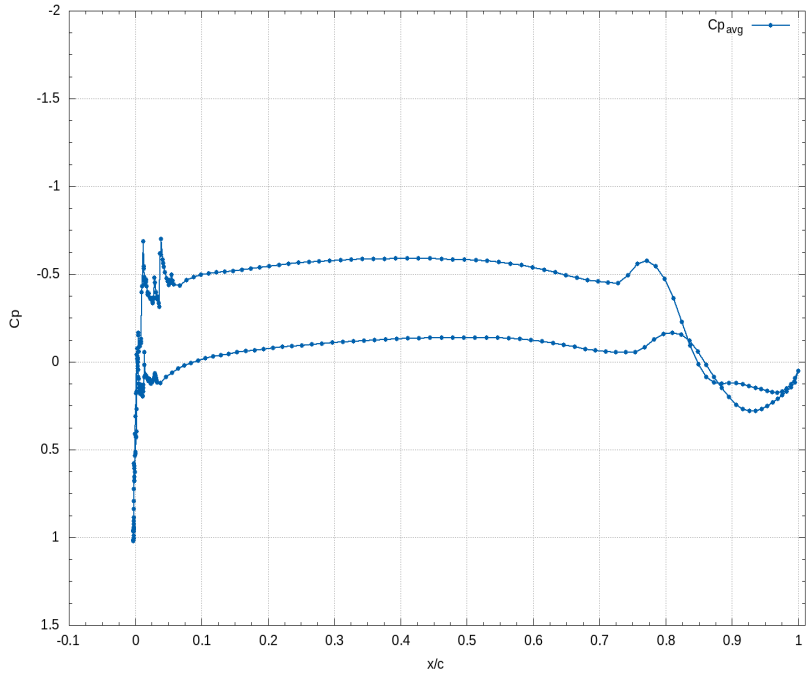

Figure 107: Pressure Coefficient for Case 2: Run 606 at $Re_c = 1$ x 10^5

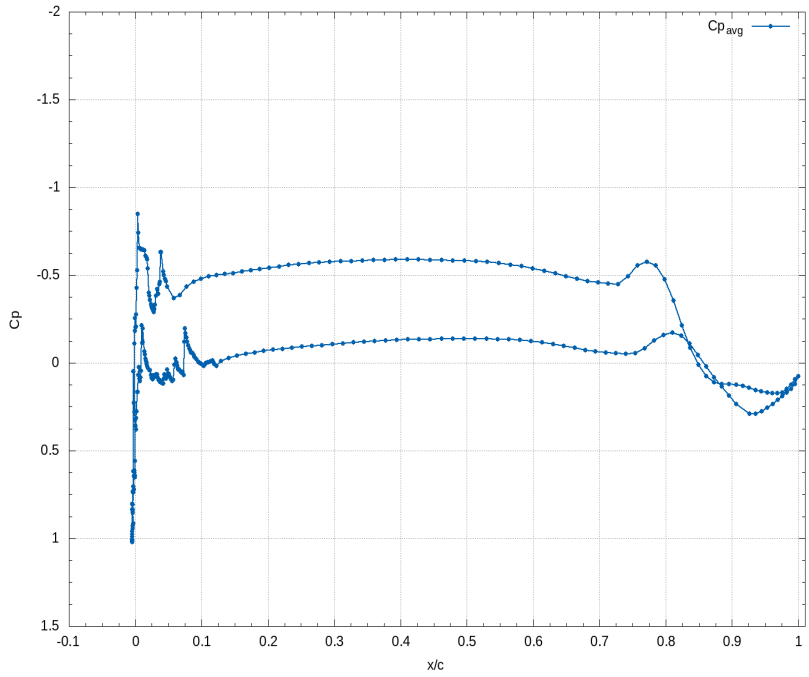

Figure 108: Pressure Coefficient for Case 3: Run 622-2D at $Re_c = 1$ x 10^5

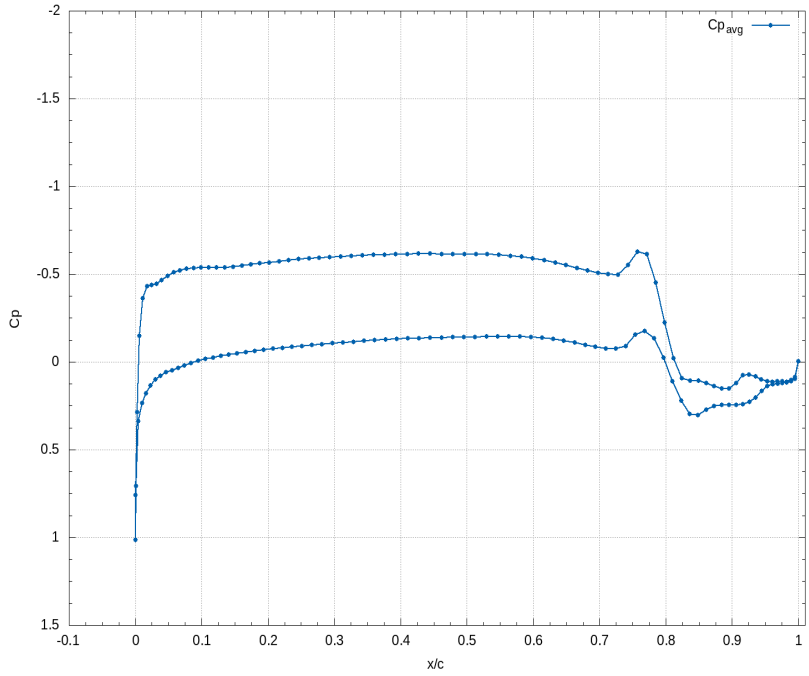

Figure 109: Pressure Coefficient for Case 4: Clean NLF-0414 at $Re_c = 2$ x 10^5

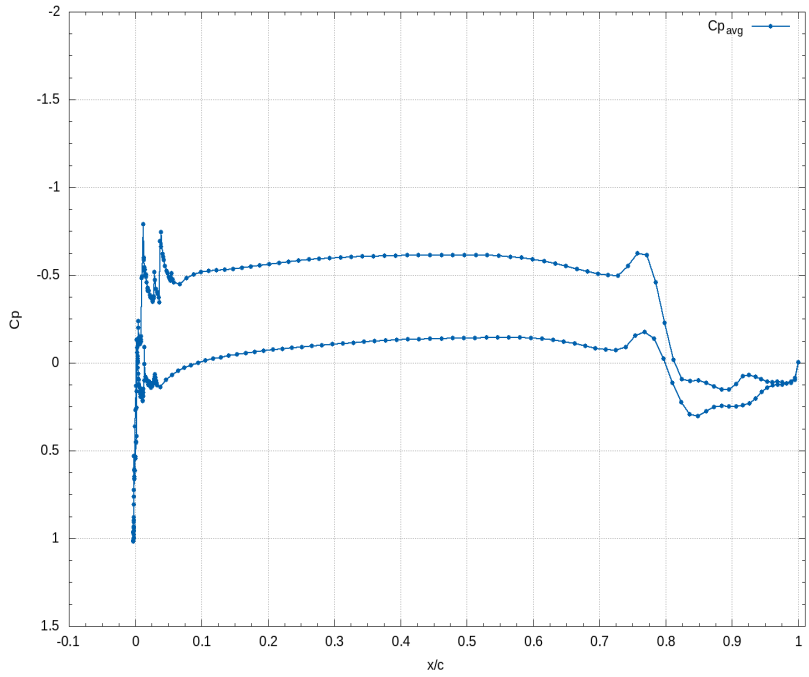

Figure 110: Pressure Coefficient for Case 5: Run 606 at $Re_c = 2$ x 10^5

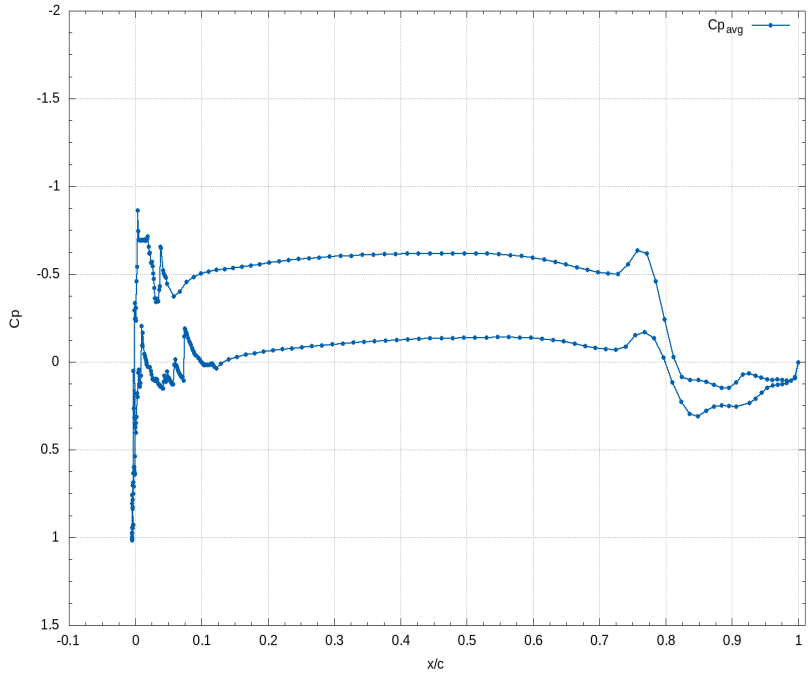

Figure 111: Pressure Coefficient for Case 6: Run 622-2D at $Re_c = 2$ x 10^5

Appendix D Skin Friction Coefficient

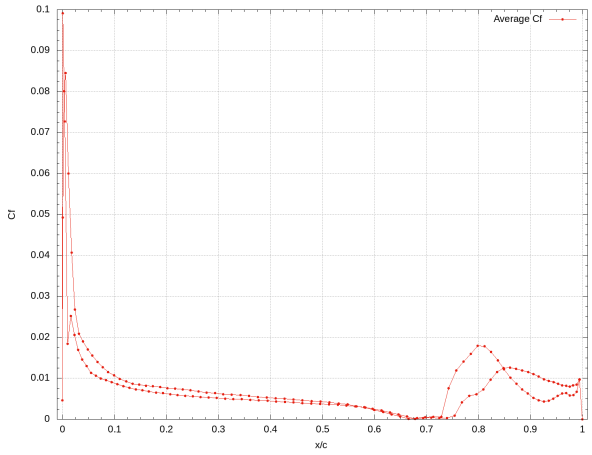

(a) Skin Friction Coefficient for Case 1: Clean NLF-0414 at $Re_c = 1$ x 10^5

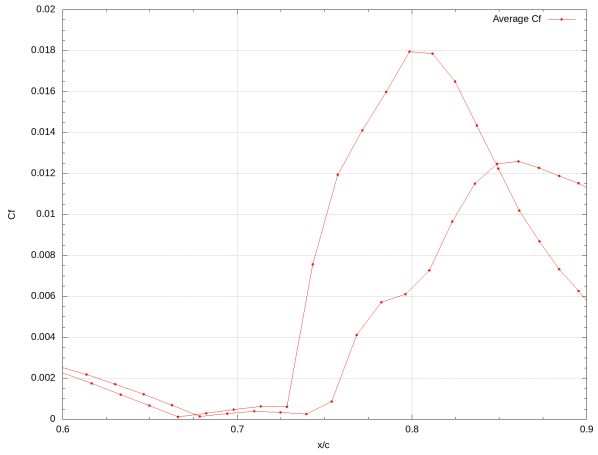

(b) Skin Friction Coefficient Close-up for Case 1: Clean NLF-0414 at $Re_c = 1$ x 10^5

Figure 112: Skin Friction Coefficient for Case 1: Clean NLF-0414 at $Re_c = 1$ x 10^5

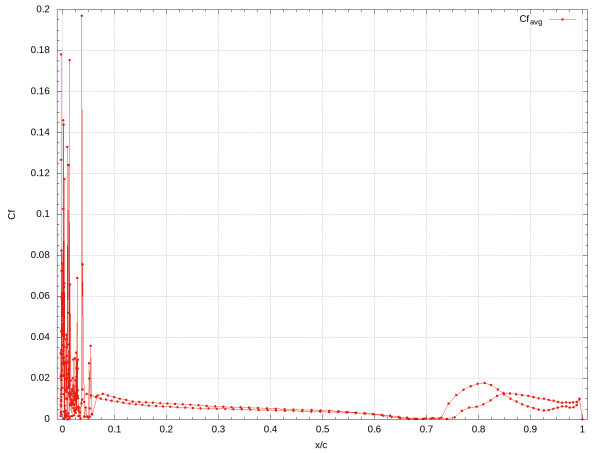

(a) Skin Friction Coefficient for Case 2: Run 606 at $Re_c = 1$ x 10^5

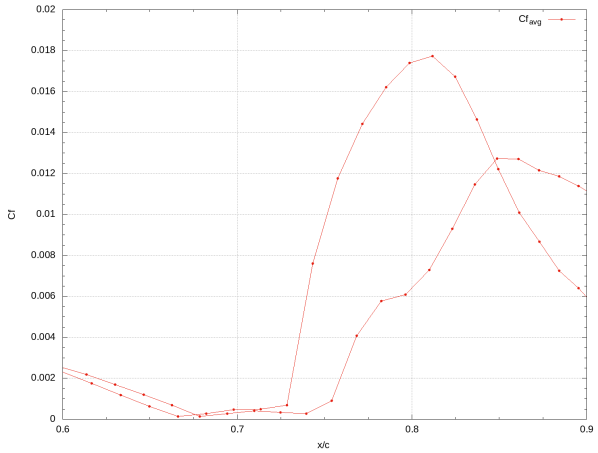

(b) Skin Friction Coefficient Close-up for Case 2: Run 606 at $Re_c = 1$ x 10^5

Figure 113: Skin Friction Coefficient for Case 2: Run 606 at $Re_c = 1$ x 10^5

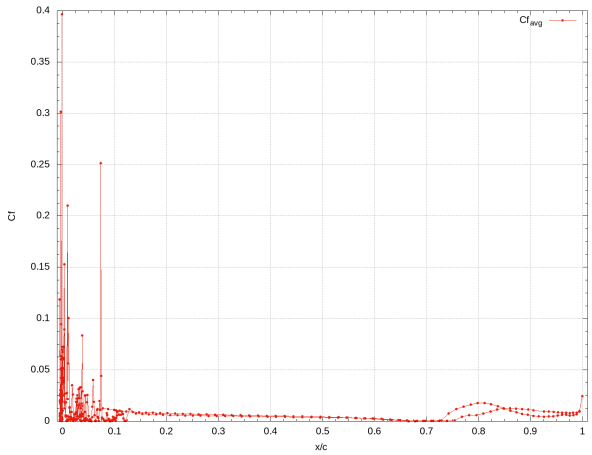

(a) Skin Friction Coefficient for Case 3: Run 622-2D at $Re_c = 1$ x 10^5

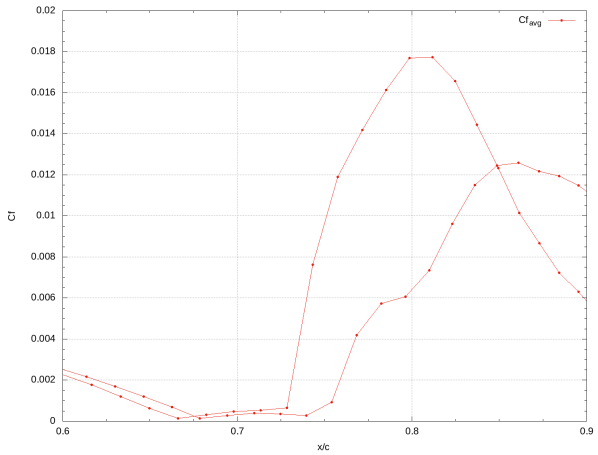

(b) Skin Friction Coefficient Close-up for Case 3: Run 622-2D at $Re_c = 1$ x 10^5

Figure 114: Skin Friction Coefficient for Case 3: Run 622-2D at $Re_c = 1$ x 10^5

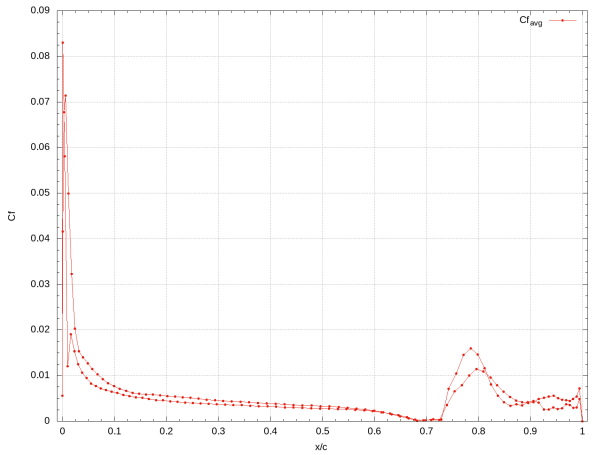

(a) Skin Friction Coefficient for Case 4: Clean NLF-0414 at $Re_c = 2$ x 10^5

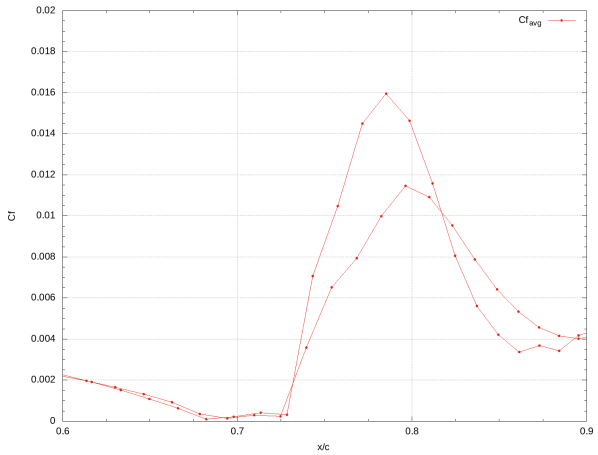

(b) Skin Friction Coefficient Close-up for Case 4: Clean NLF-0414 at $Re_c = 2$ x 10^5

Figure 115: Skin Friction Coefficient for Case 4: Clean NLF-0414 at $Re_c = 2$ x 10^5

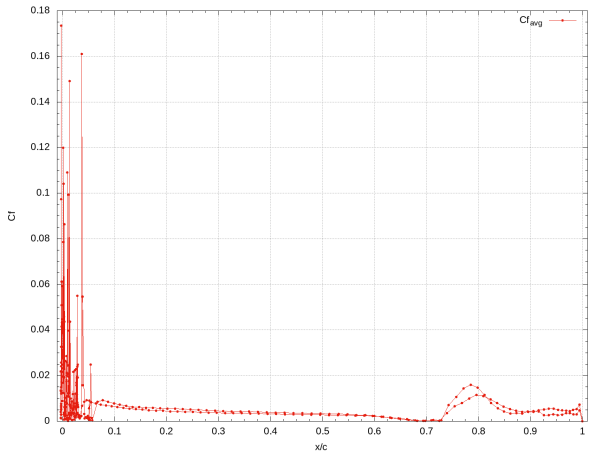

(a) Skin Friction Coefficient for Case 5: Run 606 at $Re_c = 2$ x 10^5

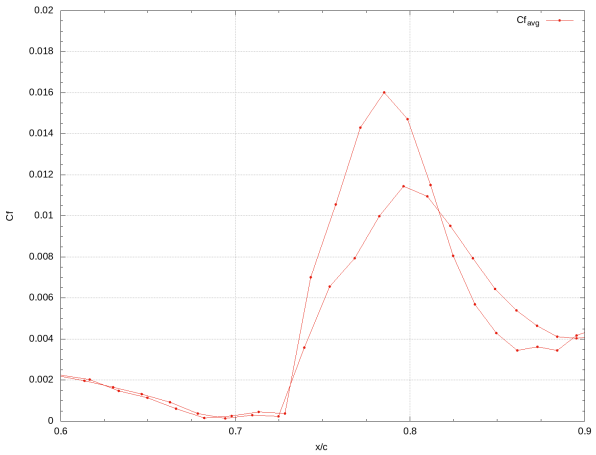

(b) Skin Friction Coefficient Close-up for Case 5: Run 606 at $Re_c = 2$ x 10^5

Figure 116: Skin Friction Coefficient for Case 5: Run 606 at $Re_c = 2$ x 10^5

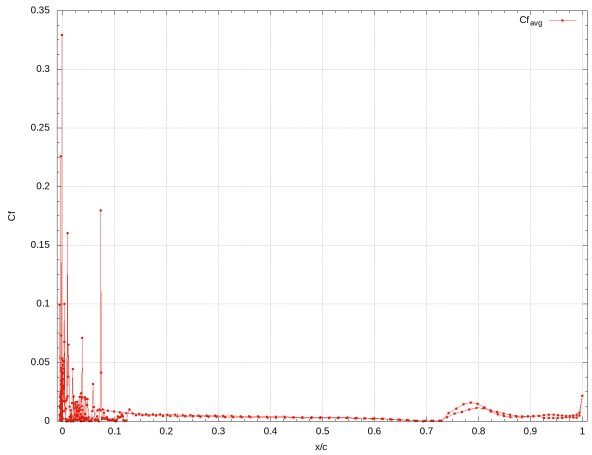

(a) Skin Friction Coefficient for Case 6: Run 622-2D at $Re_c = 2$ x 10^5

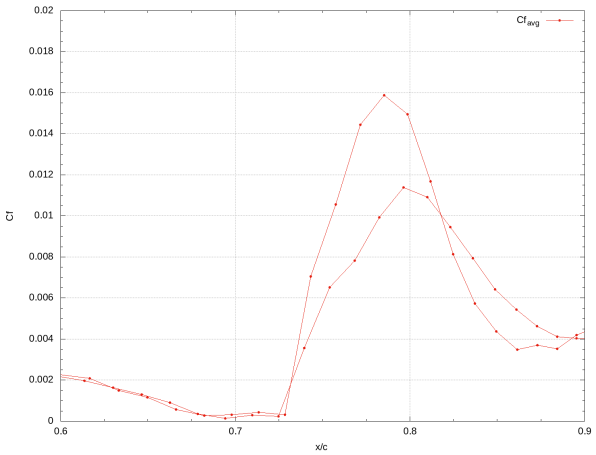

(b) Skin Friction Coefficient Close-up for Case 6:Run 622-2D at $Re_c = 2$ x 10^5

Figure 117: Skin Friction Coefficient for Case 6: Run 622-2D at $Re_c = 2$ x 10^5

Appendix E Turbulence Statistics

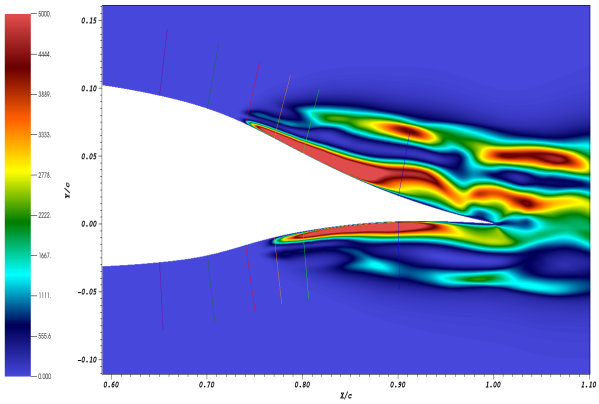

(a) Case 1: Trailing Edge Reynolds-stress Tensor Component $\overline{u^2}$ Field with Probe Lines

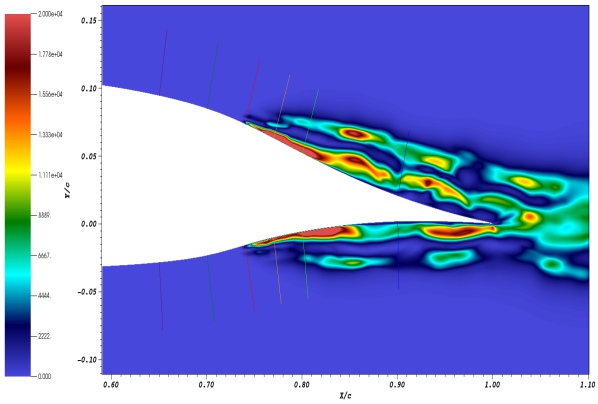

(b) Case 4: Trailing Edge Reynolds-stress Tensor Component $\overline{u^2}$ with Probe Lines

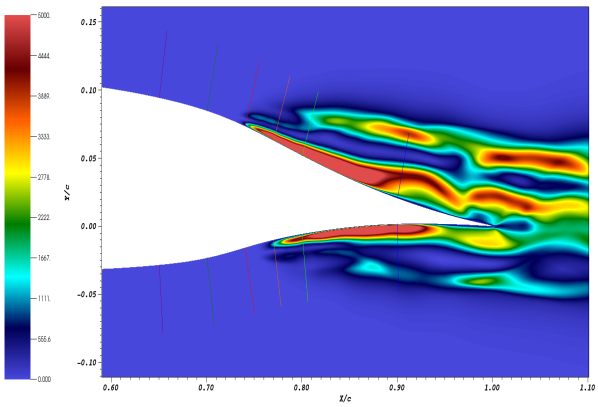

(c) Case 2: Trailing Edge Reynolds-stress Tensor Component $\overline{u^2}$ with Probe Lines

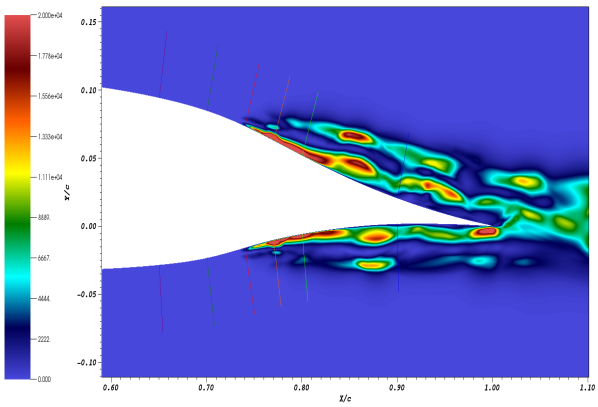

(d) Case 5: Trailing Edge Reynolds-stress Tensor Component $\overline{u^2}$ with Probe Lines

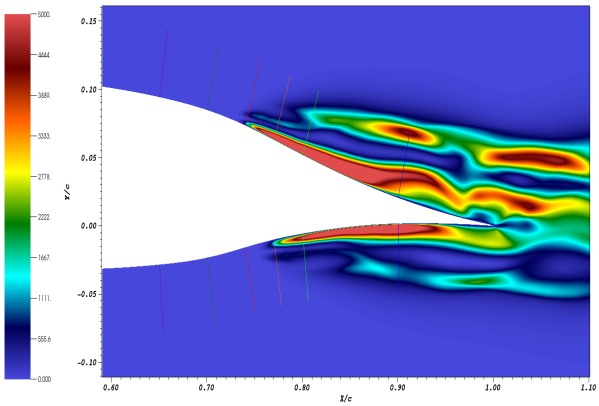

(e) Case 3: Trailing Edge Reynolds-stress Tensor Component $\overline{u^2}$ with Probe Lines

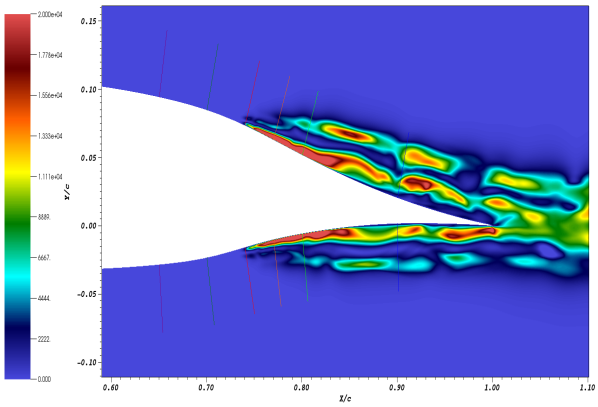

(f) Case 6: Trailing Edge Reynolds-stress Tensor Component $\overline{u^2}$ with Probe Lines

Figure 118: Trailing Edge Reynolds-stress Tensor Component $\overline{u^2}$ with Probe Lines [65% (purple), 70% (dark green), 74% (red), 77% (orange), 80% (neon green), 90% (blue)]

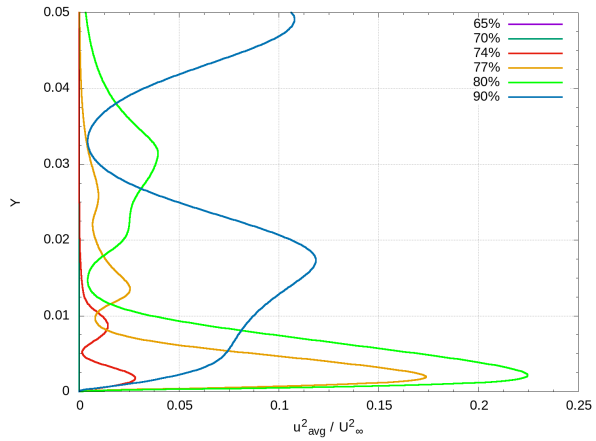

(a) Case 1: Airfoil Trailing Edge Upper Surface at $Re_c = 1$ x 10^5

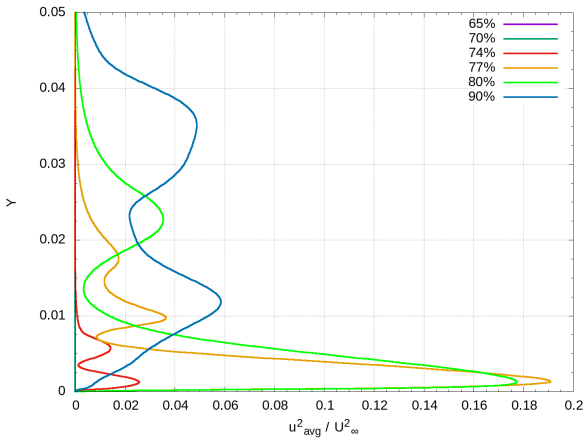

(b) Case 4: Airfoil Trailing Edge Upper Surface at $Re_c = 2$ x 10^5

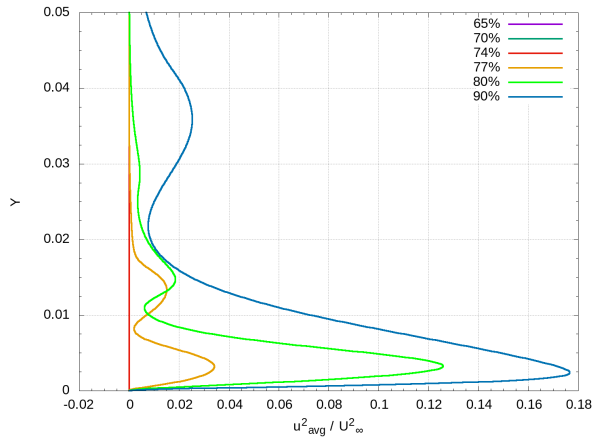

(c) Case 1: Airfoil Trailing Edge Lower Surface at $Re_c = 1$ x 10^5

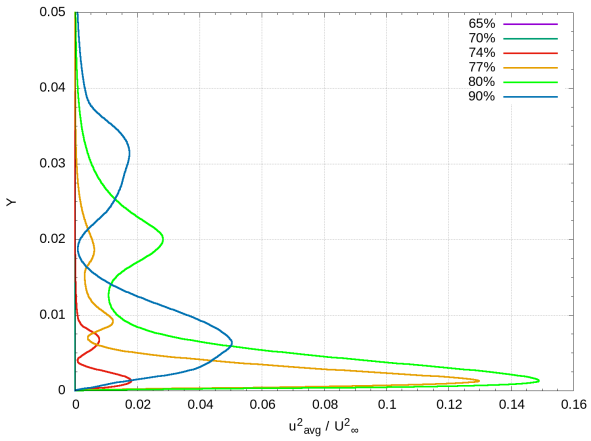

(d) Case 4: Airfoil Trailing Edge Lower Surface at $Re_c = 2$ x 10^5

Figure 119: Nondimensional Velocity Profile – Case 1 vs Case 4: Clean NLF-0414 Trailing Edge at $Re_c = 1$ x 10^5 and $Re_c = 2$ x 10^5

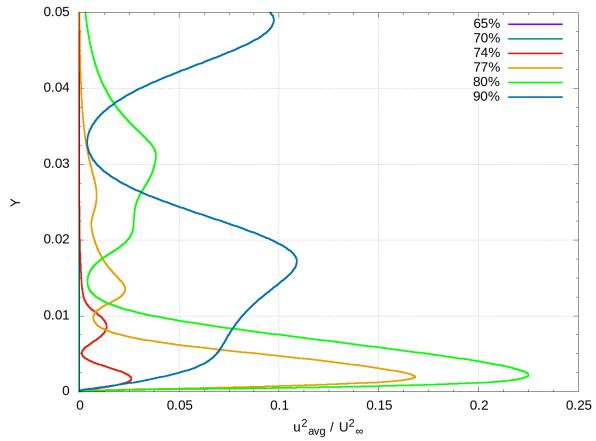

(a) Case 2: Airfoil Trailing Edge Upper Surface at Re_c = 1 x 10^5

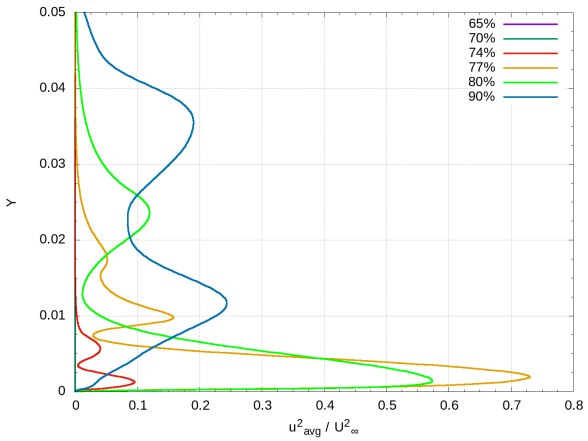

(b) Case 5 Airfoil Trailing Edge Upper Surface at Re_c = 2 x 10^5

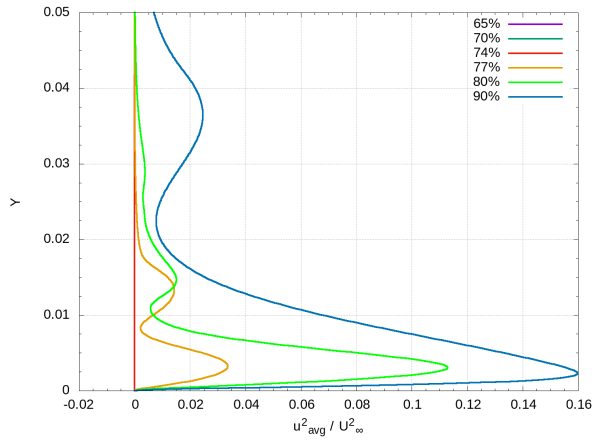

(c) Case 2: Airfoil Trailing Edge Lower Surface at Re_c = 1 x 10^5

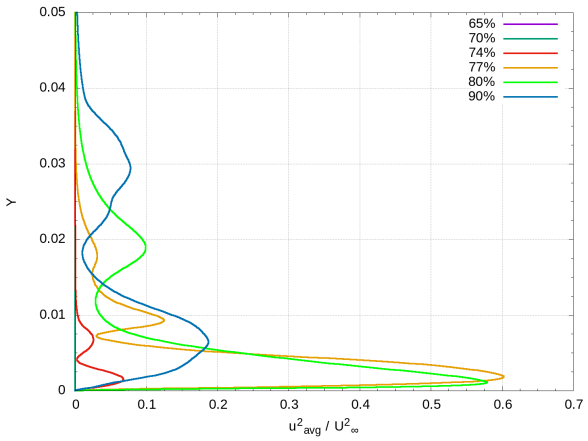

(d) Case 5: Airfoil Trailing Edge Lower Surface at Re_c = 2 x 10^5

Figure 120: Nondimensional Velocity Profile – Case 2 vs Case 5: Run 606 Trailing Edge at Re_c = 1 x 10^5 and Re_c = 2 x 10^5

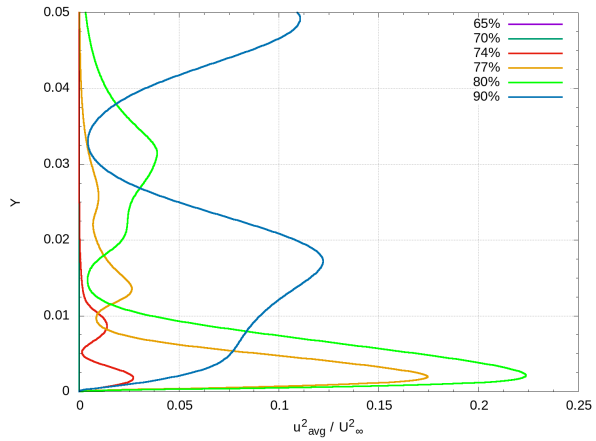

(a) Case 3: Airfoil Trailing Edge Upper Surface at Re_c = 1 x 10^5

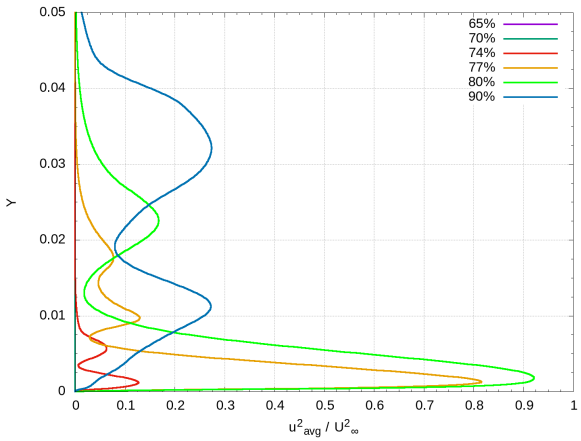

(b) Case 6 Airfoil Trailing Edge Upper Surface at Re_c = 2 x 10^5

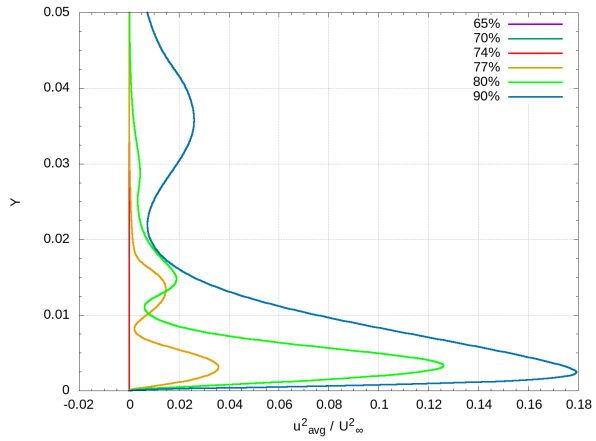

(c) Case 3: Airfoil Trailing Edge Lower Surface at Re_c = 1 x 10^5

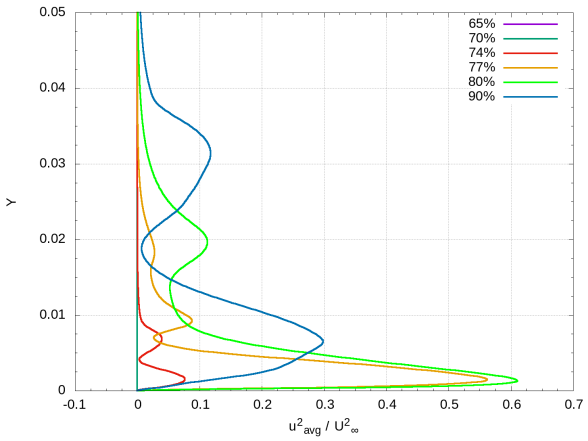

(d) Case 6: Airfoil Trailing Edge Lower Surface at Re_c = 2 x 10^5

Figure 121: Nondimensional Velocity Profile – Case 3 vs Case 6: Run 622-2D Trailing Edge at Re_c = 1 x 10^5 and Re_c = 2 x 10^5

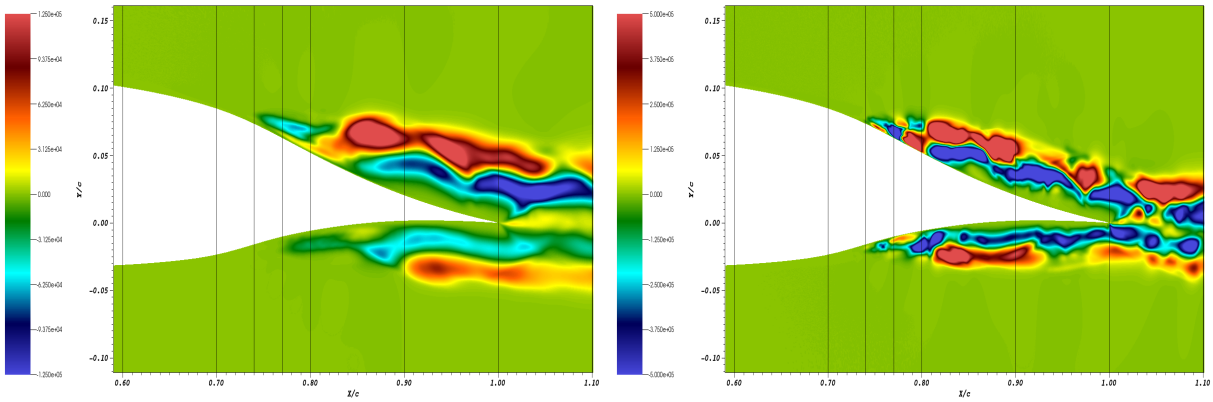

(a) Skewness Tensor Component $\overline{u^2v}$ for Case 1: Clean NLF-0414 at $Re_c = 1$ x 10^5

(b) Skewness Tensor Component $\overline{u^2v}$ for Case 4: Clean NLF-0414 at $Re_c = 1$ x 10^5

Figure 122: Skewness Tensor Component $\overline{u^2v}$ Comparison Between the Clean NLF-0414 Cases at $Re_c = 1$ x 10^5 and $Re_c = 2$ x 10^5

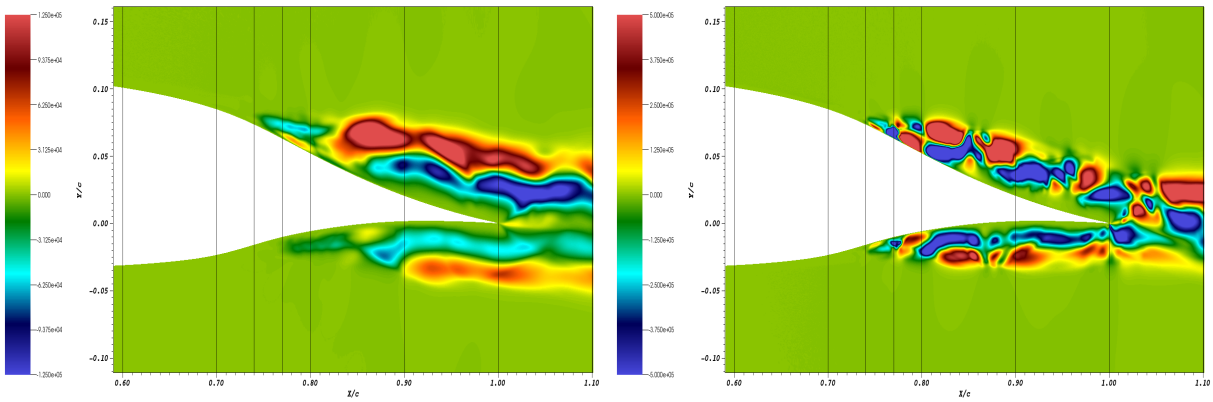

(a) Skewness Tensor Component $\overline{u^2v}$ for Case 2: Run 606 at $Re_c = 1$ x 10^5

(b) Skewness Tensor Component $\overline{u^2v}$ for Case 5: Run 606 at $Re_c = 2$ x 10^5

Figure 123: Skewness Tensor Component $\overline{u^2v}$ Comparison Between the Run 606 Cases at $Re_c = 1$ x 10^5 and $Re_c = 2$ x 10^5

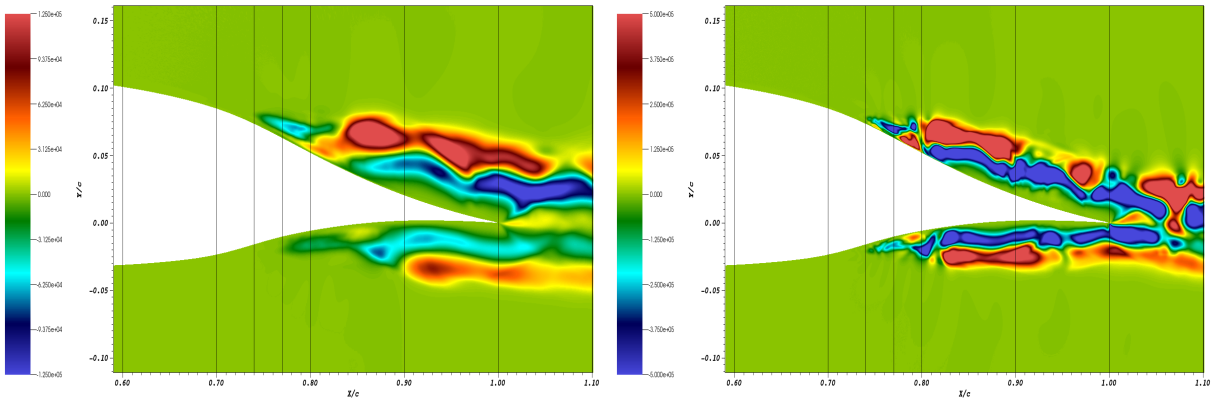

(a) Skewness Tensor Component $\overline{u^2v}$ for Case 3: Run 622-2D at Re_c = 1 x 10^5

(b) Skewness Tensor Component $\overline{u^2v}$ for Case 6: Run 622-2D at Re_c = 2 x 10^5

Figure 124: Skewness Tensor Component $\overline{u^2v}$ Comparison Between the Run 622-2D Cases at Re_c = 1 x 10^5 and Re_c = 2 x 10^5

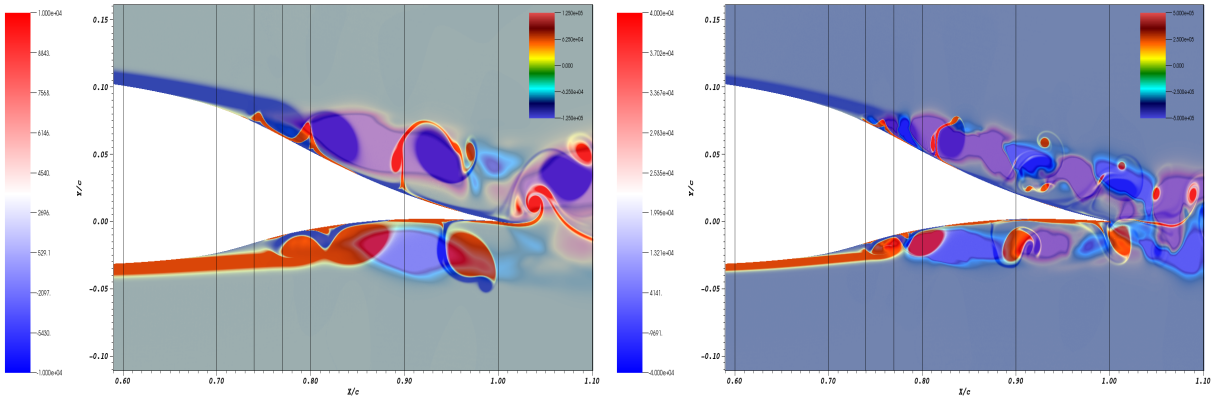

(a) Vorticity over Skewness Tensor Component $\overline{v^3}$ for Case 1: Clean NLF-0414 at Re_c = 1 x 10^5

(b) Vorticity Over Skewness Tensor Component $\overline{v^3}$ for Case 4: Clean NLF-0414 at Re_c = 2 x 10^5

Figure 125: Vorticity Over Skewness Tensor Component $\overline{v^3}$ Comparison Between the Clean NLF-0414 Cases at Re_c = 1 x 10^5 and Re_c = 2 x 10^5

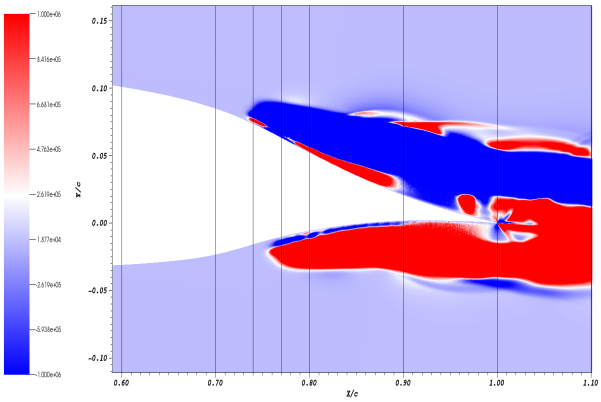

(a) Production Tensor Component P_{xy} for Case 1: Clean at Re_c = 1 x 10^5

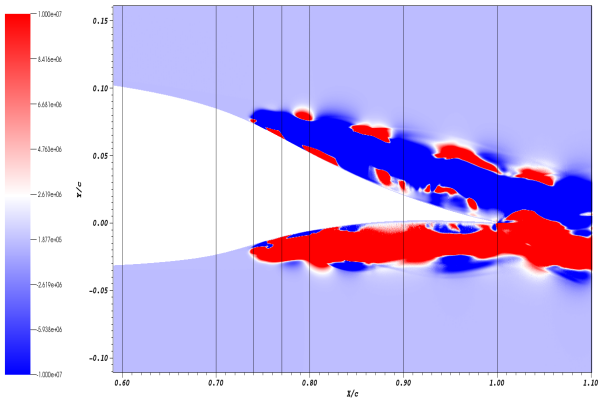

(b) Production Tensor Component P_{xy} for Case 4: Clean at Re_c = 2 x 10^5

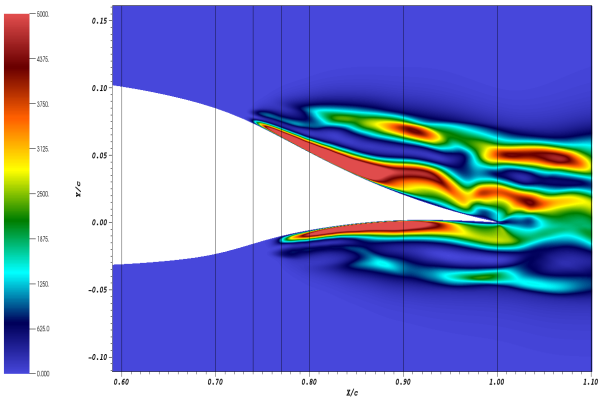

(c) Reynolds-stress Tensor Component $\overline{u^2}$ for Case 1: Clean NLF-0414 at Re_c = 1 x 10^5

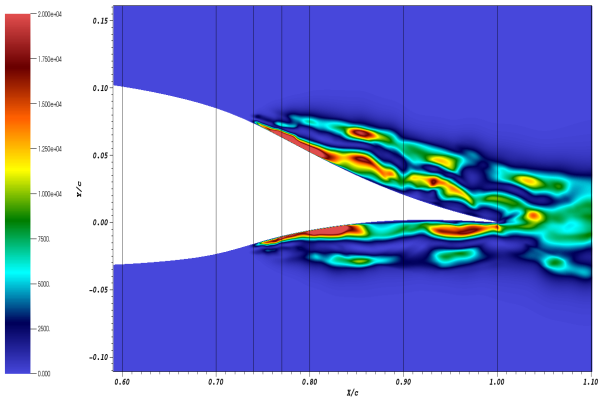

(d) Reynolds-stress Tensor Component $\overline{u^2}$ for Case 4: Clean NLF-0414 at Re_c = 2 x 10^5

Figure 126: Production Tensor Component P_{xy} Comparison Between the Clean NLF-0414 Cases at Re_c = 1 x 10^5 and Re_c = 2 x 10^5

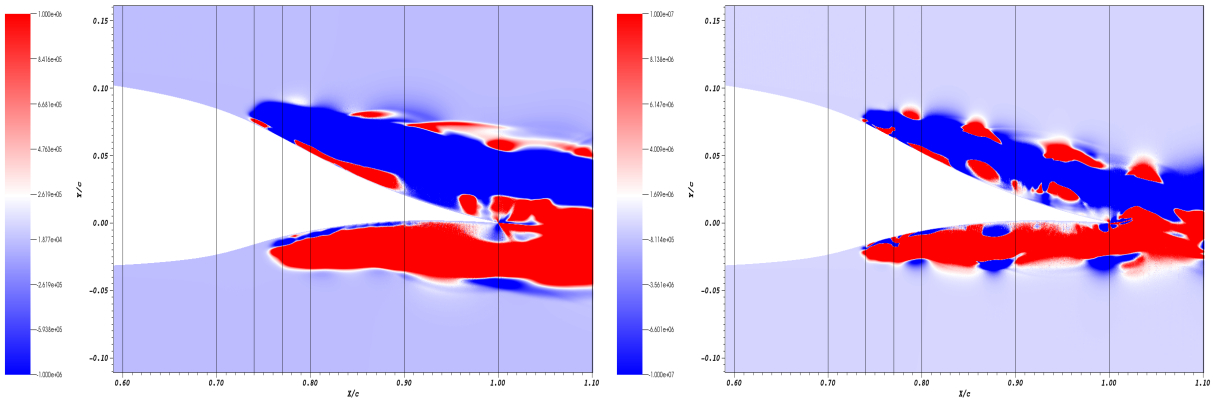

(a) Production Tensor Component P_{xy} for Case 2: Run 606 at $Re_c = 1$ x 10^5

(b) Production Tensor Component P_{xy} for Case 5: Run 606 at $Re_c = 2$ x 10^5

Figure 127: Production Tensor Component P_{xy} Comparison Between the Run 606 Cases at $Re_c = 1$ x 10^5 and $Re_c = 2$ x 10^5

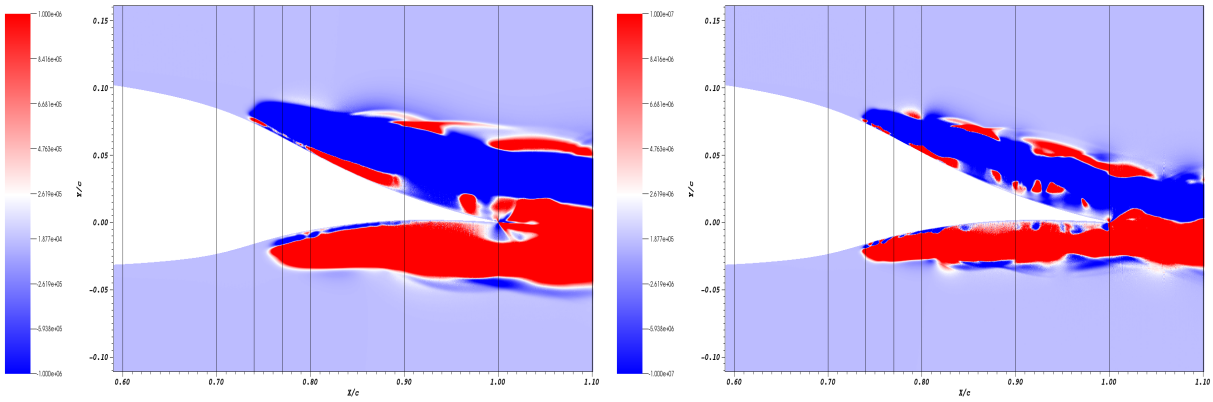

(a) Production Tensor Component P_{xy} for Case 3: Run 622-2D at $Re_c = 1$ x 10^5

(b) Production Tensor Component P_{xy} for Case 6: Run 622-2D at $Re_c = 2$ x 10^5

Figure 128: Production Tensor Component P_{xy} Comparison Between the Run 622-2D Cases at $Re_c = 1$ x 10^5 and $Re_c = 2$ x 10^5

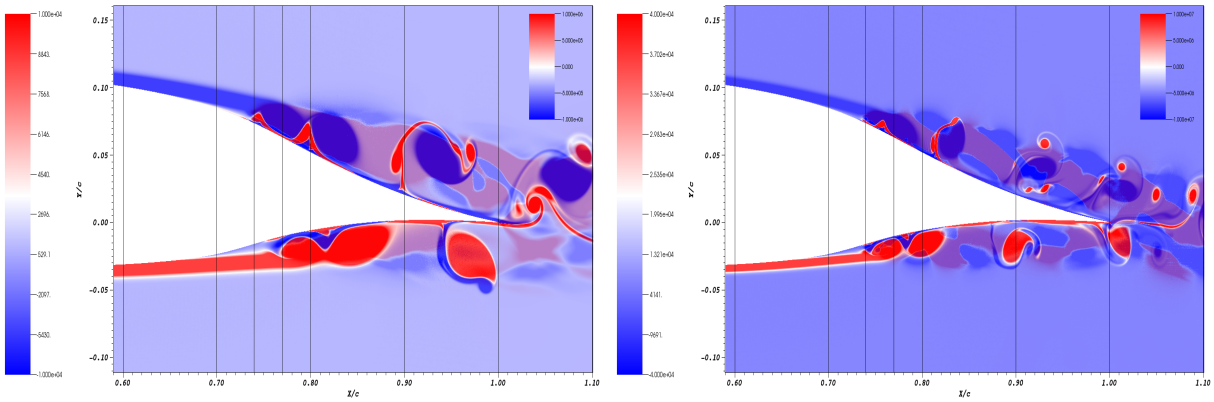

(a) Vorticity over Production Tensor Component P_{yy} for Case 1: Clean NLF-0414 at Re_c = 1 x 10^5

(b) Vorticity Over Production Tensor Component P_{yy} for Case 4: Clean NLF-0414 at Re_c = 2 x 10^5

Figure 129: Vorticity Over Production Tensor Component P_{yy} Comparison Between the Clean NLF-0414 Cases at Re_c = 1 x 10^5 and Re_c = 2 x 10^5